

UNIVERSITY OF BIRMINGHAM

MICROEMULSIFIED COLLECTOR AND DEPRESSANTS OF SULPHIDE MINERALS FOR COAL CLEANING WITH FROTH FLOTATION

by

Xuemin Zhao

School of Chemical Engineering

College of Physical and Engineering Sciences

University of Birmingham

March 2022

UNIVERSITY OF
BIRMINGHAM

University of Birmingham Research Archive

e-theses repository

This unpublished thesis/dissertation is copyright of the author and/or third parties. The intellectual property rights of the author or third parties in respect of this work are as defined by The Copyright Designs and Patents Act 1988 or as modified by any successor legislation.

Any use made of information contained in this thesis/dissertation must be in accordance with that legislation and must be properly acknowledged. Further distribution or reproduction in any format is prohibited without the permission of the copyright holder.

ABSTRACT

Flotation is the primary method for fine coal preparation with Kerosene as a collector. But low recovery of clean coal, high sulfur content, poor selectivity and high consumption are among the main factors that seriously affect the flotation efficiency. This Ph.D work aims to address some of these challenges. First, a new type of nonionic collector was therefore developed in this work. Such a new collector costs approximately 50% of that of the traditional collector with the same combustible recovery. In order to solve the problem of high sulfur content in coal, the effects of PAC (Polymeric aluminum chloride) and cooked corn starch on depressing pyrite were then studied, which have rarely been reported in the literature. More details of this work are summarized in the following:

Firstly, a new collector called MEC (Microemulsion Collector) composed of blending surfactants of Span 80 (Sorbitol fatty acid ester) and Tween 80 (Sorbitan esters and polysorbates), Kerosene, MIBC (Methyl iso-butyl carbinol) and distilled water was developed. The collector was then characterized by Dynamic Light Scattering (DLS) for size analysis, Cryo-Transmission Electron Microscope (Cryo-TEM) for morphology, electrical conductivity for structure and rheological measurement for viscosity. The small average size of the MEC indicates that MEC could disperse the oily collector and form small droplets in water to improve the combustible recovery of cleaning coal. Electrical conductivity is used to confirm the W/O structure of the new collector. The viscosity of the collector is important for collector molecue spreading on the sample surface in the flotation progress. Flotation performance studies confirmed that when the C_R (combustible recovery) was 60% and A (Ash) was 16%, the dosage of MEC was ~1000 g/t and the cost was ~7400 RMB/(10^3 t) coal slime compared to ~1000 g/t Kerosene with 14220 RMB/(10^3 t) coal slime,

due to the fact that polar oxygen functional groups on coal surface and the hydrophilic sites in MEC formed hydrogen bonding. The electrical conductivity of MEC increased with increasing concentration of mixed surfactants and water, but decreased with increasing concentration of cosurfactant. The rheological measurements of MEC indicated its Newtonian behavior with constant viscosity, which was slightly higher than that of water. The well-known EDLVO theory was then adopted to investigate the interaction mechanisms of coal samples without and with collectors. The addition of MEC and K (Kerosene) could both reduce the repulsive electrostatic interaction energies (V_E) between particles, and the reduction effect was larger for MEC than K. The hydrophobic interaction energy (V_H) and the total interaction energy (V_T) were both much more negative for MEC than for K and that of particles without reagent, signifying that the particles modified by MEC were prone to combine into larger flocs and into foam area.

Secondly, the depressants corn starch or PAC combined with the new collector were studied for depressing the pyrite. Hence the depressing effects of corn starch and PAC on pyrite were first optimized using Box-Behnken design (BBD). The optimized conditions for minimum pyrite recovery were found for corn starch as the dosage was 1490 g/t; modified pH for corn starch was 4; the heated temperature was 100°C. Under the optimized conditions, the predicted yield by BBD method was 13.92%, compared well to the actual yield of 14.01%. The optimized conditions for PAC were the dosage of PAC was 400 mg/L flotation slurry; pH of the flotation slurry was pH = 3; the concentration of PAC was 110 mL water per 1 g PAC. Under this set of optimized conditions, the predicted yield was 18.3% by BBD method, also compared well to the actual experimental yield of 18.64%.

Subsequently, combined approaches including Zeta potential, contact angle, FT-IR (Fourier Transform Infrared Spectroscopy), and XPS (X-ray Photoelectron Spectroscopy) analyses were

adopted to study the interaction mechanisms between the depressants and pyrite samples. The Zeta potential showed a steady increase of negative values with the corn starch concentration increasing, whereas the Zeta potential increased steadily from negative values to ~20 mV with the PAC concentration increasing due to the adsorption of $Al(OH)_2^+$, $Al(OH)^{2+}$, $Al_3(OH)_4^{5+}$, and $Al_2(OH)_2^{4+}$ on the surface of pyrite. The depressant-free pyrite presented a higher value of contact angle. And the contact angle of pyrite with PAC was significantly lower than that with corn starch, indicating that a much more hydrophilic surface was generated with PAC.

The XPS analyses showed that the strength of both FeOOH $2p_{3/2}$ and Fe(II)-S $2p_{1/2}$ peaks of pyrite decreased upon interaction with cooked starch, suggesting that pyrite chemically interacted with corn starch. The FeOOH concentration increased significantly from 24.46% to 41.46% with 900 g/t starch due to the formation of FeOOH coating. And the sulfate (SO_4^{2-}) concentration also increased from 4.91% to 17.09%, improving the hydrophilicity of the pyrite. Compared with the pyrite untreated with PAC, the concentration of FeOOH and sulfate (SO_4^{2-}) with 400 mg/L PAC both increased. And the O concentration increased from 46.09% to 58.11%, which would also improve the hydrophilicity of the pyrite surface.

The FT-IR results of pyrite after interaction with corn starch demonstrated that the bands at 2984 cm^{-1} and 2941 cm^{-1} due to C-H stretching of the $-CH_2$ groups increased intensity for the samples treated with corn starch. No bands were observed at 1122 and 1032 cm^{-1} for pyrite after corn starch adsorption because of the chemical interaction of corn starch with pyrite. And the results of pyrite interacting with PAC illustrated the band at 2941 cm^{-1} due to the C-H stretching of the $-CH_2$ group was very strong at the same position as that of the PAC-free. And the bands at 927 and 3362 cm^{-1} owing to hydroxyl with stretching vibration for PAC were missing after adsorbing with pyrite caused by the chemical interactions of PAC and pyrite.

ACKNOWLEDGMENTS

As a student of the Joint Ph.D., Training Program offered by the University of Birmingham (UOB) and Southern University of Science and Technology (SUSTech), I would like to express my heartfelt gratitude to my supervisor Yulong Ding in UOB and Ke Liu in SUSTech for their supervision as well as to many colleagues at UOB and SUSTech for their support during my studies.

I would also like to thank Changqing Chu and Li Weng for their detailed guidance for my experimental work as well as the review of feedback to my Ph.D. thesis.

To all my friends, junior fellow apprentice Binglong Zhao and junior female apprentice Fen Yang. Colleagues in Shenzhen Engineering Research Center for Coal Comprehensive Utilization (No. XMHT20190203001) also have given me a lot of encouragement.

Last but not least, I would like to thank my husband, my mother, my father and my lovely little sister for their everlasting support during my Ph.D period.

CONTENT

ABSTRACT I

ACKNOWLEDGMENTS IV

CONTENT V

LIST OF FIGURES IX

LIST OF TABLES XVIII

NOMENCLATURE XX

1 Introduction 1

1.1 Motivations and backgrounds 1

1.2 The outline of this thesis 9

2 Literature review 11

2.1 Collectors used in flotation 11

2.1.1 Emulsified collectors with surfactants 11

2.1.2 Types of microemulsions 21

2.1.3 Microemulsions for froth flotation 23

2.2 The depression of pyrite 33

2.2.1 Carboxymethyl cellulose (CMC) 42

2.2.2 Polysaccharide 45

2.2.3 Polymeric aluminum chloride (PAC) 57

2.3 Summary 61

3 Experimental materials and methods 63

3.1 Reagents and sample preparation 63

3.2 Particle size distribution with Dynamic Light Scattering Techniques 70

3.3 Rheological Measurements 72

3.4 Electrical conductivity 75

3.5 Cryo-Transmission Electron Microscope (Cryo-TEM) 76

3.6 Zeta potential (ζ-potential) 78

3.7 Contact Angle 82

3.8 Fourier Transform Infrared Spectroscopy (FT-IR) analyses 83

3.9 X-ray Photoelectron Spectroscopy (XPS) analyses 84

4 Results and analyses I - Characterization of MEC and interactions between MEC and coal samples 87

4.1 The preparation of MEC 87

4.1.1 The preparation of microemulsions 87

4.1.2 Screening of the MEC through froth flotation 89

4.1.3 Flotation kinetic studies 100

4.2 Particle size distribution 107

4.3 Cryo-TEM 108

4.4 Electrical conductivity 110

4.4.1 Influence of mass ratio of surfactants on the microemulsion conductivity..... 110

4.4.2 Influence of the mass ratio of cosurfactant (methyl isobutyl carbinol) on the conductivity of the microemulsion..... 111

4.4.3 Influence of H_2O concentration on the conductivity of the microemulsion 112

4.5 Rheological measurements..... 113

4.6 The EDLVO analyses of the emulsion system 114

4.6.1 Zeta potential analysis of collectors with coal sample 116

4.6.2 Contact angle analysis of collectors with coal sample 117

4.6.3 EDLVO analyses 118

4.7 Analyses of spreading velocity of MEC and Kerosene 127

4.8 A proposed mechanism for MEC attachment at the coal surface..... 130

4.9 Summary of Chapter 4 133

5 Results and analyses II - The effects of corn starch on froth flotation of pyrite and an ideal system of TXM + pyrite 136

5.1 The effect of corn starch on froth flotation of a real system 137

5.2 Box-Behnken design for studying the effect of corn starch on the recovery of pyrite . 138

5.2.1 Single-parameter experiments..... 141

5.2.2 Box-Behnken experimental design 143

5.2.3 Statistical analysis and predictions..... 146

5.3 The effect of corn starch on depressing flotation of an ideal system of TXM + pyrite 154

5.4 Summary 156

6 Results analyses III - The effect of PAC (polymeric aluminum chloride) on the flotation of pyrite and ideal system TXM + pyrite 158

6.1 Box-Behnken design of the effect of PAC on the recovery of pyrite 158

6.1.1 Single-parameter experiments 158

6.1.2 Box-Behnken experimental design 162

6.1.3 Statistical analysis 164

6.2 The effect of PAC on depressing flotation of an ideal system of TXM+pyrite 170

6.3 Summary of the chapter 6 172

7 Results analyses IV-The properties of depressants and interactions with pyrite 174

7.1 Zeta potential of pyrite with depressants 174

7.2 Contact angle of pyrite treated with corn starch or PAC 177

7.3 XPS analyses of pyrite with corn starch or PAC 179

7.4 FT-IR of pyrite and samples 194

7.5 Summary 197

8 Conclusions and future work 200

8.1 Conclusions 200

8.2 Recommendations for the future work 205

Bibliography 207

LIST OF FIGURES

Figure 1.1 The regional consumptions of the world in 2017 3

Figure 1.2 The regional consumptions of the world in 2018 3

Figure 1.3 The regional consumptions of the world in 2019 4

Figure 1.4 The regional consumptions of the world in 2020 4

Figure 1.5 China' coal energy consumption structure in 2018 6

Figure 1.6 The schematic diagram of process of collecting hydrocarbon with froth flotation 7

Figure 1.7 The structure of this Ph.D work 8

Figure 2.1 The average chord length and counts of collector droplets[25] 14

Figure 2.2 Three particles agglomeration with (a) conventional oil and (b) the new prepared HIP W/O emulsion 16

Figure 2.3 Schematic diagrams of (A) reverse micelles, (B) W/O microemulsion, (C) micelle, and (D) O/W microemulsion[35] 21

Figure 2.4 Phase diagram of a water-oil-emulsifier system, and 1φ, 2φ and 3φ refer to one phase, two-phase and three-phase 22

Figure 2.5 The yield of concentrate as a function of the dosages of collector 27

Figure 2.6 Classification of the sulfur in coal 33

Figure 2.7 Classification of desulphurization 34

Figure 2.8 Schematic representation of some of the possible reactions describing different pathways for pyrite oxidation[67] 36

Figure 2.9 The recoveries comparison of three reagents at pH = 8.5 and pH = 11 37

Figure 2.10 Flotation recoveries of sphalerite and pyrite with 2 $\times 10^{-5}$ mol/L EECTU when flotation time was 1, 2, 4, 8 min 38

Figure 2.11 Recoveries of sphalerite and pyrite with (0) no PAM , (A) adding PAM after the collector and (B) before the collector at pH = 11.0 39

Figure 2.12 Flotation recoveries of sphalerite and pyrite when flotation time was 0.5, 2, 4 and 8 min with different conditions 39

Figure 2.13 Chemical structure of the PAM and substituted PAM 40

Figure 2.14 The four types of interactions between polysaccharides and minerals[74] 41

Figure 2.15 Structure of cellulose and CMC 42

Figure 2.16 The modification methods of starch 45

Figure 2.17 The molecular configuration of (a) amylose and (b) amylopectin 46

Figure 2.18 Structural units of dextrin from Laskowski[79] 49

Figure 2.19 Structural unit of guar gum[79] 49

Figure 2.20 Effect of the proportion of 74 μm on the ash content and on the combustible recovery in lignite reverse flotation 51

Figure 2.21 Effect of the fraction of -74 μm content on the efficiency of reverse flotation of lignite 51

Figure 2.22 The individual size fractions on the ash and combustible recovery of the concentrates 52

Figure 2.23 Effect of six size distributions on the efficiency of reverse flotation of lignite. 52

Figure 2.24 The hydrolysis processing of Al species[102] 58

Figure 2.25 Concentrations of monomeric hydrolysis products of Fe(III) and Al(III)[99] 59

Figure 2.26 The mole fractions of hydrolysis products in equilibrium with amorphous hydroxides[99] 59

Figure 2.27 Schematic diagram of electrostatic patch coagulation[100] 60

Figure 2.28 Aggregate size measurement of the fine particles (-74 μm) of the minerals and coal[103] 61

Figure 3.1 The chemical structure formula of (a) MIBC, (b) DL-2 Octanol, (c) Tween 80, and (d) Span 80 66

Figure 3.2 The particle size distribution of JDMN measured by laser particle size analyzer 67

Figure 3.3 The particle size distribution of pyrite using particle size analyzer 68

Figure 3.4 The particle size distribution of TXM using particle size analyzer 68

Figure 3.5 XRD of JDMN sample 69

Figure 3.6 XRD of pyrite sample 69

Figure 3.7 XRD of TXM sample 70

Figure 3.8 Light scattering technique 71

Figure 3.9 The physical picture of Zeta potential Analyzer NanoBrook ZetaPALS (BI-200SM, Brookhaven instrument Ltd., US) 72

Figure 3.10 The structures of three dyes[113] 73

Figure 3.11 Viscosities of the nanoparticle-containing BROB, 825 and 902 with different concentrations of sunflower oil[113] 74

Figure 3.12 Dynamic viscosity η with the increasing of the volume fraction of (a) EAN and (b) [bmim][BF4] system at 30 °C[114] 74

Figure 3.13 The physical picture of HAAKE MARS 75

Figure 3.14 Sample freezing apparatus called Vitrobot 77

Figure 3.15 Automatic Electron microscope Titan Krios G3 (D3706, 300 kV) 78

Figure 3.16 Schematic diagram of zeta potential 79

Figure 3.17 Zeta potential of DDA-Kerosene emulsion and kerosene emulsion[125] 80

Figure 3.18 Comparison of zeta potentials of product from conditioning step (●) and raw coal (○) with that of the agglomerates (□) as a function of suspension pH[126] 81

Figure 3.19 The physical picture of zeta potential Analyzer NanoBrook ZetaPALS (BI-200SM, Brookhaven, United States) 82

Figure 3.20 The physical picture of contact angle measuring instrument (KRUSS DSA25S) 83

Figure 3.21 The physical picture of RAM II from VERTEX 80 (RAMII, BRUKER, Germany) 84

Figure 3.22 The physical picture of XPS instrument (PHI 5000 Versaprobe III) 86

Figure 4.1 Some physical photos of prepared MEC : (a) K :W : S : C= 38 : 11 : 34 : 17 (HLB = 6), (b) K :W : S : C= 38 : 14 : 27 : 21 (HLB = 7), (c) K :W : S : C= 65 : 3 : 13 : 19 (HLB = 7), (d) K :W : S : C= 19 : 4 : 51 : 26 (HLB = 7), (e) K :W : S : C= 46 : 6 : 31 : 17 (HLB = 7), (f) K :W : S : C= 46 : 12 : 30 : 12 (HLB = 8), (g) K :W : S : C= 43 : 12 : 35 : 10 (HLB = 8), (h) K :W : S : C= 42 : 2 : 35 : 21 (HLB = 8), (i) K :W : S : C= 51 : 13 : 27 : 9 (HLB = 9), (j) K :W : S : C= 41 : 14 : 36 : 9 (HLB = 9). (K = kerosene, W = water, S = mixed surfactant, C = co-surfactant, MIBC)..... 89

Figure 4.2 The flow chart of the flotation process 90

Figure 4.3 (a) Ash content (b) combustible recovery, and (c) improved flotation index of froth concentrate by MEC (HLB = 6) and Kerosene 94

Figure 4.4 (a) Ash content and (b) combustible recovery, and (c) improved flotation index of froth concentrate by MEC (HLB = 7) and Kerosene 96

Figure 4.5 (a) Ash content and (b) combustible recovery, and (c) improved flotation index of froth concentrate by MEC (HLB = 8) and Kerosene 98

Figure 4.6 (a) Ash content (b) combustible recovery, and (c) improved flotation index of froth concentrate by MEC (HLB = 9) and Kerosene 100

Figure 4.7 Comparison of six kinetic models fitted to the experimental data of various size fractions[137] 103

Figure 4.8 Effect of collectors on the cumulative combustible recovery during the flotation process (The experimental conditions were below: the pulp concentration was 100 g/L,

the agitation speed was 2000 r/min, the aeration rate was 0.3m^3/m^2/min, and the dosage of Kerosene or MEC were both 2000 g/t) 106

Figure 4.9 The Fuerstenau upgrading curves of collectors for coal sample 107

Figure 4.10 Size distribution of Kerosene/(Span80+Tween80)/MIBC/water microemulsion system 108

Figure 4.11 Cryo-TEM image for (a) MEC solution and (b) MEC solution after 180 days 109

Figure 4.12 Relationship between the mass ratio of surfactant and the conductivity of the microemulsion 110

Figure 4.13 Relationship between the concentration of cosurfactant and the conductivity of the microemulsion 112

Figure 4.14 Relationship between the ratio of water to oil and the conductivity of the microemulsion 113

Figure 4.15 Steady shear viscosity as a function of the shear rate for MEC at 25°C 114

Figure 4.16 Zeta potential of particles treated with Kerosene and MEC 117

Figure 4.17 The contact angle of Kerosene and MEC with the changes of the dosage of collectors 118

Figure 4.18 The interaction energies between particles with different dosages of MEC and Kerosene, (a) V_E of MEC, (b) V_E of Kerosene, (c) V_H of MEC, (d) V_H of Kerosene, (e) V_T of MEC and (f) V_T of Kerosene 123

Figure 4.19 Comparisons of interaction energies between particles surfaces modified by MEC and Kerosene ((a) V_E without and with reagents, (b) V_H without and with reagents and (c) V_T without and with reagents) 125

Figure 4.20 The Van der Waals interactions of MEC and K 126

Figure 4.21 Physical picture of Surface Tension Meter 128

Figure 4.22 The surface tension of MEC and Kerosene 128

Figure 4.23 The result of coal-oil-water contact angle 129

Figure 4.24 The proposed W/O structure of microemulsion 131

Figure 4.25 Schematic diagram of the mechanism for MEC dispersed in water forming Winsor III ($W_1/O/W_2$) microemulsion 132

Figure 4.26 Schematic diagram of the interactions between Winsor III and coal particle .. 133

Figure 5.1 The effects of dosage of raw starch and cooked starch on recovery and sulfur content of cleaning coal 138

Figure 5.2 Designed test points of CCD and BBD 140

Figure 5.3 Effect of the modified pH of corn starch on pyrite depression 142

Figure 5.4 Effect of the heated temperature of corn starch on pyrite depression with 1200 g/t corn starch and the modified pH = 3 143

Figure 5.5 The effects of (A) the dosage of corn starch and (B) modified pH of corn starch on the recovery of pyrite 151

Figure 5.6 The effects of (b) pH of corn starch and (c) heated temperature on the recovery of pyrite..... 152

Figure 5.7 The effects of (a) the dosage of corn starch and (c) heated temperature on the recovery of pyrite 153

Figure 5.8 The detailed process of the medium oxidized coal 154

Figure 5.9 The flotation result of low oxidized coal 155

Figure 5.10 The flotation result of medium oxidized coal 156

Figure 6.1 Effect of the dosage of PAC on pyrite depression 159

Figure 6.2 Effect of the pH of the flotation slurry on pyrite depression 160

Figure 6.3 Effect of the water dilution of PAC on pyrite depression 161

Figure 6.4 The recovery of pyrite as a function of (a) the dosage of PAC and (b) pH of flotation slurry..... 168

Figure 6.5 The recovery of pyrite as function of (a) the dosage of PAC and (c) the concentration of PAC 169

Figure 6.6 The effects of the dosage of PAC on the flotation result of low oxidized coal.. 171

Figure 6.7 The effects of the dosage of PAC on the flotation result of medium oxidized coal 171

Figure 7.1 Zeta potential and the recovery of pyrite as a function of corn starch concentration at pH = 11 175

Figure 7.2 Zeta potential and recovery of pyrite with the changing of..... 176

Figure 7.3 Contact angle and recovery of pyrite with the changing of corn starch concentration at pH = 11 177

Figure 7.4 Contact angle and recovery of pyrite with the changing of 178

Figure 7.5 XPS results of pyrite without and with corn starch for Fe(2*p*) 181

Figure 7.6 XPS results of pyrite without and with corn starch for S(2*p*) 183

Figure 7.7 XPS results of pyrite without and with corn starch for O(1*s*) 187

Figure 7.8 XPS results of pyrite without and with PAC for Fe(2*p*) 189

Figure 7.9 XPS results of pyrite without and with PAC for S(2*p*) 191

Figure 7.10 XPS results of pyrite without and with PAC for O(1*s*) 193

Figure 7.11 FT-IR of pyrite without and with PAC 194

Figure 7.12 FT-IR of pyrite without and with corn starch 197

LIST OF TABLES

Table 1.1 World energy consumption structure and China's coal proportion in energy structure 2

Table 1.2 The productive rate of raw coal separation 5

Table 2.1 Comparisons of emulsified collectors from the literature 18

Table 2.2 The flotation results using different collectors and frothers 25

Table 2.3 The flotation results using different collectors and frothers 26

Table 2.4 Comparisons of microemulsified collectors from the literature 29

Table 2.5 Comparisons of the CMC for froth flotations 44

Table 2.6 The gelatinization and swelling properties of different starches 47

Table 2.7 Comparisons of the Polysaccharide for froth flotations 55

Table 2.8 The Al (III) species of Polymeric aluminum chloride[102] 57

Table 3.1 The chemicals used in this study 65

Table 3.2 The instruments used in this study 67

Table 4.1 The prepared MEC when HLB = 6 87

Table 4.2 The prepared MEC when HLB = 7 88

Table 4.3 The prepared MEC when HLB = 8 88

Table 4.4 The prepared MEC when HLB = 9 88

Table 5.1 Experimental ranges and factor levels of different parameters in the design 144

Table 5.2 Experimental runs suggested by BBD 145

Table 5.3 Experimental design and results with response surface method of pyrite sample 148

Table 5.4 ANOVA results for developed models for recovery of pyrite 149

Table 6.1 Experimental ranges and factor levels of different variables in the experimental design 162

Table 6.2 Experimental runs suggested by BBD 163

Table 6.3 Experimental design and results with response surface method of pyrite sample 165

Table 6.4 ANOVA results for developed models for recovery of pyrite 166

Table 7.1 Atomic concentrations of main elements on pyrite surface without and with 300 g/t starch and 900 g/t starch 184

Table 7.2 Binding energies and atomic concentrations of Fe(2*p*) and S(2*p*) for pyrite without and with 300 g/t starch and 900 g/t starch 184

Table 7.3 Binding energies and atomic concentrations of O(1*s*) on pyrite surfaces without and with 300 g/t and 900 g/t starch 185

Table 7.4 Atomic concentrations of main elements on pyrite surface without and with the addition of 300 mg/L and 400 mg/L PAC 191

Table 7.5 Binding energies and atomic concentrations of O(1*s*) on pyrite surfaces treated with PAC 193

NOMENCLATURE

SYMBOLS

A_{11}	Hamaker constant of coal particles/J
A_{132}	Hamaker constant of particles in water/J
A_{22}	Hamaker constant of the collector/J
A_{33}	Hamaker constants of the water/J
A_{ad}	Ash of air-dried basis/%
A_c	Ash content of the froth product /%
A_f	Ash content of the feeding/%
C	A constant depending on the sample surface
C_{ad}	Carbon of air-dried basis/%
C_{KCl}	The concentration of KCl solution/(mol/L)
C_R	The combustible recovery/ %
FC_{ad}	Fixed carbon of air-dried basis/%
H	The distance between the spherical particles/m
h_0	The decay length/m
H_{ad}	Hydrogen of air-dried basis/%
I_F	the improved flotation index/ %
k	The flotation selectivity
k_1	The flotation rate constant of the combustible recovery
k_2	The flotation rate constant of the ash content
M_{ad}	Moisture of air-dried basis/%

NOMENCLATURE

M_c	mass of the froth product/ g
M_f	mass of feeding /g
N_{ad}	Nitrogen of air-dried basis/%
O_{ad}	Oxygen of air-dried basis/%
R	The radii of spherical particles/m
S	The spreading coefficient/(N/m)
S_{ad}	Sulfur of air-dried basis/%
t	collecting time/ s
V_{ad}	Volatile matter of air-dried basis/%
V_E	The electrostatic interaction energy/J
V_H	The hydrophobic interaction energy/J
V_S	The spreading velocity
V_T	The total interaction energy/J
V_W	The Van der Waals interaction energy/J
γ	shear rate/(s^{-1})
γ	The interfacial tension/(N/m)
ε_a	Ash recovery /%
ε_a	The permittivity in the vacuum/ J-1m-1
$\varepsilon_{a\infty}$	maximum ash recovery/%
ε_c	Combustible recovery /%
$\varepsilon_{c\infty}$	maximum combustible recovery/%
η	Viscosity/(Pa·s)

θ	The contact angle/°
τ	Shear stress/(Pa)
ϕ_0	particle surface electronic potentials/V
κ	The reciprocal Debye length/m
k_1	incomplete hydrophobic coefficient
γ_{WC}	The interfacial tension of water and coal surface/(N/m)
γ_{OC}	The interfacial tension of oil and coal surface/(N/m)
γ_{OW}	The interfacial tension of oil and water/(N/m)

ABBREVIATIONS

$AlCl_3$	Aluminium chloride
ANOVA	The analysis of variance
BBD	Box-Behnken design
CaO	Calcium oxide
$CaSO_4$	Calcium sulfate
CCD	Central Composite Design
Cryo-TEM	Cryo-Transmission Electron Microscope
DLS	Dynamic Light Scattering
EDLVO theory	the Extended Derjaguin-Landau-Verwey-Overbeek theory
$Fe_2(SO_4)_3$	Ferric sulfate
FeOOH	Hydroxyl oxidize iron
FeS_2	Ferrous disulfide
FT-IR	Fourier Transform Infrared Spectroscopy
H_2SO_4	sulfuric acid
HLB	Hydrophilic-lipophilic balance
JDMN	Jinda MeiNi
JDTTJM	JinDaTiaoTai JingMei
K	Kerosene

NOMENCLATURE

KCl	potassium chloride
L	The low oxidized coal
M	The medium oxidized coal
MEC	Microemulsified collector
MIBC	methyl iso-butyl carbinol
NaOH	Sodium hydroxide
O/W	Oil in water
PAC	Polymeric chloride aluminum
PDI	The polydispersity coefficient
RSM	response surface methodology
Span 80	Sorbitol fatty acid ester
Tween 80	sorbitan esters and polysorbates
TXM	TaiXi Mei
W/O	Water in oil
$W_1/O/W_2$	Water 1 in oil in Water 2
X_1	The dosage of corn starch or PAC
X_2	pH of corn starch or the pH of flootation slurry
X_3	Heated temperature or the concentration of PAC
XPS	X-ray photoelectron spectroscopy

1 Introduction

1.1 Motivations and backgrounds

According to the data of the National Bureau of Statistics of the People's Republic of China in 2019, China's total energy production was 3.62 billion tons of standard coal equivalent in 2018, which was an increase of 6.0% compared to 2016. This increasing trend was after the peak of 3.97 billion tons in 2013, then the coal production was seen to decrease to 3.87 billion tons, 3.75 billion tons and 3.41 billion tons in 2014, 2015, and 2016, respectively. But then the value kept going up. In 2018, raw coal accounted for 69.2% of primary energy production, followed by oil (7.2%), natural gas (5.4%) and primary power (18.2%). The changes in the primary energy production were -0.6 percentage, -1.1 percentage, +0.2 percentage, +1.5 percentage compared to 2016, respectively. These data suggest that the proportion of clean energy production increases while the proportion of coal production decreases, indicating that China's energy production structure become more diverse.

Data on energy consumption showed that the total energy consumption of China in 2018 was 4.72 billion tons of standard coal equivalent with an average annual growth rate of 2.7% from 2015 to 2019, which was 1% lower than that value from 2008 to 2015, demonstrating a slowed growth in total energy consumption. Among them, the total coal consumption decreased slowly from 4.24 billion tons in 2013 to 3.89 billion tons in 2016 and then went up gradually. In the energy consumption structure, raw coal accounted for 58.2% in 2018, which was 5.5 percent lower than that in 2015. Oil took 19.6% in 2018, which was the same compared to 2015, whereas the natural gas consumption was 7.4%, a 1.5 percentage increase compared to 2015. Primary electricity and other energy sources accounted for 14.7% in 2018, which was 2.8 percent higher than that in 2015.

These data show that the energy consumption structure has been continuously optimized by decreasing the proportion of coal consumption and increasing the ratio of clean energy. All in all, the proportions of coal production and consumption in the Chinese energy structure both declined, and the mining industry needs to be reformed urgently.

There is still a mass demand for coal globally at least in shut to medium term. This can be illustrated by the world energy consumption structure from 2010 to 2020 shown in Table 1.1. The proportion of coal around the world maintained at about 30% in the past decade. In China, the proportion of coal was over 58% in 2020. Thus it can be seen that the coal demand is likely to remain stable for the forseeable future, and the coal resource is still likely to be dominant in the energy consumption structure in some countries particularly China.

Table 1.1 World energy consumption structure and China’s coal proportion in energy structure

Year	World energy structure consumption/%						The proportion of coal in China's energy structure/%
	Oil	Natural Gas	Coal	Nuclear energy	Hydro-electricity	Renewables	
2010	33.6	23.8	29.6	5.2	6.5	1.3	70.5
2011	32.6	23.7	30.3	4.9	6.5	1.6	70.4
2012	32.9	23.9	29.9	4.5	6.7	1.9	68.5
2013	33.1	23.7	30.1	4.4	6.7	2.2	67.5
2014	33.1	23.7	30	4.4	6.8	2.5	66.0
2015	33.6	23.8	29.2	4.4	6.8	2.8	63.7
2016	33.3	24.1	28.1	4.5	6.9	3.2	69.8
2017	34.2	23.4	27.6	4.4	6.8	3.6	69.6
2018	33.6	23.9	27.2	4.4	6.8	4	69.2
2019	33.1	24.2	27	4.3	6.4	5	68.6
2020	31.2	24.7	27.2	4.3	6.9	5.7	56.8

The main energy source in the Asia Pacific region is coal in 2017, 2018, 2019 and 2020 as can be seen in Figure 1.1, Figure 1.2, Figure 1.3 and Figure 1.4 , respectively.

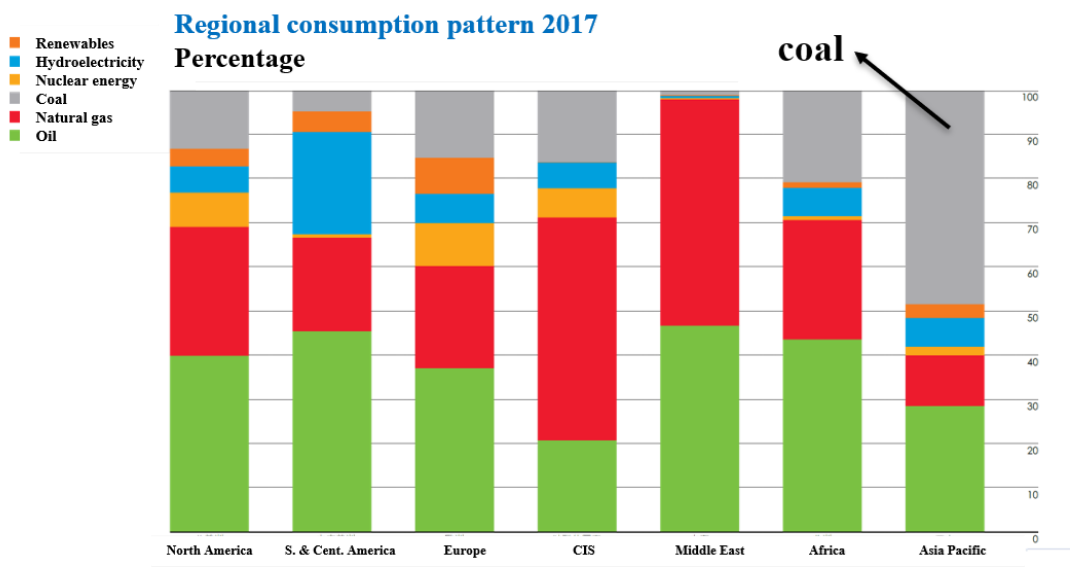


Figure 1.1 The regional consumptions of the world in 2017

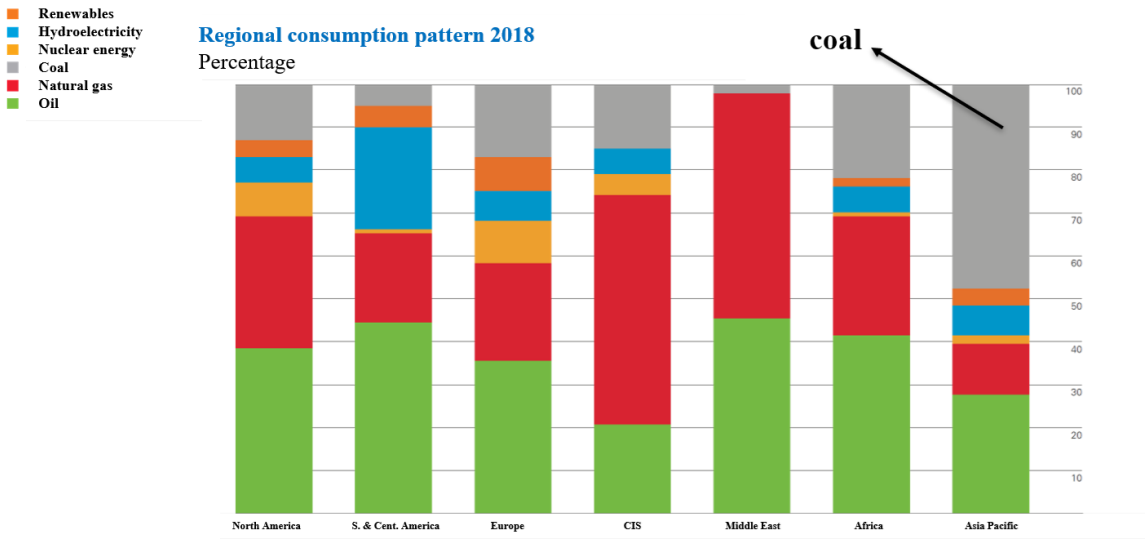


Figure 1.2 The regional consumptions of the world in 2018

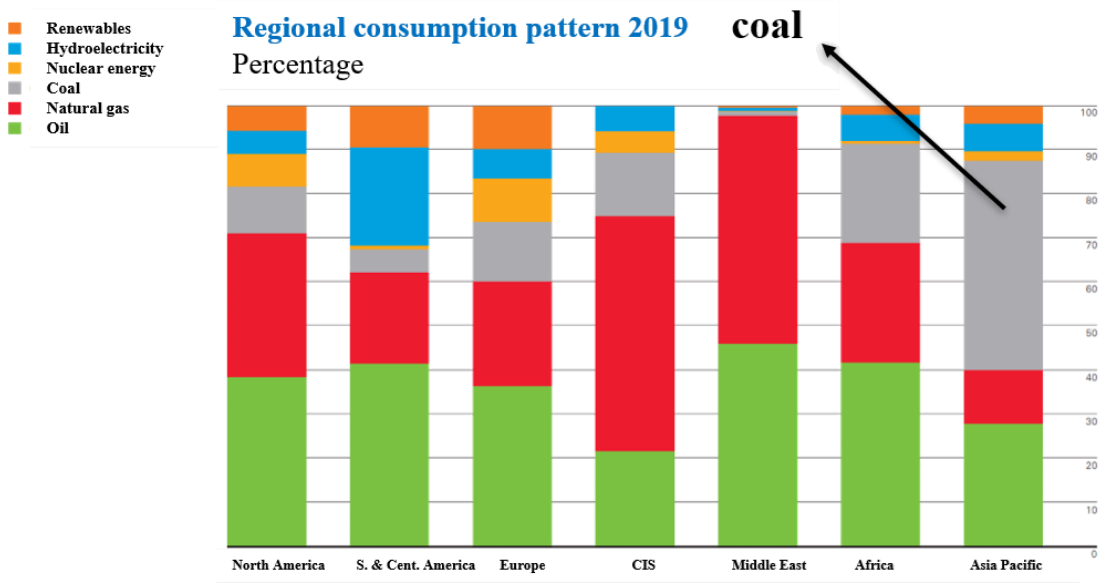


Figure 1.3 The regional consumptions of the world in 2019

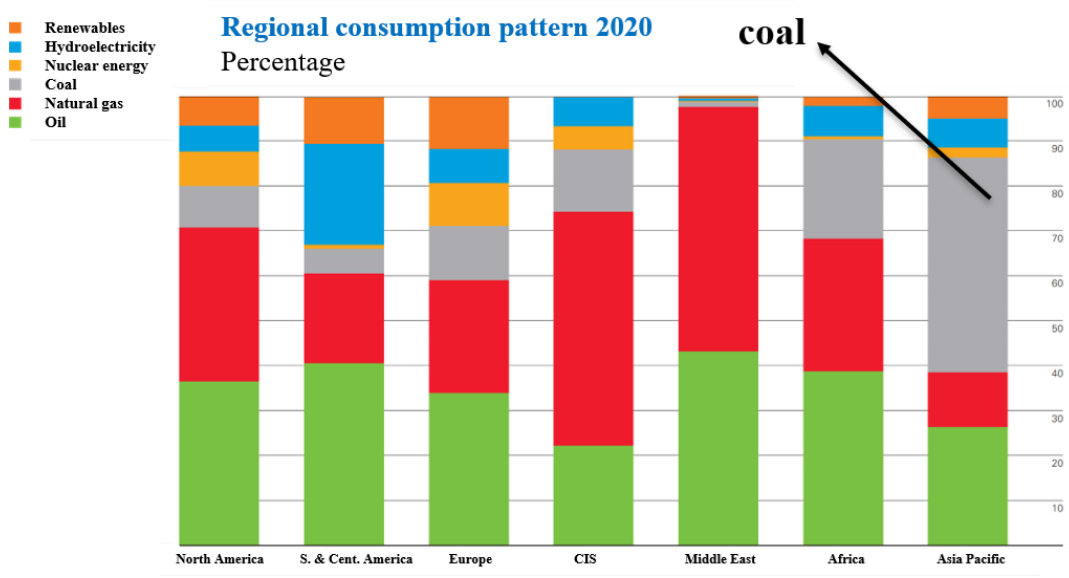


Figure 1.4 The regional consumptions of the world in 2020

The continuous use of coal in China faces challenges, not only due to the climate change related problem, but also other respects detailed in the following. First, China's coal industry faces problems associated with underdeveloped processing of raw coal and low preparation rate. Coal preparation processes help to purify energy source, achieving a high carbon content and thus an

improved comprehensive utilization of coal. According to the data of China Coal Processing and Utilization Association, 10 to 15 million tons of coal can be saved for every 100 million tons of raw coal processed. Based on the production of 3.75 billion tons of raw coal in 2015, about 300 million tons of coal can be saved. Table 1.2 shows the data of Chinese raw coal and the preparation rate from 2010 to 2018. It can be seen that the preparation rate of raw coal showed a steady increase, and the rate increased 20.9% over the five years. However, this preparation rate is still lower than some developed countries in the world such as Japan, Germany and Canada, the United Kingdom and Australia with a preparation rate of commercial coal at 100%, 95% and 75%, respectively.

Table 1.2 The productive rate of raw coal separation

Year	2010	2011	2012	2013	2014	2015	2016	2017	2018
Raw coal /billion ton	3.24	3.52	3.66	3.97	3.87	3.75	3.4	3.52	3.62
Processed raw coal/billion ton	1.65	1.8	2.05	2.21	2.42	2.44	2.35	2.47	2.6
productive rate/%	50.9	51.1	56	55.8	62.5	65.1	68.9	70.2	71.8

Secondly, the rough use of coal in China is highly unreasonable, and hence deep processing and rational utilization of coal and other technologies need to be strengthened. This is illustrated in Figure 1.5, which shows that 53.8% coal was still used in the traditional power industry through direct combustion, which was a serious waste of coal. This led to the sulfur compounds, nitrogen compounds, carbon dioxide and other emissions, which have been blamed for the severe pollution in China in recent years. In addition, the solid waste generated by combustion is also detrimental to the environment. These call for urgent development of advanced separation methods to process coal efficiently.

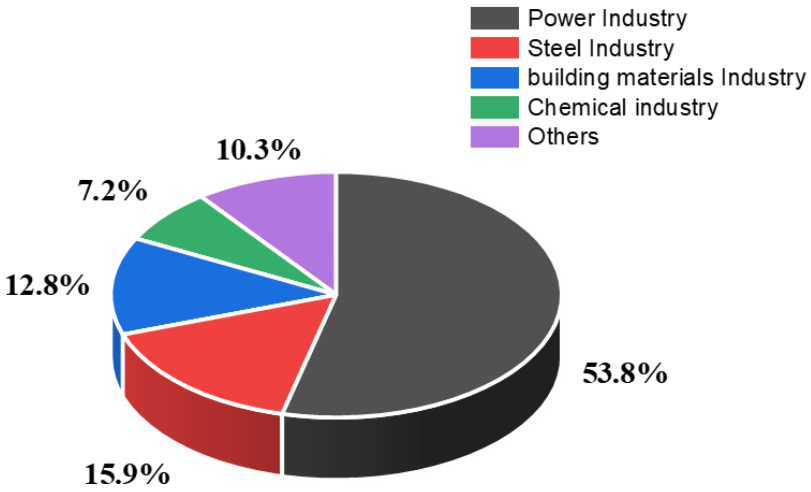


Figure 1.5 China' coal energy consumption structure in 2018

Froth flotation is an effective separation method for fine coal which is based on different hydrophobicities of organic hydrocarbons and minerals[1-3]. In flotation, air input to the slurry makes the hydrophobic particles attach to bubbles and float to cell surface for collection while the hydrophilic mineral particles are still dispersed in slurry as shown in Figure 1.6. Coal is considered as a natural floatable material because of great differences in wettability between combustible materials and minerals in raw coal. The conventional collectors like kerosene or diesel used in froth flotation are unsatisfactory in regard to efficiency and cost[4-6]. More hydrophobic agents with low-cost and low dosage are needed to improve the quality of cleaning coal and economic efficiency.

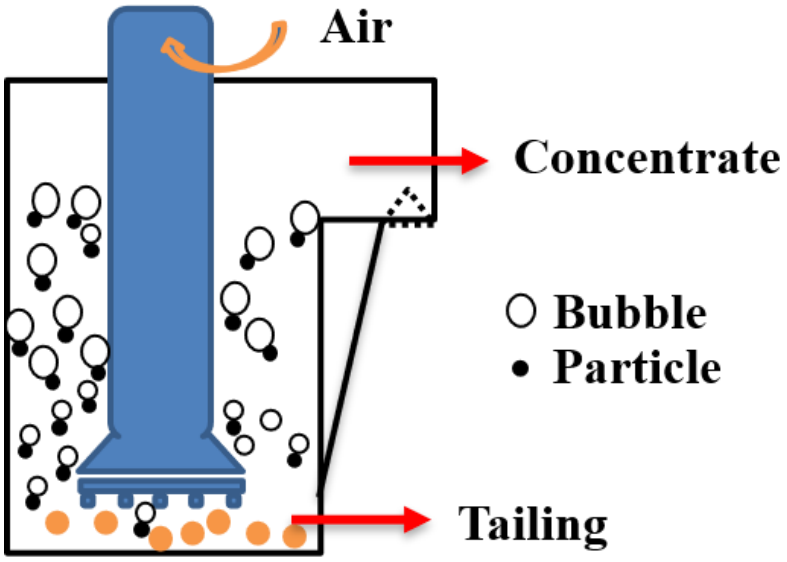


Figure 1.6 The schematic diagram of process of collecting hydrocarbon with froth flotation

Minerals like pyrite often exist in coal mines as waste because both coal and minerals are floatable and it is difficult to remove them from coal. When a large number of mineral particles are entrained with the fine hydrocarbon particles to the froth phase, the quality of the cleaned coal will be reduced, which lowers economic benefits[7]. Also, the oxidative decomposition of pyrite on the coal surface can lead to disastrous environmental problems like acid rain[8-10].

There is, therefore, a need to develop a depressant to separate pyrite from hydrocarbons in the froth flotation processing.

This Ph.D. study aims to develop a new type of nonionic collector based on Span 80, Kerosene, MIBC and Tween 80 for the flotation of fine coal slime. Flotation performance is investigated to confirm that MEC could significantly reduce the economic cost with a similar recovery. Various analytical methods, such as DLS, rheometer and conductivity meter were employed to characterize the new collector.

Causticized corn starch and raw starch were studied in-depth by researchers home and abroad, while physically modified corn starch has hardly ever been reported. So physically modified corn starch is studied in this Ph.D work. For PAC (Polymeric aluminum chloride), some researchers reported that it had a good performance regarding depressing the ash of the coal samples. Because ash is composed of kaolinite, pyrite, quartz, calcite, etc., the depressing effect of PAC on pyrite is also studied in this thesis.

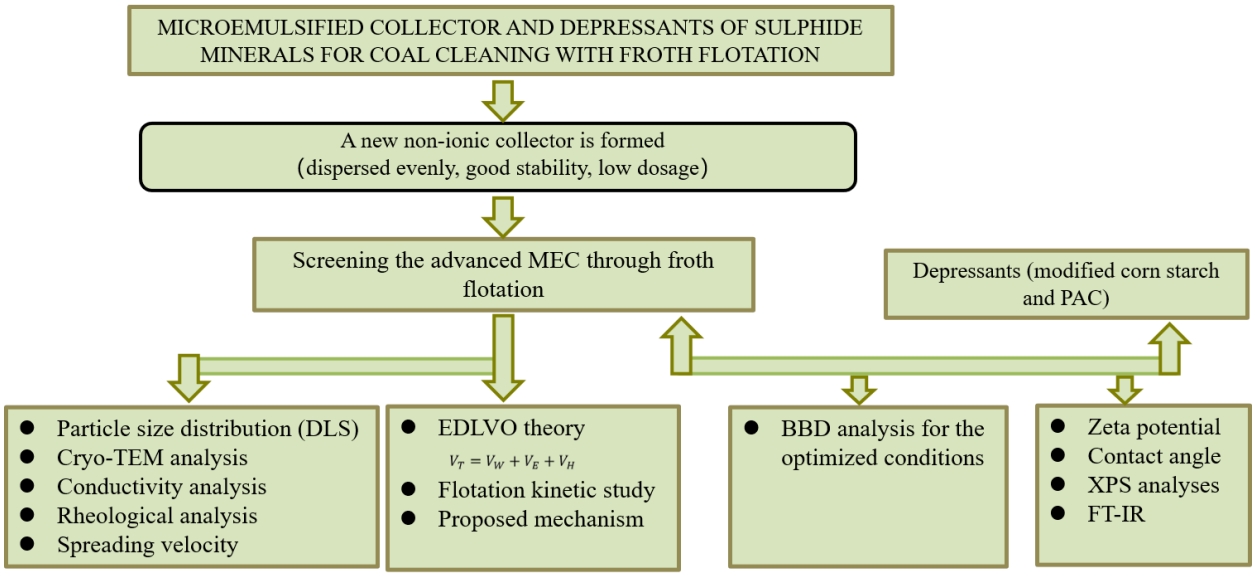


Figure 1.7 The structure of this Ph.D work

Figure 1.7 shows the structure of this Ph.D work. The work involves the following:

- The development of a new type of nonionic reagent: the new formulation is based on Span 80, Kerosene, MIBC and Tween 80, specifically for the flotation of fine coal slime to resolve the high dosage and poor dispersity of the traditional collector. The flotation performances of MEC and Kerosene were compared to obtain the optimal ratio of the MEC;
- The characterizations of the new collector: the particle size, the rheological behavior, the electrical conductivity, and dispersion behavior were measured to study the effects of

properties of the new collector on the froth flotation. The small particle size of the MEC indicates that MEC could disperse the oily collector and form small droplets in water to improve the combustible recovery of cleaning coal. Electrical conductivity is used to confirm the W/O structure of MEC. The viscosity of the collector is important factor for collector molecue spreading on the sample surface in the flotation progress. EDLVO theory is used to explain the interactions of particles without and with collectors in flotation;

- The depressant study aims to resolve the pyrite entrainment in the cleaned coal. The effects of dosage of reagent, pH of the solution and the modification temperature on the pyrite recovery are studied in detail. In addition, efforts were made to find out the primary factors that influence the pyrite recoveries;
- Mechanisms of depressants of improving the hydrophilic property of pyrite are studied using several analytical tools, including zeta potential, contact angle, FT - IR and XPS analyses.

1.2 The outline of this thesis

The thesis is composed of eight chapters: an introduction chapter, followed by a literature review and five chapters to discuss results, and finally a conclusion chapter. These are detailed in the following：

Chapter 2 gives a literature review, which summarizes the state of the art development in aspects relevant to microemulsions and depressants;

Chapter 3 presents materials and methodologies used in this work;

Chapter 4 shows the characterization results of MEC and discusses the interactions of MEC and coal samples;

Chapter 5 discusses the effects of corn starch on froth flotation of pyrite, and compares the results with an ideal TXM+pyrite system;

Chapter 6 studies the effects of PAC (polymeric aluminum chloride) on the flotation of pyrite and compares the results with an ideal TXM+pyrite system;

Chapter 7 discusses the adsorption mechanism of depressants on pyrite particles;

Chapter 8 summarizes the main findings of this Ph.D work and provides recommendations for the future research.

2 Literature review

This chapter focuses on two aspects which are highly relevant to this study:

(I) Conventional collectors such as kerosene or diesel are unsatisfactory in flotation in regard to efficiency and cost for ultra-fine high-ash oxidized coal slime because the physical and chemical adsorption of oxygen-containing functional groups always occurs on the surface of hydrocarbons[4-6]. This calls for a need to explore new collectors with a lower dosage and a better economy. This has attracted worldwide researchers to work on the area, particularly emulsified polar or non-polar oily collectors and microemulsified collectors instead of diesel or kerosene.

(II) Flotation desulfurization has been the approach to depress the floatability of pyrite entrainment with hydrocarbons in flotation. It is a challenge to find effective depressants to depress the floating of pyrite and improve the quality of cleaned coal. Among the most studies include polysaccharide polymers (starch, guar gum, dextrin), carboxymethyl cellulose (CMC) and polymeric aluminum chloride (PAC).

2.1 Collectors used in flotation

2.1.1 Emulsified collectors with surfactants

Surfactants can be categorized into three broad categories of zwitterionic, cationic, and anionic. These surfactants have been used in detergent, cosmetics, pharmaceutical, food processing, and material synthesis. A surfactant consists of hydrophilic groups on one side and hydrophobic groups on the other side.

Xu et al.[11] used 500 g/t emulsified diesel (n-octylamine: diesel = 1 : 4) for oxidized coal flotation and the yield was much higher with 500 g/t new collector (51.68%) than that with 2000 g/t diesel (37.52%) when an ash content of 15% was obtained. Zhu et al.[12] mixed oleic acid (OA) and Kerosene with the mass ratio of $\frac{\text{OA}}{\text{OA+Kerosene}} =$ 0.1, 0.2, 0.3, and 0.4, respectively, for a new flotation collector and observed that the recovery increased with the increased ratio of oleic acid (OA). The concentrate yield using 1000 g/t novel collector ($\frac{\text{OA}}{\text{OA+Kerosene}} = 0.2$) was 74.01%, which was more significant than the result using 2000 g/t kerosene (yield = 67.93%). These results indicated that the novel collectors with the addition of OA had a stronger collectivity than kerosene. Meanwhile, the flotation rate constant also grew up, indicating a better flotation performance of the emulsified collector. Cebeci et al.[13] pointed out that low-ash and high-recovery product could be obtained by a combination of 70% Kerosene, 5% emulsifier (Acorga M 5640) and 25% non-ionic surfactant (Flotigol CS), and the surfactant could disperse the oily collectors and form small droplets in water. They observed that the combustible recovery increased to 89.45% with 1250 g/t new collector compared to that of 32.03% with kerosene. In addition, the concentrates could give a higher combustible recovery with the new collector as the ash content was the same as Kerosene. Xie et al.[14] adopted a wash oil as a collector in their study and obtained a product with 10.78% (ash content) and 70.12% (yield) using 800 g/t wash oil, 40 g/t sec-octyl alcohol, and 1000 g/t sodium sulphite (depressant) with 50 g/L sodium naphthalene sulphonate-formaldehyde condensation compound (dispersant). The flotation process of rough separation-final separation with 40 g/L n-octyl alcohol and 66 g/L washing oil led to the final product with a yield of 67.32%, an ash content of 9.57%, and a perfect flotation index of 49.25%.

There were also studies[15-17] with emulsified Kerosene or diesel and the results showed that the reagent consumption could be reduced by 39% to 70%.

The synergistic interaction between Triton X-100 and diesel and their adsorption on different oxidized hydrocarbon surfaces were studied by Chang et al.[18]. The emulsification of polyethylene glycol octylphenol ether (Triton X-100) on diesel increased the adsorption of diesel oil on the coal surface and reduced the particle size of 6.7×10^{-3} mol/L diesel droplets from 90 μm to 20 μm with 1×10^{-5} mol/L Triton X-100. Laskowski et al.[19] found the emulsified kerosene with dodecyl sulfate (DDS) remarkably reduced the size of oil droplets, and the oil consumption with emulsified kerosene decreased from 30% to 1% with the same recovery and ash of the products from 8% to 4%. Boylu et al.[20] studied the effect of emulsified 5% diesel oil with 2% decanol on the entrainment in the flotation of a low-rank coal. The agglomerate flotation was done with 8000 g/t emulsified collector. They observed that the hydrophobicity of coal particles was improved at low oil dosages.

Li et al.[21] investigated the effects of ethylene oxide (EO) number in dodecyl ethoxyl ethers ($C_{12}EO_n$, n = 7, 15, 23) on the floatability of a low-rank coal (-200 μm). For $C_{12}EO_n$ with different EO numbers, the amount of $C_{12}EO_{23}$ was lowest with the same recovery (84.55%). As the number of EO in $C_{12}EO_n$ increased, a greater selectivity (low ash content) was achieved. Xia et al.[22][23] found that 1.0 mmol/L dodecyltrimethylammonium bromide (DTAB) could give a product yield of 75.37% with an ash content of 10.13%, which was twice as much as that of 4000 g/t dodecane (45.5%) likely because DTAB improved the coverage of oxygen-containing groups, improving the hydrophobic property of low-rank coal. Xing et al.[24] reported the use of 2000 g/t diesel mixed with 40% octanoic acid gave a maximum recovery of 70% with an ash content of 7.9%, which was probably due to a synergistic effect of polar reagent and nonpolar reagent. Non-polar reagent

not only adsorbed on the carbon atom sites, but also adsorbed on the oxygen-containing sites with the help of the polar reagent.

Liao et al.[25] mixed dodecane and oleic acid with a mass ratio of 4 : 1 to study the mixed collector on the flotation of low-rank coal. The average length of MC (Mixed Collector) in water was 13.81 μm, while that for oleic acid (OA) and dodecane (D) were 18 μm and 30.58 μm, respectively, as shown in Figure 2.1. And the combustible recovery and flotation efficiency of MC were higher than OA and D. And 3000 g/t MC obtained the products with the combustible recovery of 89.41% compared to 63.64% and 40.55% for OA and D.

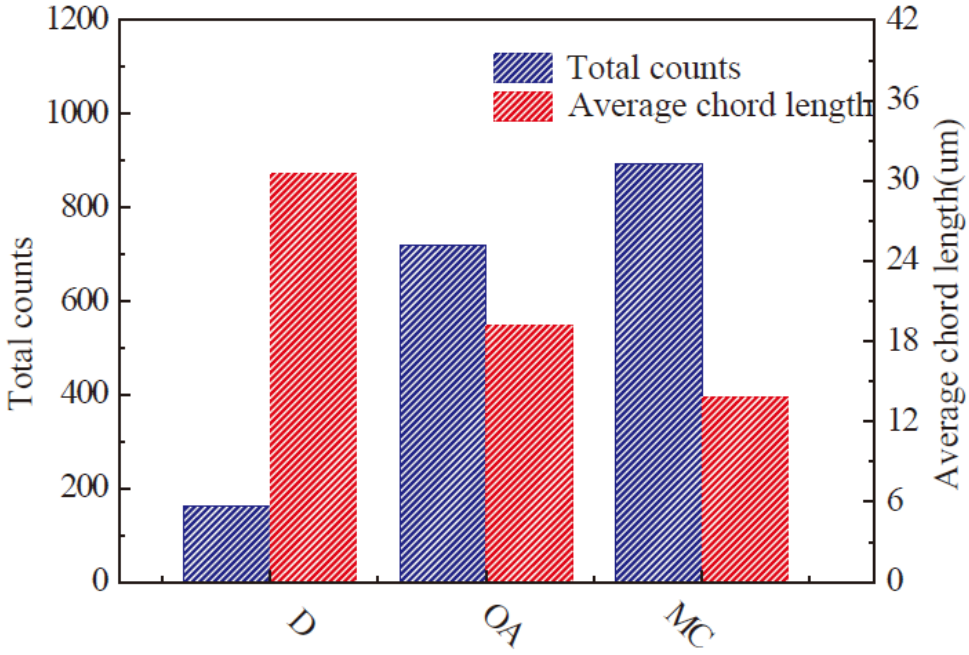


Figure 2.1 The average chord length and counts of collector droplets[25]

Xie et al.[26] prepared a new emulsified flotation agent (ZFC) with 70% water, 3% new flotation promoter and 27% diesel. The flotation rate constant of ZFC was found to be greater than that of the conventional collector diesel. Xing et al.[27] prepared a new polar compound collector (CC)

containing diesel and aliphatic acid combined with octanol and found an optimal recovery of 76.24% with a better flotation selectivity in an oxidized coal flotation. Chen et al.[28] combined 10000 g/t diesel oil, 500 g/t MIBC with 0.096 g/L didodecyl dimethylammonium bromide (DDAB) pretreatment to samples for 12 h to enhance the flotation performance of a low-rank coal. They obtained a product with ash of 5.59% and combustible recovery (R) of 90.28%, which was a one-third increase compared to the result with diesel (R = 65%). Zhang et al.[29] studied the effects of 500 g/t 10% sodium petroleum sulfonate with diesel on the flotation of a fly ash sample with 750 g/t glycol-based frother at pH = 9. Their results showed that the recovery was doubled using a 500 g/t emulsified collector (86.5%) compared with 500 g/t diesel (41%).

Lu et al.[30] developed a high internal phase water-in-oil (W/O) emulsion with 2 g Span 80, 70.83 g Sodium chloride (1 M) and 8 g Kerosene. This was dispersed into Winsor III ($W_1/O/W_2$) when mixed with water, and the hydrophilic group of Span 80 in the new emulsion and the oxygen-containing functional groups on the coal surface formed the hydrogen bonding, which was observed to promote the adhesion and expansion of the new collector on the surface of the oxidized coal.

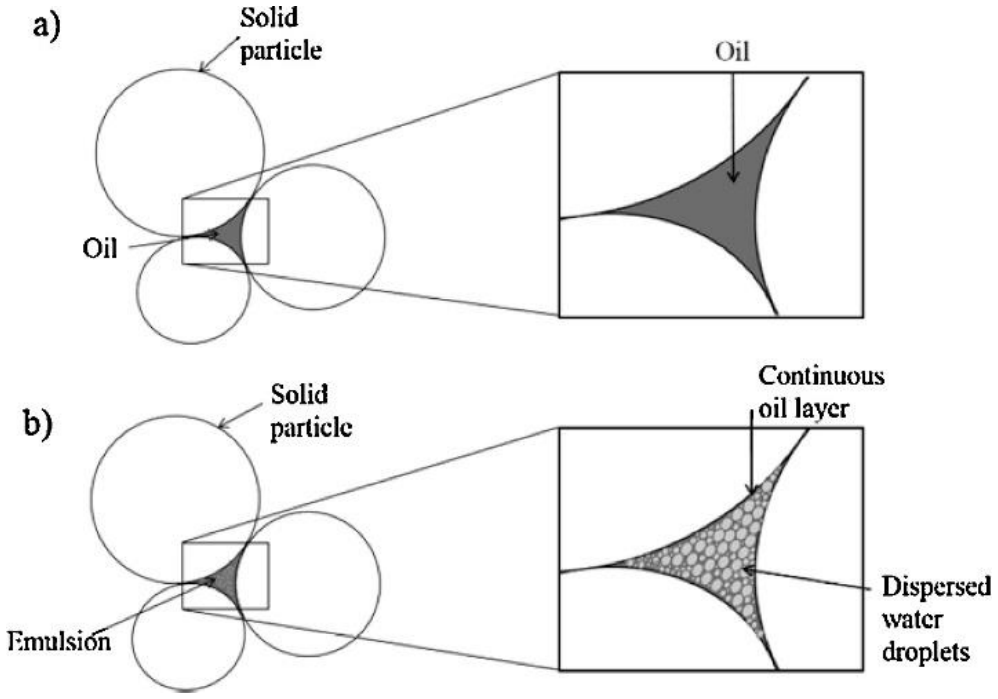


Figure 2.2 Three particles agglomeration with (a) conventional oil and (b) the new prepared HIP W/O emulsion

Netten et al.[31] prepared a water-in-oil (O/W) type high internal phase (HIP) emulsion binder with 3% diesel, 3% emulsifier, and 94% (3 wt% aqueous salt) solution for high-ash coal slime flocs and found a 7.5-fold organic liquid reduction when getting the same coal yield (90%) compared to pure diesel. The HIP emulsion referred was emulsions containing a volume rate of water bigger than $\phi = 0.74$, corresponding to the dense packing of monodisperse spheres[32]. They[33] subsequently made a series of improvements to the composition (2.5 vol% kerosene, 2.5 vol% SMO (Sorbitan mono-oleate) and 95 vol% aqueous NaCl solution), resulting in an oil savings of 90% (2% HIP emulsion, 20% Kerosene) when getting one yield of 90%. Figure 2.2 shows three-particle agglomerates using oil and HIP liquid binders. The binder for the agglomerate in Figure 2.2 (a) is diesel or pure oil, whereas an emulsion is used for agglomerate shown in Figure 2.2 (b). It comes to a conclusion that the both binders can selectively agglomerate coal particles.

Zhao et al.[34] prepared a new high internal phase (HIP) emulsion with 6.3 vol% kerosene, 3.8 vol% Span 80 and 89.9 vol% aqueous Na_2SO_4 solution to improve the separation efficiency of ultrafine coal slimes. There was also 90% oil consumption saving compared with kerosene when getting 73% combustible recovery with 0.01% HIP and 0.1% Kerosene. When 0.05 wt% organic liquid was added into the HIP emulsion, the recovery was more than 80% with 14% ash content of the cleaning coal.

Table 2.1 Comparisons of emulsified collectors from the literature

Types	Institutions		Reagents	Size/μm	Ash of feeding	Ash of froth	Dosage and C_R of traditional collector	Dosage and C_R of new collector	Refs
Cationic surfactant	China University of Mining and Technology	✓	n-octylamine: diesel = 1:4	250-500 and -45	22.39%	14.99%	2000 g/t-37.52%	500 g/t -51.68%	[11]
Anionic surfactants	Northeastern University	✓	Oleic acid (OA) :(OA+ kerosene)=1:5	125-500	19.96%	10.70%	2000 g/t-67.93%	1000 g/t-74.01%	[12]
Non-ionic surfactant	Cumhuriyet University(Turkey)	✓	kerosene + Acorga M5640+ Flotigol CS	-355	25.67%	21%	1250 g/t Kerosene-32.03%	1250 g/t 89.45%	[13]
Oil	China University of Mining & Technology	✓	wash oil	-	22.58%	12.62%	1200 g/t Kerosene 73.83%	800 g/t 77.87%	[14]
Nonionic surfactant	The University of Queensland	✓	diesel + Triton X-100	-200	7.93%	-	6.7×10^{-5} mol/L diesel 19%	4.02×10^{-5} mol/L (Triton X-100)+ 6.7×10^{-5} mol/L diesel 74.85%	[18]
Oil agglomeration	The University of British Columbia	✓	kerosene +5.4×10^{-5} mol/L dodecylamine (DDA) or 3.4×10^{-4} mol/L	-38	16.00%	5%(K+ DDA) 6% 5%(K+DDS) 4%	30% Kerosene 99%	5% (K+ DDA) or 5%(K+DDS) 99.9%	[19]

			dodecyl sulfate (DDS)						
Non-ionic emulsified collector	Taiyuan University of Technology	✓	dodecyl ethoxyl ethers($C_{12}EO_{23}$)	-200	31.46%	21%	-	4×10^{-5} mol/L $C_{12}EO_{23}$ 84.55%	[21]
Cationic surfactant	China University of Mining and Technology	✓	Dodecane +dodecyltrimethylammonium bromide (DTAB)	-500	13.80%	10.13%	4000 g/t dodecane 45.5%	1 mM DTAB 75.37%	[23]
Anionic surfactants	China University of Mining and Technology	✓	40% octanoic acid +diesel	-500	15.24%	7.90%	2000 g/t diesel-40%	2000 g/t diesel + 40 % octanoic acid-70%	[24]
Anionic surfactants	China University of Mining and Technology	✓	Dodecane: oleic acid (OA) =4:1	-500	31.67%	10.55%	40.55%	3000g/t mixed collector +300g/t DL-2-Octanol -89.41%	[25]
-	China University of Mining and Technology	✓	70% water, 3% new flotation promoter and 27% diesel	-150	21.12%	-	kinetic study Ymax= 91.32%	kinetic study Ymax= 94.19%	[26]
Anionic surfactants	China University of Mining and Technology	✓	a new collector (CC) (diesel and aliphatic acid) and 2-octanol	-250	21.18%	-	200 g/t diesel 44.51%	76.24%	[27].
Cationic surfactant	China University of Mining and Technology	✓	Diesel + didodecyldimethylammonium bromide (DDAB)	-500	16.45%	5.70%	10000 g/t diesel 65%	0.096 g/L DDAB+10000 g/t diesel 90.28%	[28]

Cationic surfactant	Wuhan University of Technology	✓	Sodium petroleum sulfonate+diesel	-	fly ash	-	500 g/t diesel 41% (carbon recovery)	500 g/t 15% sodium petroleum sulfonate +85% diesel 86.5% (carbon recovery)	[29]
W/O emulsion	Shanxi University	✓	2g Span 80+ 70.83g Sodium chloride(1M)+8 g Kerosene	74-38	-	-	0.6 wt% Kerosene-40%	0.6 wt% HIP emulsion 95%	[30]
Emulsion to agglomerate coal particle	The University of Newcastle	✓	3% diesel, 3%emulsifier, 94% (3wt % NaCl solution)	-304	10%	-	19wt% diesel-90%	3wt% binder 90%	[31]
Agglomeration with water-in-oil emulsion	The University of Newcastle	✓	2.5 vol% kerosene, 2.5 vol% SMO (Sorbitan mono-oleate) and 95 vol% 3 wt% NaCl solution	-100	10%	-	17 wt% diesel-88%	1.7 wt% emulsion 90%	[33]
Emulsion	University of Birmingham	✓	6.3 vol% Kerosene, 3.8 vol% Span 80 and 89.9 vol% aqueous Na_2SO_4 solution	-53	52.13%	14%	0.05% Kerosene 60%	0.05% emulsion 80%	[34]

2.1.2 Types of microemulsions

Microemulsions can be considered as special emulsions that are thermodynamically stable and transparent. A schematic representation of reverse micelles and various microemulsions are shown in Figure 2.3. Similarly, Moulik et al.[35] divided microemulsions into three types (Figure 2.4): O/W microemulsion (Winsor I), W/O microemulsion (Winsor II), and the three-phase system (Winsor III), which could turn reversibly from one type to the other. The amount of oil (O) and water (W) is in equilibrium with an upper oily phase and lower aqueous phase in the Winsor III system.

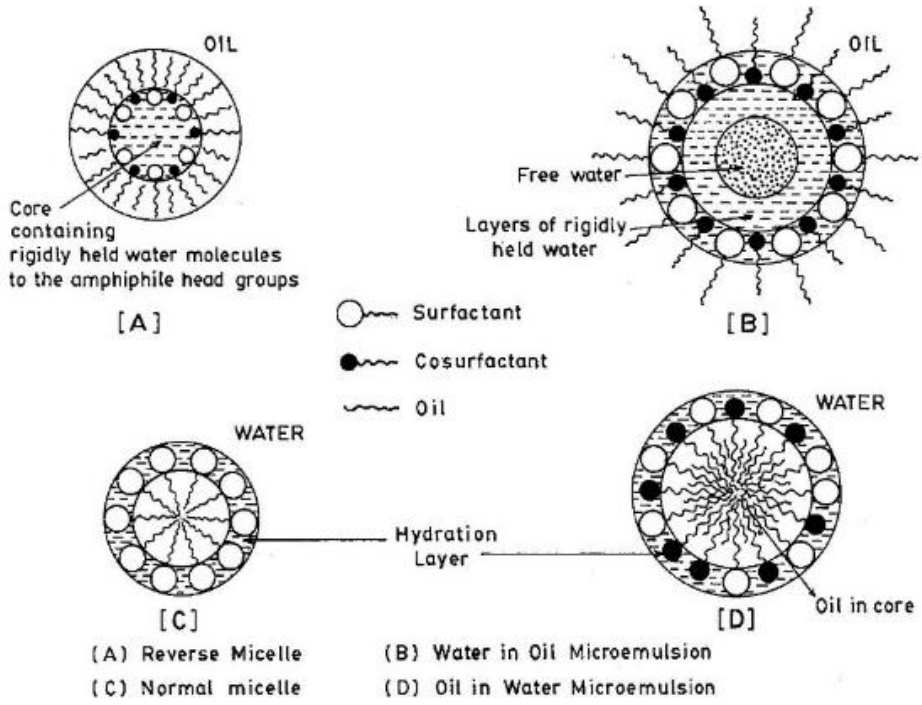


Figure 2.3 Schematic diagrams of (A) reverse micelles, (B) W/O microemulsion, (C) micelle, and (D) O/W microemulsion[35]

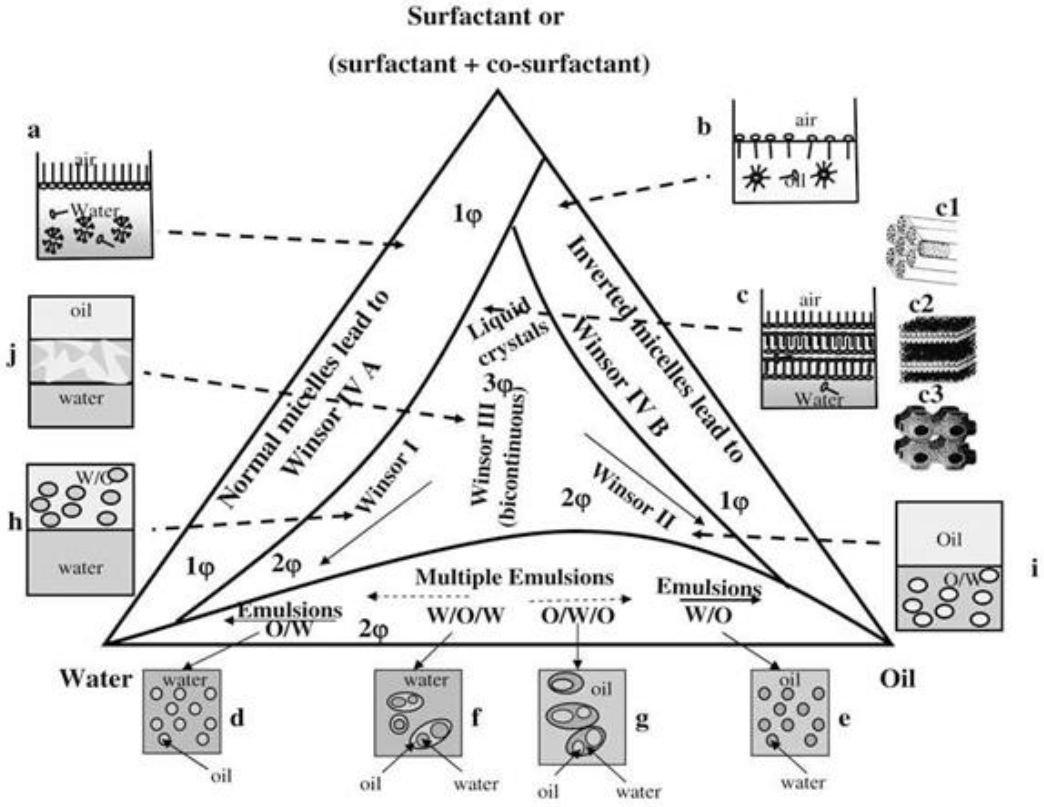


Figure 2.4 Phase diagram of a water-oil-emulsifier system, and 1φ, 2φ and 3φ refer to one phase, two-phase and three-phase

There are many applications of microemulsions; examples include oil recovery[36], food science and technology[37][38], drug delivery[39], polymers syntheses[40], manufacturing of semi-conductors [41], and melding nanoparticles[42][43].

Vollmer et al.[44] pointed out that microemulsions can be spontaneously formed, which are kinetically and thermodynamically stable. The features of the microemulsions are connected to solubilization and extract, which are characterized by microstructure and viscosity. Different interfacial compositions can determine the phase composition of microemulsion, mesoscopic structure or solubilization capacity[45-47].

2.1.3 Microemulsions for froth flotation

The unique aspects of microemulsions, including simple preparation, uniform size of the dispersed phase ($r < 100$ nm), ultra-low interfacial tension, and low viscosity, etc. make them ideal for use in the food industry, chemical field, medical and coal preparation[48-50]. More importantly, microemulsions can significantly improve the flotation efficiency with a low cost and a low dosage. Most work, so far, has focused on the coal flotation performance of oil-in-water emulsion and mixed surfactants, whereas few studies have been on microemulsion.

Watt et al.[51] studied the effect of chain length of alcohol, salinity, temperature, and various alcohols on the formation of microemulsion. In their study, W/O microemulsion using 30% w/w $NaNO_2$, diesel, Cetyltrimethylammonium bromide (CTAB) and short-chained alcohols (C_3-C_5) was formed, and more specifically the effect of high salt concentrations was investigated. They aimed to use maximum salt concentration with minimal addition of surfactant, and found that the mass ratio of $\frac{m_{CTAB}}{m_{(2\text{-propanol}+1\text{-butanol})}}$ being 68 : 32 was suitable for increasing the W/O area.

Darrell et al.[52] explored a microemulsion composed of alkylene oxide-treated alkyl phenols (ethylene oxide units: alkyl phenol units = 6, 7 and 8), fatty acids and alkylamine (surfactants) and phenol (cosurfactant) and obtained a microemulsion when water was in the range of 1-15% and the corresponding ratio of surfactant to water was 0.5:1 to 2:1.

Edward et al.[53] prepared the microemulsion with 85.6% gasoline, 1.93% water, 2.96% NP-14 + 3.04% NP-27 + 1.34% ammonium oleate + 1.03% free oleic acid (surfactant) and 4.10% methanol (cosurfactant) for industrial heat and power applications. They found the microemulsion could be stable at a temperature of -20-20℃.

Counter and John[54][55] made microemulsions for froth flotation with the following ingredients: Sample 1 with 30% component A (commercially frother), 5% fatty acid, 15% surfactant 2-butoxy ethanol, 15% polypropylene glycol, 31.5% water, and 3.5% potassium hydroxide (45%) solution in water; and Sample 2 with 50% component A, 15% 2-ethyl hexanoic acid, 14.0% surfactant 2-butoxy ethanol, 15.5% water, and 5.5% potassium hydroxide (45%) solution in water. They observed that the recovery of 6 ppm microemulsion mixed with 170 g/t diesel shown in Table 2.2 was at maximum (77.14%), which was twice as that of 3 ppm MIBC used alone.

And they also studied the microemulsions to improve the effectiveness of the collector. The following three types of microemulsion collectors were prepared: Sample I with 10% paraffinic oil, 6% fatty acid, 15% surfactant 2-butoxy ethanol, 5% alcohol blend, 63.2% water and 0.8% potassium hydroxide solid. Sample II with 10% diesel, 7% fatty acid, 12% surfactant 2-butoxy ethanol, 5% alcohol blend, 61.5% water and 2.5% potassium hydroxide (45%) solution in water. Sample III with 15% diesel, 7% fatty acid, 15% surfactant 2-butoxy ethanol, 5% alcohol blend, 55.5% water and 2.5% potassium hydroxide (45%) solution in water.

Table 2.2 The flotation results using different collectors and frothers

Col-lector	Dos-age (g/T)	Frother Used	Frother Dosage (ppm)	Active Frother Component Dosed (ppm)	Yield %	Ash %	Re-covery %
—	0	MIBC	3.0	3.0	22.10	5.09	32.28
—	0	MIBC	5.0	5.0	32.73	6.44	47.56
—	0	MIBC	8.0	8.0	43.36	7.22	64.44
—	0	Compo-nent A	3.0	3.0	22.15	5.90	32.97
—	0	Compo-nent A	5.0	5.0	28.51	6.19	41.74
—	0	Compo-nent A	8.0	8.0	34.67	6.31	51.39
—	0	Sample 1	3.0	0.9	15.51	5.91	23.12
—	0	Sample 1	5.0	1.5	29.78	6.47	44.79
—	0	Sample 1	8.0	2.4	39.00	6.76	55.62
—	0	Sample 2	3.0	1.5	36.61	6.32	54.77
—	0	Sample 2	5.0	2.5	39.00	6.56	56.83
—	0	Sample 2	8.0	4.0	42.69	6.79	62.48
Diesel	170	Compo-nent A	6.0	6.0	52.10	6.67	76.13
Diesel	170	Sample 1	6.0	1.8	52.25	7.16	76.90
Diesel	170	Sample 2	6.0	3.0	52.94	7.33	77.14

Table 2.3 The flotation results using different collectors and frothers

Collector Used	Col-lector Dosage (g/T)	Active Collector Com-ponent Dosed (g/T)	Frother	Dosage (ppm)	Yield %	Ash %	Re-covery %
—	0	0	MIBC	1.5	26.04	3.66	31.25
Diesel	170	170	MIBC	1.5	41.69	4.09	50.32
Diesel	339	339	MIBC	1.5	48.31	4.30	57.53
Sample I	180	18.0	MIBC	1.5	40.21	3.90	47.99
Sample I	359	35.9	MIBC	1.5	57.01	4.52	67.84
Sample II	180	18.0	MIBC	1.5	42.49	4.07	50.94
Sample II	359	35.9	MIBC	1.5	61.58	4.68	73.15
Sample III	180	27.0	MIBC	1.5	46.10	4.44	54.91
Sample III	359	53.9	MIBC	1.5	67.69	5.07	80.10
Paraffin Oil	180	180	MIBC	1.5	38.94	4.05	46.57
Paraffin Oil	359	359	MIBC	1.5	47.00	4.34	55.93

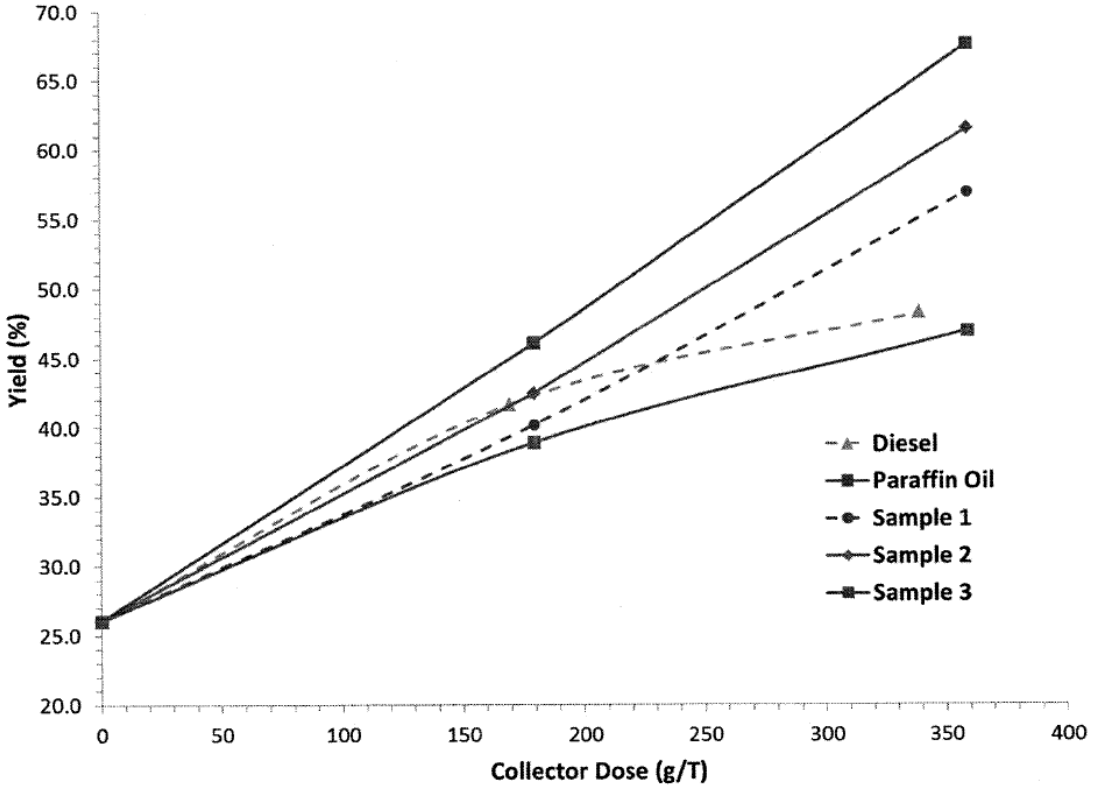


Figure 2.5 The yield of concentrate as a function of the dosages of collector

Their data demonstrated that less collector (5-50%) was required to get the same effects if the collector was in the form of a microemulsion. Table 2.3 and Figure 2.5 illustrate that the efficiency of diesel and paraffin oil tends to be steady at a certain dosage, indicating a maximum yield beyond which there was no improvement. Whereas, there was a linear relationship between the dosages of three microemulsions and the yield, indicating they can increase efficiency at lower dosages.

Collins et al.[56] prepared a water-in-oil microemulsion with ratio as below: 75.5% of decane, 15.1% seawater, 7.52% of 2 (2-ethyl caproyl) sulfosuccinate sodium, 1.88% sodium dodecyl sulfate. They found that the microemulsion could be stable at room temperature and 70°C. They also found that microemulsion with 62.5% decane, 25% seawater, 8.75% deamination LS3 and 3.75% of SDS could be stable at 40-80°C. This finding was used to deploy in the water-soluble or water-dispersible oil field or gas field.

Li et al.[57] studied the performance of an microemulsified diesel consisting of NP-10, pentanol, diesel, and water for coal flotation. It was found to be a 50% diesel reduction for microemulsified diesel with the same recovery (90%) and higher separation efficiency. Zhu et al.[58] from the same group subsequently prepared an ionic liquid microemulsion using 1-alkyl-3-methylimidazolium chloride, n-alcohol and n-dodecane, and showed the microemulsion dosage was reduced by about 43% with the same flotation behavior.

Zhang et al.[59] studied the effect of a new microemulsified collector on a low-rank coal. It consisted of diesel oil and dodecyl trimethylammonium bromide (DTAB). The yield of the cleaned coal was about 90% when a synergistic effect of diesel and DTAB occurred at a mass ratio of 2: 1.

Li et al.[57] and Zhao et al.[60] prepared microemulsion collectors with an average particle size less than 100 nm and the oil consumption was only about 28%-75% of the conventional collector. Ahmed and Drzymala[61] applied a direct-contact flotation procedure (coal sample mixed with reagents directly followed by the conventional method) and a coal yield of ~90% using 12000 g/t three-phase system (dodecane : $C_{12}E_4$: pentanol = 3 : 1 : 1) was achieved compared to < 60% with the normal contact flotation procedure.

Table 2.4 Comparisons of microemulsified collectors from the literature

Types	Research institutions		Reagents	Application	Ash of concentrate	Dosage and C_R of conventional collector	Dosage and C_R of the new collector	Refs
W/O microemulsion	The University of Newcastle	✓	30% w/w $NaNO_2$ +diesel+Cetyltrimethylammonium bromide (CTAB) +short-chained alcohols (C_3-C_5)	-	-	-	-	[51]
Microemulsion	Esso Research and Engineering Company	✓	fatty acids(C_{12}-C_{20}) and alkyl phenyl polyethoxy alkanols, alkylene polyamines as surfactants and phenol as cosurfactants	Fuel	-	-	-	[52]
W/O microemulsion	-	✓	85.6% gasoline, 1.93% water, 2.96% NP-14+ 3.04% NP-27+ 1.34% Ammonium oleate+ 1.03% Free oleic acid (surfactant) and 4.10% methanol	industrial heat and power	-	-	-	[53]
Microemulsion	New South Wales	✓	50% component A, 15% 2-ethyl hexanoic acid, 14.0% surfactant 2-butoxy ethanol, 15.5% water, and 5.5% potassium hydroxide (45%) solution in water	froth flotation	7.33%	32.28%	77.14%	[54]
Microemulsion	New South Wales	✓	15% diesel, 7% fatty acid, 15% surfactant 2-butoxy ethanol, 5% alcohol blend, 55.5% water and 2.5% potassium hydroxide (45%) solution in water	froth flotation	5.07%	57.53%	80.10%	[55]
W/O microemulsion	London	✓	75.5% of decane, 15.1% water, 7.52% of 2 (2-ethyl caproyl) sulfosuccinate sodium, 1.88% sodium dodecyl sulfate	oil field or gas field	-	-	-	[56]
O/W microemulsion	Shandong University of Science and Technology	✓	NP-10: pentanol : diesel: water=9:6:25:30	froth flotation	23.11% - 11%	700 g/t diesel 82%	600 g/t microemulsion 92%	[57]

Microemulsion	Shandong University of Science and Technology	✓	0.5 mmol surfactant(1-hexadecyl-3-methylimidazolium chloride ([C_{16}mim]Cl)) +2 mmol dodecane + 60% water+n-pentanol	froth flotation	21.6% - 12%	24 kg/t n-dodecane 76%	17 kg/t microemulsion 76%	[58]
Microemulsion	China University of Mining and Technology,	✓	15 min ultrasonic treatment DTAB: diesel = 1:2	froth flotation	12.24%-7%	8000 g/t diesel 70%	6000 g/t microemulsion 95%	[59]
O/W microemulsion	King Abdulaziz University	✓	35% dodecane, 55% dodecyl tetra (ethylene glycol) ether ($C_{12}E_4$), 10% water	froth flotation	3.38% - 2.48%	10000 g/t 60%	12000 g/t (dodecane:$C_{12}E_4$: pentanol = 3:1:1) 90%	[61]

2.2 The depression of pyrite

Most high-sulfur coals in China contain mainly sulphide minerals, which can be removed primarily by physical methods (Figure 2.6). The contents of sulfate sulfur and organic sulfur in coal are very low.

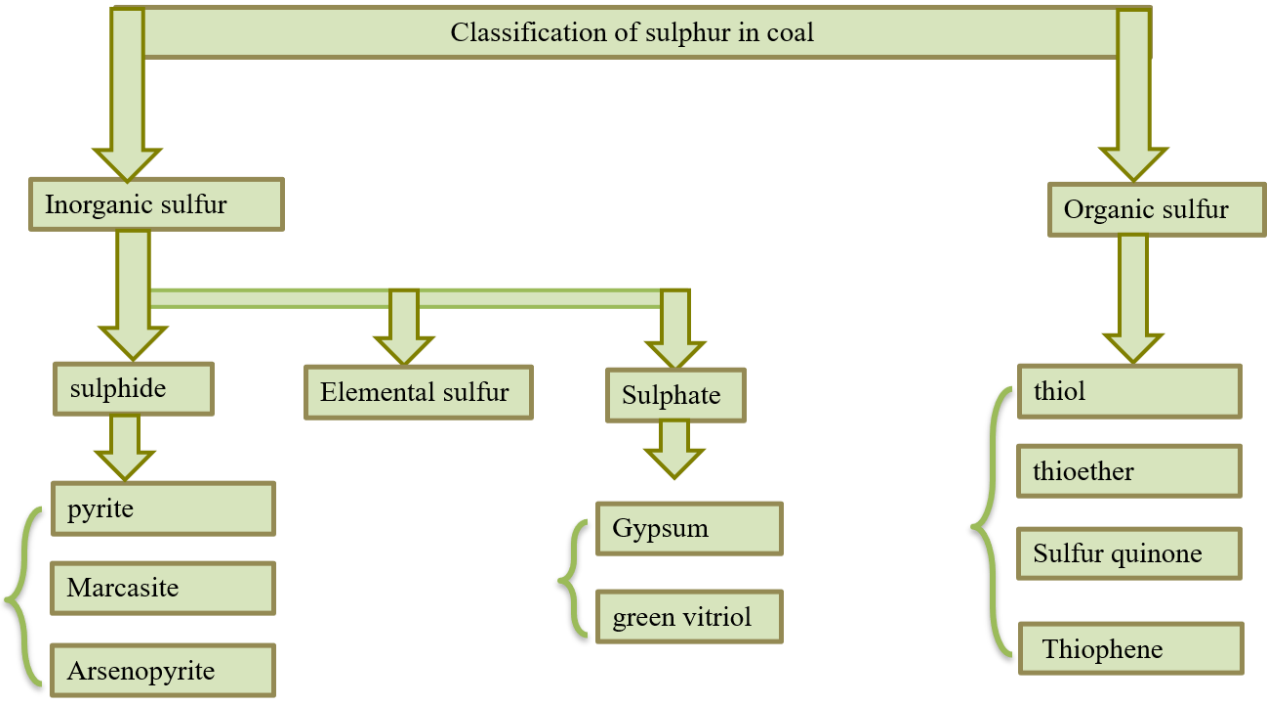


Figure 2.6 Classification of the sulfur in coal

The currently used desulfurization methods can be divided into three categories: desulfurization prior to combustion, desulfurization during coal combustion, purification of gas after combustion, as shown in Figure 2.7.

- **Physical methods**

There are several physical methods for desulfurization. Examples include gravity-based separation desulfurization, flotation desulfurization, magnetic separation desulfurization, oil agglomeration

and selective agglomeration. The primary mechanism for the physical desulfurization is to separate pyrite from coal particles with different physical properties in an aqueous solution.

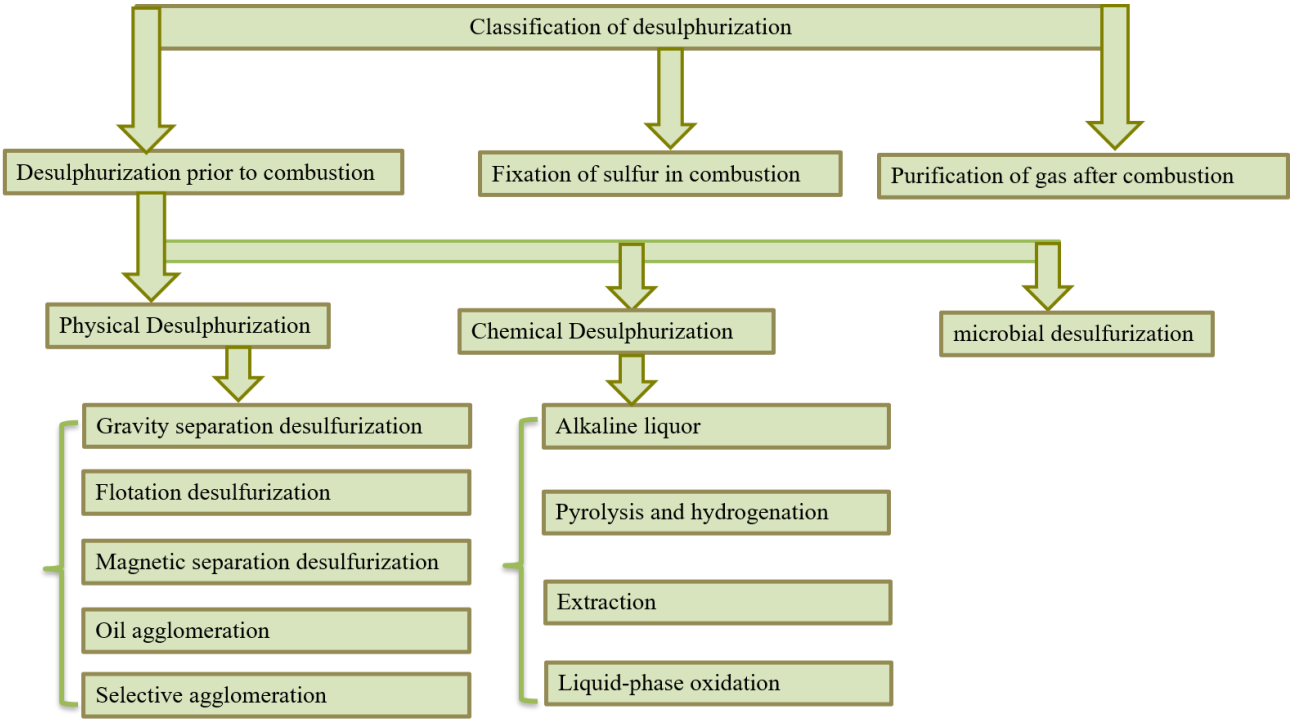


Figure 2.7 Classification of desulphurization

- **Chemical methods**

Chemical desulfurization methods include alkaline liquor, pyrolysis and hydrogenation, and liquid-phase oxidation:

(a) Alkaline liquor method refers to a process that uses molten sodium hydroxide or calcium hydroxide to convert the sulfur into soluble substances under high temperature and pressure. The disadvantage of this method is its complexity and corrosion.

(b) Pyrolysis and hydrogenation method refers to a process that converts the sulfur on coal to a soluble calcium sulfhydrate via carbonization, acid leaching and hydrogenation.

(c) The extraction method under supercritical conditions refers to a process that uses methanol or ethanol to improve the dissolved capacity of organic minerals in an aqueous solution via hydrogen bonds and dipole bonds.

(d) Liquid-phase oxidation method oxidizes sulfur-containing compounds to give soluble sulfate in acidic or alkaline conditions. This method is harsh, complex with high investment and operation costs.

- **Microbial desulfurization**

(a) Leaching method. This method converts inorganic sulfur into sulfuric acid under the action of micro-organisms. For this to occur, a certain amount of water containing micro-organisms is sprayed onto the surface of coal, and pyrite converts into sulphuric acid under the action of micro-organisms, which become part of wastewater flowing to the bottom of coal stockpiles.

(b) Surface oxidation method

This method uses air bubbles which are pumped from the bottom of a coal suspension, and the hydrophilic particles remain in the bottom. Hydrophobic micro-oxidized pyrite becomes hydrophilic under the action of microorganisms, whereas hydrophobic particles rise to the surface of the suspension to remove sulfur in coal.

This work uses flotation desulfurization as shown in Figure 2.7 to depress the floatability of pyrite. As the flotability of pyrite is dependent on the degree of oxidation, the development of effective depressants is important to alter the oxidization of the pyrite to depress the flotability of pyrite and improve the quality of cleaned coal.

Inorganic depressants (such as cyanide, metabisulphite, etc.) are detrimental to the environment and increase the plant operating cost in spite of efficiency[72]. As a result, biodegradable organic depressants from various sources have been used as alternatives[62][63]. These include CaO, polysaccharide polymers (corn starch, potato starch, wheat starch), and sodium carboxymethyl cellulose (CMC)[64-66].

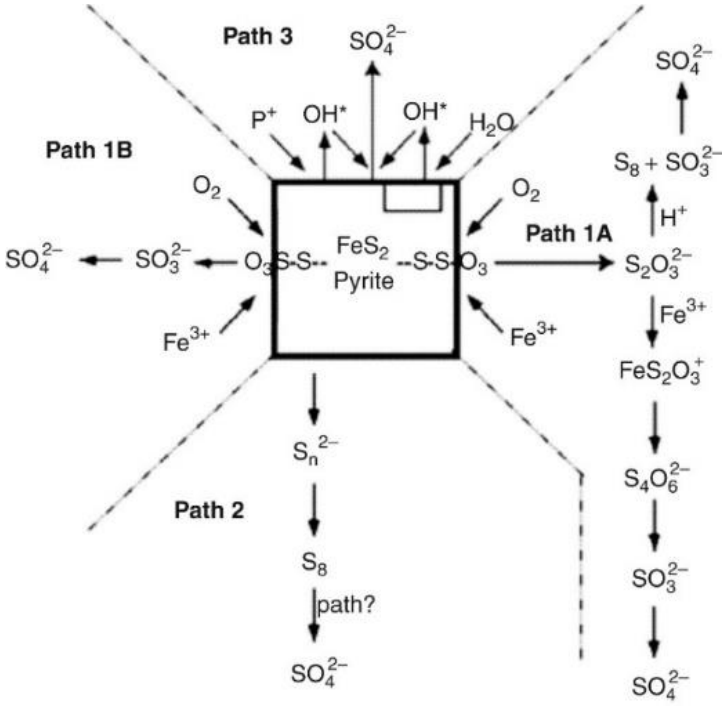


Figure 2.8 Schematic representation of some of the possible reactions describing different pathways for pyrite oxidation[67]

Possible pathways for pyrite oxidation are shown in Figure 2.8[67]. Here Path 1A involves thiosulfate detaching and reacting, which is in accordance with the previous study[68]; whereas Path 1B is a thiosulfate pathway with the S-S bond breaking rather than Fe-S bond, resulting in the sulfite oxidization to sulfate. Path 2 is a sulfide-elemental sulfur-sulfate pathway, whereas Path 3 uses the S oxidation to sulfate driven by radicals. Note that these pathways are simplified and there are many more reactions that could fully describe them[69].

Pyrite is perfectly floatable when pH >= 11 with thiol collectors[70]. Shen et al.[71] studied the effects of ethyl ethoxycarbonyl thionocarbamate (EECTC), ethyl ethoxycarbonyl thiourea (EECTU) and Potassium ethyl xanthate (KEX) on the depression of sphalerite with pyrite. EECTU was found to have a better selectivity with O_2 input than the other two reagents with the pyrite recovery varying from 20.3% (pH = 8.5) to 7.3% (pH = 11) shown in Figure 2.9 and Figure 2.10.

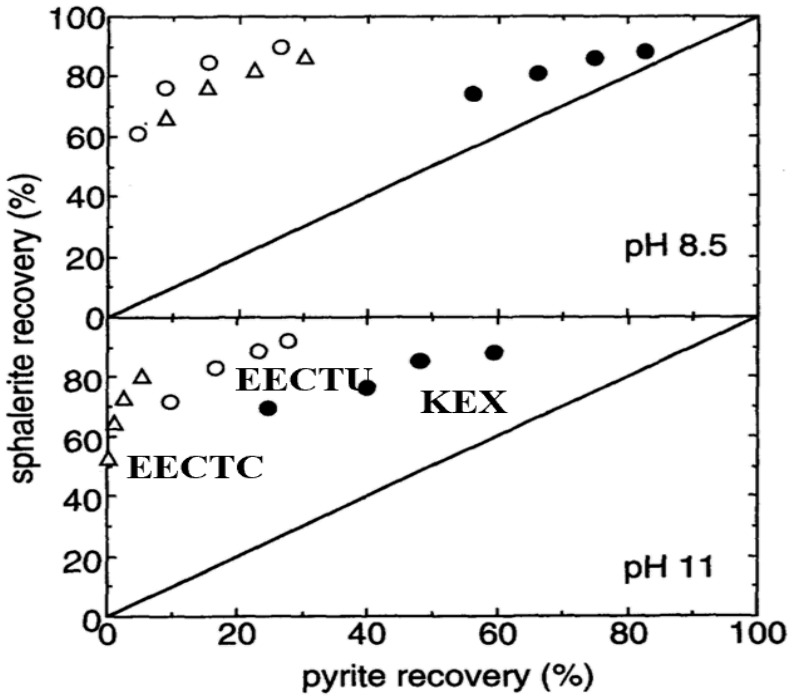


Figure 2.9 The recoveries comparison of three reagents at pH = 8.5 and pH = 11

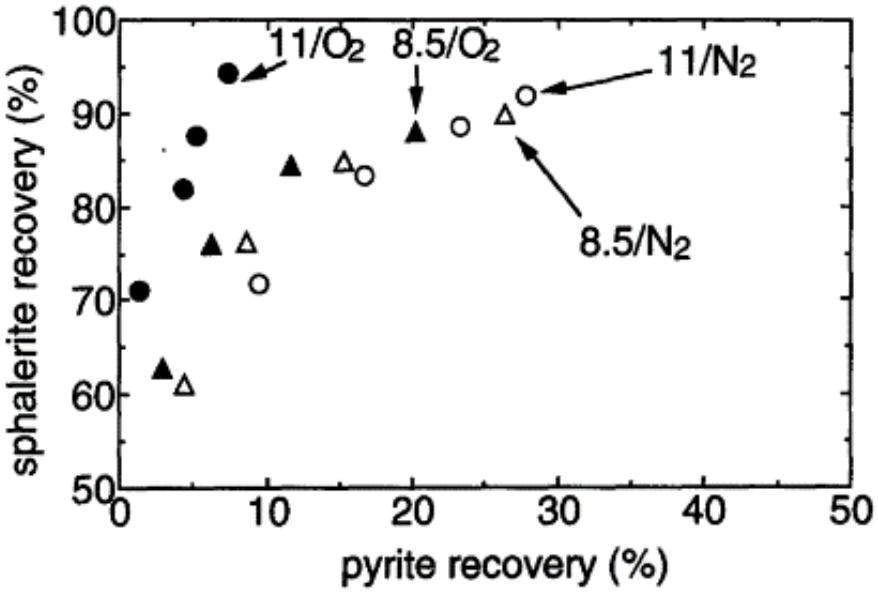


Figure 2.10 Flotation recoveries of sphalerite and pyrite with 2 ×10^{-5} mol/L EECTU when flotation time was 1, 2, 4, 8 min

Four polyacrylamide (PAM) polymers, including hydroxyl (PAM-H), thiourea (PAM-T), carboxyl (PAM-C) or sulfonate (PAM-S), have been used as depressants added before potassium isobutyl xanthate (KIBX) by Boulton et al.[72]. PAMs were found to depress pyrite without depressing sphalerite in the following order: PAM-H > PAM-C > PAM-T > PAM-S, and PAM-C had a better selectivity than the other PAMs shown in Figure 2.11.

pH values larger than 11 are necessary to markedly depress pyrite flotation in the presence of xanthate collectors as shown in Figure 2.12. The flotation of copper-activated sphalerite is independent of pH, but pyrite recovery reduced from 80% after 8 min (pH = 8.5) to 15% (pH = 12.0). The pyrite recovery with isobutyl xanthate (IBX) collector decreased from 51% to 21% with ethoxycarbonyl thionocarbamate (ECTC) at pH = 11 when the flotation time was 8 min while the recovery of sphalerite slightly decreased.

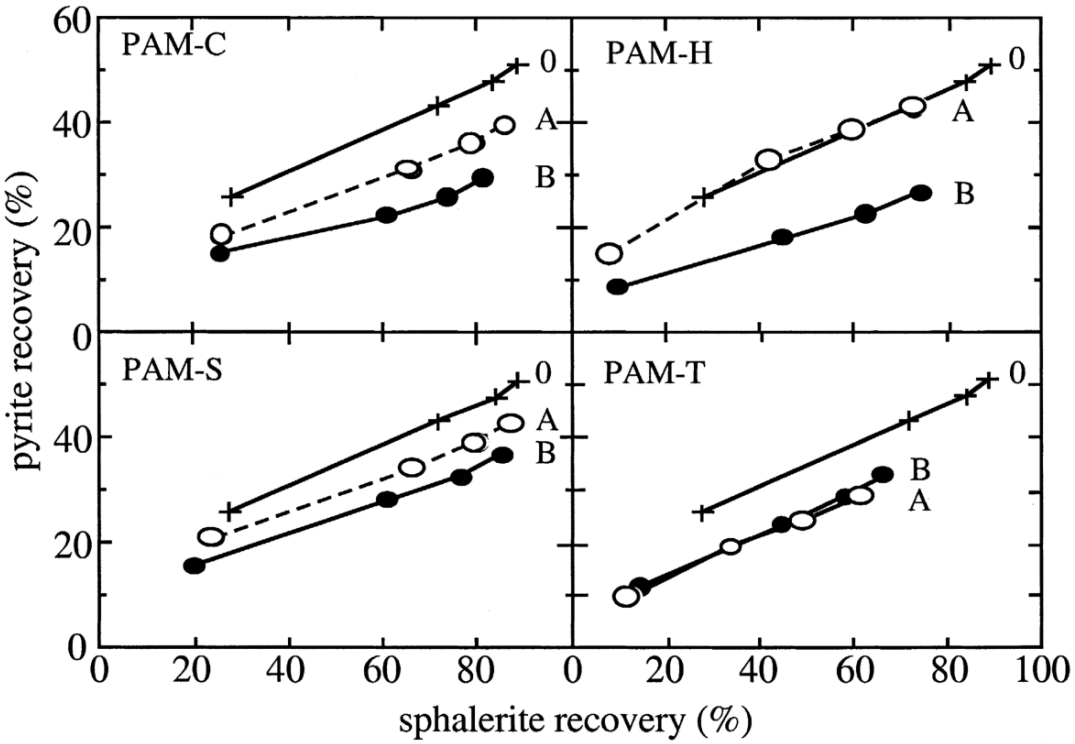


Figure 2.11 Recoveries of sphalerite and pyrite with (0) no PAM , (A) adding PAM after the collector and (B) before the collector at pH = 11.0

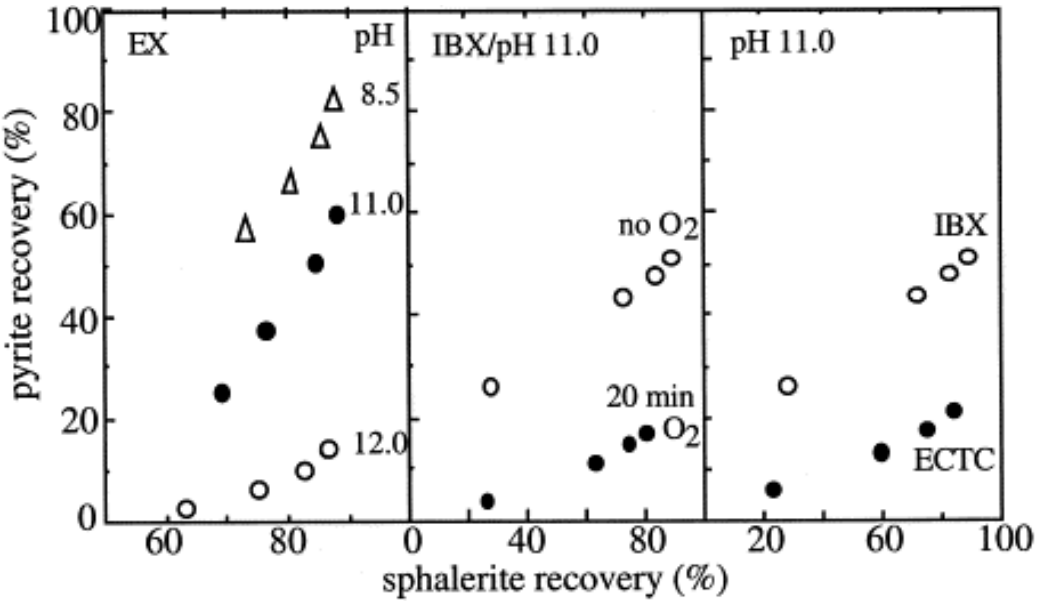


Figure 2.12 Flotation recoveries of sphalerite and pyrite when flotation time was 0.5, 2, 4 and 8 min with different conditions

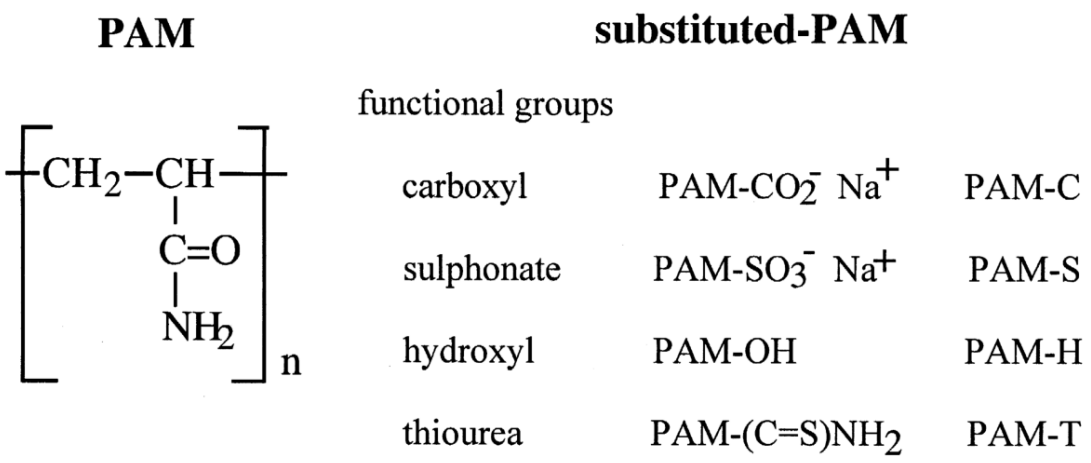


Figure 2.13 Chemical structure of the PAM and substituted PAM

The interactions[65][73] between polysaccharides and minerals are complex because polymer structures are complex and mineral surfaces are heterogeneous. Boulton et al.[74] reported that the adsorption of polymers on mineral surfaces can be divided into four types as shown in Figure 2.14. The first is electrostatic interaction due to the attraction of polymers and mineral surfaces with opposite charges. The second is hydrophobic interactions between the polymer and hydrophobic parts of minerals. The third is due to hydroxyl groups and metal cations on mineral surfaces can form hydrogen bonds. The last one is due to chemical bonds between the anionic functional groups and the metallic cations of mineral[75][76].

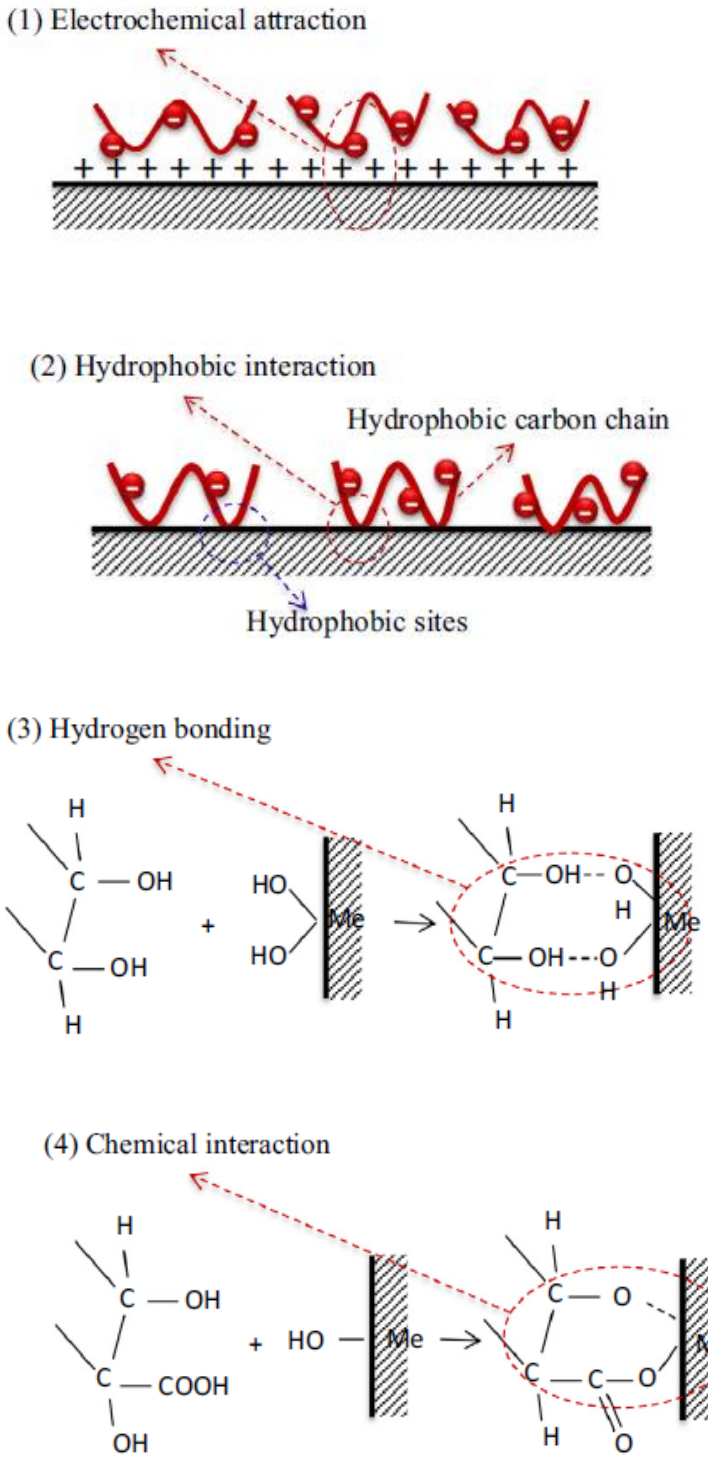


Figure 2.14 The four types of interactions between polysaccharides and minerals[74]

2.2.1 Carboxymethyl cellulose (CMC)

CMC is effective for pyrite depression and its structure is shown in Figure 2.15. One can see carboxyl groups in CMC, so it can interact with different metal species on the pyrite surface. The interaction of carboxyl groups in CMC with the metal ions on the pyrite surface is better than that of hydroxyl groups in polysaccharides. CMC is often classified as polysaccharides, but the structure is different from starch or guar gum. Such a difference makes them negatively charged and capable of adsorbing from -OH and -COO- groups in their structure[77]. The C-1, 4 connects the basic unit β-D-glucose monomers in the linear structure of CMC as shown in Figure 2.15.

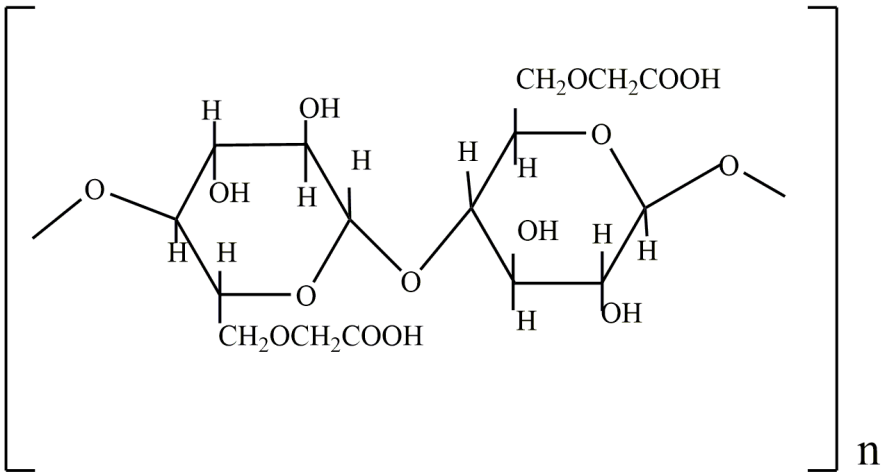


Figure 2.15 Structure of cellulose and CMC[78]

Ahmadi et al.[79] used starch ($(C_6H_{10}O_5)_n$), dextrin, carboxymethyl cellulose as depressants to study their effects on pyrite flotation. The results showed that the pyrite recovery was decreased by 7.37%, 8.15%, and 9.99% when the concentrations of CMC were 50, 100 and 150 ppm, respectively.

Bicak et al.[63] found an interesting phenomenon when they added 10^{-2} M Ca^{2+} to 200 ppm CMC, which was found to improve the effect of CMC for pyrite depressing, from 90% to 50% at pH =

9. This was attributed to the existence of $Ca(OH)^+$ on the surface of pyrite which reduced the repulsive forces between CMC and pyrite. In addition, $Ca(OH)_2$ or CaO on the pyrite surface was thought to be conducive to forming hydrogen bonds between CMC and pyrite.

Laskowski and Liu[80] reported that polymers adsorbed on the mineral surfaces through interactions with metal-hydroxy species, but Rath et al.[81] thought that apart from hydrogen bonding, hydrophobic bonding and electrostatic interaction were also the reasons for their interactions, which is in accordance with Boulton's report[74].

Feng et al.[82] studied the order of adding reagents of CMC (degree of substituent = 0.9, MW = 700000) and PAX (potassium amyl xanthate) on the depression of chlorite and pyrite. Pre-adsorption of CMC and then PAX could depress pyrite from 92.73% to 82.16% due to the competitive adsorption of the two reagents.

Table 2.5 Comparisons of the CMC for froth flotations

Research institutions	Collectors	Frother	Depressants	Recovery	Conditions	Size/μm	Refs
Hacettepe University(Turkey)	10^{-4} M SIPX	-	10^{-2} M Ca^{2+} 200 ppm CMC 10 ppm guar gum	90%-50% pH=9 15%-5% pH=9	-	pyrite (150 -75)	[63]
Central South University	10^{-4} mol/LPAX (potassium amyl xanthate)	10^{-4} mol/LMIBC	100 mg/L CMC	92.73%-82.16%	pH=9	pyrite (150 -75)	[82]
Pennsylvania State University	100 g/t xanthate	100 g/t MIBC	100 g/L CMC	Yield (63.7%-68%) Sulfur (0.69%-0.62%)	pH=7	coal -500	[91]
The University of Queensland	256 g/t F1234 (isopropyl ethythiocarbamate)	173 g/t Polyfroth W34 (a mix of polyglycol ethers)	300 g/t 2% w/w CMC solution 500 g/t, Perox 3/30(hydrogen peroxide-oxidized wheat starch)	CMC 76%- 21.1% Perox 3/30 76%- 2%	pH=9	pyrite -106	[92]

2.2.2 Polysaccharide

Polysaccharide includes starch, dextrin and guar gum. Starch ($(C_6H_{10}O_5)_n$) is divided into linear amylose or branched amylopectin and it is one of the depressants for pyrite. Physical modification of starch refers to a process that uses heat, physical field, ultra-high pressure and extrusion[83], whereas chemical modifications include esterification, cross-linking, acid hydrolysis, grafting, oxidation, acetylation etc.[84-86] as illustrated in Figure 2.16. Most modified starch products are chemically modified by using chemical reagents.

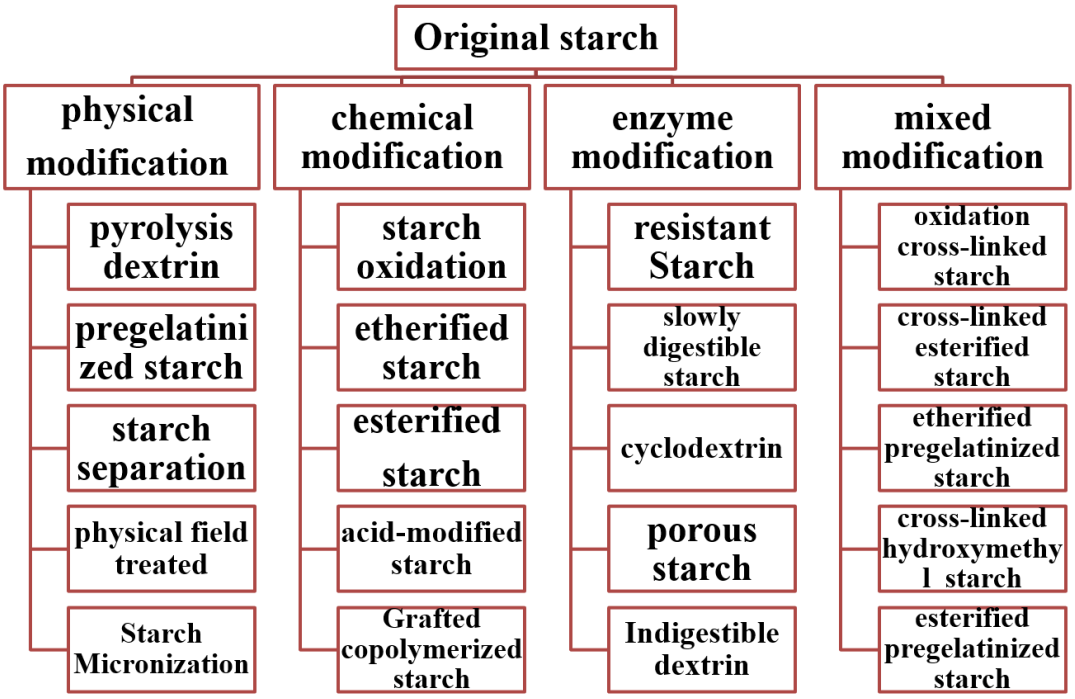
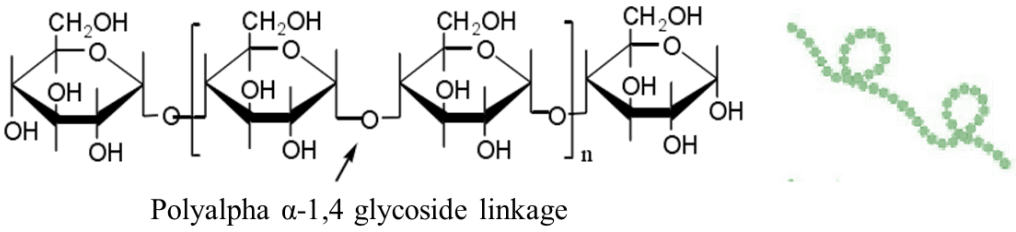


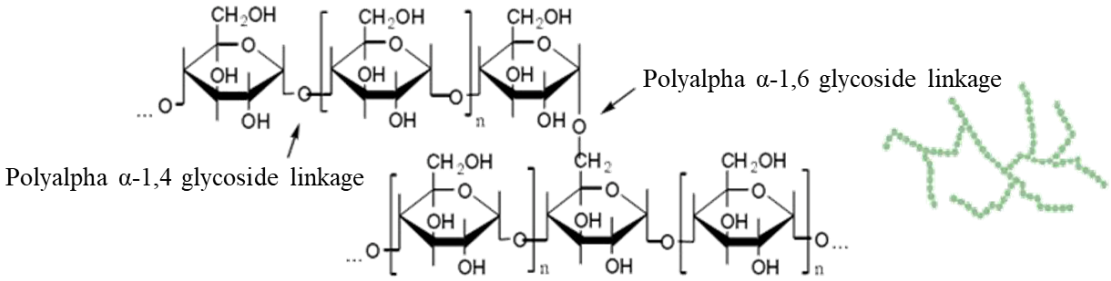
Figure 2.16 The modification methods of starch

Amylose from starch is a linear polymer consisting of D-glucose linked by α-1,4 glycosidic bonds. Each molecule contains 200 to 980 glucose residues (Figure 2.17 (a)) and it presents a spiral state with 6 - 8 glucose.

Amylopectin is a highly branched macromolecule, which accounts for 70% - 90% of starch. Each glucose in the main chain is connected by α-1,4 glycosidic bonds, which are twisted into helices. Branches of amylopectin are connected to the main chain by α-1,6 glycosidic bonds. The spaces between branches were 11-12 glucose residues (Figure 2.17 (b)). There are about 600 to 6000 glucose residues in amylopectin and the molecular weight is over one million. And the properties of starch are shown in Table 2.6.



(a) amylose



(b) amylopectin

Figure 2.17 The molecular configuration of (a) amylose and (b) amylopectin

Table 2.6 The gelatinization and swelling properties of different starches

Name	Gelatinization temperature /℃	Swelling power	Retrogradation
corn starch	64-72	24	high
cassava starch	59-69	71	low
potato starch	56-66	1153	medium
wheat starch	58-64	21	high
rice starch	68-78	19	high
sweet potato starch	58-72	46	medium

Pugh et al.[87] reported starches with anionic characteristics due to oxidation and hydrolysis, dextrin and gums could reduce the natural floatability of sulphur by froth flotation with a xanthate collector. Lawal et al.[88] studied starch isolated from hybrid maize through oxidization and dilution with acid. Their process yielded products with less swelling power and more solubility. Oxidized starch absorbed more water and oil than native starch. Wang et al.[89] studied the physicochemical properties of oxidized starch and waxy corn starch by sodium hypochlorite. More carbonyl and carboxyl groups were obtained, which promoted starch hydration and increased swelling capacity.

The dextrin depressing pyrite in sulfide flotation, however, has rarely been reported. Kydros and Gallios[90] showed that the use of 50 ppm dextrin could effectively depress pyrite at pH = 4 in the presence of 20 ppm potassium ethyl xanthate (KEX, collector). The froth products, $CuSO_4$-activated sphalerite, contained 28% Zn with 75% recovery, whereas pyrite was found to be depressed.

Xu and Aplan[91] proposed the use of various polysaccharides such as corn starch, potato starch, wheat starch, guar gum mixed with Fe^{2+}, Al^{3+}, Cu^{2+} to depress pyrite and improve the yield in the

coal processing. They adjusted the slurry pH with 5% H_2SO_4 to pH = 5 or 7, and used 100 g/t MIBC or No. 2 fuel oil, and 100 g/t xanthate for flotation. The ash content was observed to be reduced by 1% - 1.5% compared to that without depressants. Fletcher et al.[92] pointed out that gelatinization of starch achieved by NaOH, CaO, H_2O_2 etc. determined the starch structure during flotation. The hydrogen peroxide-oxidized wheat starch with hydrogen peroxide and native wheat starch depressed pyrite due to the greater molecular size and branches on the starches extending from the pyrite surface plane for hydrophilicity.

Researchers[87][93] reported that the hydroxyl groups play a crucial role in the depressing process for polysaccharides. The larger size of the starches, the more hydroxyl groups will be provided at per adsorption site. Another characteristic of starch molecules is the presence of branches that can extend from the surface of pyrite further into the aqueous phase. The branched chains had greater steric freedom than the chains, loops, and tails generally attached to the polymer chain[94], allowing the hydroxyl groups to interact with the water phase and enhance the depression, which is in agreement with the assumption from Flethcher[93].

Dextrin is obtained by thermally degrading starch under acidic conditions. The chains will be broken down and reconnect with the fragments of existing chains to form low molecular weight molecules with many branches[62][87][95]. Dextrin resembles amylopectin with a molecular weight ranging from 800 to 70,000, as shown in Figure 2.18[78].

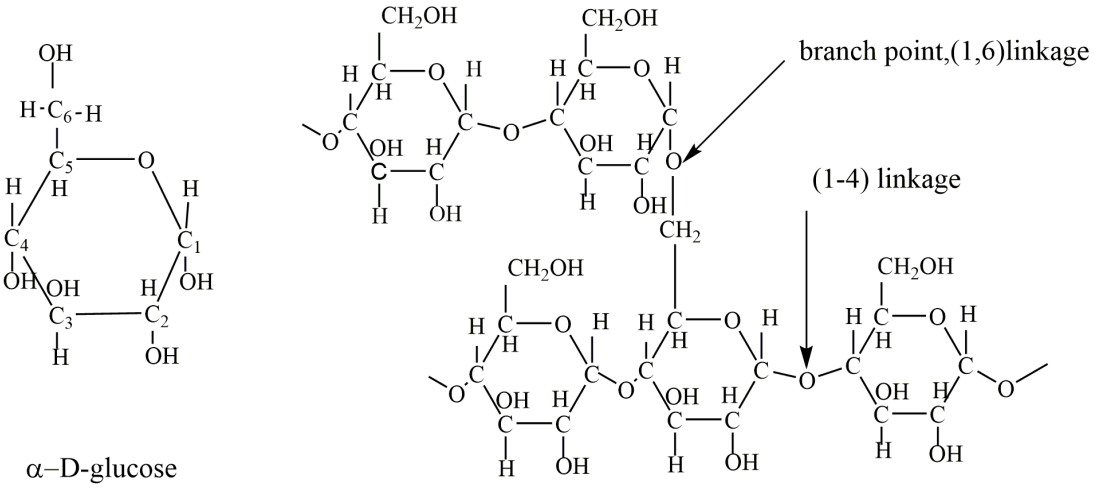


Figure 2.18 Structural units of dextrin from Laskowski[79]

Guar gum is a branch of polysaccharide and the structure of guar gum is shown in Figure 2.19. The iron hydroxide on the surface of pyrite is in reaction with dextrin. Oxidation on the pyrite surface improve the dextrin adsorption.

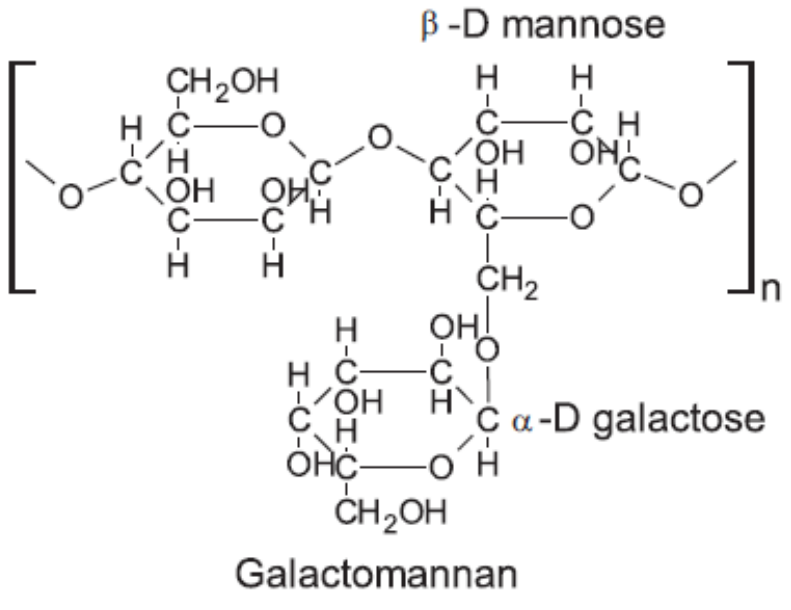


Figure 2.19 Structural unit of guar gum[79]

Zhang et al.[96] reported lignite sample with 0.3 M NaCl solution experiment for starch depressant with reverse flotation. 2500 g/t corn starch with the ratio of corn starch and NaOH being 4:1, 5000 g/t Dodecylamine hydrochloride (DAH) and 200 g/t MIBC were added and a concentrate ash content of 11.30% with a recovery of 65.29% were obtained.

$$C_R = \frac{M_C(100 - A_C)}{M_F(100 - A_F)} \times 100\% \quad (2\text{-}7)$$

$$I_E = \frac{M_T}{(100 - A_F)} \frac{A_T - A_F}{A_F} \times 100\% \quad (2\text{-}8)$$

Where C_R is the conventional recovery and E_F is the Reverse flotation efficiency index.

It could be seen from Figure 2.20 and Figure 2.21 that the highest reverse flotation performance was obtained when -74 μm size fraction was 42.34% with ash content of 11.30% and recovery of 65.29%. And the maximum reverse flotation efficiency was achieved with the -425 μm size fraction with 42.34% fine particles (-74 μm) concluded from Figure 2.22 and Figure 2.23.

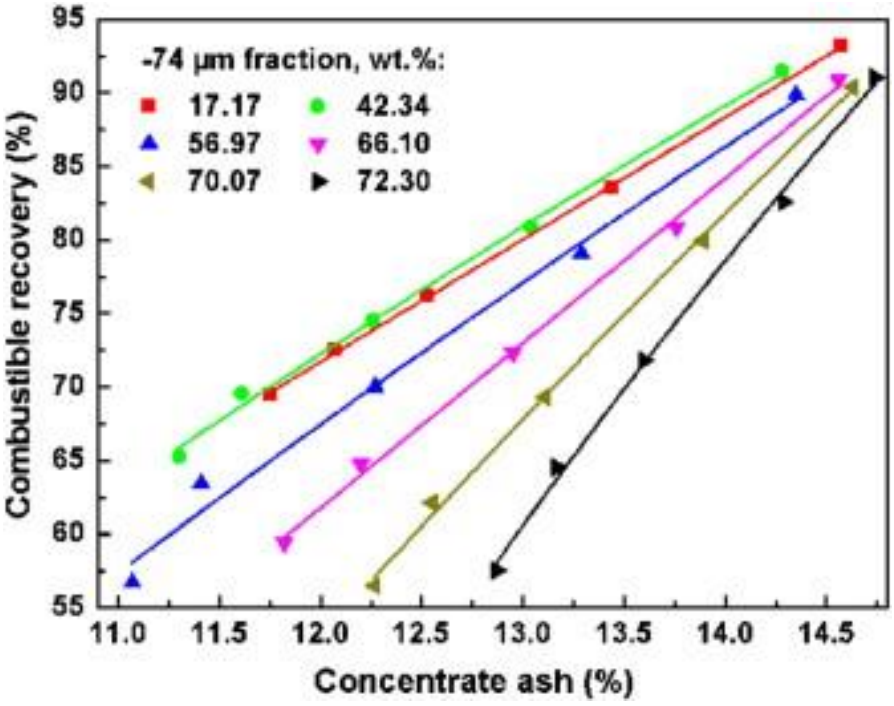


Figure 2.20 Effect of the proportion of 74 µm on the ash content and on the combustible recovery in lignite reverse flotation

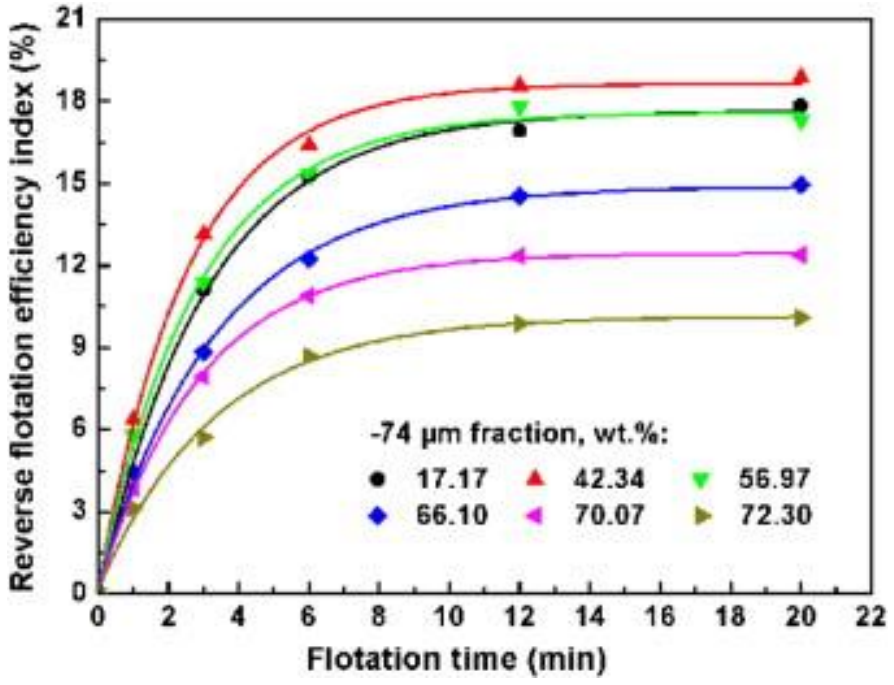


Figure 2.21 Effect of the fraction of -74 µm content on the efficiency of reverse flotation of lignite

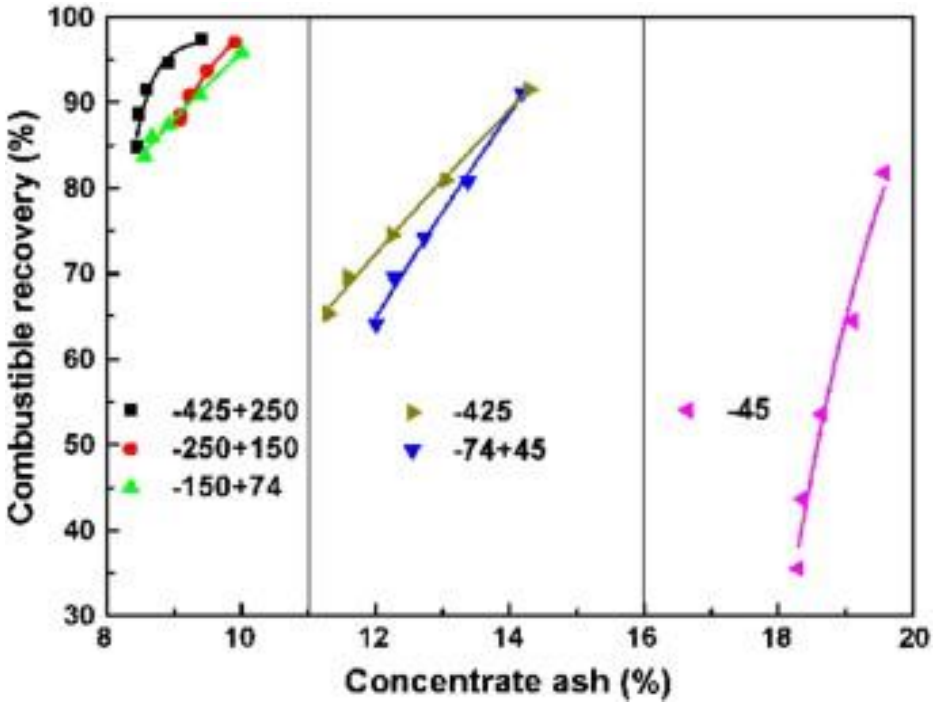


Figure 2.22 The individual size fractions on the ash and combustible recovery of the concentrates

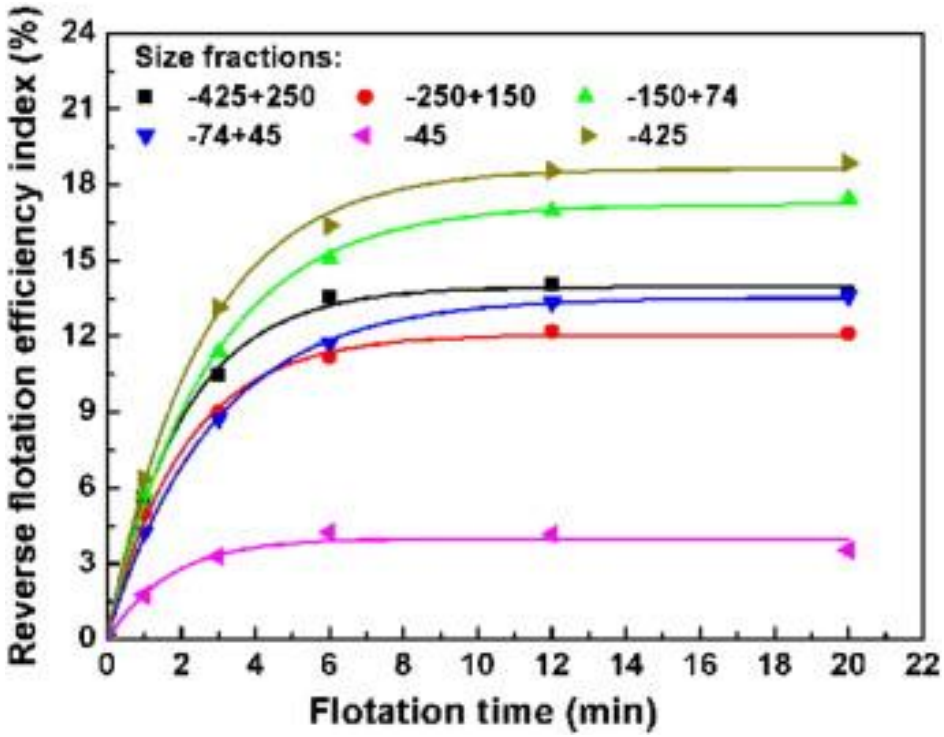


Figure 2.23 Effect of six size distributions on the efficiency of reverse flotation of lignite

Starch was employed as a depressant on pyrite flotation with a dosage of 1.7 or 17 mg/dm^3 at a pH of 6.5 or 10[97], whereas the collector (Aerophine 3418 A, belonging to dialkyl dithiophosphinate group) and frother (MIBC) were kept at 40 mg/L and 10 mg/L, respectively. Results showed that the flotation recovery decreased from 43.5% to 10.4% at pH = 10 and from 74.9% to 59.2% at pH = 6.5. Better performance of starch at alkaline condition (pH = 10) is due to the starch interacting with metal-hydroxylated species on the pyrite.

The adsorption of polysaccharides onto mineral surfaces has not yet been clearly understood. It is assumed there is an electrostatic force between starch and pyrite, and they are opposing charged. Then the interaction between the hydrophobic part of pyrite and starch's complementary part occurs. Finally, the chemical bond between (COO^-) or SO_4^{2-} and iron on the pyrite surface may happen[65][75].

Fornasiero et al.[98] found that pyrite was hydrophobic at pH = 5, and cation existed in the form of $Fe(OH)^{3+}$, $Fe(OH)^{2+}$, $Fe(OH)_2^+$ etc. on the pyrite surface. Bicak et al.[63] found that the addition of 0.1 mg/L guar gum decreased pyrite recovery dramatically from 20% to 5%. Moreover, pyrite depression performed better at pH = 11 due to the reaction of guar gum with hydroxyl iron through hydroxyl groups on the pyrite surface. Furthermore, Rath et al.[81] observed the reaction of hydroxyl groups in polymers with cation like $Fe(OH)^{3+}$, $Fe(OH)_2^+$, $Fe(OH)^{2+}$ etc. at a pH greater than 7.

Dextrin, Guar gum, causticized corn starch and raw starch were studied in-depth by researchers home and abroad shown in Table 2.7, while physically modified corn starch has hardly ever been reported. So modified corn starch will be studied for depressing the pyrite in the froth flotation in this Ph.D work. Moreover, it was reported[63][78][95] that calcium ions acting as ‘‘bridges” deposits on the mineral surfaces could improve the bonding between the hydroxyl groups on polymers and

minerals, so calcium oxide will also be employed to strengthen the hydrophilicity of mineral particles in this work.

Table 2.7 Comparisons of the Polysaccharide for froth flotations

Research institutions	Collectors	Frother	Depressants	Recovery	conditions	Size/μm	Refs
University of British Columbia	10^{-4} mol/L sodium isopropyl xanthate	-	20 mg/L Dextrin	from 70% to 20 %	pH=8	-	pyrite 150-70	[62]
University of South Australia	120 g/t potassium isobutyl xanthate KIBX	Aerofroth 65	100 g/t polyacrylamide PAM -hydroxyl	50%-25%	pH=11.5	pyrite -45	[72]
University of Tehran(Iran)	20 ppm Potassium Isopropyl xanthate (KIPX) + Potassium Amyl xanthate(KAX)	16 ppm Poly Propylene Glycol (A65)	150 ppm Diethylenetriamine (DETA)	95.63% - 51.00%	-	Pyrite 20-100	[79]
Indian Institute of Science	10^{-3} mol/LPotassium ethyl xanthate	-	50 ppm dextrin or 50 ppm guar gum	95%-20%	pH=10.5	pyrite 150 -75	[81]
Aristotle University	20 ppm potassium ethyl xanthate		50 ppm dextrin	21%	pH=4	pyrite 75-45	[90]
China University of Mining and Technology	5000 g/t Dodecylamine hydrochloride (DAH)	200 g/t MIBC	2500 g/t 1% causticised corn starch solution (corn starch : NaOH = 4 : 1	65.29%	pH=7	lignite -45, 45-75, 75-150, 150-250, 250-425 A=15.19%	[96]
Istanbul Technical University	40 mg/dm^3 Aerophine 3418 A(dialkyl dithiophosphinate group)	10 mg/L MIBC	17 mg/L starch	74.9%-59.2% 43.5%-10.4%	pH = 6.5 pH=10	Pyrite -100	[97]

University of Utah	-	-	-	65% (pH=10) 50% (pH=3)	120s ultrasonic pretreatment (40 kHz) pH=10, CO_2 saturated water, N_2 input	pyrite 109-75	[167]

Xuemin Zhao

2.2.3 Polymeric aluminum chloride (PAC)

Polymeric aluminum chloride (PAC) is not a pure chemical and it includes three species of Al (III), as shown in Table 2.8: monomer Al_a (Al^{3+}, $Al(OH)^{2+}$, $Al(OH)_2^{+}$, $Al(OH)_4^{-}$ ions etc.), the polymer Al_b, and the precipitate Al_c. The structure of Al_b is still under debate and an area of research[99-102]. Al_c is the amorphous precipitate. The hydrolysis processing of Al species is shown in Figure 2.24. When the Al (III) salts are added in solution, the hydrolysis reaction takes place due to the typical aqueous chemical equilibrium.

Table 2.8 The Al (III) species of Polymeric aluminum chloride[102]

Degree of polymerization	Possible chemical formula	Ferron assay
Monomer	Al^{3+}, $AI(OH)^{2+}$, $Al(OH)_2^{+}$, $A1(OH)_4^{-}$	Al_a
Oligomer	$Al_2(OH)_2^{4+}$, $Al_2(OH)_5^{+}$, $Al_3(OH)_4^{5+}$	
Low-mer	$Al_6(OH)_{12}^{6+}$, $Al_6(OH)_{15}^{3+}$, $Al_8(OH)_{20}^{4+}$	Al_{b1}
Mid-mer	$Al_{13}(OH)_{32}^{7+}$, $Al_{13}O_4(OH)_{24}^{7+}$ (Al_{13})	Al_{b2}
High-mer	$Al_{15}(OH)_{36}^{9+}$,$Al_{30}O_8(OH)_{56}^{15+}$($Al_{30}$)	
Sol, gel	$(Al_{13})_n$,$Al(OH)_3^a$	Al_c
Precipitates	$[Al(OH)_3]_n^a$	

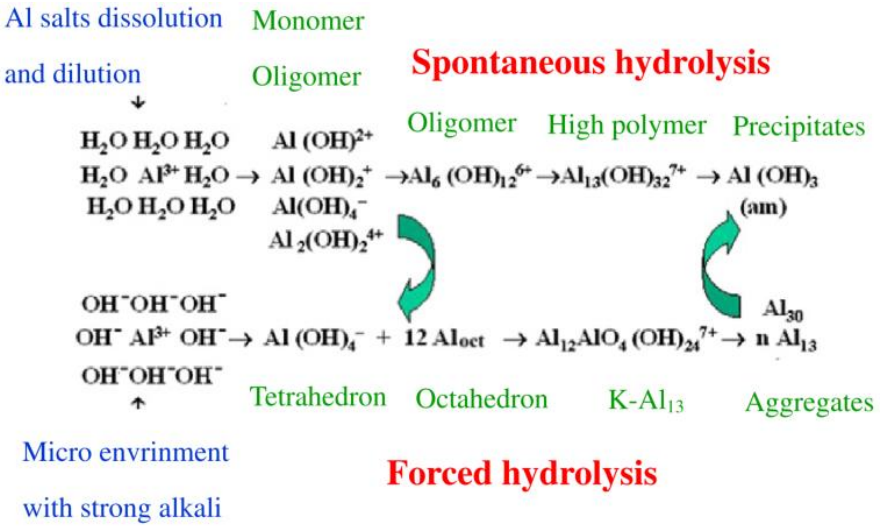


Figure 2.24 The hydrolysis processing of Al species[102]

For Al, the possible polynuclear forms include $Al_2(OH)_2^{4+}$ and $Al_3(OH)_4^{5+}$. It can be seen in Figure 2.25 and Figure 2.26 that the dominant component in PAC is $Al(OH)_4^-$ when pH >= 10.

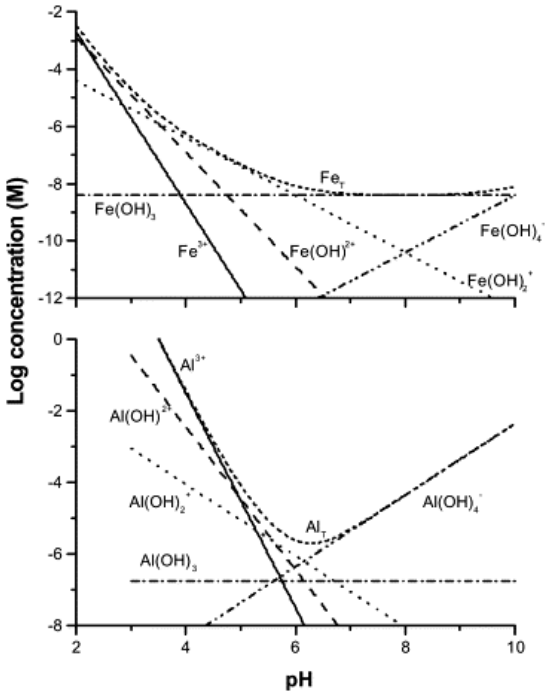


Figure 2.25 Concentrations of monomeric hydrolysis products of Fe(III) and Al(III)[99]

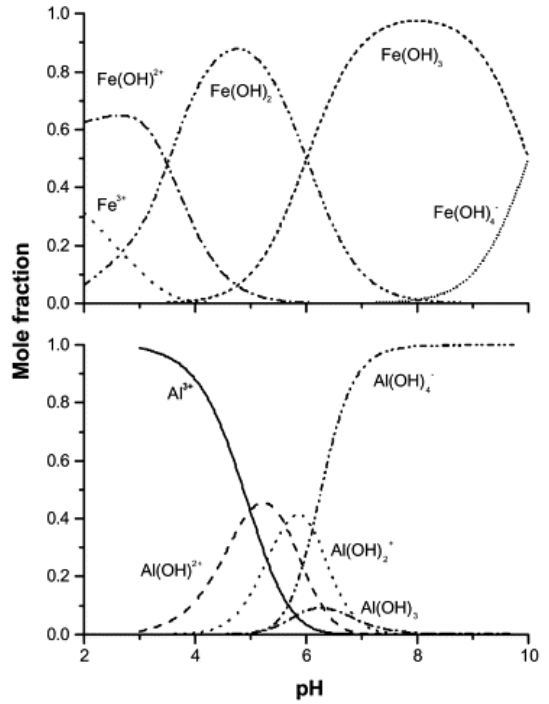


Figure 2.26 The mole fractions of hydrolysis products in equilibrium with amorphous hydroxides[99]

Ye et al.[100] reported that different species have different pathways to form electrostatic patches. A schematic diagram about the formation of electrostatic forms by Al_a and other species is illustrated in Figure 2.27. Al_a species is unstable after the addition and eventually forms positively charged colloidal or amorphous hydroxide precipitate that can neutralize the clay particles with negative charges. As for the electrostatic patches of Al_b and particles, they could be formed through the rapid adsorption of Al_b onto clay particles and aggregation. And the electrostatic formation mode of Al_c is similar to that of Al_b.

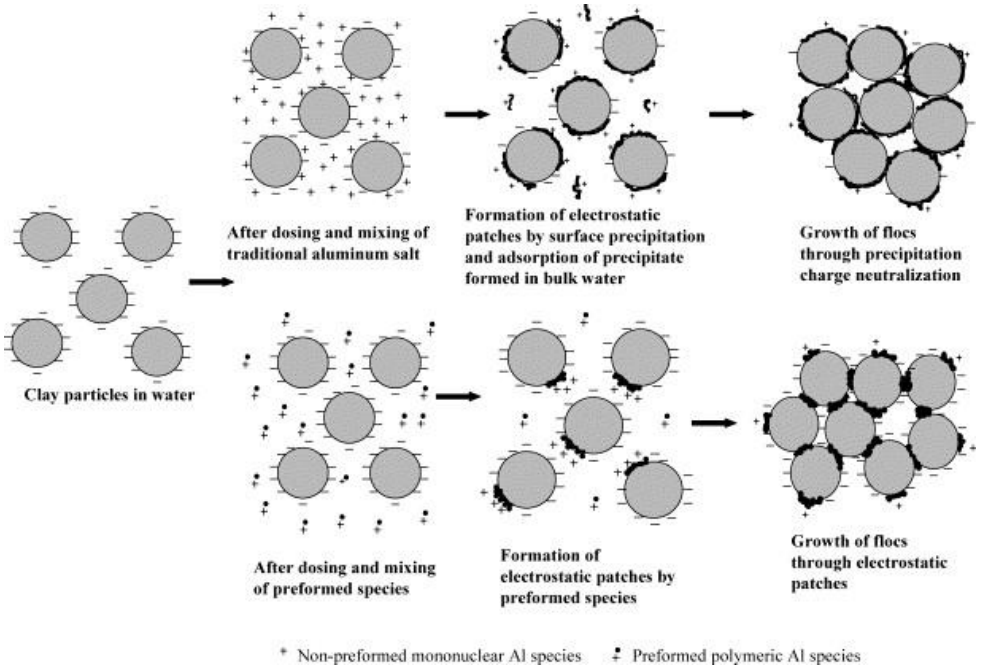


Figure 2.27 Schematic diagram of electrostatic patch coagulation[100]

Liang et al.[103-105] reports that polyaluminum chloride (PAC) has a good performance regar-ding depressing the ash of the coal samples. 20 mg/L PAC selectively aggregates minerals heavier than 2.0 g/cm^3 but does not aggregate the hydrocarbons (Figure 2.28). The ash of the cleaned coal is reduced from 13% to 9.52% and the yield goes down from 40% to 30.25% with 20 mg/L PAC[103].

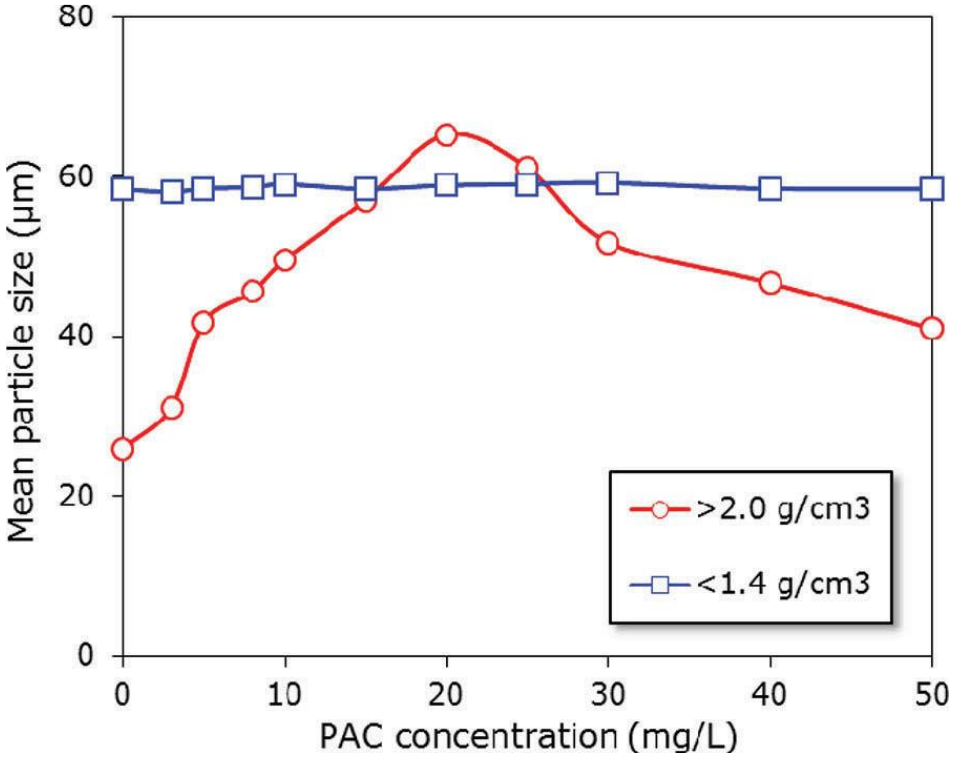


Figure 2.28 Aggregate size measurement of the fine particles (-74 μm) of the minerals and coal[103]

2.3 Summary

(1) For coal, these non-ionic surfactants were more effective than oily collectors via the hydrogen bonding to oxygenated sites on the coal surface or hydrophobic bonding of the hydrocarbon chain to hydrophobic sites on the coal surface. The cationic surfactants and anionic surfactants were also used by many researchers, whereas non-ionic surfactants have rarely been reported. Therefore, non-ionic surfactants (Span 80 + Tween 80) will be selected for preparing influential collectors used in flotation in this work;

(2) Most microemulsions in literature have been used in other fields like cosmetics, fuel, heat and power industry, and few microemulsions were applied to froth flotation. This Ph.D work therefore

explores microemulsions composed of Kerosene (collector) and flotation frothers MIBC (co-surfactants) in froth flotation;

(3) Dextrin, Guar gum, causticized corn starch and raw starch were studied in-depth by researchers home and abroad, while physically modified corn starch has hardly ever been reported. So modified corn starch will be studied for depressing the pyrite in the froth flotation in this Ph.D work;

(4) Previous studies paid most attention to the effect of alkalinity on the industrial waste water coagulation behaviors of PAC. And some researchers also reported that PAC had a good performance regarding depressing the ash of the coal samples. Because ash is composed of Kaolinite, pyrite, quartz, calcite, etc., the depressing effect of PAC on pyrite is studied in this work. And it is aimed in filling the gap in the literature on the depressing characteristics of PAC with regards to the pyrite flotation process in this study.

3 Experimental materials and methods

This work used Span 80, Kerosene, MIBC, Tween 80 and distilled water for the preparation of the new collector MEC. DL-2-Octanol was used as the frother for froth flotation. PAC and corn starch were used as depressants in the flotation. Actual sample (JDMN), pure mineral (pyrite), and an ideal system (TXM+pyrite) were studied. The details of these materials will be discussed in this chapter. Various devices were used for materials characterization and performance assessments. These will also be detailed in this chapter.

3.1 Reagents and sample preparation

As indicated above, Kerosene, DL-2-Octanol, Span 80, Tween 80 and non-ionic co-surfactant MIBC, depressants (PAC, corn starch) were used in this work. All the reagents are listed in Table 3.1. Kerosene is obtained from the fractional distillation of petroleum between 150 and 275°C, resulting in an aromatic hydrocarbon mixture containing C_{10}-C_{16} per molecule.

HLB is the hydrophilic-lipophilic balance of a surfactant, determined by calculating values for the different regions of the molecule by Davies' method:

$$HLB = 7 + \sum_{i=1}^{m} H_i - n \times 0.475 \tag{3-1}$$

The microemulsions were prepared by mixing kerosene (K), surfactant (Span 80 and Tween 80) with HLB = 6, 7, 8, 9, and MIBC first. This is followed by titrating with distilled water to form a low-viscosity, isotropic, golden yellow solution from an initial turbid, opaque solution. The weight percentage of water was determined by equilibrium titration.

Particle size distributions of solid materials including JDMN, pyrite, and TXM are shown in Figure 3.2, Figure 3.3 and Figure 3.4, respectively using laser particle size analyzer (Beckman LS13320, US).

And the proximate analysis results of JDMN are below: M_{ad} is 3.06%, A_{ad} is 55.56%, V_{ad} and FC_{ad} are 20.2% and 21.18%, respectively. M is the moisture content, A is the ash content, V is the volatile matter content, FC is the fixed carbon content, and ad is air-dried basis. The ultimate analysis results of JDMN are below: C_{ad} is 31.98%, S_{ad} is 1.40%, O_{ad} is 5.33%, H_{ad} is 2.09% and N_{ad} is 0.58%. The ash content (A_{ad}) of JDMN is 55.56%, and the C_{ad} is only 31.98%, indicating that JDMN is high-ash coal slime. The hydrogen content decreases with the deepening of metamorphism. H_{ad} is only 2.09%, which proves the high metamorphism and the hydrophobic property of JDMN.

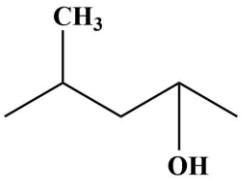
And the proximate analysis results of TXM are below: M_{ad} is 0.62%, A_{ad} is 3.01%, V_{ad} and FC_{ad} are 7.48%, and 88.89%, respectively. The ultimate analysis results of TXM are below: C_{daf} is 90.18%, S_{daf} is 0.14 %, H_{daf} is 3.2 %, N_{daf} is 0.73 %, and O_{daf} is 2.74%. daf is dry-ash-free basis. This indicates that the sample is a high-quality carbon fuel with high carbon content but low sulfur and low ash, which will be mixed with pyrite for ideal system.

The JDMN, pyrite, and TXM were analyzed with XRD and the results are shown in Figure 3.5, Figure 3.6, and Figure 3.7, respectively, where K represents Kaolinite, Q represents Quartz, P represents Pyrite, and C represents Calcite.

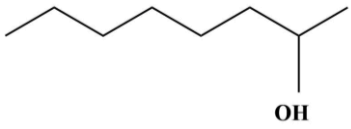
The compositions of chemicals are given in Table 3.1. And the instruments used in this study are shown in Table 3.2.

Table 3.1 The chemicals used in this study

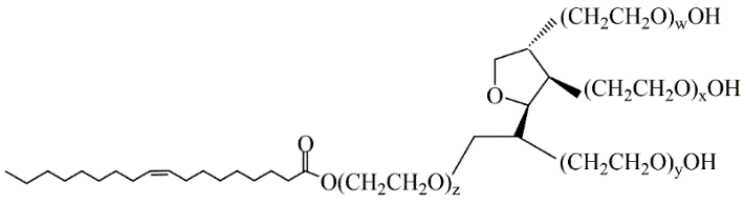
Chemical	Supplier	Role	Formula
Kerosene	Cyanamid	Collector	Mixture (C_{10}-C_{16})
DL-2-Octanol	Merck	Frother	$CH_3(CH_2)_5CH(OH)CH_3$
Span 80	Aladdin	Surfactant	Shown in Figure 3.1
Tween 80	Aladdin	Surfactant	Shown in Figure 3.1
MIBC	Aladdin	Co-surfactant	$(CH_3)_2CHCH_2CH(OH)CH_3$
PAC	-	Depressant	Mixture (monomer Al_a, polymer Al_b, precipitate Al_c)
Corn Starch	Merck	Depressant	$(C_6H_{10}O_5)_n$



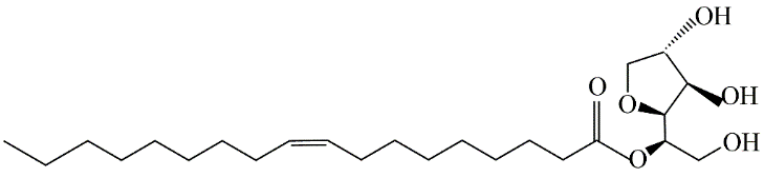
(a)



(b)



(c) x + y + z + w = 20



(d)

Figure 3.1 The chemical structure formula of (a) MIBC, (b) DL-2 Octanol, (c) Tween 80, and (d) Span 80

Table 3.2 The instruments used in this study

Instrument name	Model	Manufacturer
Industrial analyzer	5E-MAG6700II	Kaiyuan Instruments
Elemental analyzer	YX-CHN5000	Youxin Instruments
Sulfur meter	5E-3200B	Kaiyuan Instruments
Ultrasonic cleaner	SB25-12DT	NINGBO SCIENTZ
Balance (0.001g)	BSA124S	Sartorius
Balance (0.1g)	HTP-312	HUACHAO
Blender	VM0198	Vita-Mix Manufacturing Corporation
Air dry oven	DHG9246A	JINGHONG
Vacuum drying oven	DZ-2BCII	Taisite
Magnetic Stirrer	SHT	Shandong Hualu
Flotation machine (60mL)	XFG-II	Wuhan Exploration Machinery Factory
Flotation machine (1L)	XFG-IV	Wuhan Exploration Machinery Factory

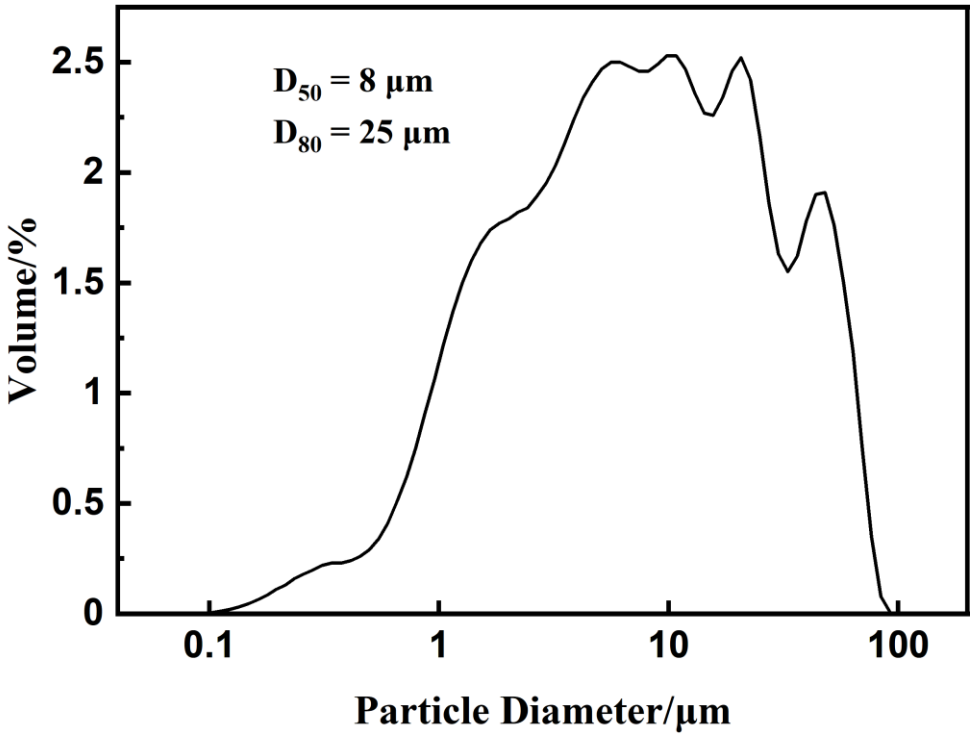


Figure 3.2 The particle size distribution of JDMN measured by laser particle size analyzer

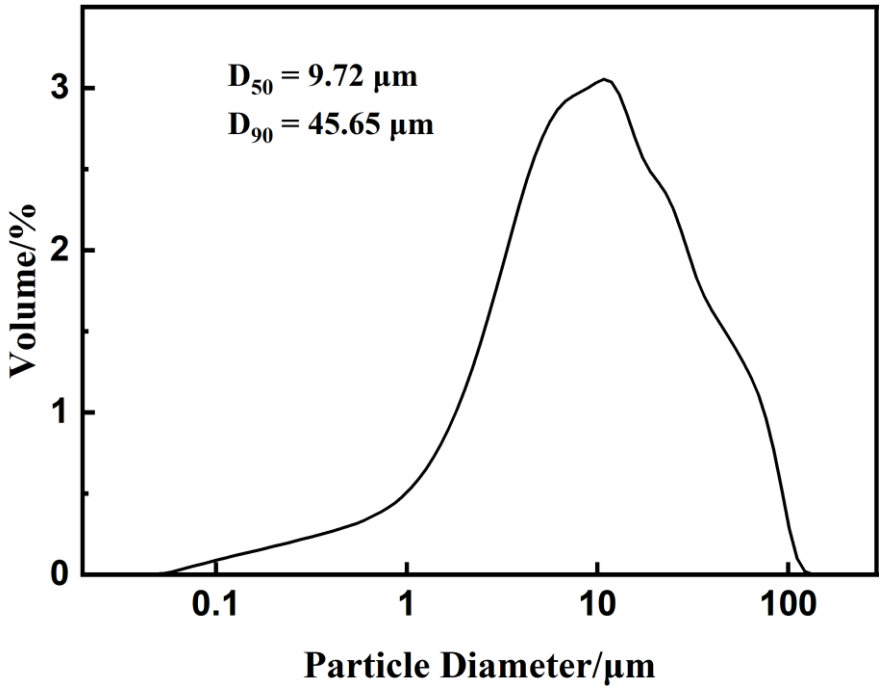


Figure 3.3 The particle size distribution of pyrite using particle size analyzer

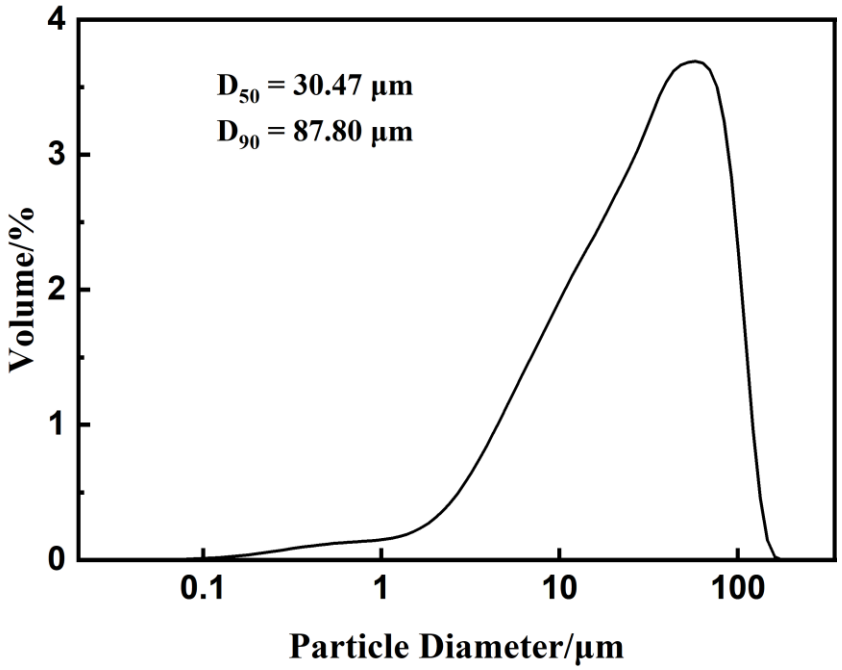


Figure 3.4 The particle size distribution of TXM using particle size analyzer

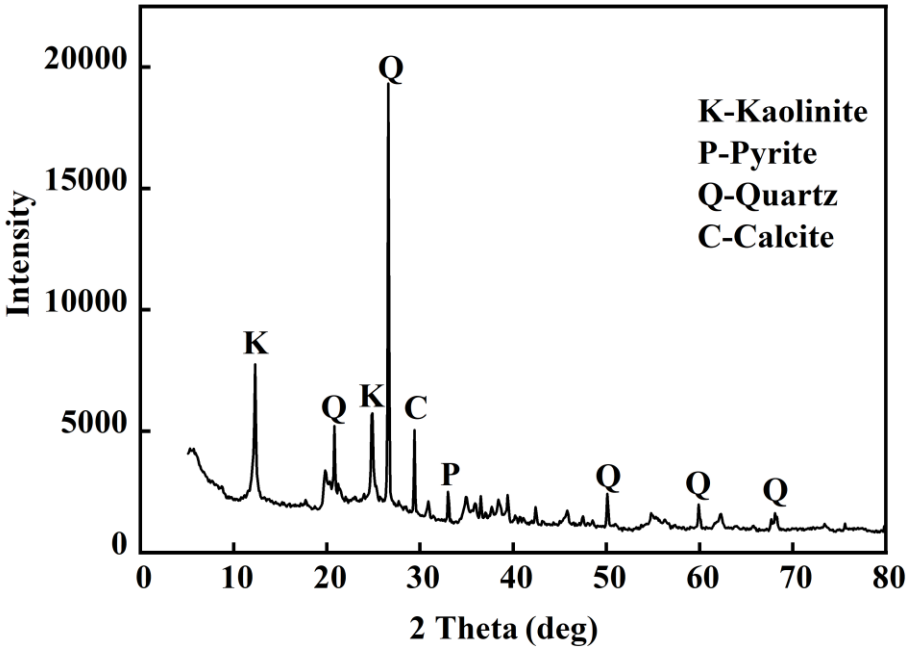


Figure 3.5 XRD of JDMN sample

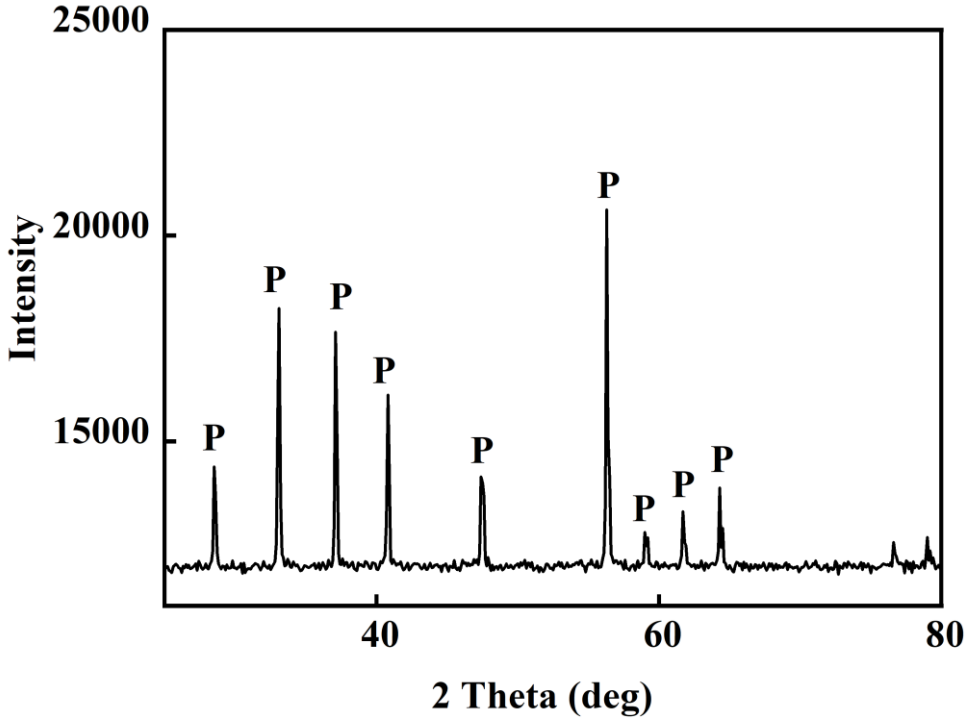


Figure 3.6 XRD of pyrite sample

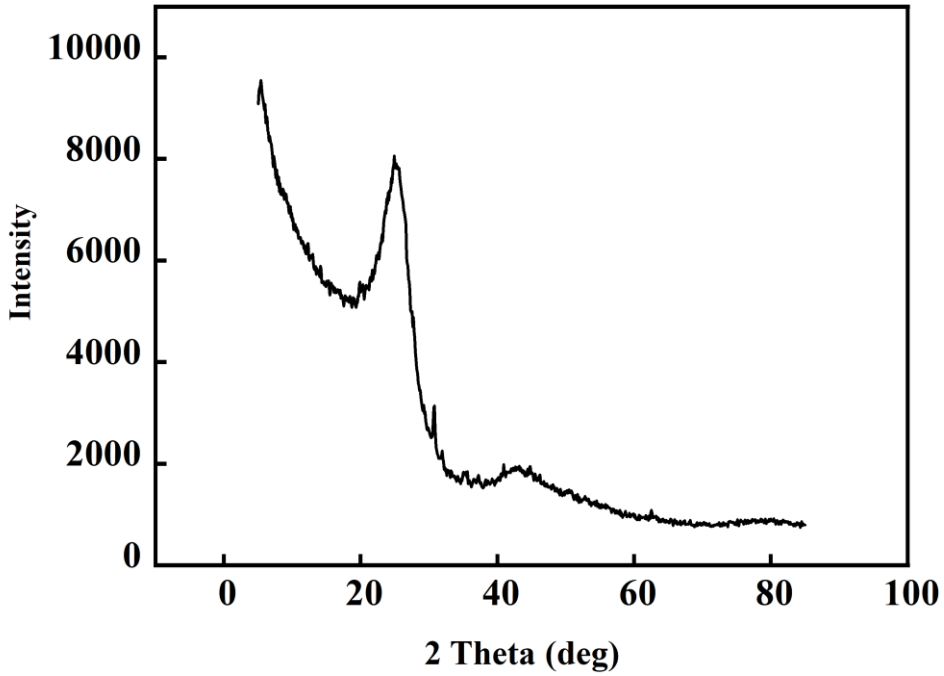


Figure 3.7 XRD of TXM sample

3.2 Particle size distribution with Dynamic Light Scattering Techniques

Dynamic light scattering (DLS) is one of the most common techniques for characterizing emulsions and microemulsions for their droplet size[106]. This dynamic light scattering method measures the speed of light scattered from the dispersed droplets under Brownian motion and converts the intensity of light to droplet size as shown in Figure 3.8[107]. The so-called Stokes-Einstein equation is used to calculate the size (Eq.(3-1)) assuming that the droplets are spherical[108].

$$d_h = \frac{\kappa T}{3\pi\eta D} \tag{3-1}$$

where κ is Boltzmann constant (1.380649×10^{-23} J/K), T is absolute temperature (K), η is the viscosity of the solvent and D is diffusion coefficient.

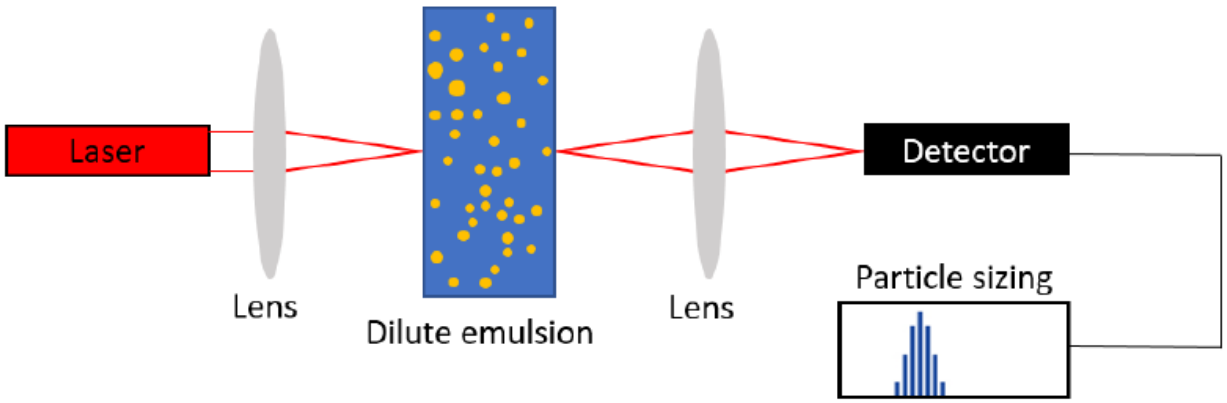


Figure 3.8 Light scattering technique

Comparing DLS and SLS (static light scattering) results has been used to define micelles sizes home and abroad, because DLS results alone are not a definitive argument for spherical structures. SLS method with three angles (45°, 90°, 135°) is performed to exclude the fluctuations dependent on angle. Kunz et al.[109] revealed the existence of nano-droplets in water-ethanol-long-chain alcohol perfume tinctures. The presence of nano-droplets of water/ethanol/repellent systems[110] was characterized with both the DLS and SLS methods. The DLS measurements were conducted with the same percentage of ethanol for the systems with citriodiol, ethyl 3-[(acetyl)(butyl)amino] propanoate, N,N-diethyl-m-methylbenzamide, and para-menthane-3,8 - diol, 1 - methyl propyl 2 - (2 hydroxyethyl) piperidine-1-carboxylate, respectively. The sizes of the system increased to the peak (> 1 nm) and decreased with the oil concentration with a low polydispersity, confirming the presence of spherical nanodroplets. They also [111] found nano-clustering was present in the water-free and surfactant-free microemulsions glycerol/ethanol/1-octanol with Dynamic Light Scattering. The DLS method was also used to measure the particle size of water-benzyl alcohol and ethanol, ethyl lactate or γ-valerolactone[112].

The DLS system used in this study is a NanoBrook Zeta PALS potential Analyzer (Brookhaven, US) for measuring the particle size of prepared MEC; see Figure 3.9. It uses a laser with a wavelength of 633 nm and detects the scattered light at an angle of 90º. All measurements were conducted at ambient temperature.

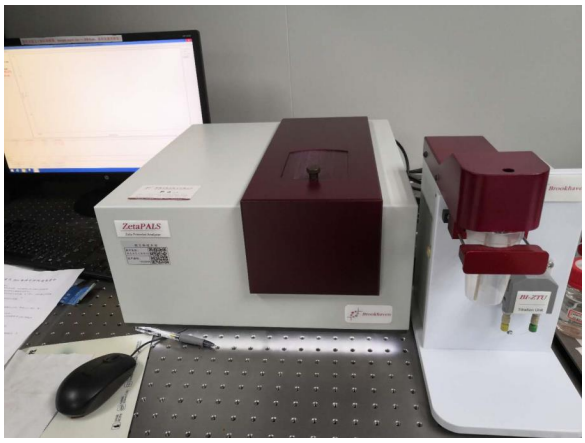


Figure 3.9 The physical picture of Zeta potential Analyzer NanoBrook ZetaPALS (BI-200SM, Brookhaven instrument Ltd., US)

3.3 Rheological Measurements

The rheological analysis of microemulsions can give the relationship of viscosity (η) as a function of shear rate (γ). Xie et al.[113] measured the viscosities of the sunflower oil of different concentrations containing dispersed dyes (Yellow BROB, Red 902 and Blue 825); see Figure 3.10 and Figure 3.11. It can be seen that the viscosity of the microemulsions increases gradually with the increasing content of oil. Oliver et al.[114] studied microemulsion composed of dodecane/ hexadecyl-3-methyl-imidazolium chloride ([C_{16}mim][Cl])/ ethylammonium nitrate(EAN)/ decanol and another system dodecane/ hexadecyl-3-methyl-imidazolium chloride ([C_{16}mim][Cl])/ (1-butyl-3-methylimidazolium tetrafluoroborate([bmim][BF_4]) / decanol. The microemulsions were found to exhibit a Newtonian behavior. The mean values of viscosities vary with the volume

fraction of room-temperature ionic liquids (RTIL) at 30°C. There is a proximate linear change for the viscosity of [bmim][BF_4] system, while for the EAN system, an obvious change of the slope is shown in Figure 3.12.

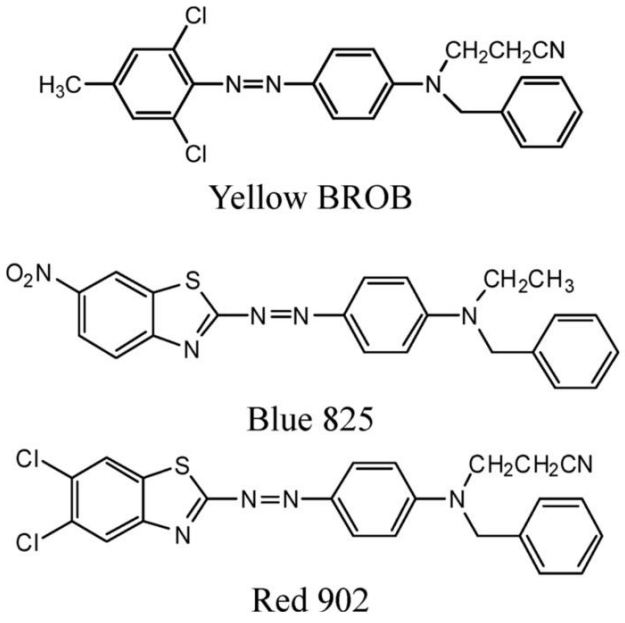


Figure 3.10 The structures of three dyes[113]

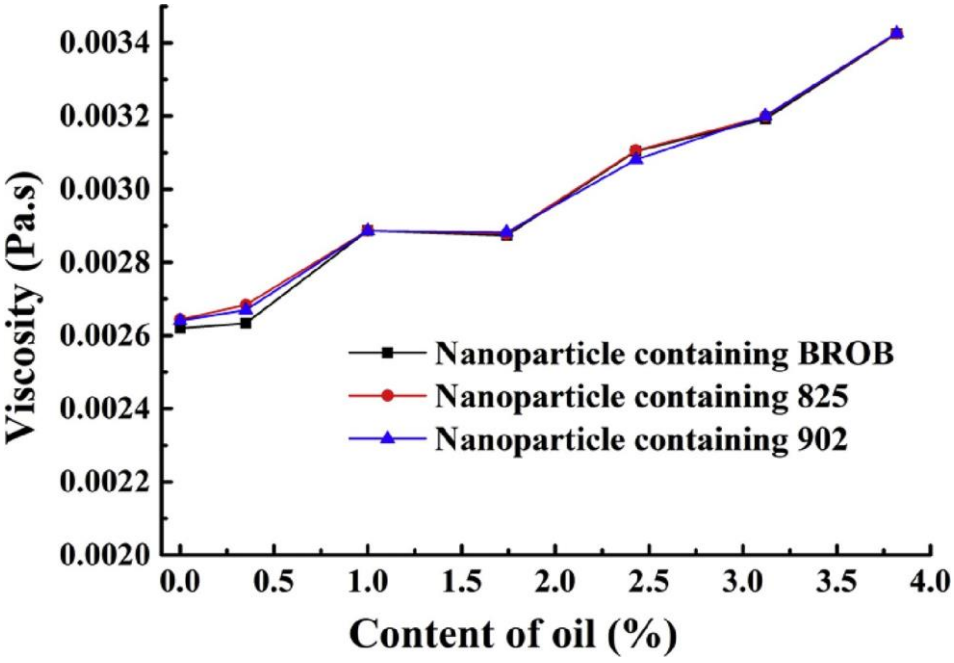


Figure 3.11 Viscosities of the nanoparticle-containing BROB, 825 and 902 with different concentrations of sunflower oil[113]

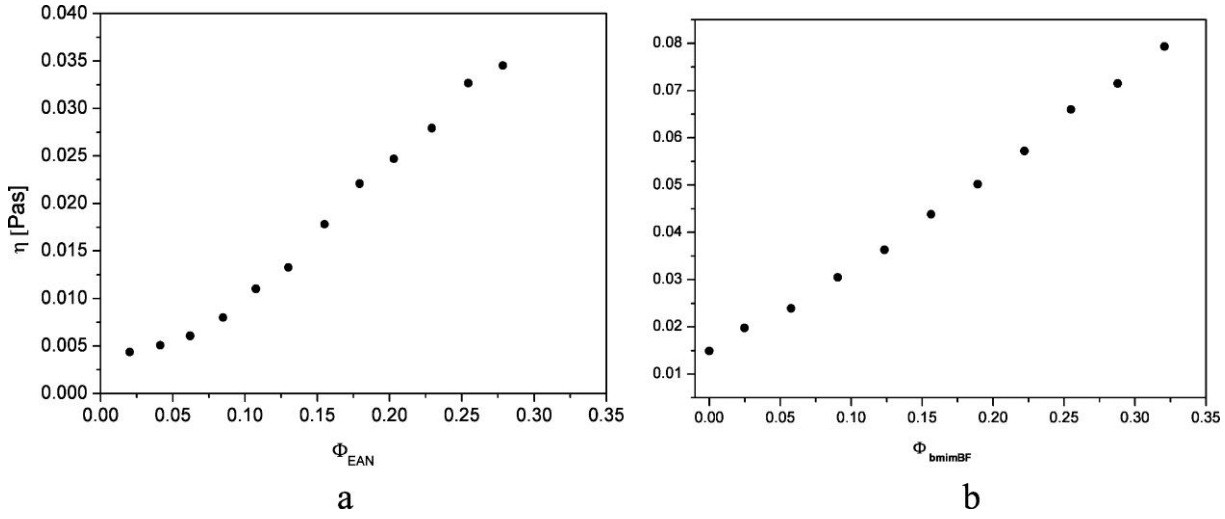


Figure 3.12 Dynamic viscosity η with the increasing of the volume fraction of (a) EAN and (b) [bmim][BF4] system at 30 °C[114]

Fluids can be divided into two broad categories of Newtonian fluids and non-Newtonian fluids. The non-Newtonian fluids include plastic, pseudo-plastic and dilatant fluids. Bao et al.[115] conduc-

ted rheological measurements of sodium salicylate and 2-hydroxyethyl dimethyl hexadecyl ammonium acetate systems at different temperatures. Their results demonstrated micelles formed in dilute solutions over 60°C. It was assumed that sodium salicylate might be inserted into the cationic head groups of the surfactant, resulting in the formation of wormlike micelles.

This work uses the HAAKE MARS Rheometer (Thermo scientific) for the rheology measurements, which has a 60 mm diameter 0° cone-and-plate geometry shown in Figure 3.13. In a typical experiment, a sample was placed and kept for 1 min on the plate with any overflow of the sample gently scraped away before measurement to avoid the edge effect. The temperature was controlled to be at 25 ± 0.5 °C. The experiments gave a relationship between viscosity (η) and shear rate (γ).

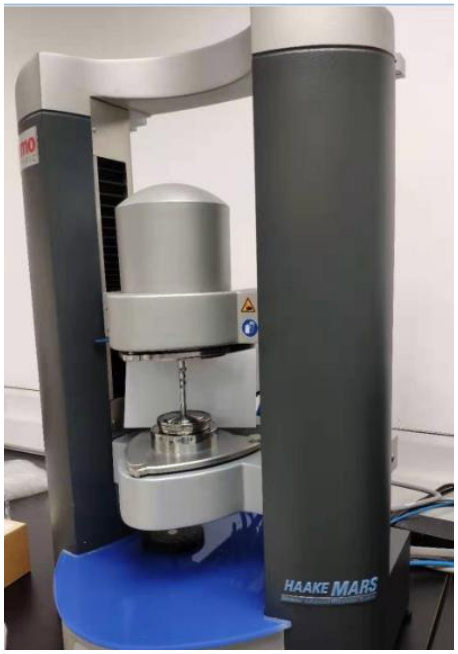


Figure 3.13 The physical picture of HAAKE MARS

3.4 Electrical conductivity

Electrical conductivity could be used to characterize the structure of microemul sions[116-120]. The Winsor I (O/W microemulsions) and the Winsor III microemulsions (three-phase systems) have a

relatively high conductivity compared to the Winsor II systems (W/O microemulsions). In spite of that, the electrical conductivity of Winsor II system is in the range of 10^{-6}-10^{-5} $S \cdot m^{-1}$, which was still higher than that of apolar solvents (10^{-16} -10^{-12} $S \cdot m^{-1}$).

Testard et al.[121] demonstrated that the curvature of microemulsion (water / didodecyldimethylammonium bromide (DDAB) / dodecane) decreased as the amount of water was increasing. Ali et al.[122] measured the electrical conductivities of D_2O / n-heptane / didodecyldimethylammonium bromide–poly(oxyethylene) monododecyl ether/water and found that the values dropped as the ratio of surfactant was increasing. Murashova et al.[123] studied the conductivity of sodium bis-(2-ethylhexyl) phosphate (NaDEHP) - bis-(2-ethylhexyl) phosphoric acid (DEHPA)-Kerosene-water. An increase in DEHPA concentration (100 - 400 mmol/L) decreased the conductivity of the microemulsion, while 0.1 mol/L DEHPA had no effect on the electrical conductivity.

In this work, a DDS-307 Conductometer (Shanghai Leichi Instrument Factory) and a Pt-electrode cell were used to measure the electrical conductivities of MEC. The cell constant K was 0.995 cm^{-1}. The conductivity of standard liquid 1 mmol/L KCl solution was found to be 143.06 $\mu S \cdot m^{-1}$, consistent with the results reported from the manufacturer. The mass ratios of ingredients in the microemulsion were Kerosene: Water : Surfactant : MIBC =15 : 4 : 10 : 5.6. The ingredients were mixed uniformly to be completely transparent before the electrical conductivity was measured. For valid comparisons, when the concentration of one component was changed, the others were fixed.

3.5 Cryo-Transmission Electron Microscope (Cryo-TEM)

A Cryo-TEM was used to observe the microemulsions in this work, which was a Titan Krios G3 system (D3706, 300 kV). For doing so, samples were prepared with a device called Vitrobot at

room temperature, as shown in Figure 3.14. A typical sample used three μL solution which was dropped onto a grid in the chamber, and two filters were used to adsorb any excess solution. This would form suspended thin films on the mesh holes. The grid was then rapidly immersed in liquid ethane (-165 °C) after ~5 s. The samples were then transported by a cryogenic rack and tested with the Cryo-TEM as shown in Figure 3.15. The images were recorded on a Gatan multiscan CCD and processed with Digital Micrograph software package.



Figure 3.14 Sample freezing apparatus called Vitrobot

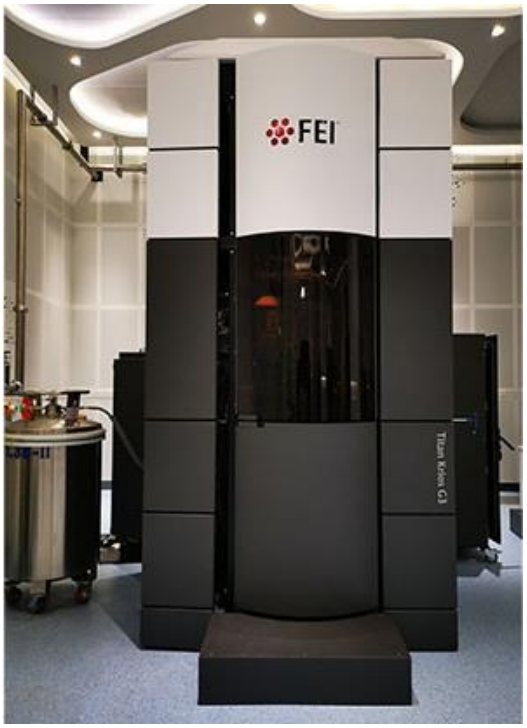


Figure 3.15 Automatic Electron microscope Titan Krios G3 (D3706, 300 kV)

3.6 Zeta potential (ζ-potential)

The zeta potential is proportional to the droplet moving velocity in the sample activated by the electric field. Here, the ζ-potential is defined as the potential between the droplet surface and the continuous phase, as illustrated in Figure 3.16.

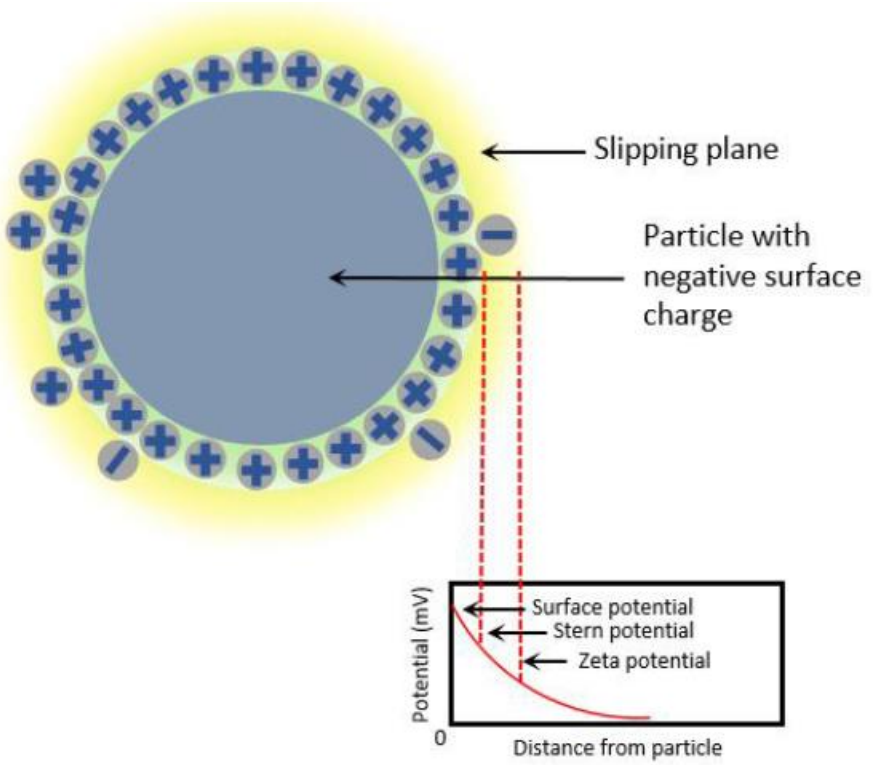


Figure 3.16 Schematic diagram of zeta potential

Xie et al.[113] measured the zeta potential and surface tension of sunflower oil synergy polymeric microemulsions. They found that the zeta potentials of three disperse dyes microemulsions were between -45 and -60 mV. Chen et al.[124] studied the interactions of Triton X-100/ sodium nonylphenol polyoxyethylene ether sulfate/cetyl trimethyl ammonium bromide/ sodium dodecyl sulfate systems. Their results showed that the zeta potential of micelles became more negative with an increasing content of nonylphenol polyoxyethylene ether sulfate apart from CTAB. Liu et al.[125] showed that kerosene emulsified by Dodecylamine (DDA) became positively charged at pH = 8.0, 9.0, and 9.5 when the weight ratio of DDA were 20%, 50% and 80% in DDA-Kerosene system, respectively, as shown in Figure 3.17, which indicated the increased DDA concentration caused the zeta potential of oil droplets to move in the positive direction.

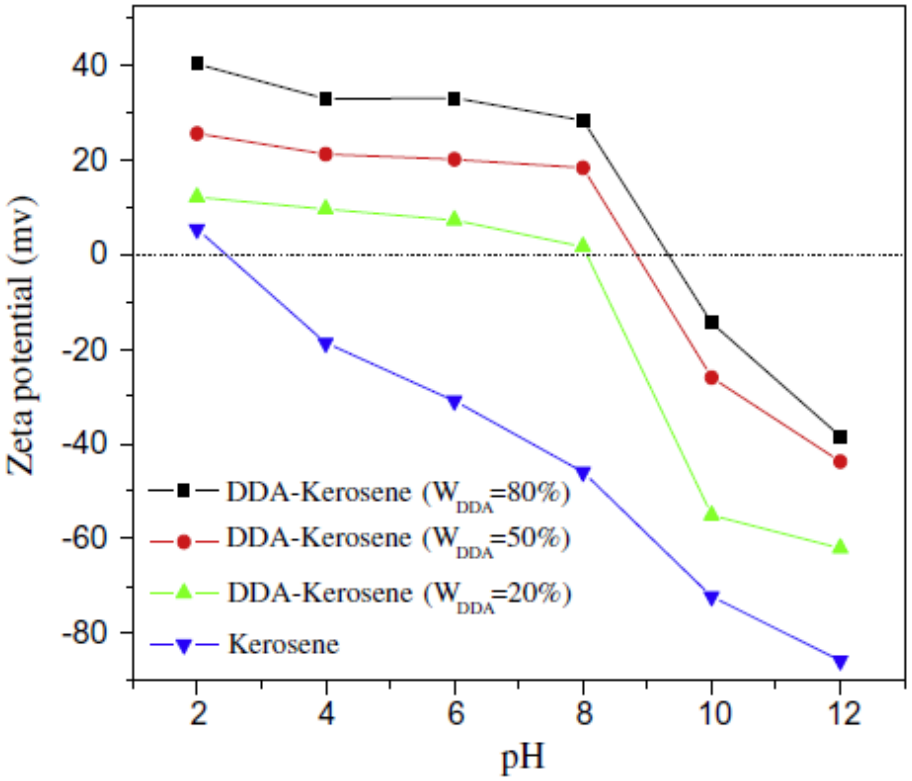


Figure 3.17 Zeta potential of DDA-Kerosene emulsion and kerosene emulsion[125]

Gurses et al.[126] observed the variations of zeta potentials of agglomerates of raw coal and products from the conditioning step with an increase in suspension pH; see Figure 3.18. They indicated that this could be used to predict the agglomeration process and the performance of selective oil agglomeration.

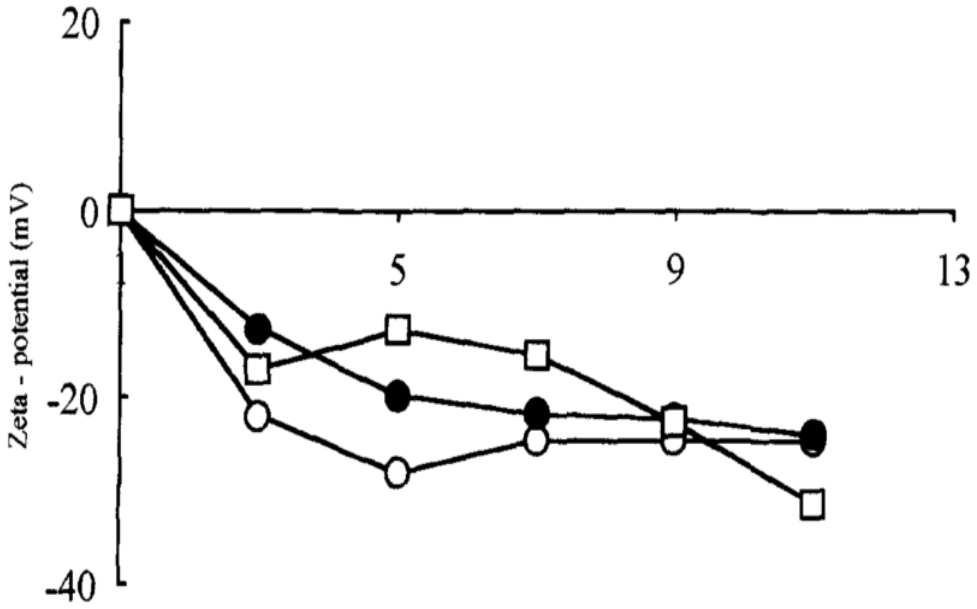


Figure 3.18 Comparison of zeta potentials of product from conditioning step (●) and raw coal (○) with that of the agglomerates (□) as a function of suspension pH[126]

In this study, the Zeta(ζ) potential of coal particles is measured with a NanoBrook ZetaPALS (Brookhaven, US) system shown in Figure 3.19, which is based on the electrophoresis method. In a typical measurement, about 0.05 g coal sample was transferred to a 30 mL potassium chloride solution (1×10^{-2} M). The mixture was agitating at 800 rpm for three minutes, when different dosages of MEC or kerosene (500 g/t, 1000 g/t, 1500 g/t, 2000 g/t, and 2500 g/t) were added with another 5 min agitation. Five mL suspension was then taken and placed into a tube. Finally, a 1mL supernatant sample was measured by the potential Analyzer. All measurements were conducted at the room temperature. For each of the suspensions, ten measurements were conducted, and the mean was taken for the analysis.

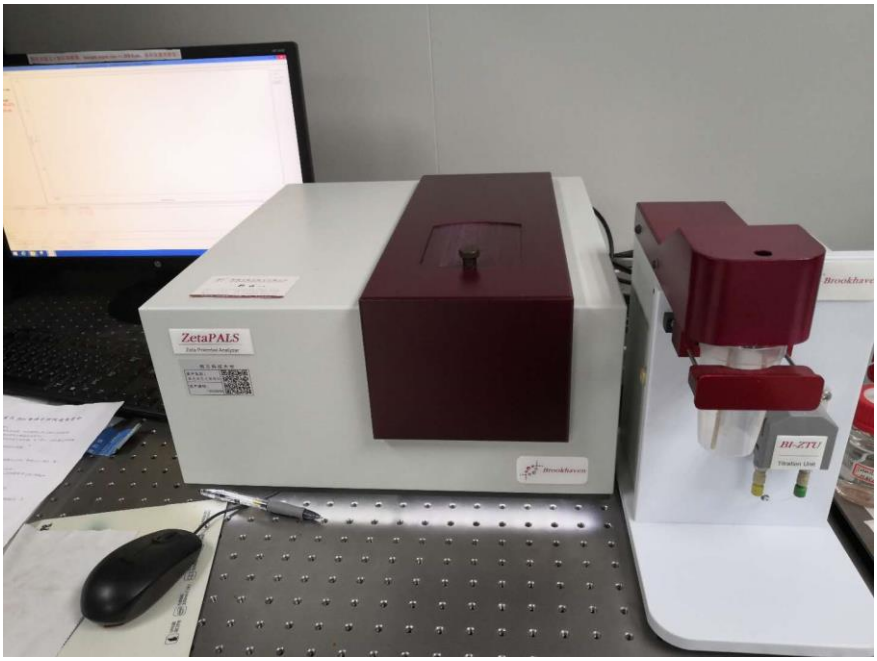


Figure 3.19 The physical picture of zeta potential Analyzer NanoBrook ZetaPALS (BI-200SM, Brookhaven, United States)

3.7 Contact Angle

Contact angle reflects the floatability differences of minerals. The contact angle of minerals with a higher extent of hydrophobicity gives a larger floatability.

The floatability of the mineral is defined by Eq.(3-2):

$$\text{Floatability} = 1 - \cos\theta \tag{3-2}$$

Where θ is the contact angle and hence an indication of wettability.

In this work, a KRUSS DSA25S was used for measuring the contact angles of samples without and with Kerosene or MEC as shown in Figure 3.20. Coal samples modified by different dosages of MEC or Kerosene (0, 500 g/t, 1000 g/t, 1500 g/t and 2000 g/t) were prepared with a press machine (HY-12) at a pressure set to 20 MPa for 8 min. This gave samples with a thickness of 2

mm. One such a sample was then placed in a rectangular glass chamber with smooth surfaces on both sides to the KRUSS machine for measurements.

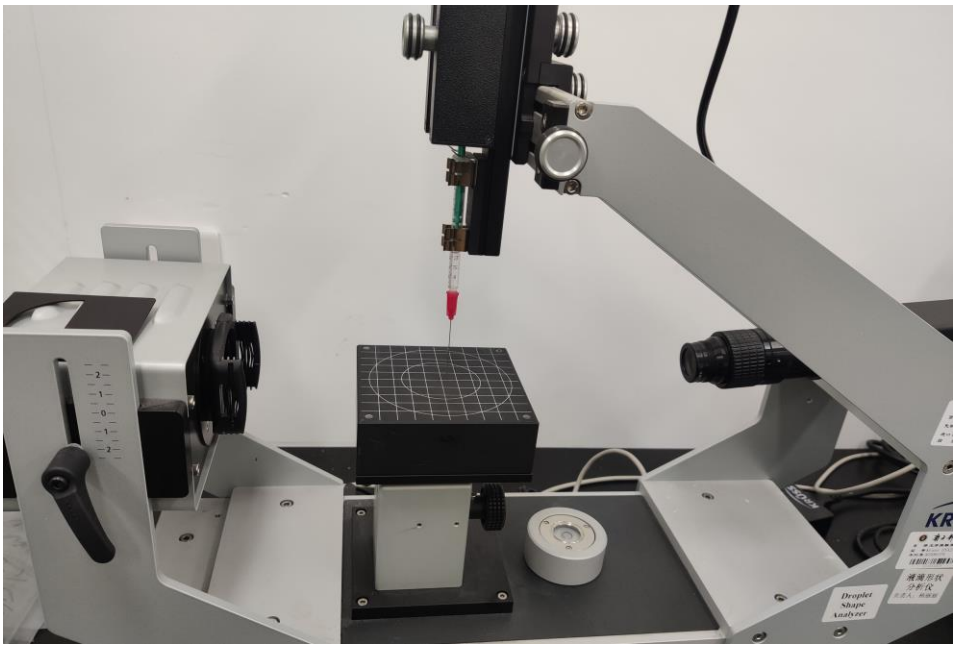


Figure 3.20 The physical picture of contact angle measuring instrument (KRUSS DSA25S)

3.8 Fourier Transform Infrared Spectroscopy (FT-IR) analyses

The adsorption behavior of the pyrite surface without and with depressants in an aqueous environment is of great importance to the understanding of the flotation process. In this work, functional groups of pyrite samples and depressants were studied with VERTEX 80 FT-IR (RAMII, BRUKER, Germany) as shown in Figure 3.21. The scanning was from 4000 to 600 cm^{-1} with a resolution of 2 cm^{-1}. For the measurement of the functional groups of the collector, a mixture of reagent and pyrite was made in a magnetic stirrer for 24 h before dried for the measurements. Then the plates of the above sample and KBr were prepared at a mass ratio of 100: 1. They were ground

in an agate mortar before pressed at 20 MPa to form round plate samples. All the experiments were conducted at the ambient temperature.

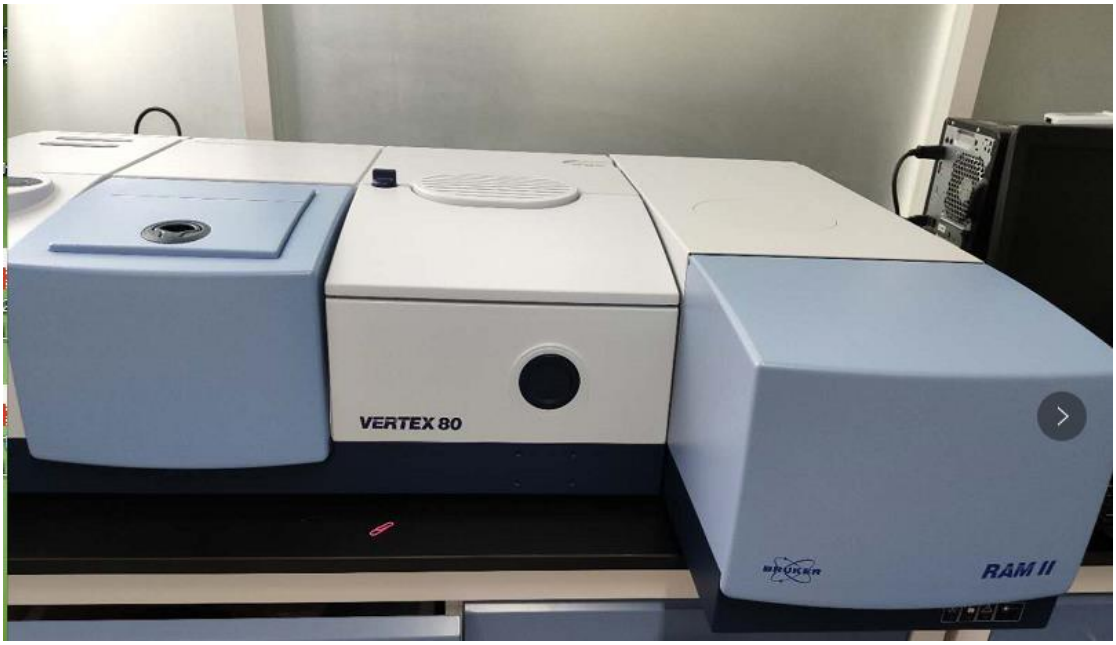


Figure 3.21 The physical picture of RAM II from VERTEX 80 (RAMII, BRUKER, Germany)

3.9 X-ray Photoelectron Spectroscopy (XPS) analyses

The XPS analysis can provide information on the elemental composition and chemical state of the samples through exciting out photoelectrons from the sample surface to a depth of 1-10 nm and then analyzing the energy of the emitted electrons directly. It is a non-destructive and sensitive surface analysis method and can be used to detect changes in valence states of adsorbed species.

Rath et al.[81] used the XPS method to analyze pyrite with and without guar gum and dextrin, indicating the presence oxide and sulfate layer on the pyrite surface. Han et al.[127] studied the elements on the pyrite adsorbing starch using a XPS for the mineral surface components changes and the chemical adsorption of starch on the pyrite was proven by peak shift of Fe (II). Smart et al.[128] reviewed the assignments of S 2p XPS spectra from the surface of sulphide minerals like

160.1-161.2 eV for S^{2-}, 162.1-162.6 eV for S_2^{2-}, 161.9-163.2 eV for polysulphides (S_n^{2-}), and 163.0-164.2 eV for sulphur (S_n^0). Harmer et al.[129] observed the negative charging of the chalcopyrite surface layer in a leaching process under an acidic condition via the BE (binding energy) of C1s < 284.8 eV indicating an excess of electrons. Mikhlin et al.[130] studied the adsorption of xanthate on the surface of galena (PbS) by XPS, and the chemical adsorption on the xanthate was obtained via S $2p_{3/2}$ spectroscopy.

In this study, XPS analyses were done on pyrite samples treated with corn starch and PAC. In a typical measurement, 2.0 g pyrite samples were used, which was firstly ultrasonicated before treated with certain amounts of reagents. Corn starch or PAC solution was then added to the sample under magnetic stirring for 30 minutes. Then the samples were separated, filtered, washed with deionized water, and dried for XPS analysis.

The XPS analyses were carried out with a PHI 5000 VersaProbe III spectrometer (Figure 3.22), which uses monochromatic Al K(alpha) X-ray source, with 200 μm 50 W 15 kV. The instrument work function was calibrated to give binding energy (BE) of 83.95 eV for the Au $_{4f\,7/2}$ line on the metallic gold sample. The PHI 5000 VersaProbe III charge neutralization system was fully achieved by monitoring the C 1s peak position (284.8 eV) the same during the experiment.

High-resolution analyses were carried out with 200 μm X-ray beam over a 500 × 500 microns area. The analyzer pass energy was 69.0 eV with a step size of 0.125 eV. Spectra have been charge corrected to the mainline of the C1s and set to Binding energy of 284.8 eV. The vacuum pressure in the PHI 5000 VersaProbe II analysis chamber was set at or below 10^{-9} Torr. The PHI MultiPak software (version 9.8) was utilized to analyze the acquired data. During element curve fitting, a "Shirley" background subtraction method was used and the fitting curve line-shape was the

"Gaussian-Lorentzian" function. In addition, the FWHM lock (Full-Width at Half-Maximum) was set amongst those peaks from the same element but different chemical state peaks, whereas the area ratio lock and peak position lock were set on elements with known spin-orbit splitting.



Figure 3.22 The physical picture of XPS instrument (PHI 5000 Versaprobe III)

4 Results and analyses I - Characterization of MEC and interactions between MEC and coal samples

In this chapter, results of the new collector, MEC, through screening with froth flotation are presented. The flotation experiment process, the dosages of reagents, equipment parameters etc., are described in detail. The characterization of MEC is performed with Dynamic Laser Scattering measurement, electrical conductivity, rheological analysis, and cryo-transmission electron microscope, for demonstrating the properties of the MEC. The spreading velocity of MEC and Kerosene is calculated. The interactions of MEC with coal samples are analyzed with the EDLVO theory. A mechanism of MEC attachment to the coal surface is also proposed.

4.1 The preparation of MEC

4.1.1 The preparation of microemulsions

The prepared MEC at different values of HLB (6, 7, 8 and 9) are shown in Table 4.1, Table 4.2, Table 4.3, and Table 4.4, respectively.

Table 4.1 The prepared MEC when HLB = 6

Kerosene/%	Water/%	Surfactant/%	MIBC /%
37.2	13.2	32.1	17.5
39.7	10.2	32.7	17.4
35.7	13.3	38.1	12.9
38.1	11.2	33.8	16.9

Table 4.2 The prepared MEC when HLB = 7

Kerosene/%	Water/%	Surfactant/%	MIBC /%
38.3	14.1	26.6	21
43.2	11.8	28.7	16.2
64.4	3.4	12.9	19.2
46	6.1	30.7	17.2
19.3	3.6	51.4	25.7

Table 4.3 The prepared MEC when HLB = 8

Kerosene/%	Water/%	Surfactant/%	MIBC /%
41.9	15.1	29.5	13.4
45.5	12	30.3	12.2
38.2	14.2	33.2	14.5
43	11.8	34.9	10.3
42.1	2.2	34.8	20.9

Table 4.4 The prepared MEC when HLB = 9

Kerosene/%	Water/%	Surfactant/%	MIBC /%
43.8	15	30.9	10.2
48.5	13.7	32.5	5.3
41.4	14.2	36.0	8.4
43.8	11.8	36.0	8.4
51.4	12.7	27.3	8.6

Figure 4.1 shows the photos of the prepared MEC. It can be seen that the samples are transparent and they are stable for at least half a year.

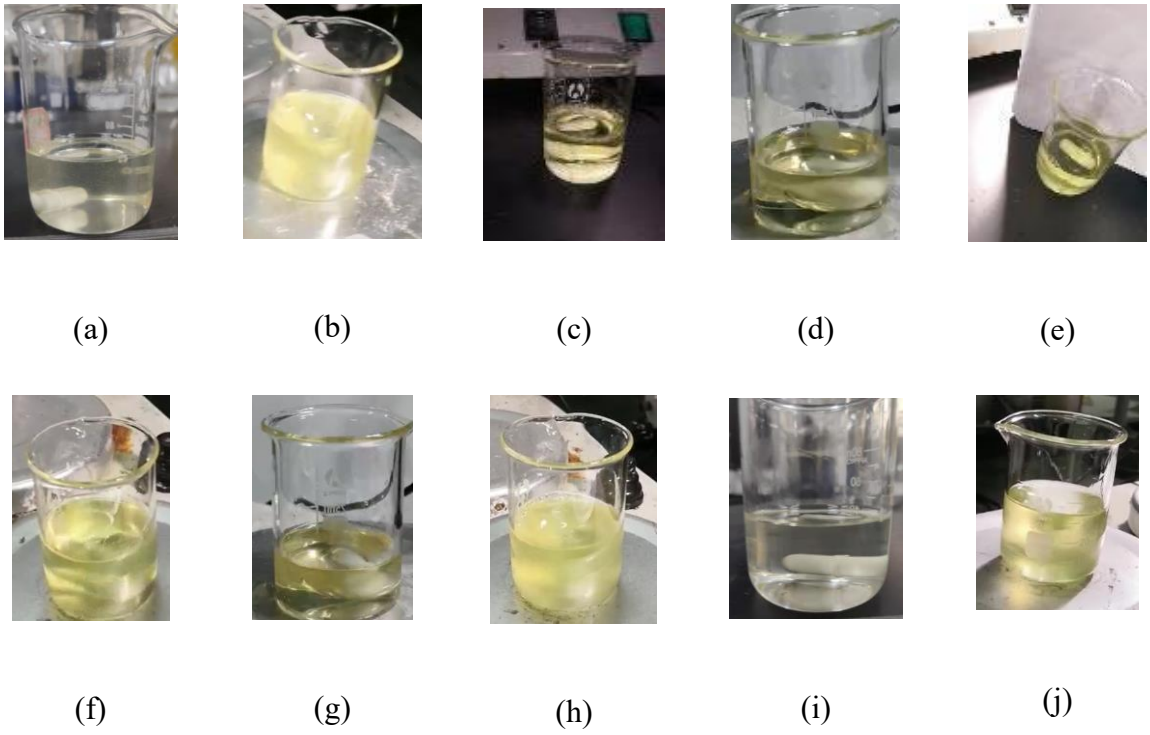
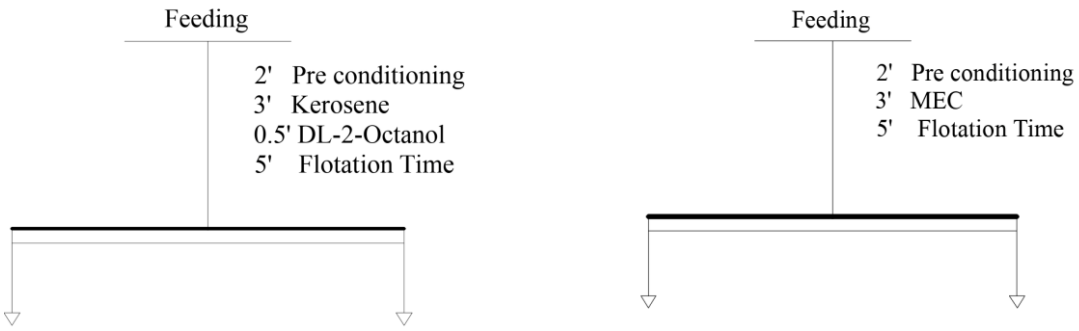


Figure 4.1 Some physical photos of prepared MEC : (a) K :W : S : C= 38 : 11 : 34 : 17 (HLB = 6), (b) K :W : S : C= 38 : 14 : 27 : 21 (HLB = 7), (c) K :W : S : C= 65 : 3 : 13 : 19 (HLB = 7), (d) K :W : S : C= 19 : 4 : 51 : 26 (HLB = 7), (e) K :W : S : C= 46 : 6 : 31 : 17 (HLB = 7), (f) K :W : S : C= 46 : 12 : 30 : 12 (HLB = 8), (g) K :W : S : C= 43 : 12 : 35 : 10 (HLB = 8), (h) K :W : S : C= 42 : 2 : 35 : 21 (HLB = 8), (i) K :W : S : C= 51 : 13 : 27 : 9 (HLB = 9), (j) K :W : S : C= 41 : 14 : 36 : 9 (HLB = 9). (K = kerosene, W = water, S = mixed surfactant, C = co-surfactant, MIBC)

4.1.2 Screening of the MEC through froth flotation

Figure 4.2 shows the flotation process in this study. A XFD flotation machine with a cell of 1 L (XFG-IV, Wuhan Exploration Machinery Factory, China) was used for the flotation experiments with a concentration of 100 g/L. An agitation speed of 2000 rpm and a dosage of DL-2-Octanol of 800 g/t dry coal were used in all flotation experiments. In a typical experiment, the pre-conditioning of the coal was carried out first under stirring at 2000 rpm for 2 min. Then Kerosene and DL-2-Octanol were injected at 2000 rpm for 3 min, 0.5 min, respectively or only MEC was injected at 2000 rpm for 3 min. The aeration rate was set to 0.2 $m^3/m^2/min$. And the froth flotation

time is 5 min. Finally, the froth products and tailings were then filtered and dried in an oven at 80°C before weighing for mass and ash analyses.



(a) Kerosene as the collector (b) MEC as the collector

Figure 4.2 The flow chart of the flotation process

The combustible recovery (C_R) and the improved flotation index (I_F) of the froth products are calculated by Eqs. (4-1) and (4-2) given in the following:

$$C_R = \frac{M_C(100 - A_C)}{M_F(100 - A_F)} \times 100\% \quad (4\text{-}1)$$

$$I_F = \frac{M_C}{M_F(100 - A_F)} \frac{A_F - A_C}{A_F} \times 100\% \quad (4\text{-}2)$$

where M_F (g), A_F (%), M_C (g), A_C (%) are the mass of the feeding, the ash of the feeding, the mass of the cleaned coal and the ash of the cleaned coal, respectively.

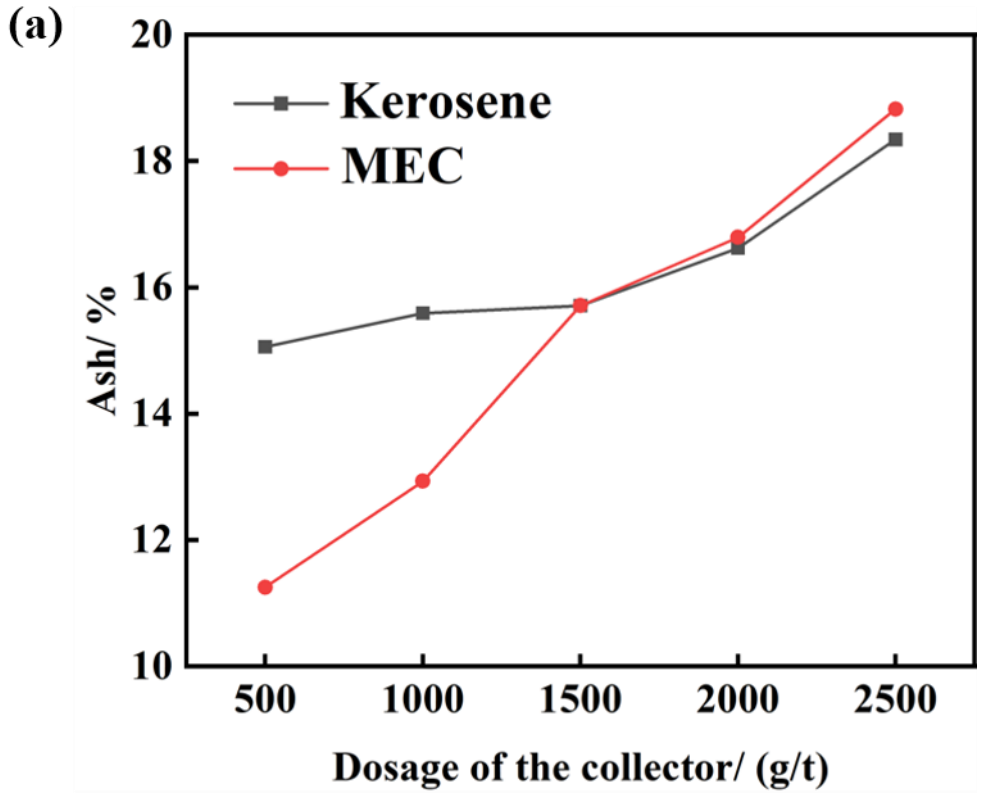
Figure 4.3- Figure 4.6 show the ash content, combustible recovery and improved flotation index of the clean coal obtained using 500, 1000, 1500, 2000 and 2500 g/ton-dry-coal of MEC, corresponding to HLB = 6, 7, 8, 9 and Kerosene, respectively. It can be seen that the results for MEC and Kerosene show a similar trend in the flotation process. When C_R was around 60%, the

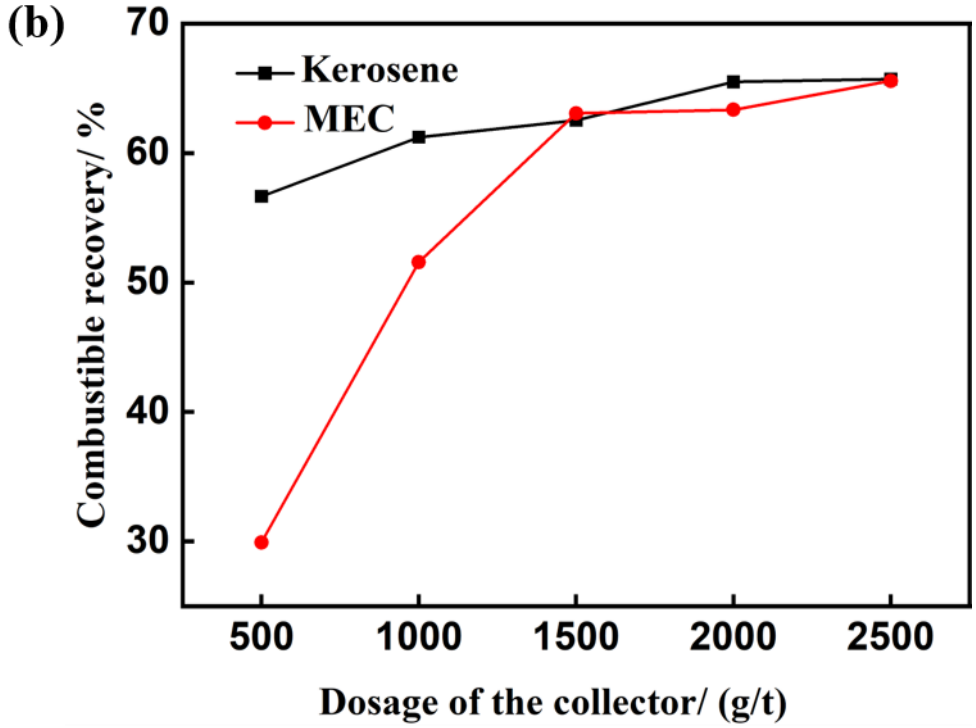
dosage of MEC (HLB = 6) was 1500 g/t, giving a cost of 11400 RMB/(10^3 t) dry coal slime. This is significantly lower compared to the cost of Kerosene with 18000 RMB/(10^3 t) dry coal slime. When the dosage of MEC (HLB = 7) was 1000 g/t, the cost of MEC was 7400 RMB/(10^3 t) dry coal slime, which was approximately half of that of Kerosene with 14220 RMB/(10^3 t) dry coal slime. With a dosage of MEC (HLB = 8) of 1500 g/t, the cost of MEC was estimated at 12150 RMB/(10^3 t) dry coal slime, which was considerably lower than that of kerosene of 18000 RMB/(10^3 t) dry coal slime when C_R was around 60%. The floatation results of MEC with HLB = 9 were found to be inferior to that of Kerosene, because the hydrocarbons could not float up with a low frother content (less than 10%) in MEC. It can be concluded that the co-surfactant (MIBC) plays an important role for the flotation performance of MEC because the MIBC can not only act as the frother but also the co-surfactant combined with surfactant via hydrogen bonding to the oxygen site on the coal surface, and hydrophobic bonding to the hydrophobic sites on the coal surface. As a result of the above, the MEC with HLB = 7 was chosen for further study in this work.

An inspection of the results (Figure 4.4) shows that the ash content, the combustible recovery and the improved flotation index all increase slowly with the increasing dosage of the collectors. When the dosage of collectors is greater than 1000 g/t, the improved flotation index and combustible recovery of MEC surpass that of Kerosene, indicating that the flotation effect with a higher dosage of MEC is better than that of Kerosene. Meanwhile, the ash content of cleaned coal is lower than 16%, and the cost of MEC is 7400 RMB/ (10^3 t) dry coal slime (compared to that of Kerosene with 14220 RMB/ (10^3 t) dry coal slime). Therefore, the best reagent condition obtained in this study is with a dosage of MEC of 1000 g/t, and the values of A, C_R and I_F being 15.91%, 63.72% and 55.27%, respectively, which are 15.59%, 61.22% and 53.1%, higher than that with 1000 g/t

Kerosene. So the MEC is superior to the conventional collector regarding separation efficiency and economic cost.

It is therefore concluded that the surfactant addition to the MEC can significantly reduce the dosage of the oil consumption, which could be interpreted in such a way that the presence of surfactants makes the oil droplets smaller, leading to the reduction in the energy barrier for the particle-droplet system. MEC can also enhance the flotation efficiency due to the polar moiety on the coal surface and the hydrophobic part of MEC forming hydrogen bonds. Another explanation is that the surfactants are linked to the oxygen site on the coal surface via hydrogen bonding, and to the hydrophobic sites on the coal surface through hydrophobic bonding[30].


(a)
Kerosene
MEC
Ash/ %
20
18
16
14
12
10
500
1000
1500
2000
2500
Dosage of the collector/ (g/t)


(b)
Kerosene
MEC
Combustible recovery/ %
70
60
50
40
30
500
1000
1500
2000
2500
Dosage of the collector/ (g/t)

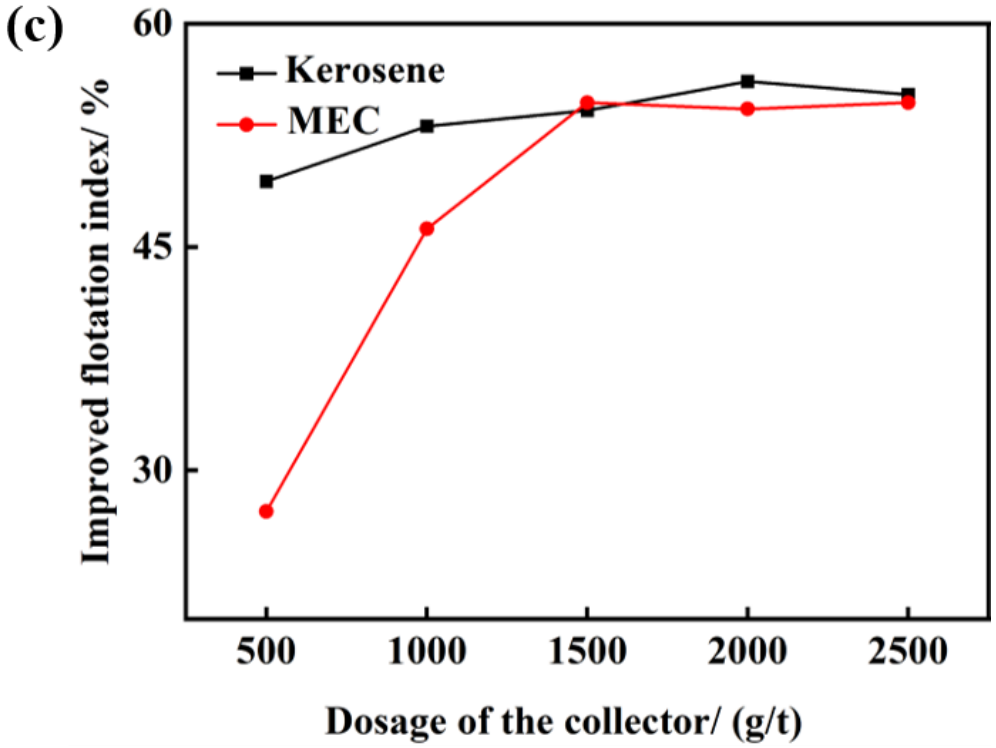
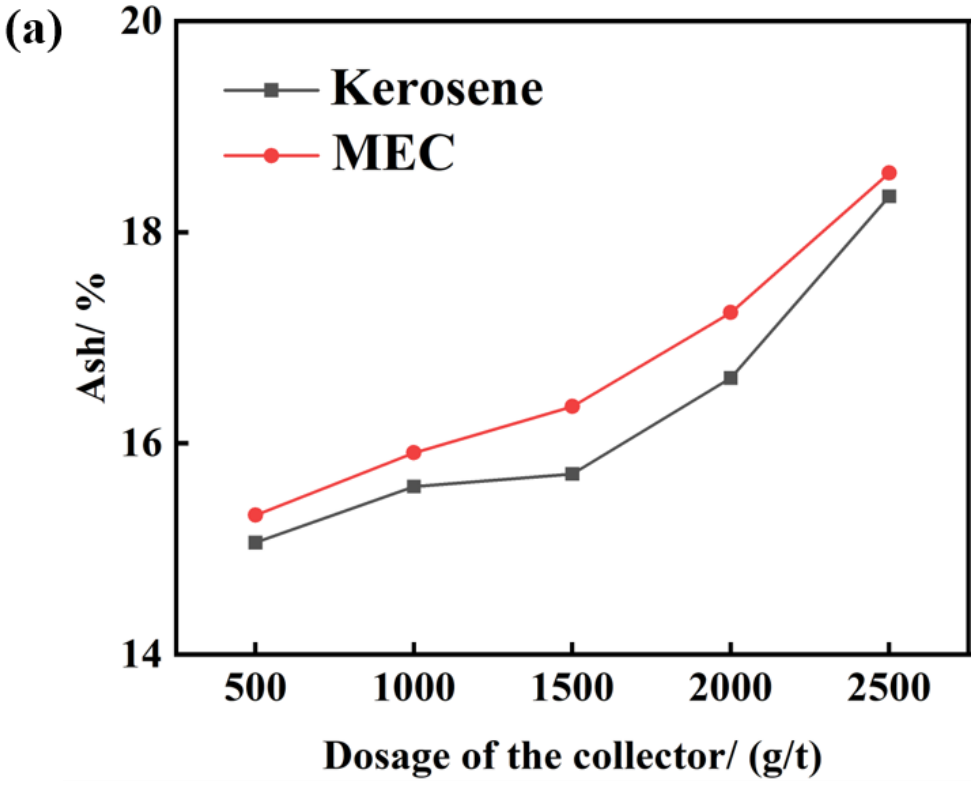
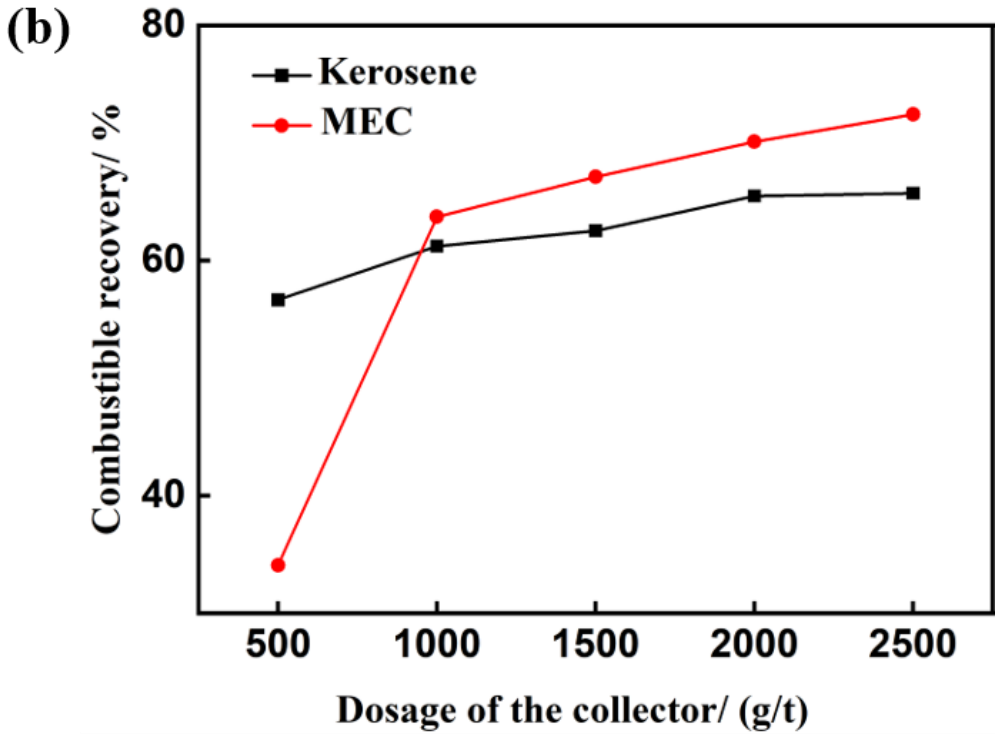


Figure 4.3 (a) Ash content (b) combustible recovery, and (c) improved flotation index of froth concentrate by MEC (HLB = 6) and Kerosene


(a)
Kerosene
MEC
Ash/ %
20
18
16
14
500
1000
1500
2000
2500
Dosage of the collector/ (g/t)


(b)
Kerosene
MEC
Combustible recovery/ %
80
60
40
500
1000
1500
2000
2500
Dosage of the collector/ (g/t)

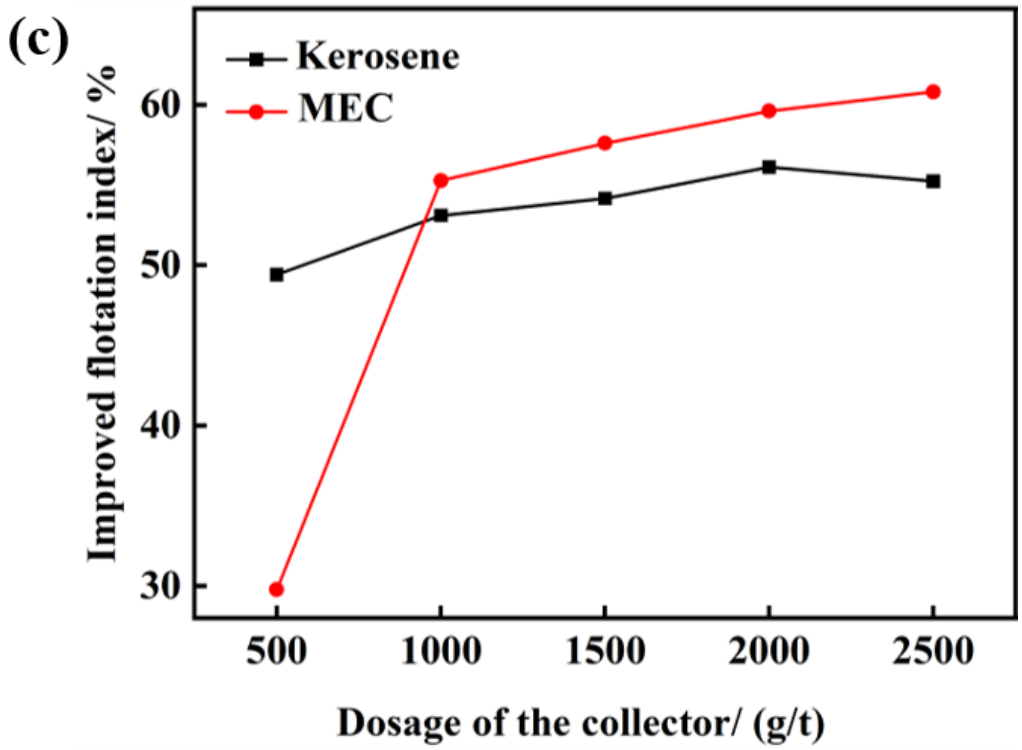
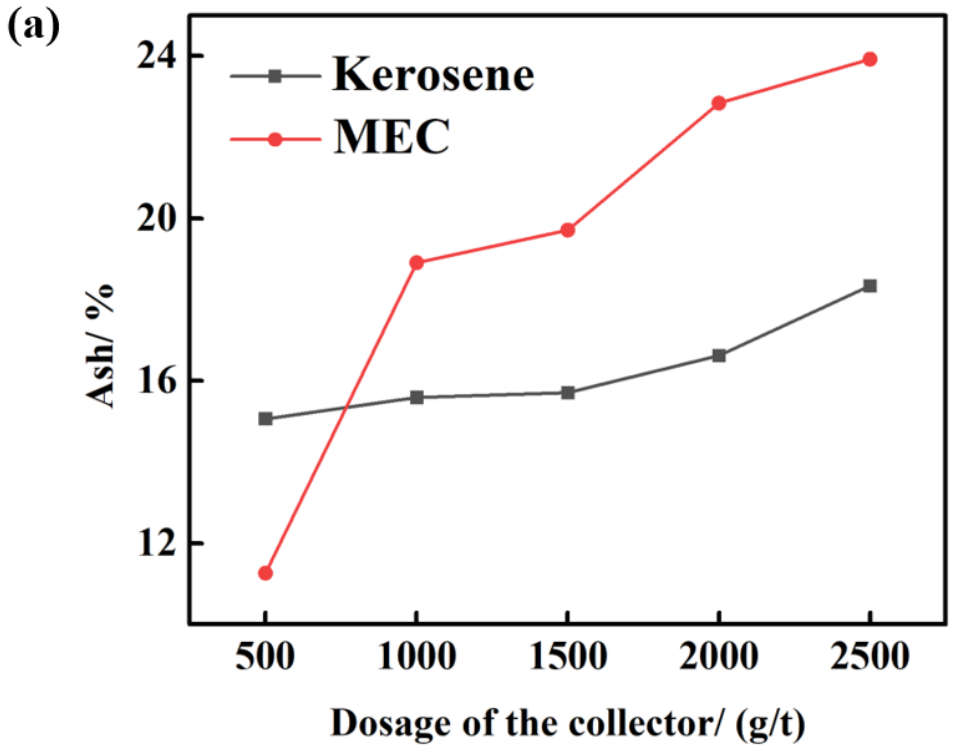
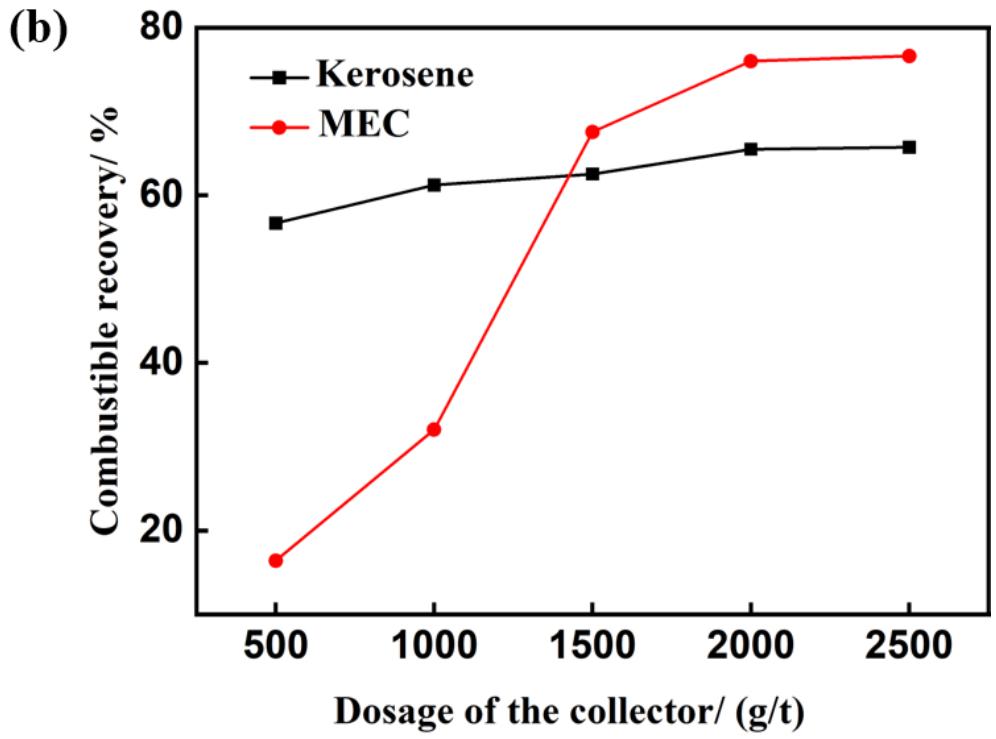


Figure 4.4 (a) Ash content and (b) combustible recovery, and (c) improved flotation index of froth concentrate by MEC (HLB = 7) and Kerosene


(a)
Kerosene
MEC
Ash/ %
24
20
16
12
500
1000
1500
2000
2500
Dosage of the collector/ (g/t)


(b)
Kerosene
MEC
Combustible recovery/ %
80
60
40
20
500
1000
1500
2000
2500
Dosage of the collector/ (g/t)

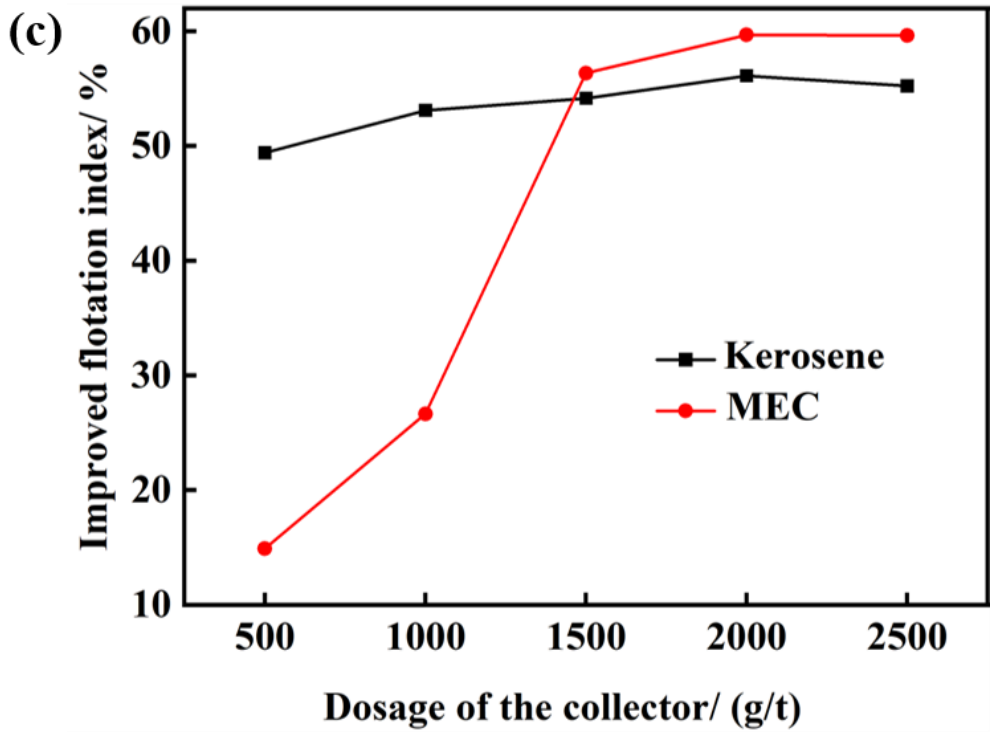
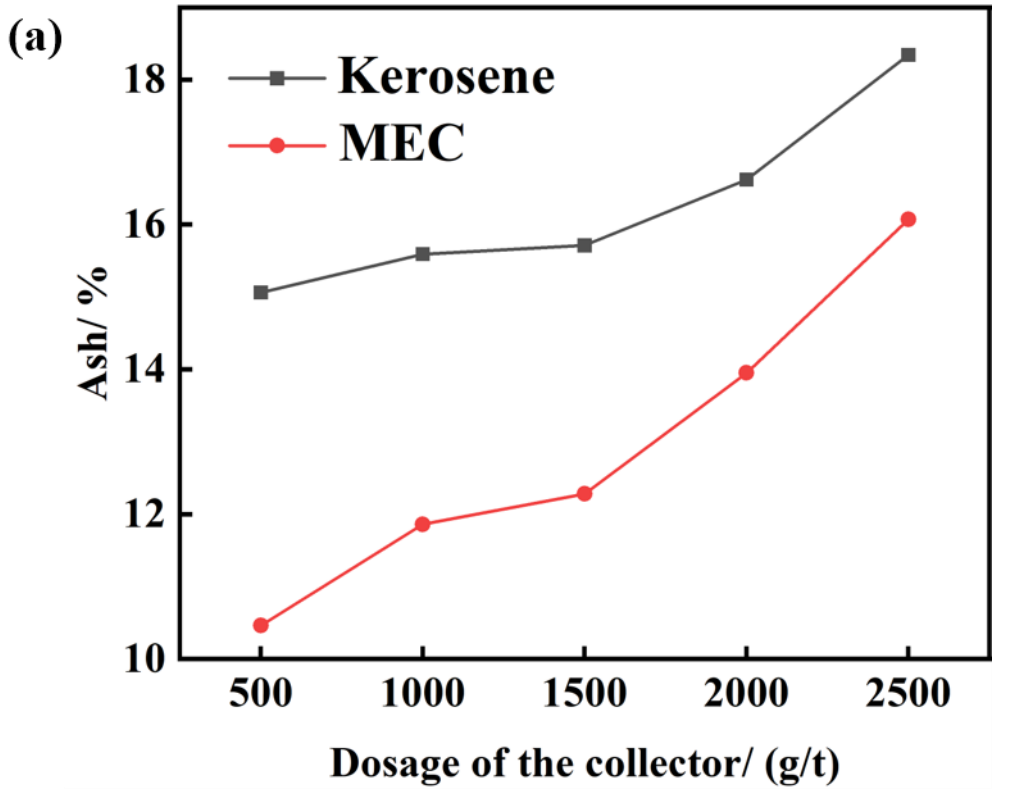
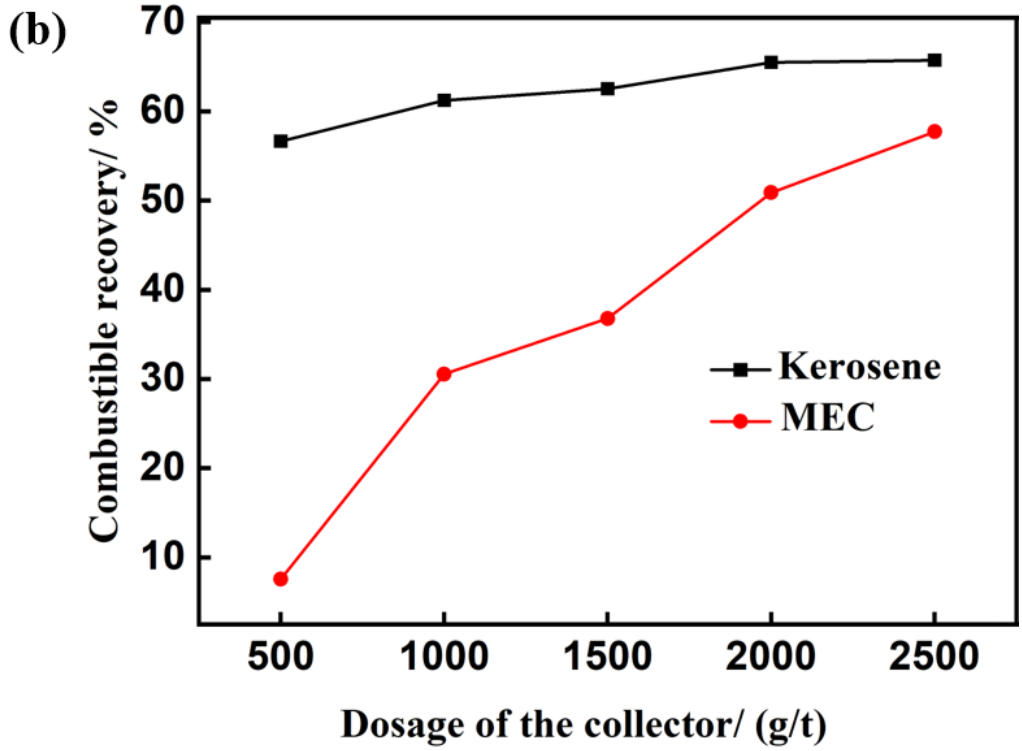


Figure 4.5 (a) Ash content and (b) combustible recovery, and (c) improved flotation index of froth concentrate by MEC (HLB = 8) and Kerosene


(a)
Kerosene
MEC
Ash/ %
18
16
14
12
10
500
1000
1500
2000
2500
Dosage of the collector/ (g/t)


(b)
Combustible recovery/ %
70
60
50
40
30
20
10
Kerosene
MEC
500
1000
1500
2000
2500
Dosage of the collector/ (g/t)

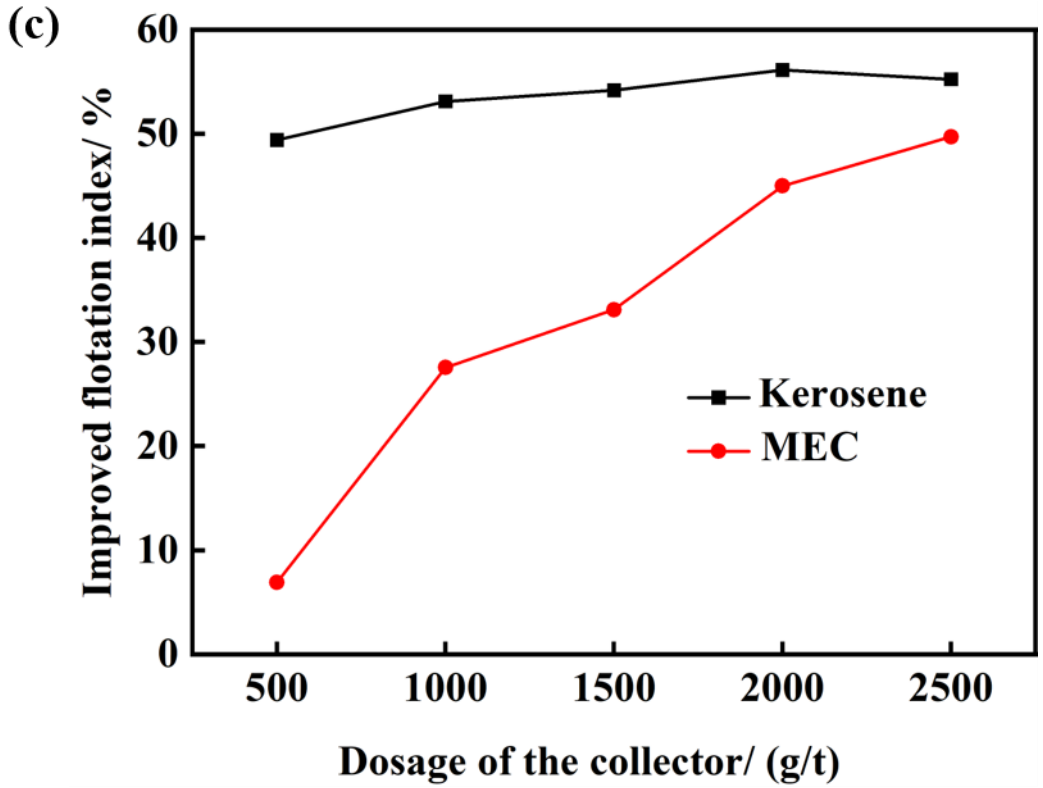


Figure 4.6 (a) Ash content (b) combustible recovery, and (c) improved flotation index of froth concentrate by MEC (HLB = 9) and Kerosene

4.1.3 Flotation kinetic studies

Flotation kinetics could combine the recovery and the rate using the mathematical models, since the flotation process is theoretically considered as a time-rate recovery process.

There have been many flotation kinetic studies using either or both of the classical first-order kinetics model and other models [131-135].

Mehran et al.[79] studied the effects of organic depressants including guar gum, starch, dextrin, carboxymethyl cellulose (CMC) on the pyrite depression with a modified Halimond tube. Seven experiments were carried out under the following conditions: aeration and collecting time were 10,

20, 30, 60, 180, 300 and 720 s; the collector was KAX (potassium amyl xanthate) + KIPX (potassium isopropyl xanthate) and the conditioning time was 4 min; frother of pine oil was added and the conditioning time was 30 s. Their recovery results were fitted to the following models：the classical first-order model (4-3), the first-order model with a rectangular distribution of flotabilities (4-4), the fully mixed reactor model (4-5), and the second-order model with a rectangular distribution of flotabilities (4-8):

- The first-order model

$$\mathrm{Y} = Y_{\infty}[1 - \exp(-k_1 t)] \tag{4-3}$$

- The first-order model with rectangular distribution of flotabilities

$$Y = Y_{\infty}\{1 - \frac{1}{k_2 t}[1 - exp\ (-k_2 t)]\} \tag{4-4}$$

- Fully mixed reactor model

$$Y = Y_{\infty}(1 - \frac{1}{1 + t/k_3}) \tag{4-5}$$

- Improved gas/solid adsorption model

$$\mathrm{Y} = Y_{\infty}(\frac{k_4 t}{1 + k_4 t}) \tag{4-6}$$

- Second-order kinetic model

$$\mathrm{Y} = \frac{Y_{\infty}^2 k_5 t}{1 + Y_{\infty} k_5 t} \tag{4-7}$$

- Second-order model with rectangular distribution of flotabilities

$$Y = Y_{\infty}\{1 - \frac{1}{k_6 t}[ln\ (1 + k_6 t)]\} \quad (4\text{-}8)$$

where, Y is the recovery when time is t; Y_{∞} is the ultimate recovery; and k_1, k_2, k_3, k_4, k_5, k_6 denote the flotation rate constant.

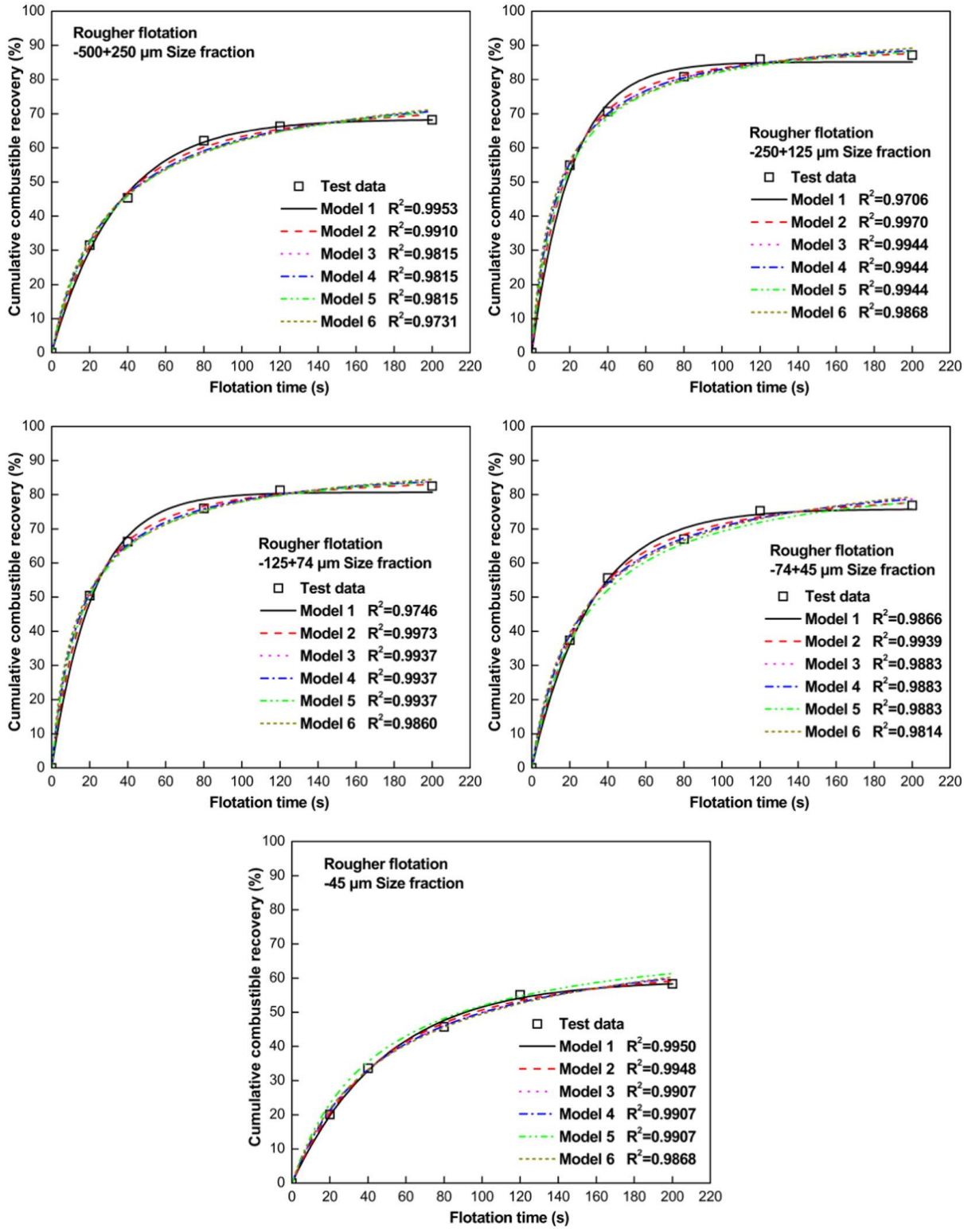


Figure 4.7 Comparison of six kinetic models fitted to the experimental data of various size fractions[137]

Feng et al.[136] observed that the flotation kinetics increased with ultrasonication, which was explained to have an activating effect on the coal flotation. Ni et al.[137] employed six kinetic models for fitting their experimental data shown in Figure 4.7, and found that all R^2 values were all greater than 0.97, indicating that six kinetic models all fitted to the data. Such fitting to multi-models also indicates difficulties in mechanistic understanding of the rate-limiting steps.

Xia et al. [138][159] evaluated the flotation rates of the novel collectors and diesel in the froth flotation using the following equations:

$$\varepsilon_c = \frac{M_c(100 - A_c)}{M_f(100 - A_f)} \times 100\% \quad (4\text{-}9)$$

$$\varepsilon_a = \frac{100 M_c A_c}{M_f A_f} \times 100\% \quad (4\text{-}10)$$

where ε_a and ε_c are the ash recovery and combustible recovery, respectively; M_f and M_c denote the masses of the feeding and the froth product, respectively; and A_c and A_f denote the ash contents of the froth product and the feeding material, respectively. Since the combustible recovery and ash are positively correlated to the residue in the slurry[139][140], a second-order kinetic model is used to describe the flotation rate in this study:

$$\varepsilon_c = \frac{\varepsilon_{c\infty}^2 k_1 t}{1 + \varepsilon_{c\infty} k_1 t} \quad (4\text{-}11)$$

$$\varepsilon_a = \frac{\varepsilon_{a\infty}^2 k_2 t}{1 + \varepsilon_{a\infty} k_2 t} \quad (4\text{-}12)$$

where $\varepsilon_{c\infty}$ (%) is the maximum combustible recovery, assumed to be 100% in this study, and k_1 (min^{-1}) denotes the flotation rate constant of the combustible recovery; $\varepsilon_{a\infty}$ is the maximum recovery, assumed to be 100%; and k_2 (min^{-1}) represents the flotation rate constant of the ash

content; and *t* (min) is the collecting time. The *k* values are generally used to evaluate the flotation rate[137].

In order to further study the difference between the recoveries of cleaned coal and ash, the are used in this study to approximate, analyze and interpret the coal flotation results[141-143], which are based on Eqs. (4-11) and (4-12), and has the following forms:

$$\varepsilon_c = \frac{\varepsilon_{c\infty}^2 k \varepsilon_a}{\varepsilon_{a\infty}(\varepsilon_{a\infty} - \varepsilon_a) + \varepsilon_{c\infty} k \varepsilon_a} \tag{4-13}$$

The $\varepsilon_{c\infty}$ and $\varepsilon_{a\infty}$ in Eq. (4-13) are assumed to be 100%, and if k_1/k_2 is defined as *k*, then Eq. (4-13) can be given by:

$$\varepsilon_c = \frac{100 \times k \times \varepsilon_a}{100 + k\varepsilon_a - \varepsilon_a} \tag{4-14}$$

Eq. (4-14) indicates that a greater *k* value gives a more superior flotation selectivity.

Figure 4.8 shows the effect of collectors on the cumulative combustible recovery in the froth flotation of this study. A correlation coefficient, R^2, of over 0.9890, is seen, suggesting that the second-order kinetic model represents the experimental data. Figure 4.8 also shows that a high rate of recovery and the maximum recovery are obtained with the MEC in the froth flotation. The experimental results also fit well with the Fuerstenau upgrading curve ($R^2 > 0.98$) in Figure 4.9, indicating that data are represented well by the second-order kinetic model[27]. The *k* value of MEC (k_{MEC} = 12.16) is larger than that of *K* (k_k = 11.36), indicating that MEC has a better flotation selectivity. The value of the *k* also indicates that the MEC is more easily absorbed onto the surface of the cleaned coal than on the surface of ash. The flotation results shown in Figure 4.4 indicates a stronger collectivity of MEC but a relatively low selectivity compared with Kerosene. This is

due to the higher ash with MEC, and can be explained that MEC has a greater effect on fine particles than that on the coarse ones. This leads to improved hydrophobicity of MEC on fine coal particles, which is beneficial for excessive aggregation of hydrophobic flocs, largely increasing the selectivity loss because of entrainment[144].

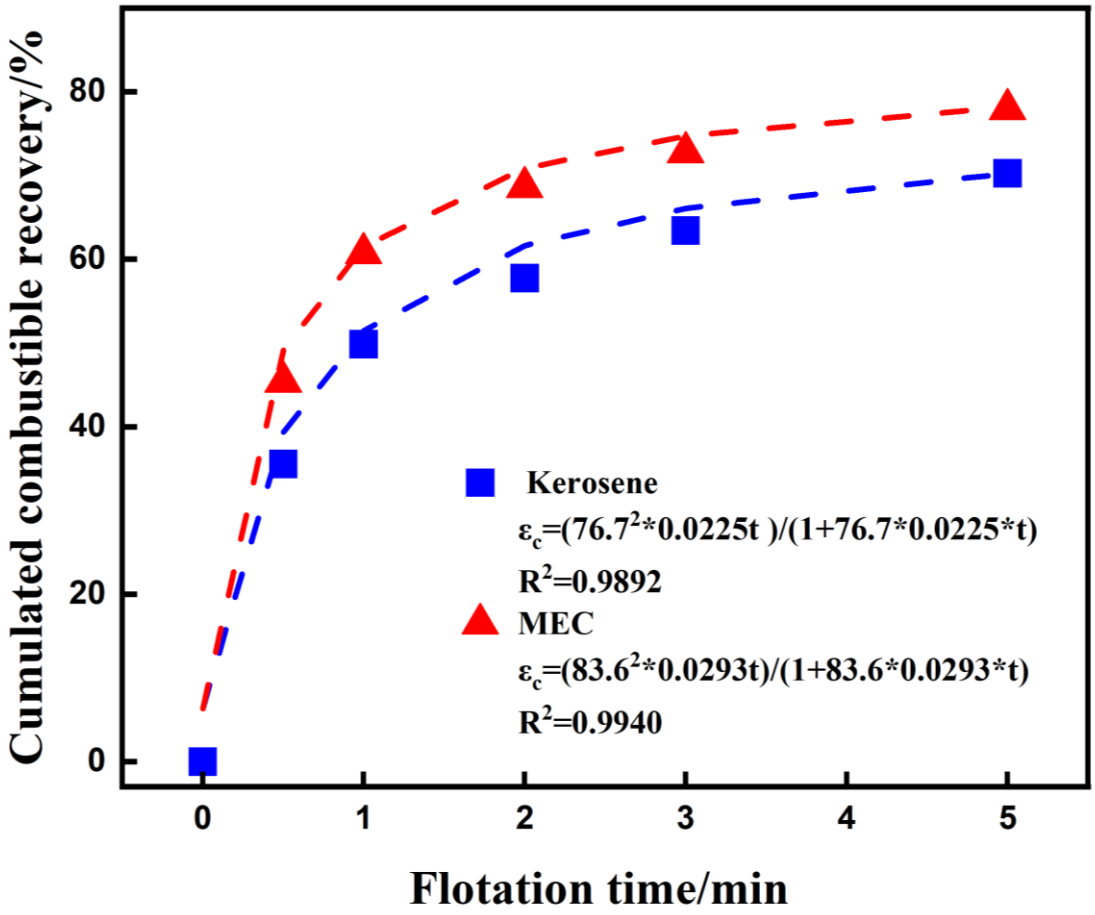


Figure 4.8 Effect of collectors on the cumulative combustible recovery during the flotation process (The experimental conditions were below: the pulp concentration was 100 g/L, the agitation speed was 2000 r/min, the aeration rate was 0.3m^3/m^2/min, and the dosage of Kerosene or MEC were both 2000 g/t)

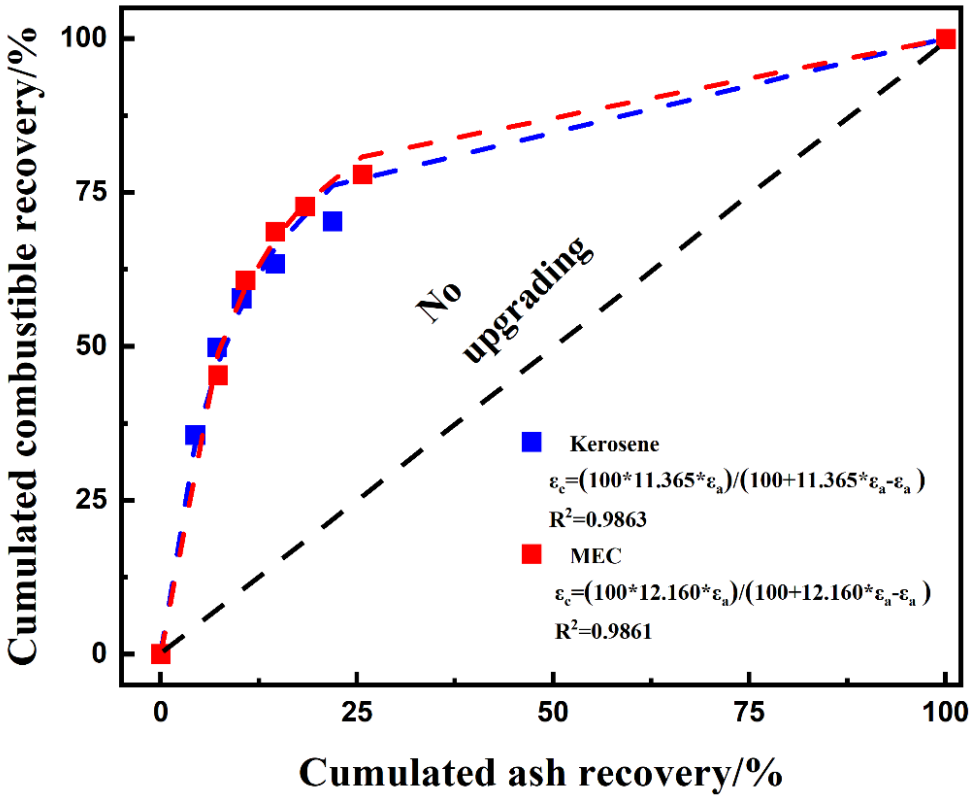


Figure 4.9 The Fuerstenau upgrading curves of collectors for coal sample

4.2 Particle size distribution

Dynamic light scattering measurements were utilized for measuring the particle size of the prepared microemulsions and the results are shown in Figure 4.10. One can see a narrow size distribution of the MEC with the peak particle size at 92.5 nm, in accordance with the definition of the microemulsion (0-100 nm). The polydispersity coefficient (PDI) represents the degree of uniform dispersion of a microemulsion. The smaller the dispersion coefficient, the more concentrated the particle size distribution. The polydispersity coefficient of the microemulsion is estimated at 0.373, indicating that the dispersion of MEC prepared is of excellent quality.

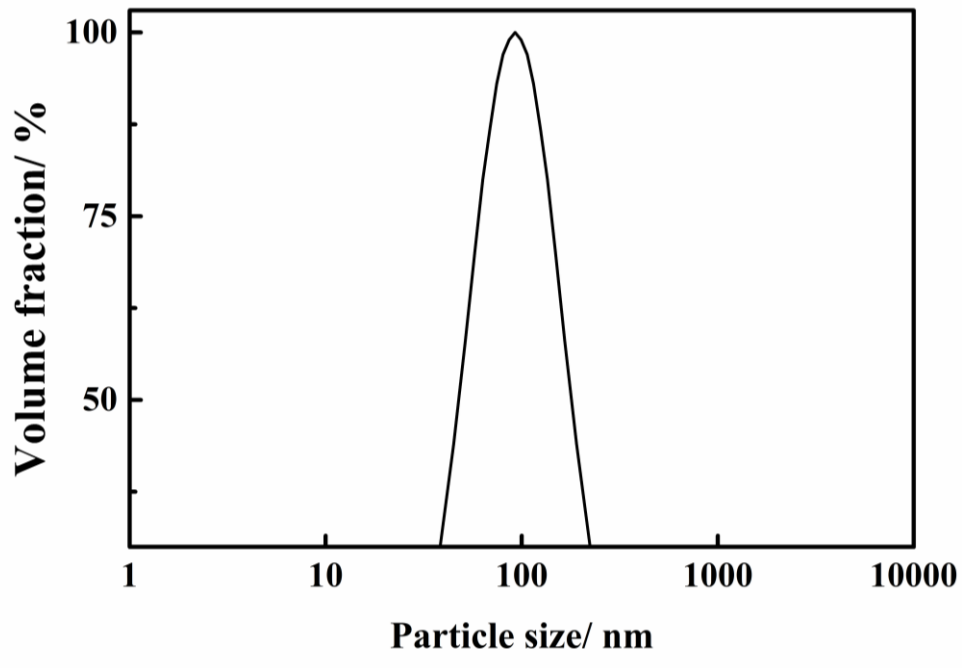
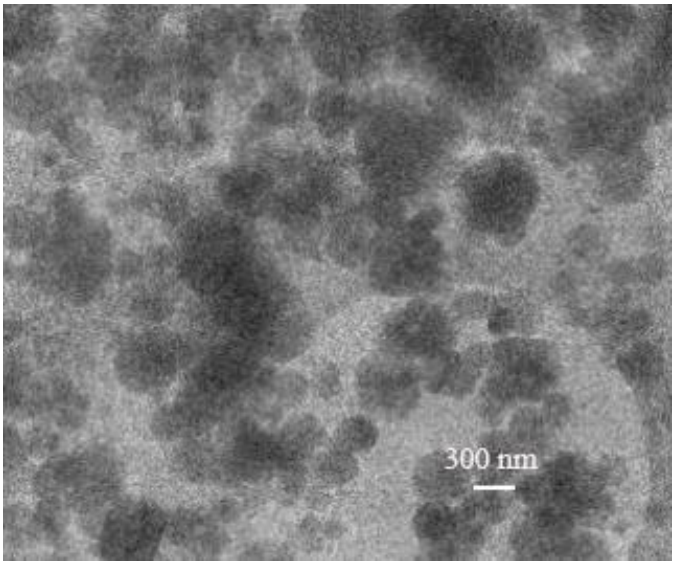


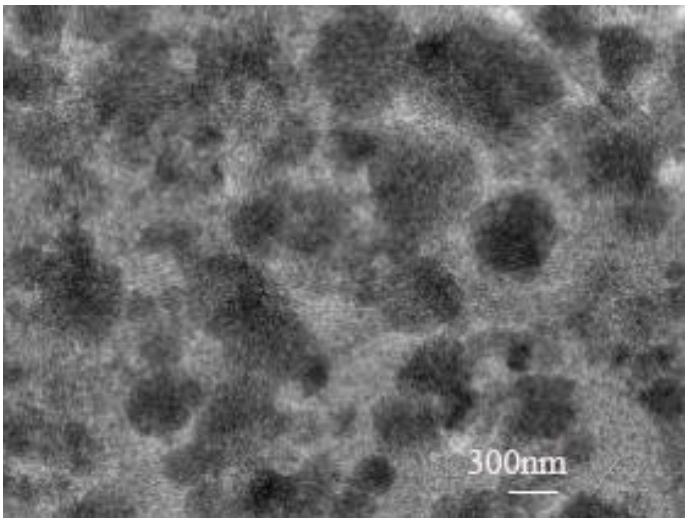
Figure 4.10 Size distribution of Kerosene/(Span80+Tween80)/MIBC/water microemulsion system

4.3 Cryo-TEM

The morphology of MEC was characterized by a cryo-TEM analysis. Figure 4.11 shows the results. The micrograph shows that a small number of droplets have a spherical structure with radii larger than 100 nm. The results from the TEM analyses are in broad agreement with the DLS analyses. The Cryo-TEM analyses of the MEC also show that the droplets remain spherical and stable at the room temperature for over 180 days.



(a) MEC solution



(b) After 180 days

Figure 4.11 Cryo-TEM image for (a) MEC solution and (b) MEC solution after 180 days

4.4 Electrical conductivity

4.4.1 Influence of mass ratio of surfactants on the microemulsion conductivity

The influence of the concentration of surfactants on the conductivity is presented in Figure 4.12. One can see a slow increase of the conductivity of the microemulsion with the increasing concentration of the mixed surfactant, to ~20 g of the dosage, when the conductivity jumps sharply to 4.07 $\mu S \cdot cm^{-1}$, which was one order of magnitude higher than that of the value at the beginning.

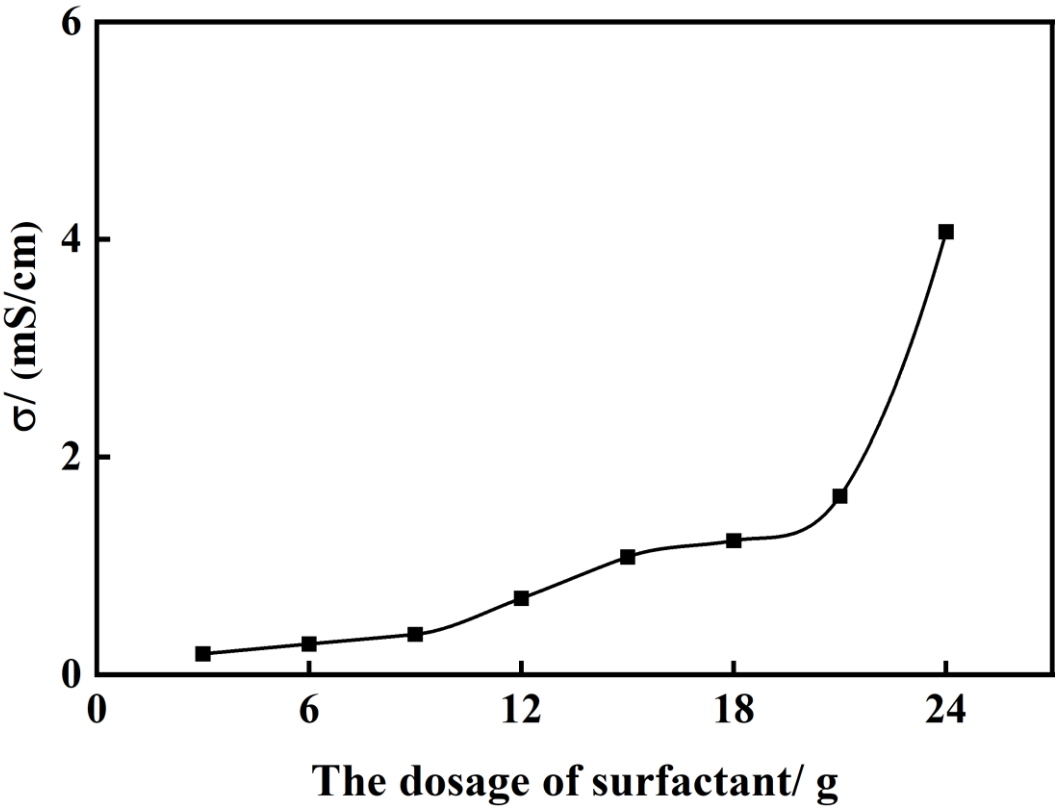


Figure 4.12 Relationship between the mass ratio of surfactant and the conductivity of the microemulsion

For non-ionic microemulsion, water molecules interact with hydrophilic moiety of the surfactant by hydrogen bonding, thus infiltrating into the interfacial film of oil-water. These water molecules are regarded as the bridge to the interfacial film for H^+ in microemulsion. H^+ in interfacial film has

a trend to move toward the outside of the interfacial film under an electric field, which plays a conductivity role to a certain extent. The greater the content of surfactant, the more water molecules binding to it, the greater penetration of H^+ moving out of the interfacial film, and higher the electrical conductivity. And the results confirm the Winsor II (W/O) structure of MEC.

4.4.2 Influence of the mass ratio of cosurfactant (methyl isobutyl carbinol) on the conductivity of the microemulsion

The effect of the concentration of cosurfactant (MIBC methyl isobutyl carbinol) on the microemulsion conductivity is illustrated in Figure 4.13. One can see a clear decrease in the conductivity of the microemulsion with the increase of the cosurfactant concentration.

The roles of cosurfactants include the following aspects: (1) Reducing the viscosity of the system; (2) Reducing interfacial tension; (3) Increasing the fluidity of the interface; (4) Increasing the fluidity of the hydrocarbon tail, thus allowing more oil to penetrate into this area; and (5) Affecting the solubility characteristics of the water and oil phases due to insoluble of two phases.

The electrical conductivity of the microemulsion decreases sharply with increasing concentration of the MIBC first. It is then seen to decrease slowly when MIBC is above 3.5 g. The effect of MIBC on the conductivity is mainly achieved by changing the strength of the interfacial film. In the microemulsion, the cosurfactant MIBC is beneficial to the formation of an interfacial film, and the orientation is similar to that of the surfactant molecules, namely, hydrophilic part is combined with H_2O molecules, and the alkyl groups are adsorbed by oil molecules.

For non-ionic systems, the hydroxyl group of MIBC can form hydrogen bonds with EO (Ethylene oxide) chain, and weaken the hydrophilicity of surfactant molecule, which hinders the interactions between the surfactant and the water molecules, and leads to the reduction of the amount of H^+

penetrating into the interfacial film. Therefore, the conductivity of the microemulsion system shows a clear decrease with the increasing concentration of MIBC.

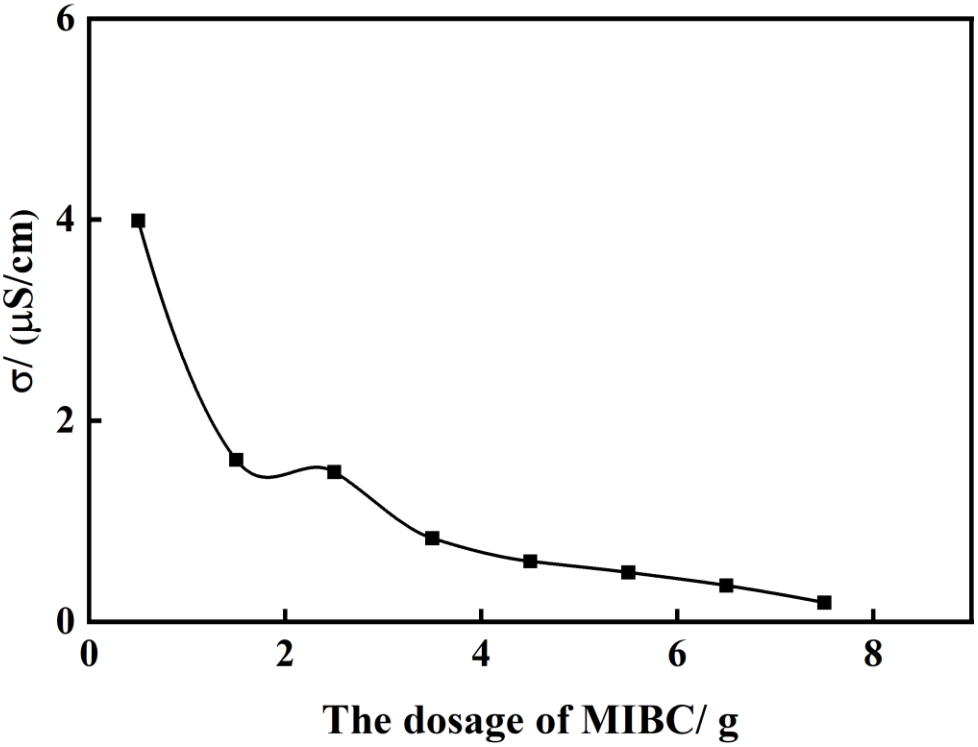


Figure 4.13 Relationship between the concentration of cosurfactant and the conductivity of the microemulsion

4.4.3 Influence of H_2O concentration on the conductivity of the microemulsion

The effect of H^+ concentration in the water phase on the microemulsion conductivity was studied and the results are shown in Figure 4.14. These results demonstrate that the increase of H^+ concentration in the aqueous phase significantly improves the conductivity of the microemulsion. When the ratio of water to oil is 0.53, the conductivity of the microemulsion reaches a high level of 6.6 μS/cm.

In a W/O microemulsion, the electrical conductivity is often determined by the dispersed droplets since the continuous phase (oil) is non-conductive. The concentration of the dispersed droplets

increases with increased addition of water, which often also increases the diameter of the dispersed phase. The increased size of the dispersed droplets reduces the density of surfactant molecules in the interface film, making the interfacial film less consolidated. It is therefore much easier for electrolytic ions to penetrate through the interface film, which is beneficial for the increase of the conductivity.

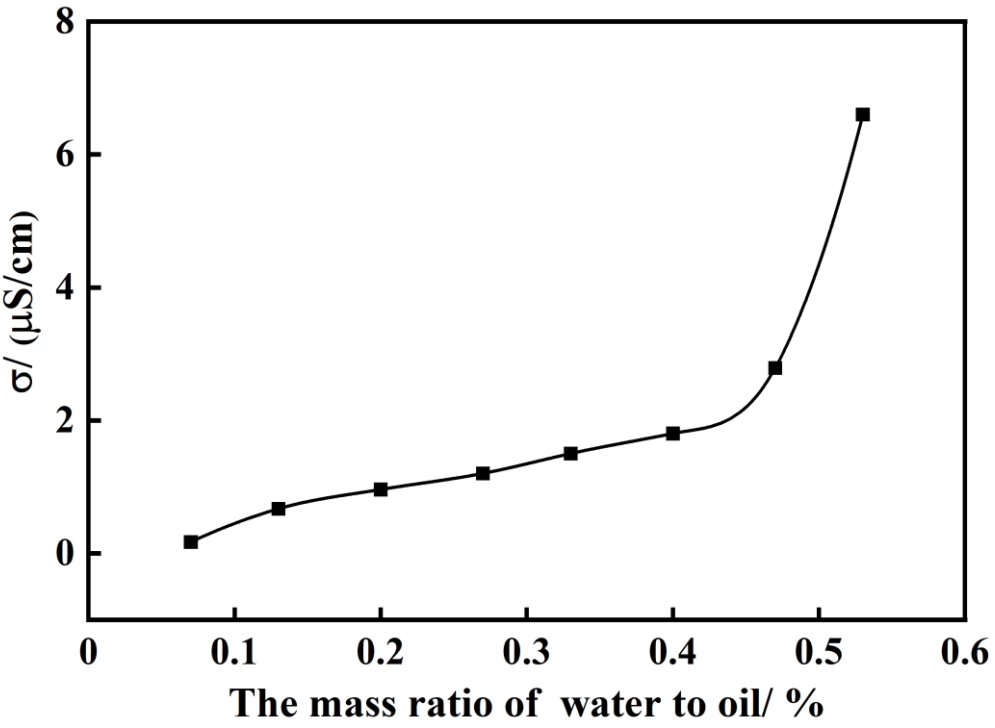


Figure 4.14 Relationship between the ratio of water to oil and the conductivity of the microemulsion

Since the ratio of surfactants and water could increase the conductivity of MEC, the results further confirm the Winsor II (W/O) structure of MEC.

4.5 Rheological measurements

The rheological analyses of the microemulsions provide the viscosity (η) information in the form of shear stress (τ) as a function of shear rate (γ). Figure 4.15 shows the results. One can see that the viscosity is the same as that of water, which indicates that microemulsion does not increase the

viscosity. Figure 4.15 also indicates the Newtonian behavior of MEC, which is of great significance for controlling mobility and increasing the separation efficiency.

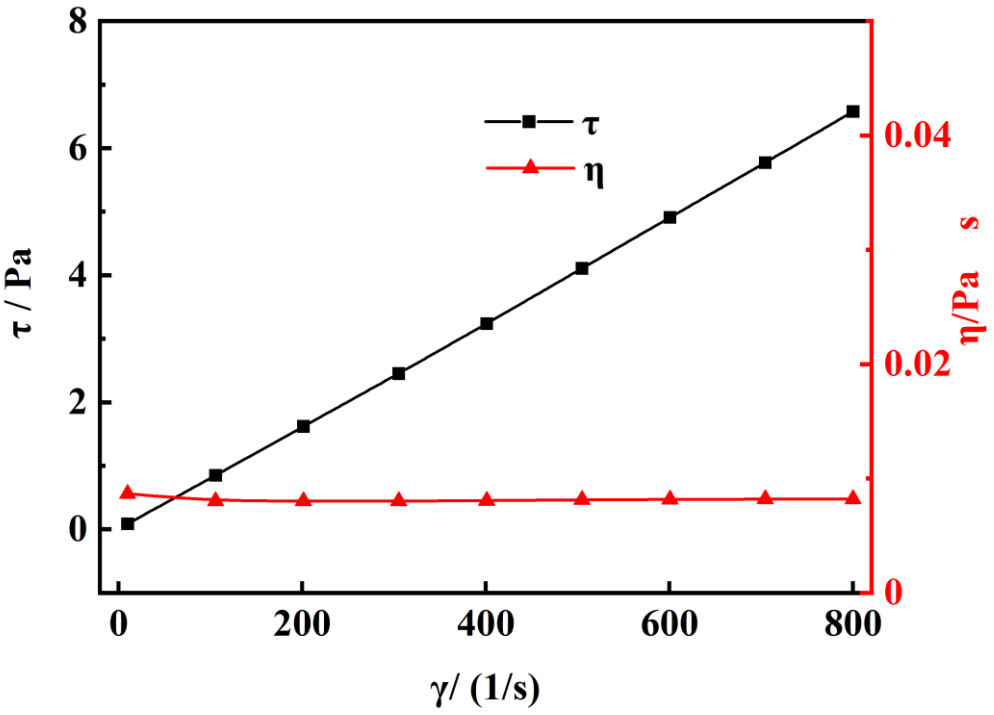


Figure 4.15 Steady shear viscosity as a function of the shear rate for MEC at 25°C

4.6 The EDLVO analyses of the emulsion system

It is well known that the Extended Derjaguin-Landau-Verwey-Overbeek (EDLVO) theory can be used to quantitatively predict the total interaction energy (V_T) between particles in an aqueous solution[145-149]. The V_T can be calculated with the following Eq. (4-15):

$$V_T = V_W + V_E + V_H \tag{4-15}$$

where V_w is the Van der Waals interaction energy, V_E is the electrostatic interaction energy, and V_H is the hydrophobic interaction energy.

The Van der Waals interaction is calculated with Eq. (4-16) [150][151]:

$$V_W = -\frac{A_{132} \times R}{12H} \tag{4-16}$$

where H is the distance between spherical particles and R is the radius of spherical particles. The average particle size of the coal slime is 8 μm; thus R = 4 μm. A_{132} is the Hamaker constant for particles in water, given by[152]:

$$A_{132} = \left(\sqrt{A_{11}} - \sqrt{A_{33}}\right)\left(\sqrt{A_{22}} - \sqrt{A_{33}}\right) \tag{4-17}$$

where A_{11}, A_{22} and A_{33} refer to the Hamaker constants of the coal particles, the collector, and the water in the vacuum, given respectively by $A_{11} = 6.16 \times 10^{-20}$, $A_{33} = 3.8 \times 10^{-20}$ J [153][154].

Since the components of MEC and K were similar, the Hamaker constants of both are assumed to be the same ($A_{22} = 4.0 \times 10^{-20}$ J), and therefore V_w is the same.

Considering two spherical particles approaching to each other in water, the electrical double-layer interaction can be quantified by[155][156]:

$$V_E = \frac{1}{2}\varepsilon_a R\varphi_0^2 ln\left[1 + exp\left(-\kappa H\right)\right] \tag{4-18}$$

where ε_a is the vacuum permittivity (8.854×10^{-12} C^2 $J^{-1}m^{-1}$); H is the distance of the two particles. φ_0 is particle surface electronic potential usually substituted by the ζ-potential; and κ is the reciprocal Debye length, and is calculated by[157]:

$$\kappa^{-1} = \frac{0.304}{\sqrt{C_{KCl}}} \tag{4-19}$$

where C_{KCl} is the concentration of KCl solution (1×10^{-2} mol/L), giving κ^{-1} of 3.04 nm.

The hydrophobic interaction energy (V_H) could be calculated as Eq.(4-20)[158]:

$$V_H = -2.51 \times 10^{-3} R k_1 h_0 exp\ (-\frac{H}{h_0}) \quad (4\text{-}20)$$

where k_1 is incomplete hydrophobic coefficient given by $k_1 = \frac{\exp\left(\frac{\theta}{100}-1\right)}{e-1}$ ($0 < k_1 < 1$); θ is the contact angle of coal in water; h_0 is the decay length with a unit of nm given by h_0 = (12.2 ± 1.0) k_1.

4.6.1 Zeta potential analysis of collectors with coal sample

Figure 4.16 shows the zeta potential of MEC and Kerosene at different concentrations. It is observed that the potential of MEC increases with an increased dosage of MEC. The negative value of raw coal without the use of collectors is -24.88 mV, which decreases to -19.01 mV, -17.47 mV, -16.84 mV and -15.42 mV, respectively for MEC values of 500 g/t, 1000 g/t, 1500 g/t and 2000 g/t. For Kerosene, the corresponding zeta potential are -21.03 mV, -18.66 mV, -17.89 mV and -16.15 mV, respectively. Therefore, the 2000 g/t MEC show the most favorable conglomeration ability, indicating that the MEC increases the coalescing ability of coal samples due to the reduced repulsive interactions among particles.

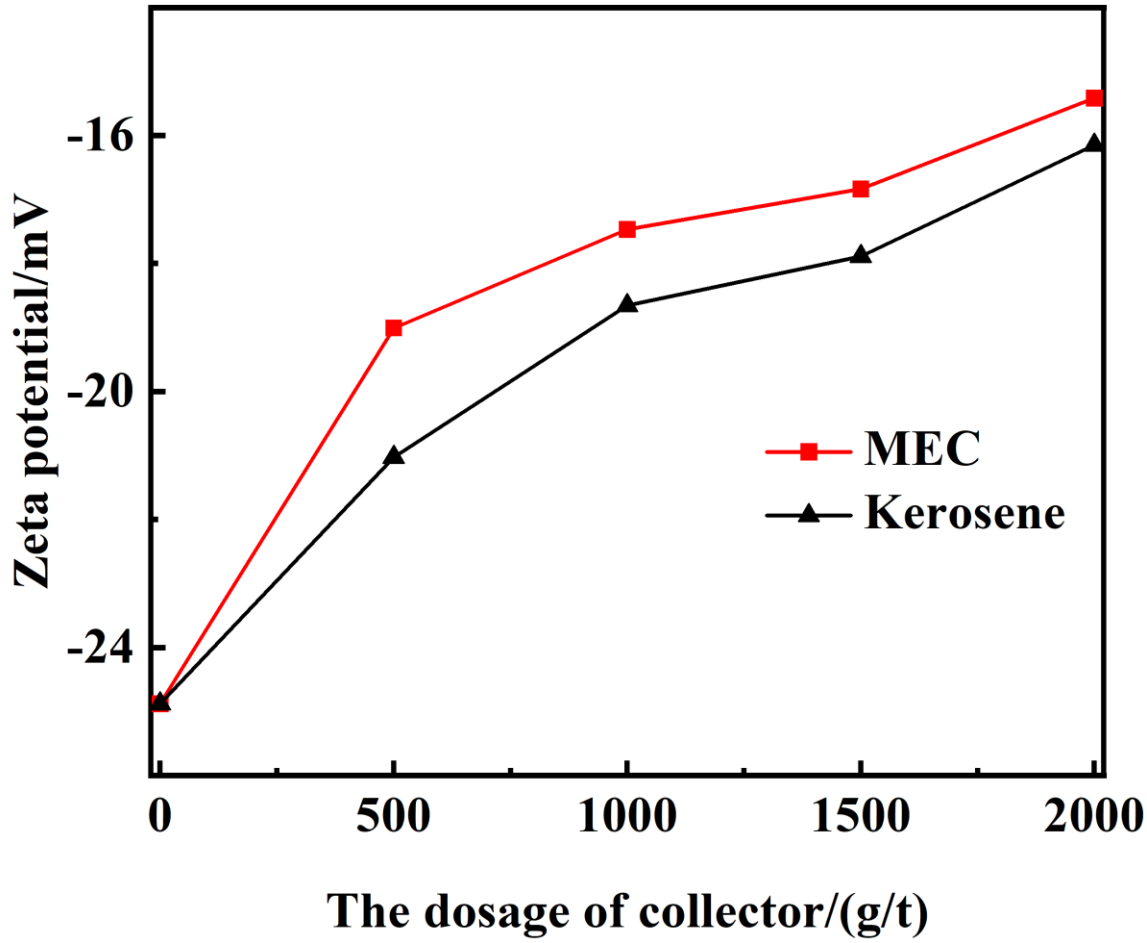


Figure 4.16 Zeta potential of particles treated with Kerosene and MEC

4.6.2 Contact angle analysis of collectors with coal sample

Figure 4.17 shows the contact angle of the coal sample in interaction with reagents, which is greater than that of the reagent-free sample. The use of Kerosene or MEC can increase the contact angle and improve the hydrophobicity of the sample. When the dosage of the collectors increases, the contact angle grows up and the particles become more hydrophobic. Therefore, the hydrophobicity of the particle and the cleaned coal yield would increase with the use of Kerosene and MEC. The best flotation effect is obtained when the collector addition is 2000 g/t due to the highest contact angle under the condition of this study.

The contact angle tests demonstrate that the contact angle of MEC is larger than that of Kerosene, indicating that MEC could interact more easily with hydrophilic groups of the sample via hydrogen bonding and the outwards hydrophobic groups of MEC could further improve the hydrophobicity of the sample. Additionally, smaller oil droplets can spread more quickly on the sample surface, and hence improve the flotation recovery and rate.

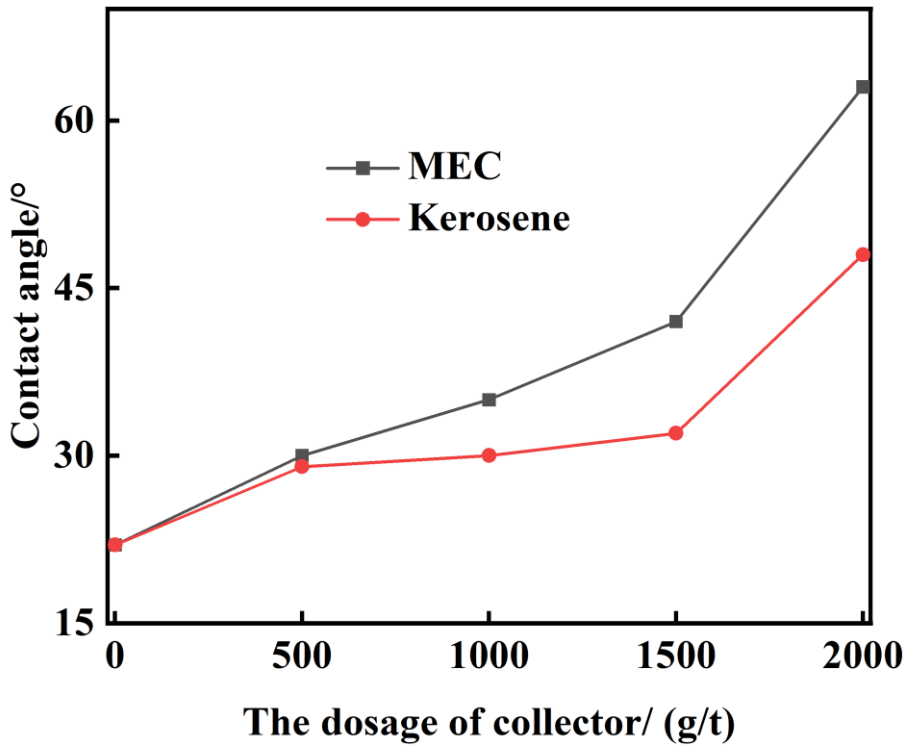


Figure 4.17 The contact angle of Kerosene and MEC with the changes of the dosage of collectors

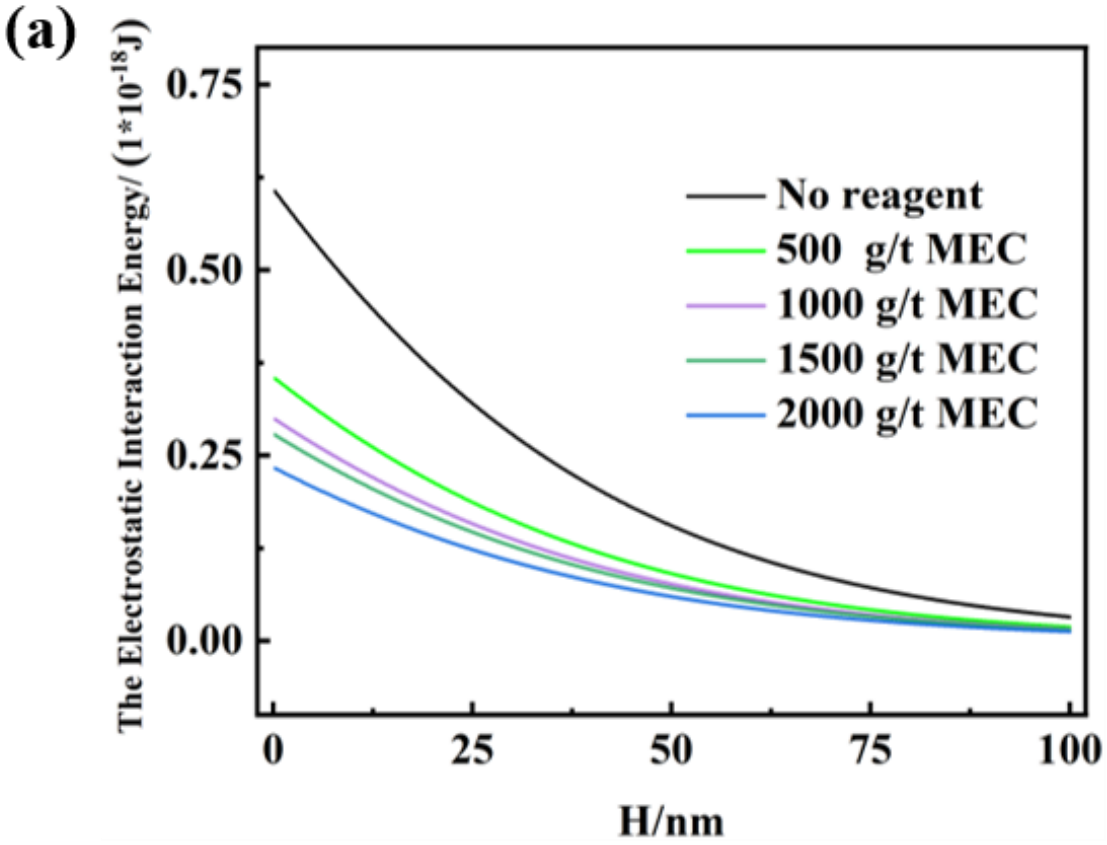
4.6.3 EDLVO analyses

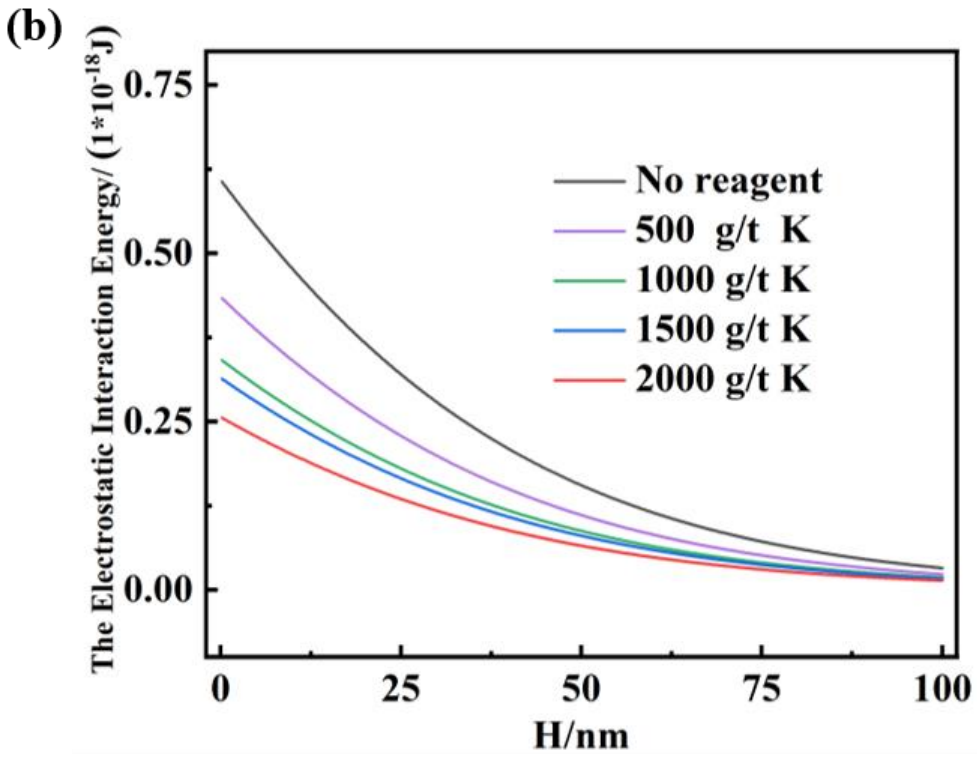
Figure 4.18 (a) and (b) show the electrostatic interaction energies (V_E) at various dosages of MEC or Kerosene. They are all positive, indicating repulsive forces dominating between the electronic double layers of particles surfaces. There are confirmed by Zeta potential measurements as shown in Figure 4.16, where the negative values of ζ potential manifests that the surfaces of coal particles

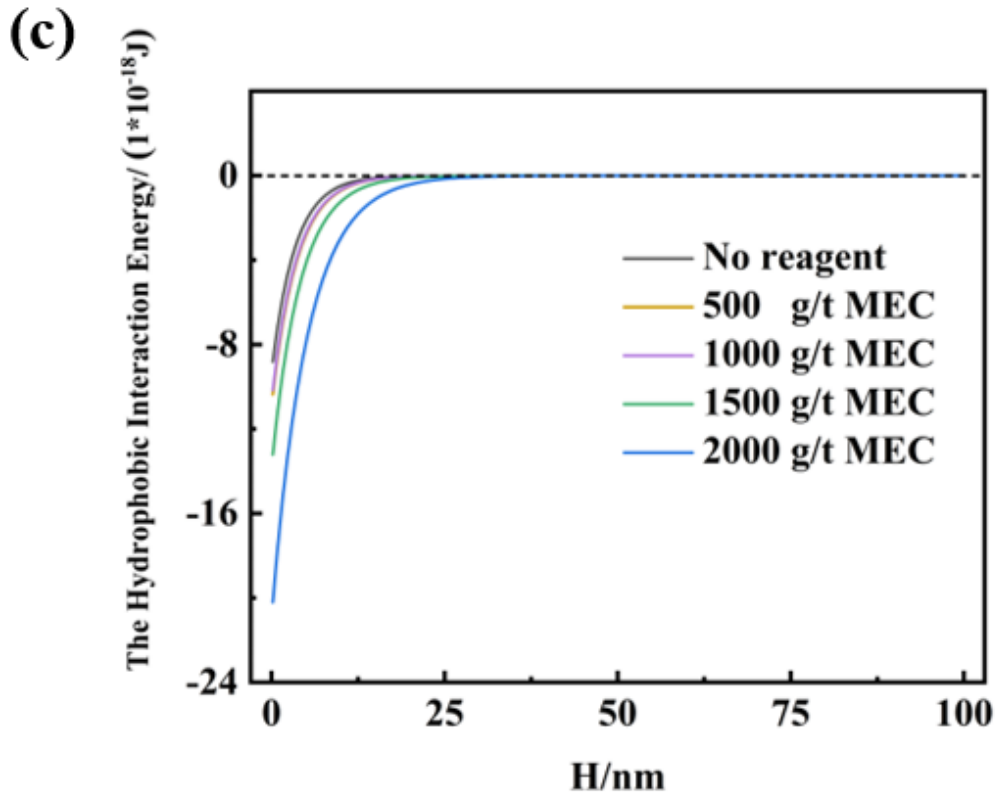
are actually negatively charged, leading to positive electronic interaction energies. The positive V_E has a negative effect on the flotation of coal slime. With increasing collector dosage, the V_E decreases, showing that the surface modifications by MEC or Kerosene could reduce the repulsive forces between particles and weaken the adverse effect of the positive V_E on flotation.

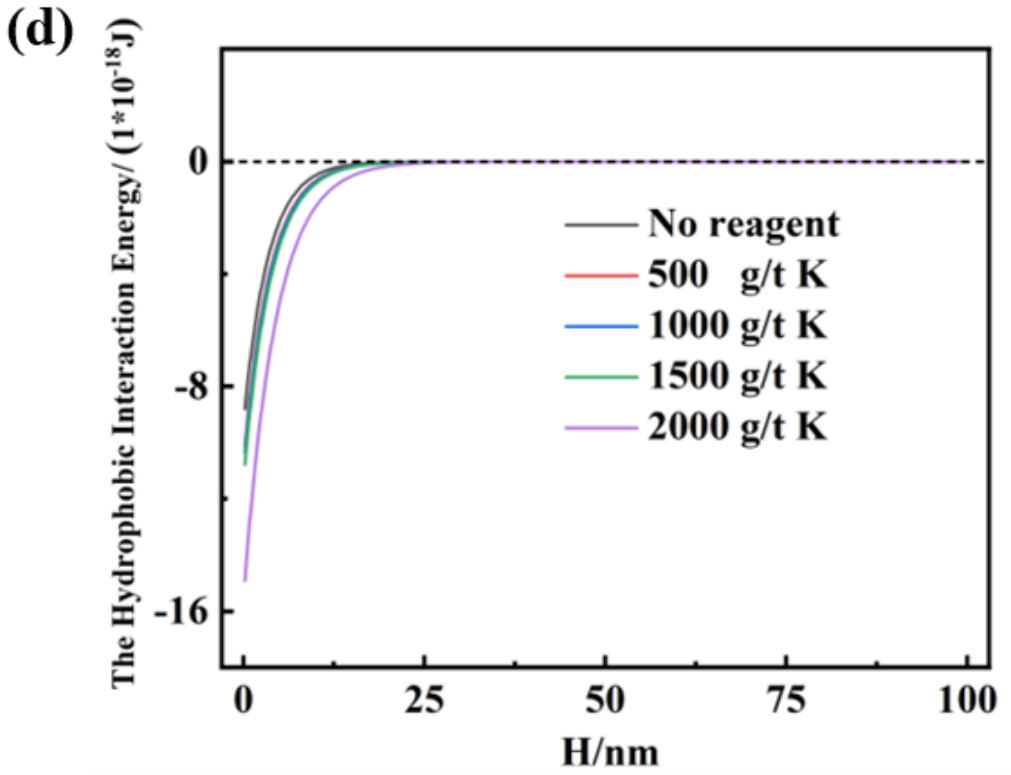
Figure 4.18 (c) and (d) show the hydrophobic interaction energies (V_H) as a function of distance between particle surfaces. One can see that V_H becomes increasingly more negative with increasing dosage of MEC or Kerosene. These negative values of V_H illustrate attractive forces between coal particle surfaces in the water environment of polarity. The magnitude of V_H is obviously larger than V_E and V_W. The V_H becomes more negative with an increasing dosage of collectors, indicating that MEC or K makes the surfaces of coal particles less polar and more prone to agglomerate in an aqueous environment. The contact angle measurements (Figure 4.17) also confirm that the collector modification on coal surfaces makes the surfaces more hydrophobic, i.e. less polar, leading to a stronger attractive interaction. The total interaction energies (V_T) between surfaces of coal particles are obtained by combining V_E, V_W and V_H and are shown in Figure 4.18 (e) and (f). With the surfaces of two particles approaching each other, the V_T increases first in positive directions, indicating that a net repulsive force exists between the two particles at a certain distance, which is originated from V_E (Figure 4.18 (a) and (b)). This V_T reaches a maximum energy barrier for agglomeration and the V_T then plunges from positive to negative quickly, signifying a net attractive force between the two approaching particles. When the dosage of MEC increases from 500 g/t to 2000 g/t, the flocculation barriers decreases from 0.33×10^{-18} J to 0.07×10^{-18} J, and the particle distance reaching the maximum V_T energy barrier points increased from 19 nm to 38 nm. When the dosage of K increases from 500 g/t to 2000 g/t, the flocculation barriers decreases from 0.33×10^{-18} J to 0.09×10^{-18} J, and the particle distance reaching the energy barrier point increases

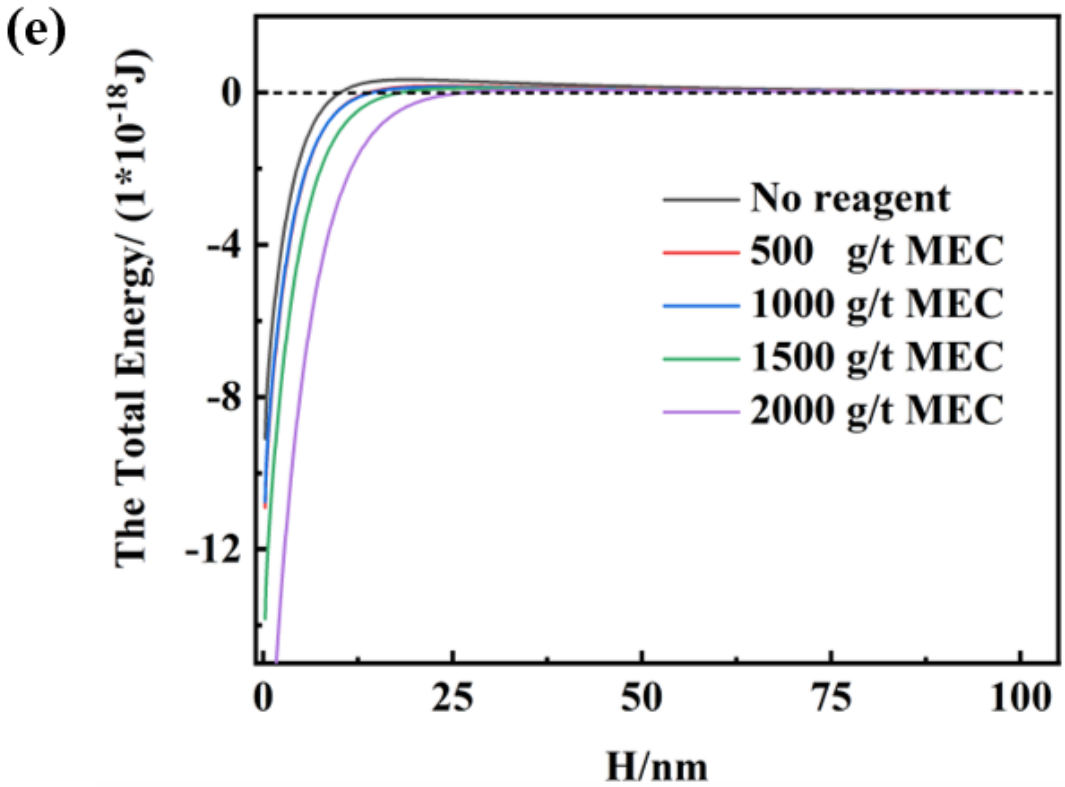
from 19 nm to 31 nm. Besides the reduced energy barrier for flotation by MEC, the value of V_T is much more negative, representing a much stronger attractive force between the two approaching particles, leading to a higher probability of MEC aggregation.




(b)
The Electrostatic Interaction Energy/ (1*10-18J)
0.75
0.50
0.25
0.00
0
25
50
75
100
H/nm
No reagent
500 g/t K
1000 g/t K
1500 g/t K
2000 g/t K


(c)
The Hydrophobic Interaction Energy/ (1*10-18J)
0
-8
-16
-24
0
25
50
75
100
H/nm
No reagent
500 g/t MEC
1000 g/t MEC
1500 g/t MEC
2000 g/t MEC


(d)
The Hydrophobic Interaction Energy/ (1*10-18J)
0
-8
-16
0
25
50
75
100
H/nm
No reagent
500 g/t K
1000 g/t K
1500 g/t K
2000 g/t K


(e)
The Total Energy/ (1*10-18J)
0
-4
-8
-12
0
25
50
75
100
H/nm
No reagent
500 g/t MEC
1000 g/t MEC
1500 g/t MEC
2000 g/t MEC

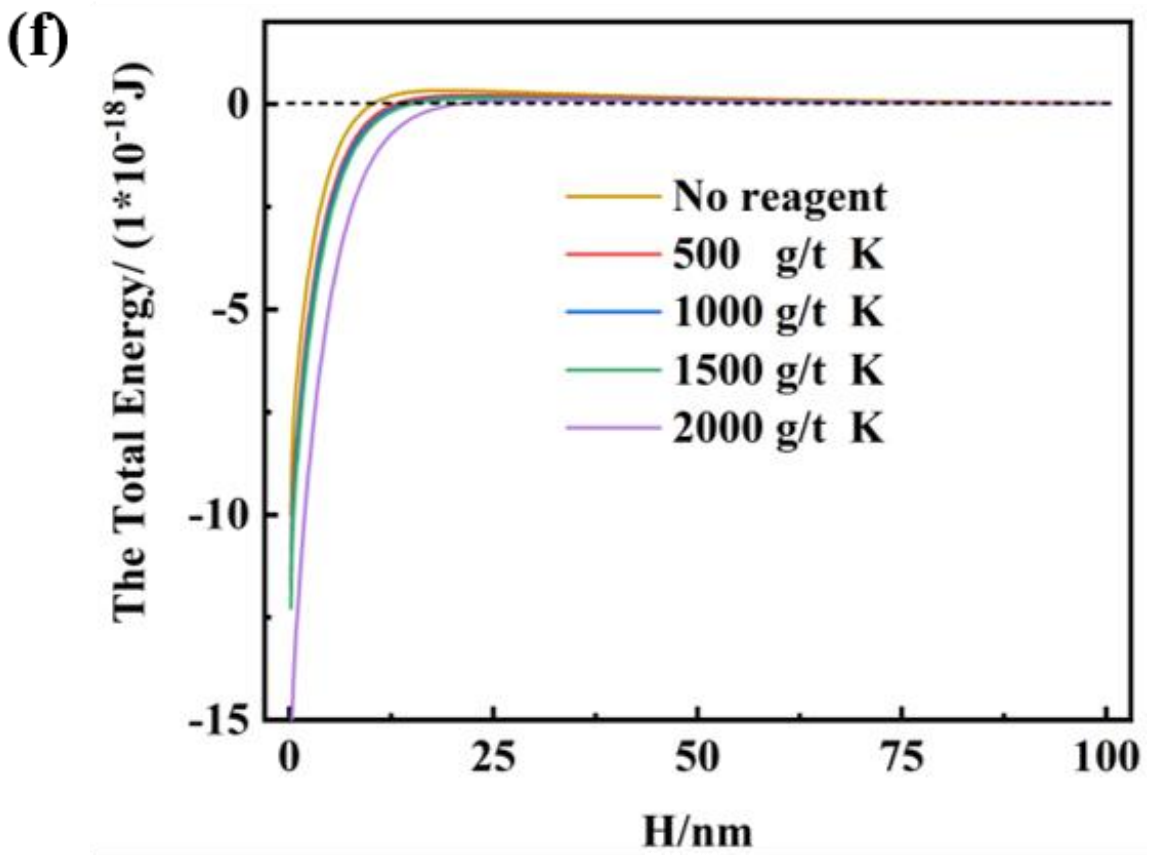
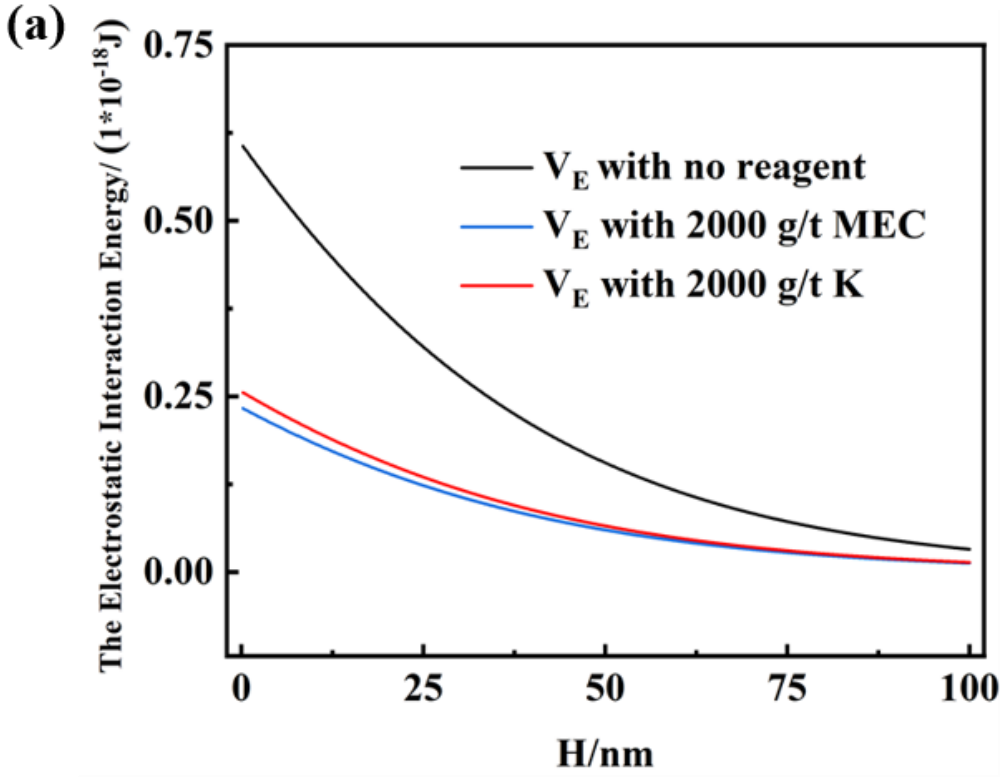
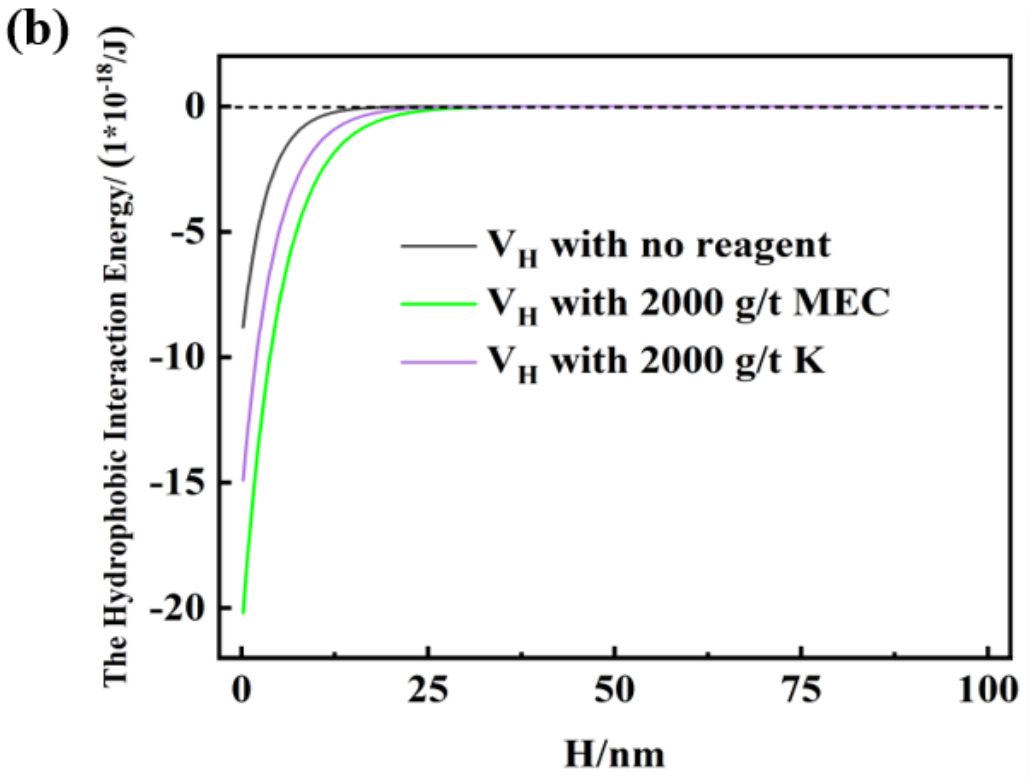


Figure 4.18 The interaction energies between particles with different dosages of MEC and Kerosene, (a) V_E of MEC, (b) V_E of Kerosene, (c) V_H of MEC, (d) V_H of Kerosene, (e) V_T of MEC and (f) V_T of Kerosene


(a)
The Electrostatic Interaction Energy/ (1*10-18J)
0.75
0.50
0.25
0.00
0
25
50
75
100
H/nm
VE with no reagent
VE with 2000 g/t MEC
VE with 2000 g/t K


(b)
The Hydrophobic Interaction Energy/ (1*10-18/J)
0
-5
-10
-15
-20
0
25
50
75
100
H/nm
VH with no reagent
VH with 2000 g/t MEC
VH with 2000 g/t K

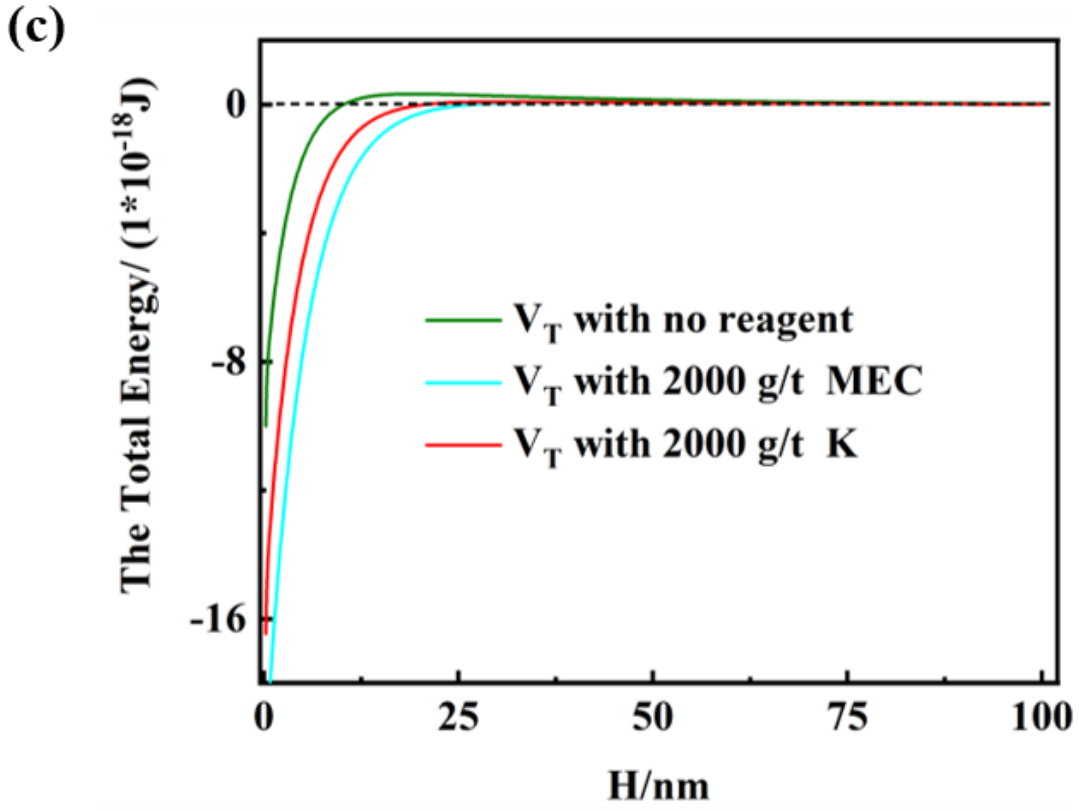


Figure 4.19 Comparisons of interaction energies between particles surfaces modified by MEC and Kerosene ((a) V_E without and with reagents, (b) V_H without and with reagents and (c) V_T without and with reagents)

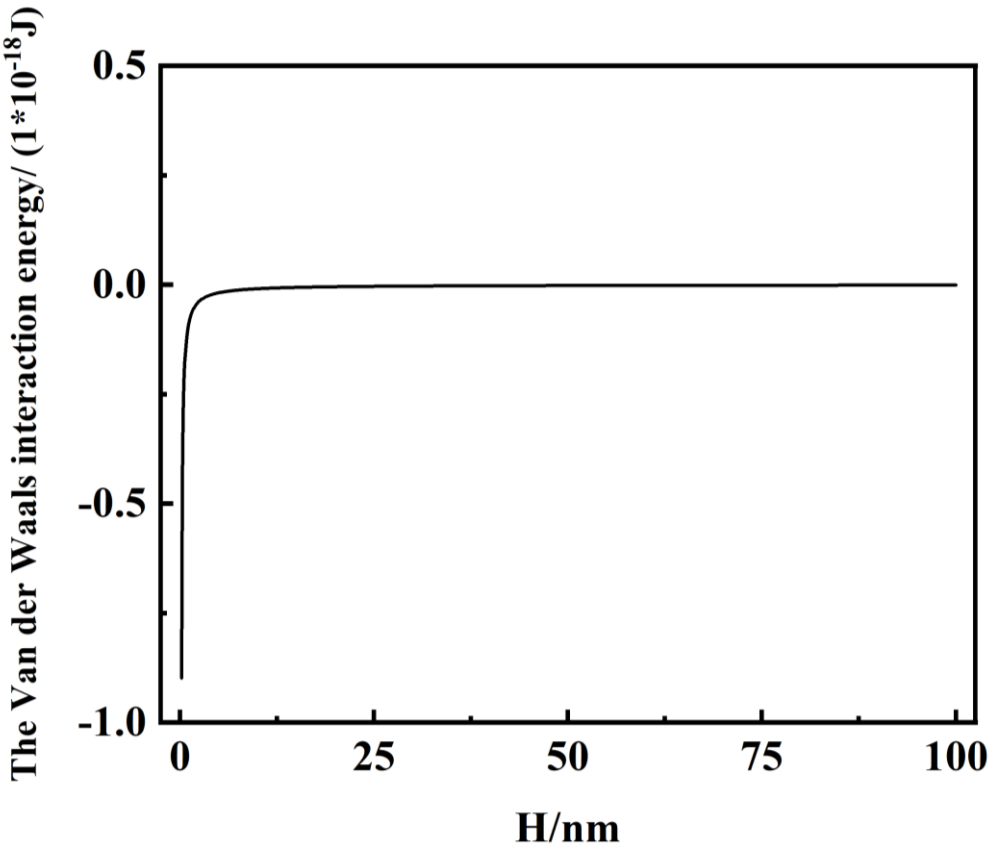


Figure 4.20 The Van der Waals interactions of MEC and K

Figure 4.19 shows the V_E, V_H and V_T with no reagent, 2000 g/t MEC and 2000 g/t Kerosene. The van der Waals interactions of MEC and Kerosene are approximated the same as explained in Section 3.9, and shown graphically in Figure 4.20, which is negative and represents attractive interactions between the two approaching particles. The addition of MEC or K can reduce the repulsive electrostatic force between the particles (Figure 4.19 (a)), and the reduction effect is larger for MEC than for K. The smaller electrostatic repulsive force with MEC may be due to the modification by the surfactants that affects the properties of oil droplets, leading to a reduced repulsive interaction between the coal particles.

The hydrophobic interaction energies (V_H) are much more negative for MEC than that for K as well as that for cases without the use of reagent (Figure 4.19 (b)). The total interaction energy (V_T)

of MEC is much more negative than that of K and without reagent (Figure 4.19 (c)), signifying that the particles modified by MEC are prone to combine into large flocs and move into foam area, resulting in improved flotation beneficiation for coal slimes.

4.7 Analyses of spreading velocity of MEC and Kerosene

The interfacial tension of Kerosene and water, and MEC and water was measured with a Surface Tension Meter (K100, KRUSS, GERMANY) as shown in Figure 4.21 at the room temperature. During the measurements, a square platinum plate was dipped into the interface of two liquids. The tensiometer measures the pulling force of the liquid on the plate, which can be used to calculate the surface tension.

A KRÜSS DSA25S instrument was used for contact angle measurements. Coal sample/water/oil interface was obtained by attaching a small oil bubble to the coal sample surface in water to obtain the contact angle in water. The spreading velocity of MEC and Kerosene can then be calculated by using the interfacial tension, viscosity and coal-oil-water contact angle[159].



Figure 4.21 Physical picture of Surface Tension Meter

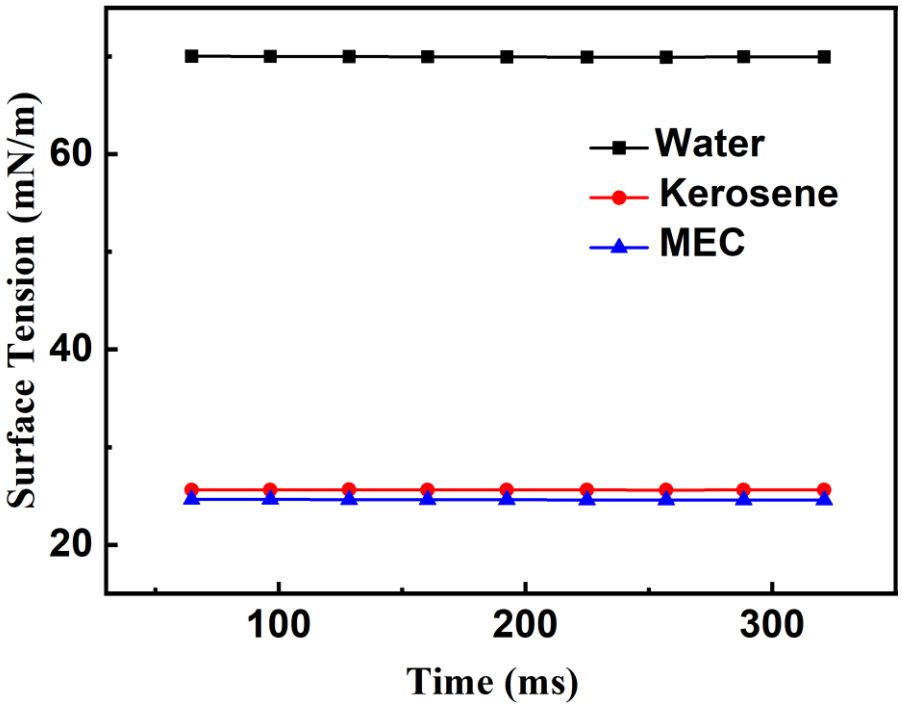


Figure 4.22 The surface tension of MEC and Kerosene

In a typical measurement of the contact angle, a coal sample plate was thoroughly immersed in the distilled water. A steel syringe pumped by a syringe pump injected the K or MEC drop into the water. The contact process between the oil droplets and the plate was recorded by a high-speed camera with a speed of 253 frames per second and a resolution of 1328 × 754 pixels. Figure 4.23 shows a typical result of the measurement.

Compared with Kerosene, the contact angle of MEC is lower, which is due to the hydrogen bonding between polar groups of MEC and the oxygen-containing groups on the coal surface[27] and the lower interfacial tension. The spreading coefficient (S) of the oil phase replacing water on a solid surface is defined by Eq. (4-21):

$$S = \gamma_{wc} - (\gamma_{oc} + \gamma_{ow}) \tag{4-21}$$

where the subscripts o, w, c represent the oil, water, and coal sample, respectively, and γ is the interfacial tension.

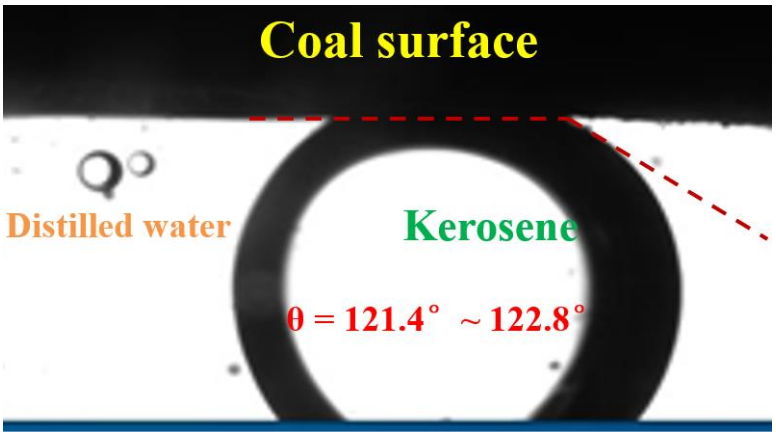


Figure 4.23 The result of coal-oil-water contact angle

The sign (positive or negative) of S depends on the if the oil wets coal surface completely or not[160][161].

By combining Eq. (4-21), with the Young's equation, Eq. (4-22), one has Eq. (4-23):

$$\gamma_{\mathrm{wc}} - \gamma_{\mathrm{oc}} = \gamma_{\mathrm{ow}} \cos\ \theta \tag{4-22}$$

$$S = \gamma_{\mathrm{ow}}(\cos\ \theta - 1) \tag{4-23}$$

where θ is the contact angle of coal-oil-water system.

The results show the spreading coefficient is negative and zero for Kerosene and MEC, respectively. One can conclude that the coal surface is completely wetted by MEC but only partly by Kerosene. The flotation progress requires that the collectors must spread rapidly on the sample surface for the bubbles later anchoring on the sample surface. Moxon et al.[161] reported the following spreading velocity (V_S):

$$V_s = C\frac{S}{\eta} = \mathrm{C}\frac{\gamma_{\mathrm{ow}}(\cos\ \theta - 1)}{\eta} \tag{4-24}$$

where γ_{ow} is the interfacial tension of oil and water, C is a constant depending on the sample surface, and η is the viscosity of oil. The η_{MEC} and $\eta_{Kerosene}$ are 8.36 mPa·s and 2.21 mPa·s, respectively. The interfacial tensions (Figure 4.22) of γ_{MEC} and $\gamma_{Kerosene}$ are 24.62 mN/m and 25.62 mN/m, respectively.

Insertion of these data into Eq.(4-24) gives the spreading velocity for MEC and Kerosene as zero and a positive value, respectively. It can be concluded that, therefore, the MEC spread slower than Kerosene because of the relatively high viscosity of MEC.

4.8 A proposed mechanism for MEC attachment at the coal surface

In this subsection, mechanisms for MEC attachment onto the coal surface are proposed, based on the results of this work, and understanding from both fundamental interactions between particles. The proposed W/O structure of microemulsion is shown in Figure 4.24, with water and kerosene

connected by Span 80, Tween 80 and MIBC. The hydrophilic groups are placed inwards and the hydrophobic groups are outwards. The amount of cosurfactant is less than surfactant to form microemulsion. The hydrophilic parts of Span 80 and Tween 80 would be inserted into the aqueous phase to expose the hydroxyl groups towards water molecules.

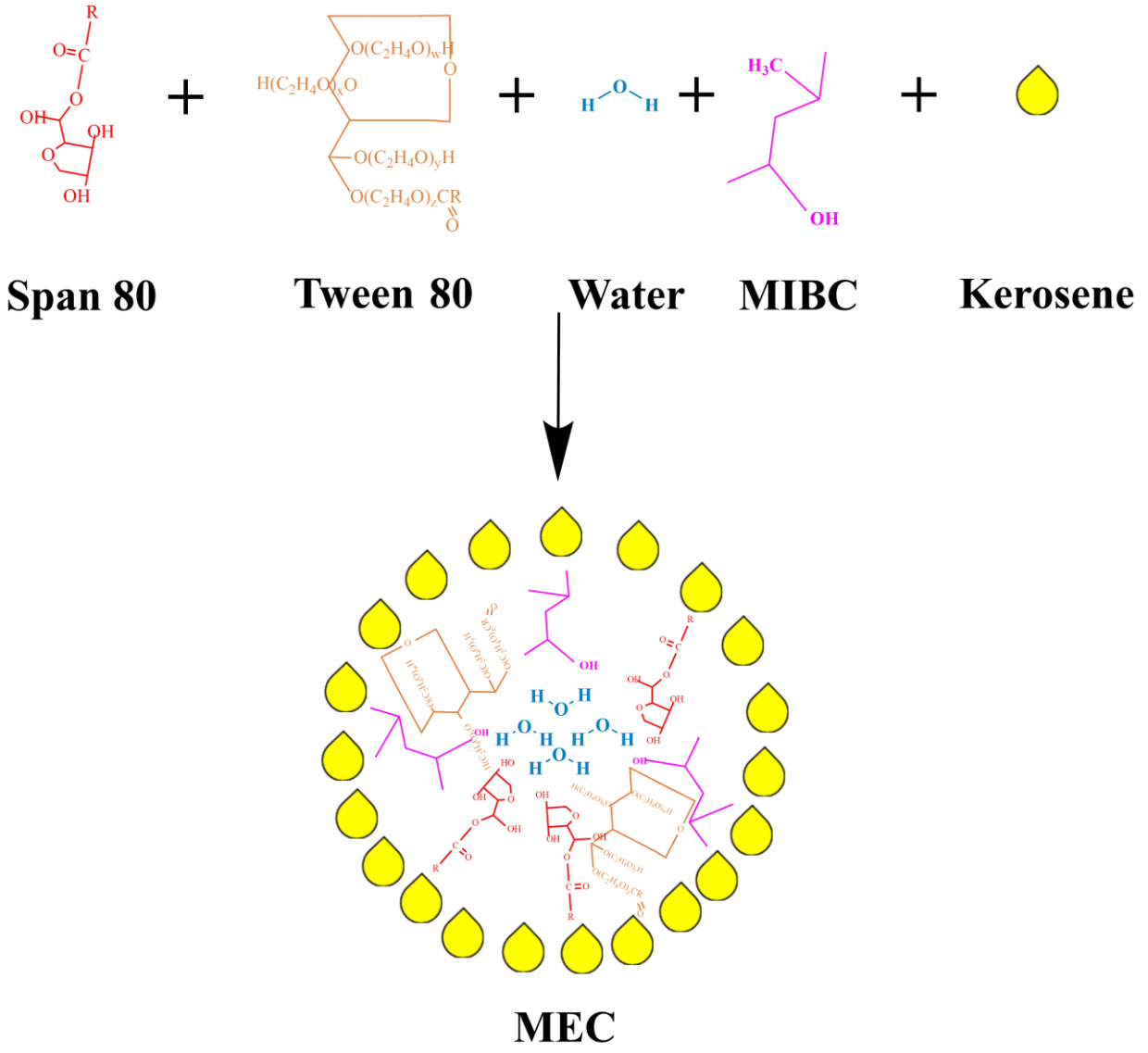


Figure 4.24 The proposed W/O structure of microemulsion

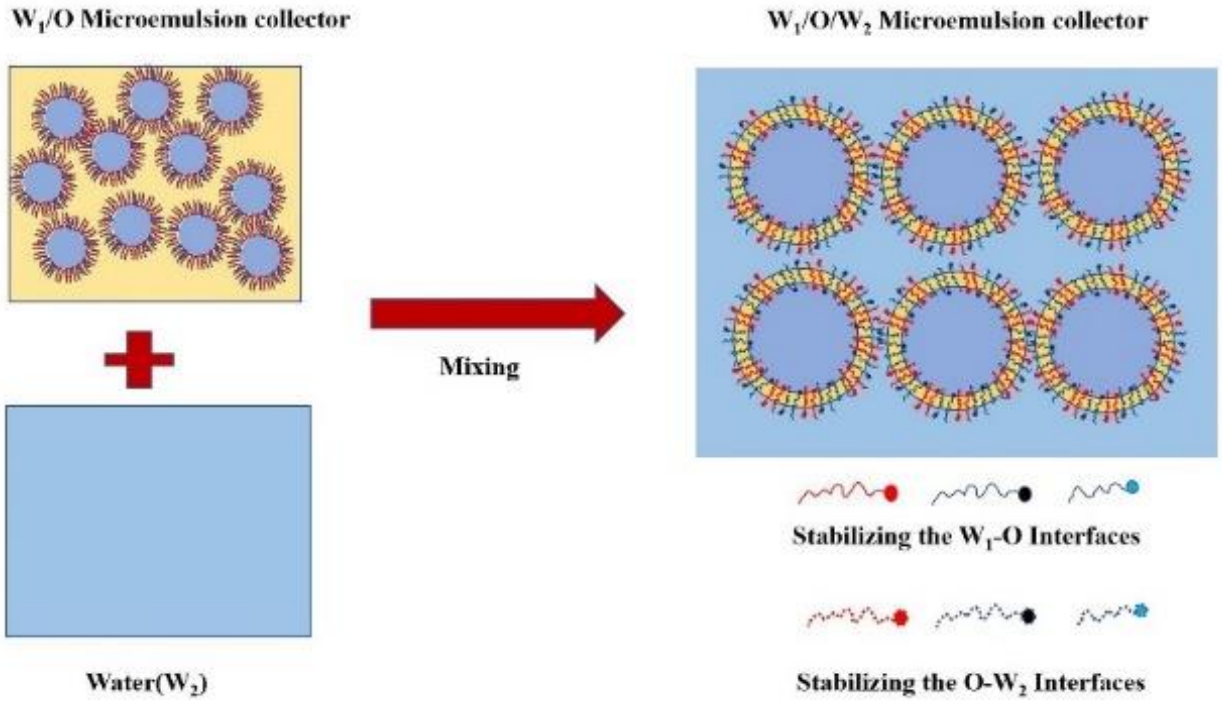


Figure 4.25 Schematic diagram of the mechanism for MEC dispersed in water forming Winsor III ($W_1/O/W_2$) microemulsion

A proposed formation process for MEC dispersed in water is shown in Figure 4.25. The excessive Span 80 and Tween 80 in the oil phase can improve the stability of the interface due to the increasing numbers of Span 80 and Tween 80 in the external O-W_2 interface and generate new Winsor III when the microemulsion fragments exist in water (W_2).

The stability of Winsor III can also be supported by the formation of hydrogen bonds between Span 80 + Tween 80 and water molecule and the hydrophobic bonds between Span 80 + Tween 80 and kerosene. The hydrophobic bonds are due to an unsaturated bond in the carbon chain of Span 80 and Tween 80 and without unsaturated bonds in oil molecule[162][163].

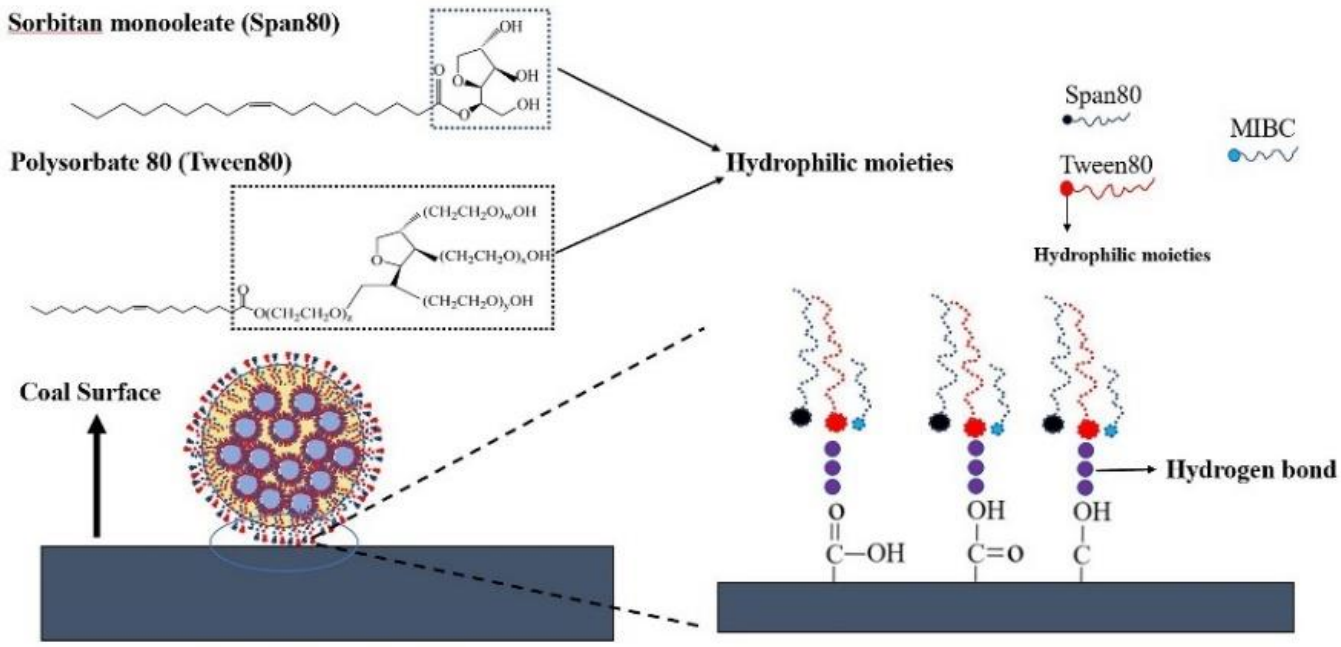


Figure 4.26 Schematic diagram of the interactions between Winsor III and coal particle

A proposed interaction between MEC and sample is shown in Figure 4.26. As mentioned before, the hydrocarbon chains of surfactant (Span 80 + Tween 80) point to the oil phase, while the hydrophilic parts may be head W_2-the external water phase. The hydrogen bonds between oxygen-containing functional groups of coal like C=O, -OH, -COOH and the hydrophilic groups of surfactant (Span 80 + Tween 80) are formed. Therefore, the fine coal particles are floatable because these hydrogen bonds are beneficial for emulsion droplets to attach to the coal surface.

4.9 Summary of Chapter 4

This chapter focuses on the preparation, characterization and performance measurements of a new collector MEC through froth flotation. The main outcomes are as follow:

(1) The microemulsions are successfully prepared by mixing Kerosene, blending surfactant (Span 80 and Tween 80 (HLB = 6, 7, 8, 9), MIBC and distilled water. The new collector MEC and Kerosene showed similar trends in the flotation process. When C_R(combustible recovery) = 60% and A (ash) = 16%, the dosage of MEC (HLB = 7) and kerosene are both 1000 g/t. The cost of MEC is estimated at 7400 RMB/ (10^3 t) dry coal slime, which is approximately 50% of that of Kerosene with 14220 RMB/ (10^3 t) dry coal slime. A higher flotation rate is obtained by using MEC compared to Kerosene in the froth flotation;

(2) The average particle size of MEC was 92.5 nm, so it could disperse the oily phase and form small droplets in water to improve the combustible recovery of cleaning coal by improving the collision probability of MEC and coal particle in froth flotation.

(3) The morphology of MEC obtained from Cryo-TEM analysis shows several large spherical droplets with a diameter greater than 100 nm, which is due to the sample damage during the filters adsorbing excess solution for Cryo-TEM analyses;

(4) The conductivity of the microemulsion increases with increasing concentration of mixed surfactant and water concentration. It decreases clearly with the increase of the cosurfactant concentration. And these results confirm the W/O structure of the new collector.

(5) The viscosity of the collector is important for collector molecue spreading on the sample surface in the flotation progress. The viscosity of MEC is 8 mPa·s, which is four times as much as that of water (2 mPa·s), and the microemulsion is Newtonian liquid with constant viscosity. MEC spreads slower than Kerosene on the coal surface because of the higher oil viscosity of MEC, while the viscosity of Kerosene is nearly equal to that of water. The better flotation

performance of MEC indicates the dispersing the oily phase and forming small droplets in water offset the side effect of high viscosity spreading on the sample surface;

(6) The addition of MEC or K can reduce the repulsive electrostatic interaction energies (V_E) between particles, and the reduction effect is larger for MEC than for K. The hydrophobic interaction energies (V_H) are much more negative for MEC than for K as well as that for particles without reagent. The total interaction energy (V_T) of MEC is much more negative than that for K and that of particles without reagent, signifying that the particles modified by MEC are prone to combine to give large flocs and enter into the foam area in froth flotation.

5 Results and analyses II - The effects of corn starch on froth flotation of pyrite and an ideal system of TXM + pyrite

This chapter represents the effects of corn starch on a froth flotation system for pyrite and an ideal system, aimed to verify the performance of cooked starch in regard to sulfur content and the recovery. An experimental flow diagram, reagent conditions, equipment parameters and pulp concentration of flotation etc. are discussed in detail. The Box-Behnken design (BBD) is employed to obtain the optimized parameters for the dosage of corn starch, modified pH of corn starch, and operating temperature. The effect of corn starch on depressing the flotation of ideal system (TXM+pyrite) were studied with medium oxidized TXM and low oxidized TXM.

It is generally believed that hydrophilic ferric hydroxyl compounds are formed on the surface of pyrite in alkaline media, which hinders the adsorption of the collector. Another hypothesis is that ion exchange occurs between OH- and the collector on the surface of pyrite to desorb the collector film on the surface of pyrite.

Wang et al.[164] believed the preference of chemisorption of OH^- on the pyrite surface as shown in Eq.(5-1):

$$FeS_2 + OH^- \rightarrow FeS_2 - OH_{ad} + e \qquad (5\text{-}1)$$

Chen et al.[165] showed that when lime was used to adjust the pH of pulp, the zeta potential of pyrite was more positive than that of NaOH, which was attributed to the adsorption of Ca^{2+} or $Ca(OH)^+$ on the surface of pyrite. Szargan et al.[166] showed that the adsorption of calcium ions could reduce the adsorption of xanthate on the pyrite surface and enhance the depression of pyrite. Hu et al.[167]

observed the $CaSO_4$ and $Ca(OH)_2$ formation on the surface of pyrite after 320 mg/L lime was treated due to the alkaline condition and the oxidization.

5.1 The effect of corn starch on froth flotation of a real system

A XFD flotation machine with a cell of 1 L (XFG-IV, Wuhan Exploration Machinery Factory, China) was used for flotation with a slurry concentration of 100 g/L. The agitation speed of the impeller was kept at 1870 r/min and the aeration rate was set to 0.2 $m^3/m^2 \cdot min$ with a dosage of MEC and DL-2-octanol maintained at 1000 g and 100 g per ton of dry feed coal. The pH of the flotation slurry was adjusted to pH = 11 with calcium oxide (CaO). The dosages of raw corn starch or cooked corn starch were 0, 30, 120, 240 g/t. In a typical experiment, the cooked starch was prepared in the following way: 5.27 g starch was placed in 400 ml distilled water, and the mixture was kept agitating at 500 rpm using a magnetic agitator in the water bath of 90℃. 100 g JDTTJM was mixed with 900 mL water, as well as a certain amount of corn starch, which was mixed at a shear spread of 40.53 m/s for 40 s using a high-speed mixer (MICCRAD-15, Germany). This resulted in a pulp which was then transferred into the flotation cell for pre-conditioning for 3 min, before MEC and DL-2 Octanol were injected into the slurry and stirred for 3 min and 30 s, respectively. Finally, the froth products and tailings were then filtered and dried in an oven at 80°C before weighing and analyses.

Figure 5.1 shows the results, which indicate that the cooked starch is better than the raw starch in terms of sulfur content and the recovery, demonstrating that the cooked starch could depress the pyrite in a real system.

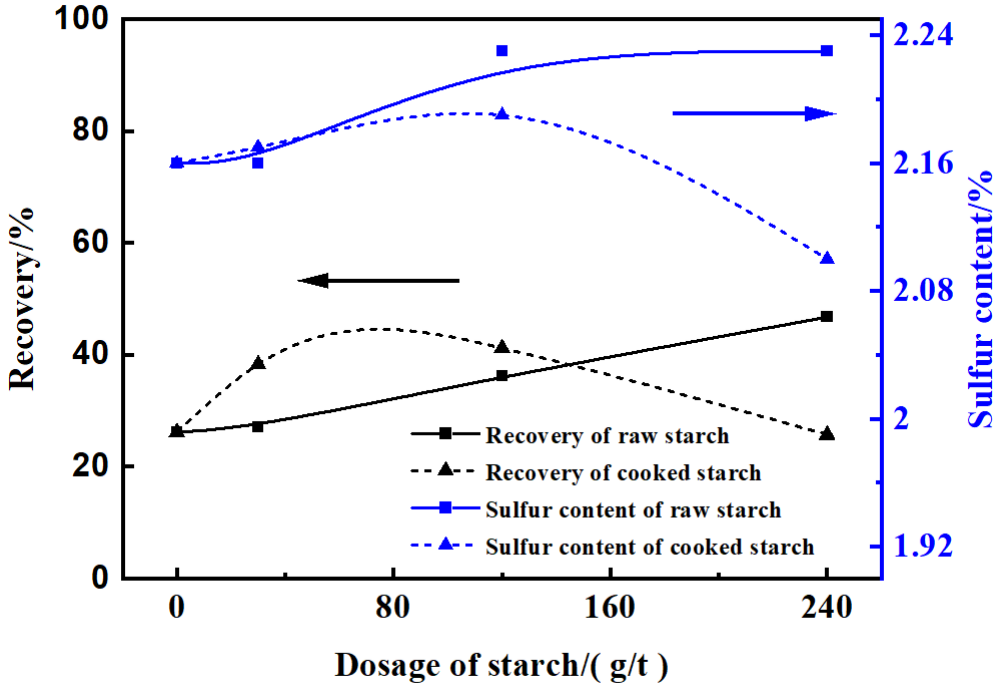


Figure 5.1 The effects of dosage of raw starch and cooked starch on recovery and sulfur content of cleaning coal

5.2 Box-Behnken design for studying the effect of corn starch on the recovery of pyrite

The Box-Behnken design (BBD) based on the response surface methodology (RSM) was employed to obtain statistical models for pyrite recovery optimization. Factors including the dosage of corn starch, modified pH of corn starch, and heated temperature for corn starch were analyzed to understand the ascendancy and interactional effects on the formulation stability.

This method was proposed by G.E.P. Box and K.B. Wilson in 1951 based on the so-called concept of Response Surface Methods (RSM). This method is to find an experimental design method for describing the optimal results of consecutive tests. A first-order polynomial model is used to reflect

the functional relationship between the factors and response values as shown in Eq.(5-2). The model is clearly an approximate one rather than an accurate one, but it is easy to use.

$$y = \beta_0 + \beta_1 x_1 + \cdots + \beta_k x_k \tag{5-2}$$

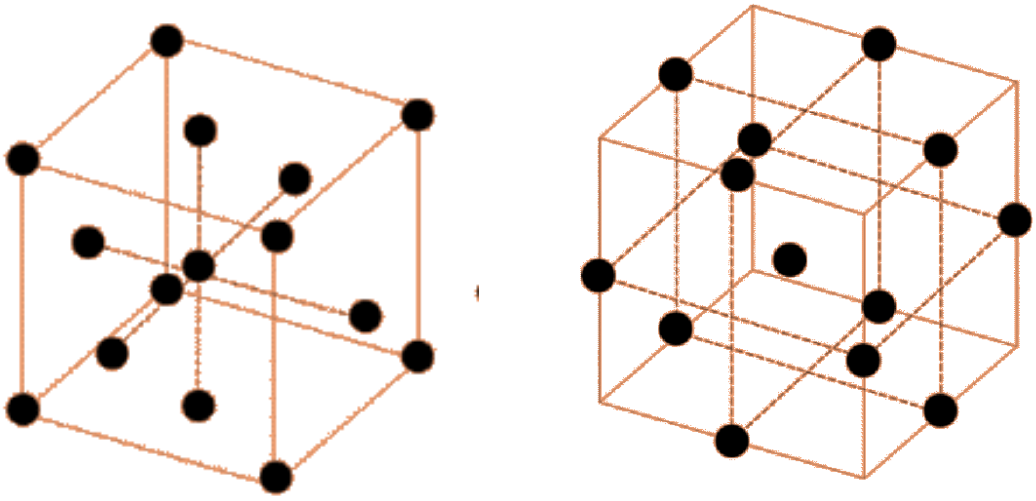
Later, Mead and Pike[168] enriched the theory of RSM from response curve analysis, which laid the theoretical foundation for the popularization and use of the RSM.

In 1960 s, a great progress has been made in the second-order model, with the Central Composite Design (CCD) and Box-Behnken Design (BBD) being used for the first time. The first-order model of response surface analysis uses low-order polynomials to describe the response surface, which is only suitable for flat surfaces or surface with no significant fluctuation or obvious slope. The second-order model can be flexible and close to express the response surface in various forms. Therefore, when there is curvature on the response surface, the second-order model is the most suitable one, and the following functional relationship is used as Eq.(5-3):

$$\begin{aligned} y &= \beta_0 + \sum_{i=1}^{k} \beta_i x_i + \sum_{i=1}^{k} \beta_{ii} x_i^2 + \sum_{\substack{i=1 \\ i<j}}^{k} \sum_{j=1}^{k} \beta_{ij} x_i x_j \\ &= \beta_0 + \beta_1 x_1 + \cdots + \beta_k x_k + \cdots + \beta_{11} x_1^2 + \cdots \\ &\quad + \beta_{kk} x_k^2 + \beta_{12} x_1 x_2 + \cdots + \beta_{(k-1)k} x_{k-1} x_k \end{aligned} \tag{5-3}$$

The test points (x_{11}, …, x_{k1}, y_1), …, (x_{1n}, …, x_{kn}, y_n) can be obtained from experiments, then β_0, β_1, β_2…… $\beta_{(k-1)k}$ can be estimated by Eq. (5-3). The established regression equation can be used to estimate the extreme point and fixed point of the test and to find the optimal test conditions.

The Box-Behnken Design (BBD) and Central Composite Design (CCD) are different greatly in the selection of test points; see Figure 5.2. The test points of CCD design include the cubic points, the axial point and the center point, while the test points of BBD are the midpoints of the cube edges.



(a) CCD (b) BBD

Figure 5.2 Designed test points of CCD and BBD

Compared with the CCD, the BBD does not need continuous tests and the number of experiments is 17 times compared to that of 20 times for CCD. Therefore, the BBD experimental Design is often applied to the nonlinear experimental research. In addition, the BBD does not arrange all factors into high level tests, which is especially suitable for some tests with stringent conditions or high safety requirements. Therefore, the BBD is used in this study. The effects of starch dosage, pH value of modified starch and heated temperature of starch on pyrite recovery were studied to determine the primary and secondary effects of various factors on the recovery of pyrite.

5.2.1 Single-parameter experiments

Single-factor experiments were designed to investigate the effect of starch content on the recovery of pyrite. In this set of experiments, the flotation slurry was set as pH = 11 adjusted with calcium oxide (CaO) and the starch was modified with a pH = 3 solution adjusted with sulfuric acid (H_2SO_4). The heated temperature for corn starch was set as 75℃ for 0.5 h. The dosages of corn starch were 300, 600, 900, 1200 and 1500 g/t. For all the flotation tests, the agitation speed of the impeller was kept at 2200 r/min and the dosages of MEC and DL-2-Octanol were maintained respectively at 2000 g/t and 500 g/t dry feeding pyrite. The pre-conditioning of the pulp was carried out under stirring at the regular speed (2200 r/min) for two minutes. After this process, the sample was conditioned with corn starch for three minutes. Then the MEC and DL-2-Octanol were injected for 3 min and 0.5 min, respectively. The aeration rate was set to 0.1 $m^3/m^2/min$. The flotation concentrate product was collected until there was no froth product left in the flotation cell.

The results show that the optimal amount of starch is 1200 g/t. As a result, a dosage of starch of 1200 g/t was used in all following experiments.

The single factor experiments were also designed to investigate the effect of modified pH of cooked starch on the recovery of pyrite. In this set of experiments, the pH of flotation slurry was pH = 11. The dosage of corn starch was 1200 g/t and the heated temperature was 75℃ for 0.5 h. The modified pH of the cooked starch was 3, 5, 7, 9 and 11. For all the flotation tests, the agitation speed of the impeller was kept at 2200 r/min and the dosages of MEC and DL-2-Octanol were maintained respectively at 2000 g/t and 500 g/t dry feeding pyrite. The pre-conditioning of the pulp was carried out under stirring at the regular speed (2200 r/min) for two minutes. After this process, the sample was conditioned with corn starch for three minutes. Then the MEC and DL-2-

Octanol were injected for 3 min and 0.5 min, respectively. The aeration rate was set to 0.1 $m^3/m^2/min$. Figure 5.3 shows the recovery as a function of pH. As a result, the dosage of starch was set at 1200 g/t and the modified pH of cooked starch was set as pH = 3 in the subsequent experiments.

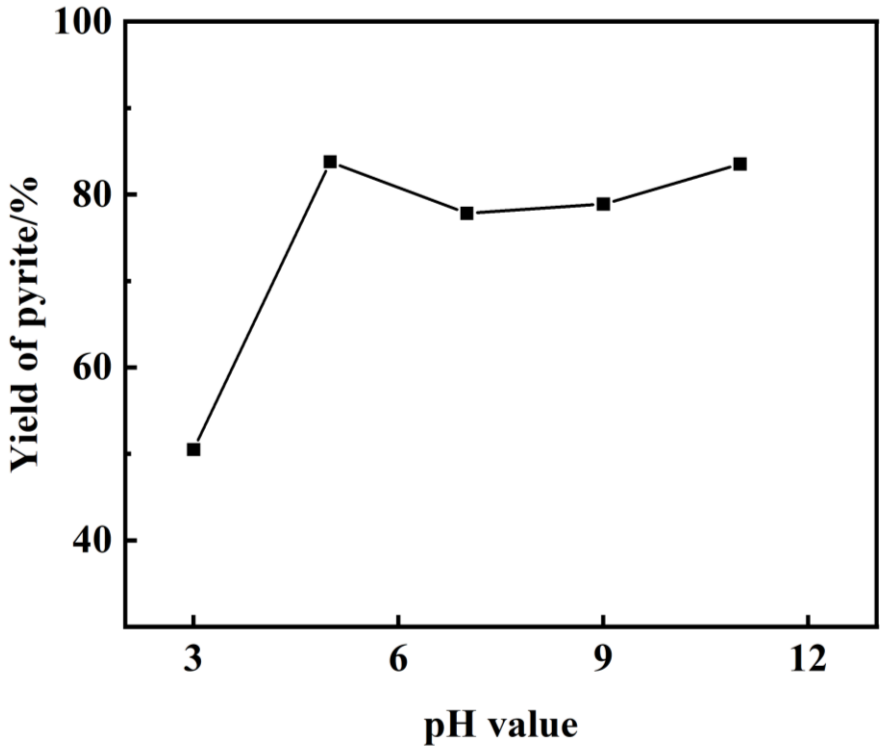


Figure 5.3 Effect of the modified pH of corn starch on pyrite depression

Single-factor experiments were also designed to investigate the effect of the heated temperature of corn starch on the recovery of pyrite. In this set of experiments, the dosage of corn starch was 1200 g/t and the modified pH was 3. The heated temperatures were set to 65℃, 75℃, 85℃, 95℃, and 105℃ for 0.5 h. Other conditions were the same as previous experiments. Figure 5.4 shows the dependence of the recovery on the heated temperature. One can see that the optimal heated temperature of corn starch is 105℃ over the temperature range investigated in this work.

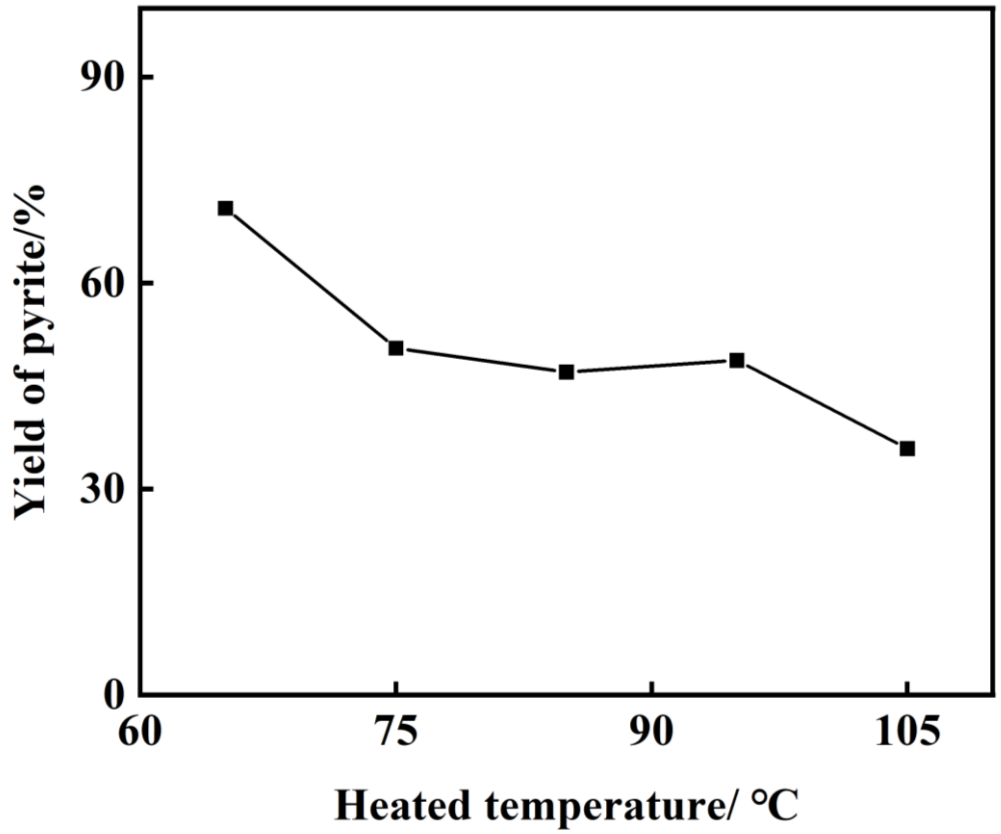


Figure 5.4 Effect of the heated temperature of corn starch on pyrite depression with 1200 g/t corn starch and the modified pH = 3

5.2.2 Box-Behnken experimental design

In this work, the effects of the dosage of corn starch, modified pH of corn starch, and heated temperature were investigated. Table 5.1 gives the selected experimental range for each of the parameter. Based on these, the Box-Behnken design (BBD) was used for the experimental design. Table 5.2 shows the BBD plans. It can be seen that seventeen sets of experiments should be conducted to investigate the effects of the single parameter and their interactions on the responses.

Table 5.1 Experimental ranges and factor levels of different parameters in the design

Actual parameters	Unit	Code parameters	Level		
			-1	0	1
The dosage of corn starch	g/t	X_1	1500	1200	1800
pH of corn starch		X_2	5	3	7
Heated temperature	℃	X_3	85	105	65

Table 5.2 Experimental runs suggested by BBD

Run	Dosage of cooked starch	pH value	Temperature
	g/t (X_1)	X_2	℃ (X_3)
1	-1	0	1
2	1	-1	0
3	-1	1	0
4	0	-1	-1
5	-1	0	-1
6	1	0	-1
7	1	1	0
8	1	0	1
9	-1	-1	0
10	0	1	-1
11	0	-1	1
12	0	1	1
13	0	0	0
14	0	0	0
15	0	0	0
16	0	0	0
17	0	0	0

5.2.3 Statistical analysis and predictions

5.2.3.1 Results

The experimental results, together with the predicted values related to the pyrite recovery are shown in Table 5.3. There are 17 sets of experiments as stated in Section 5.2.2 with 12 sets being factorial tests, corresponding to the factorial points. There are 5 sets of central tests corresponding to the zero points, which are used to estimate the error.

5.2.3.2 The analysis of variance (ANOVA)

The analysis of variance (ANOVA) is a technique to demonstrate the quality of the model based on experimental data[169][170]. It can evaluate the fitness of regression model. At the same time, the ANOVA can also be used to predict the influence of each parameter and interactions between different parameters on the response[171]. The analysis of variance is often expressed by F-value and p-value, with the p-values and F-values to determine the interactions between the parameters. P-value helps to decide whether to reject the null hypothesis. If p-value is 0.05, that means that 5% of the time one would see a test statistic as extreme as the one that is found if the null hypothesis was true. At this time, the parameters have a significant impact on the response. Table 5.4 shows the ANOVA results for each response. As can be seen from the table, X_1 (the dosage of corn starch), X_2 (the modified pH), X_3 (heated temperature), and X_1X_3 (the dosage of corn starch and heated temperature) are significant model terms, and X_3^2 (heated temperature) is an extremely significant model term. The interaction parameters of X_1X_2, X_2X_3, and quadratic parameters of X_1^2 and X_2^2 are not significant for the pyrite recovery. The F-value of the model of 18.91 and the corresponding p-value of lower than 0.0001 imply that the model is significant. Therefore, the model is in good agreement with the experimental results. The lack of fit p-value for the pyrite recovery is 0.1539,

which is an indication of insignificance. The "Lack of Fit F-value" of 3.06 means the Lack of Fit is not significant relative to the pure error.

As shown in Table 5.3, the experimental results were filled to ‘Actual value’. Then click the ‘Yield (Analized)’ button for analysis. One model will be chosen, then ANOVA will be analyzed. And then it can be optimized to get the predicted values.

Table 5.3 Experimental design and results with response surface method of pyrite sample

Run	Dosage of cooked starch	pH value	Temperature	Recovery, %	
	g/t(X_1)	X_2	°C(X_3)	Actual value	Predicted Value
1	-1	0	1	75.34	78.57
2	1	-1	0	15.45	16.75
3	-1	1	0	17.8	16.5
4	0	-1	-1	42.77	44.7
5	-1	0	-1	31.6	37.57
6	1	0	-1	74.55	71.32
7	1	1	0	30.34	38.24
8	1	0	1	72.29	66.32
9	-1	-1	0	24.88	16.98
10	0	1	-1	72.5	67.83
11	0	-1	1	70.67	75.34
12	0	1	1	75.14	73.21
13	0	0	0	17.43	22.15
14	0	0	0	16.98	22.15
15	0	0	0	20.54	22.15
16	0	0	0	28.31	22.15
17	0	0	0	27.49	22.15

Table 5.4 ANOVA results for developed models for recovery of pyrite

Resource	d_f	Regression model			
		Sum of Squares	Mean Square	F Value	P Value
X_1	1	231.23	231.23	4.16	0.0808
X_2	1	220.61	220.61	3.97	0.0867
X_3	1	648.36	648.36	11.66	0.0112
X_1X_2	1	120.67	120.67	2.17	0.1842
X_1X_3	1	529	529	9.51	0.0177
X_2X_3	1	159.52	159.52	2.87	0.1342
X_1^2	1	3.63	3.63	0.065	0.8056
X_2^2	1	3.38	3.38	0.061	0.8123
X_3^2	1	7506.72	7506.72	134.99	< 0.0001
Model	9	9466.28	1051.81	18.91	0.0004
Residual	7	389.26	55.61	—	—
Lack of fit	3	271.2	90.4	3.06	0.1539
Pure Error	4	118.06	29.52	—	—
Cor Total	16	9855.54	—	—	—

5.2.3.3 The interaction between different parameters

The response surface of the interactions between the starch dosage, pH value, and heated temperature and different responses can be observed in Figure 5.5, Figure 5.6, and Figure 5.7, respectively. The impacts of the dosage of corn starch and modified pH of corn starch on the

recovery of pyrite are demonstrated in Figure 5.5. As can be observed, the recovery of pyrite increases with increasing dosage of corn starch or pH of corn starch.

The impacts of modified pH of corn starch and heated temperature on the recovery of pyrite are demonstrated in Figure 5.6. An increase in the heated temperature leads to a noticeable decrease in the recovery of pyrite. The increasing heated temperature at a low pH reduces the recovery of pyrite first but a continuing increase of the heated temperature leads to an increase in the recovery of pyrite. This trend can be attributed to the opposite effect of the heated temperature on the recovery of pyrite.

The impacts of the dosage of corn starch and heated temperature on the recovery of pyrite are shown in Figure 5.7. An increase in the heated temperature is seen to lead to a noticeable decrease in the recovery of pyrite. The increasing heated temperature at a low dosage of corn starch reduces the recovery of pyrite first, but a further increase in the heated temperature beyond a certain limit leads to an increase in the recovery of pyrite. This trend can be attributed to the opposite effect of heated temperature on the recovery of pyrite. The results also show that the effect of heating temperature on the pyrite recovery is more significant than that of modified pH value and the dosage of corn starch.

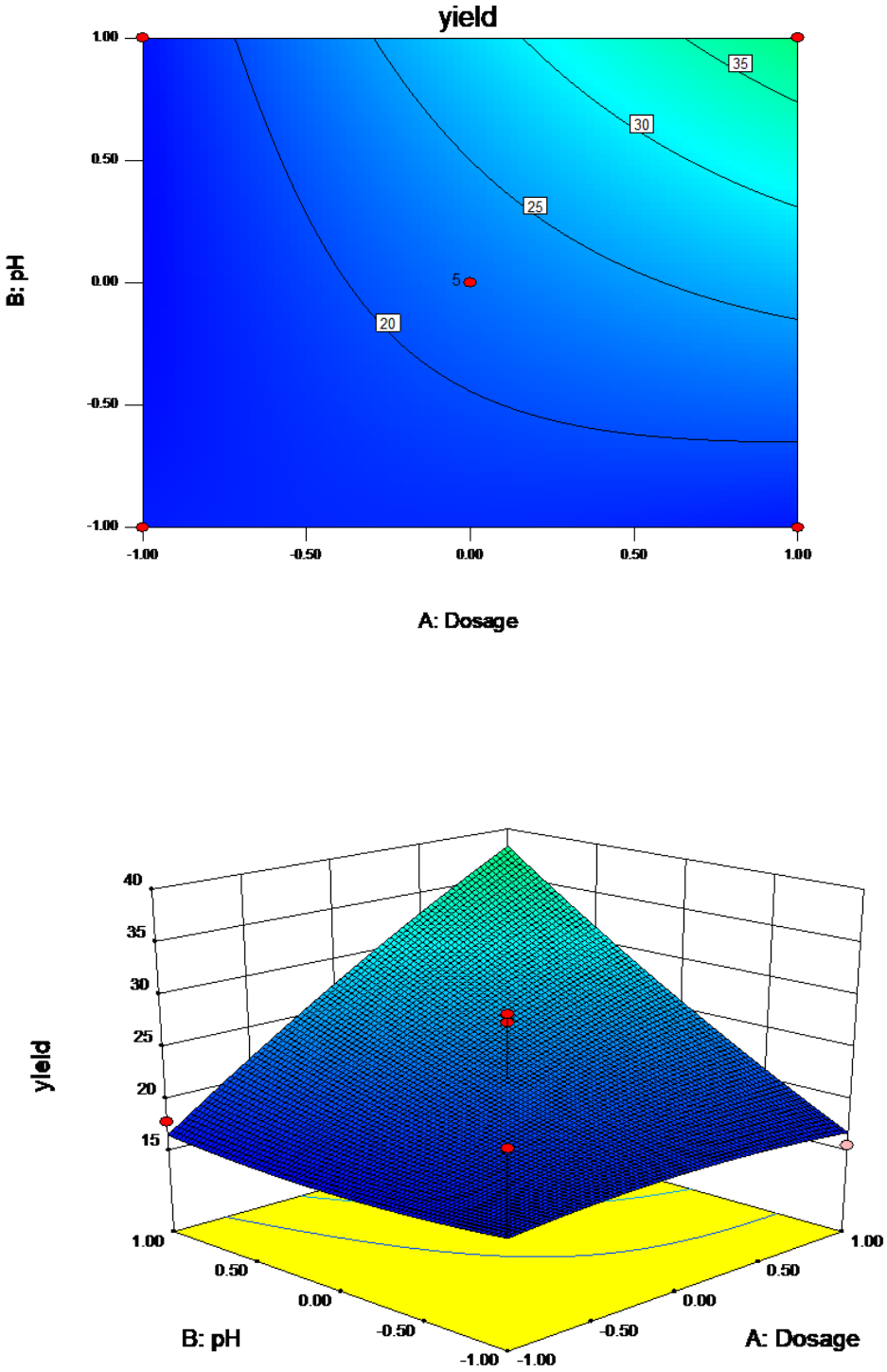


Figure 5.5 The effects of (A) the dosage of corn starch and (B) modified pH of corn starch on the recovery of pyrite

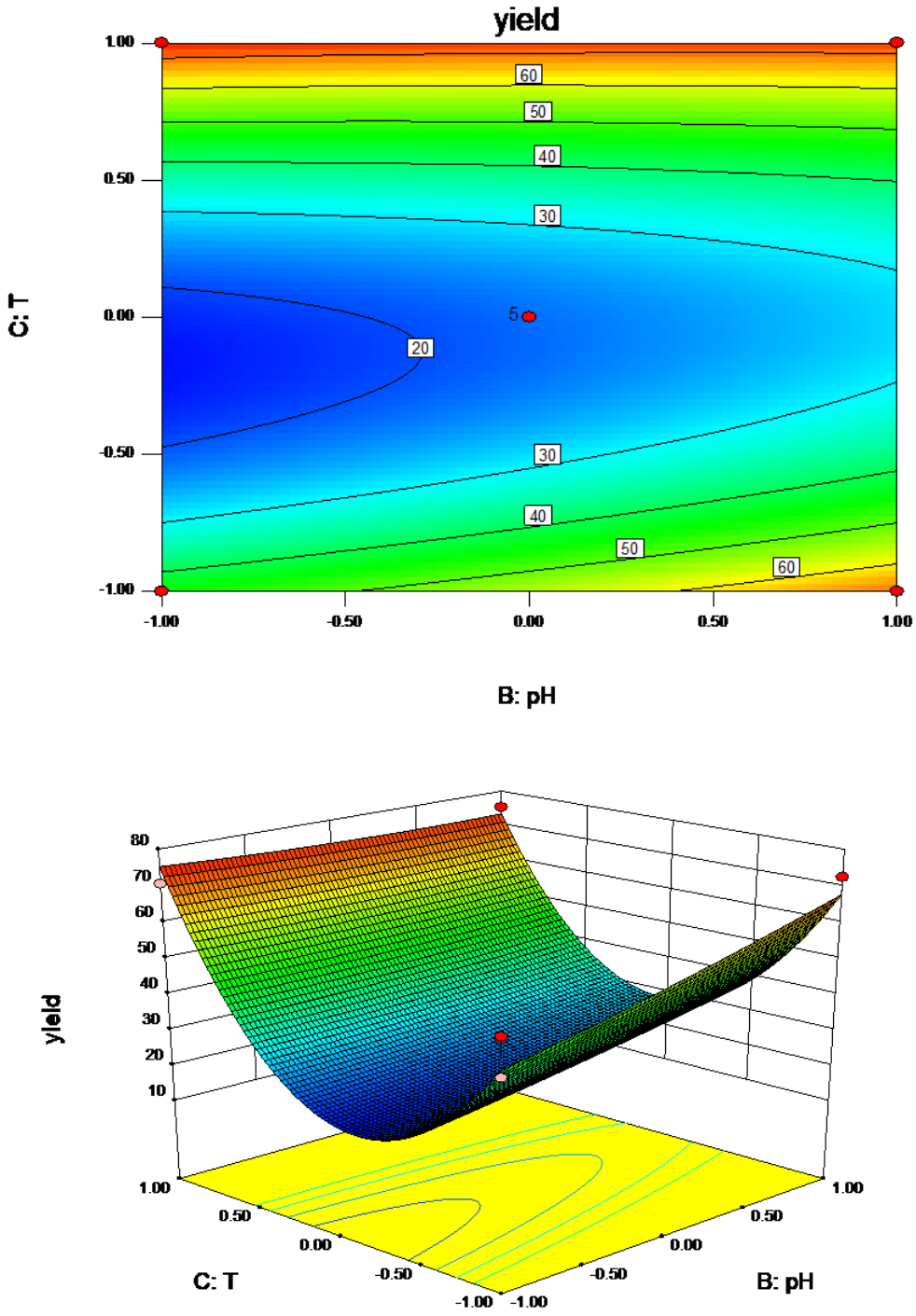


Figure 5.6 The effects of (b) pH of corn starch and (c) heated temperature on the recovery of pyrite

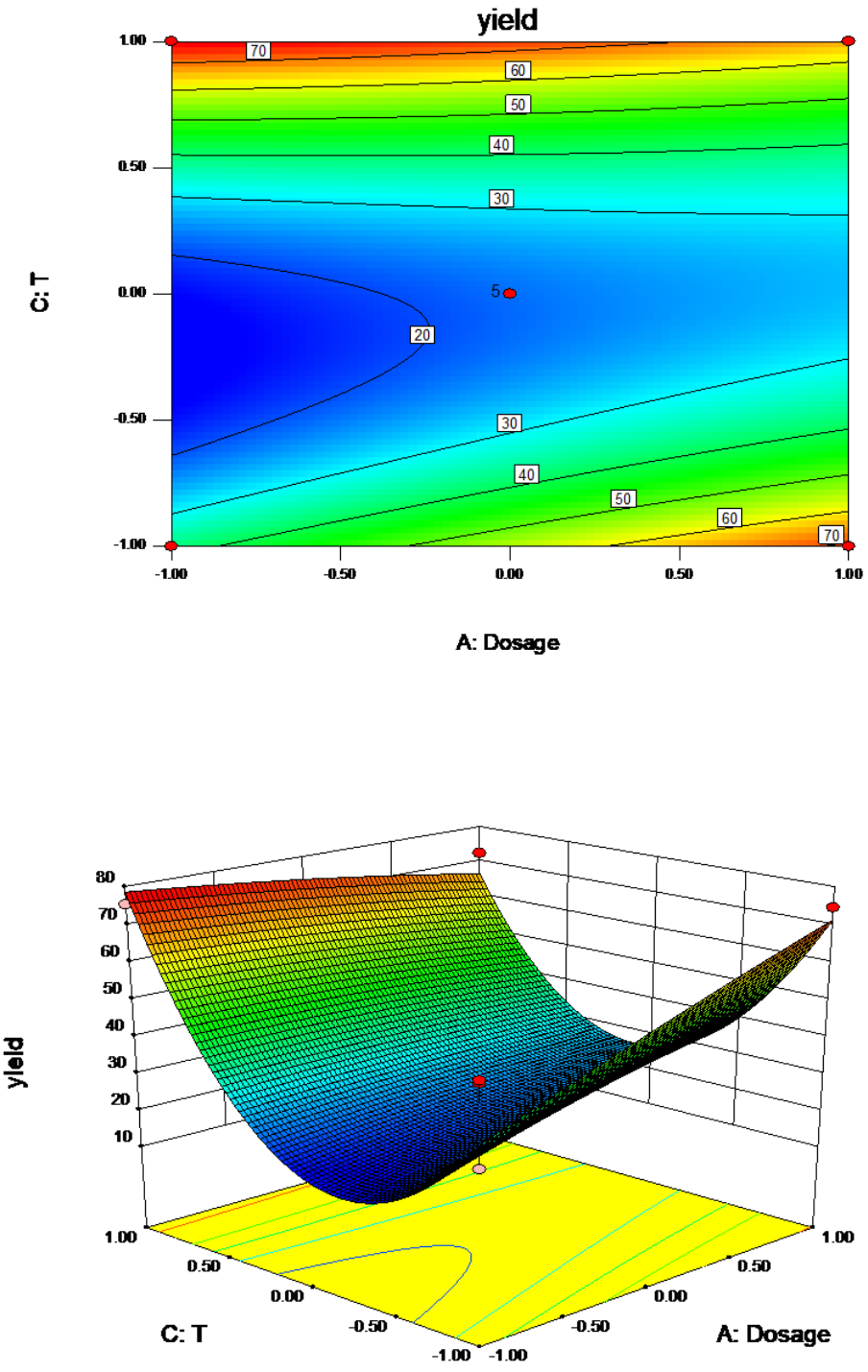


Figure 5.7 The effects of (a) the dosage of corn starch and (c) heated temperature on the recovery of pyrite

5.2.3.4 Multi-objective optimization for pyrite recoveries

Having established the model for each response, multi-objective optimization can be achieved by considering different responses. A numerical method was used in this work, which is based on the 'desirability method'. For doing so, the minimum recovery of pyrite (Y) was selected for response and input. The parameters for the minimum recovery were：X_1 = 1490 g/t，X_2 = 3.7，and X_3 = 102℃；Due to the limitation of the equipment in the actual experiments, the above parameters are optimized to X_1 = 1490 g/t，X_2 = 4，and X_3 = 100℃. According to the optimized conditions, the predicted yield was 13.92%, which compares well to the actual yield of 14.01%.

5.3 The effect of corn starch on depressing flotation of an ideal system of TXM + pyrite

Both medium oxidized coal (M) for low ash and high carbon content TXM obtained by oxidizing coal in the oven at 160℃ for 2 h, and the untreated coal were used in the work. The untreated coal is also called low oxidized coal (L). The process for producing the medium oxidized coal is shown in Figure 5.8. And these two types of coal were studied.

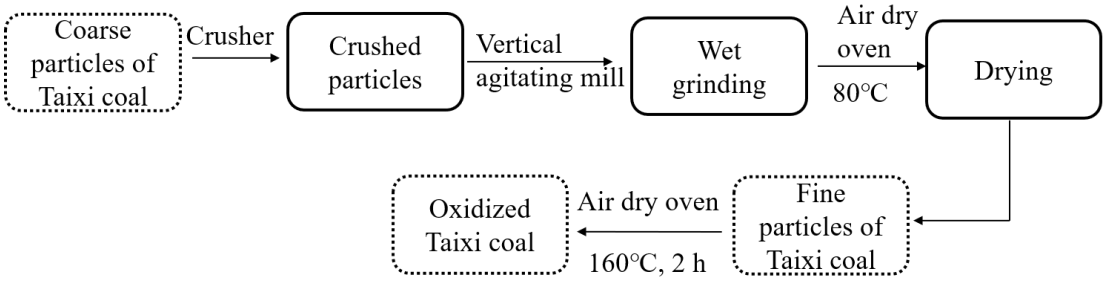


Figure 5.8 The detailed process of the medium oxidized coal

Other conditions are as follows: The pH of flotation slurry was set at pH = 11 adjusted with calcium oxide (CaO) and the starch was modified with pH = 3 solution adjusted with sulfuric acid (H_2SO_4).

The concentration of the pulp was set as 100 g/L. The heated temperature for corn starch was 105℃ for 0.5 h. The dosages of corn starch were 600, 900, 1200, 1500 and 1800 g/t. For all the flotation tests, the agitation speed of the impeller was kept at 2200 r/min and the dosages of MEC and DL-2-Octanol were maintained respectively at 2000 g/t and 600 g/t dry feeding. The pre-conditioning of the pulp was carried out under stirring at a regular speed (2200 r/min) for two minutes. After this process, the sample was conditioned with corn starch for three minutes. Then the MEC and DL-2-Octanol were injected for 3 min, and 0.5 min, respectively. The aeration rate was set to 0.2 $m^3/m^2/min$.

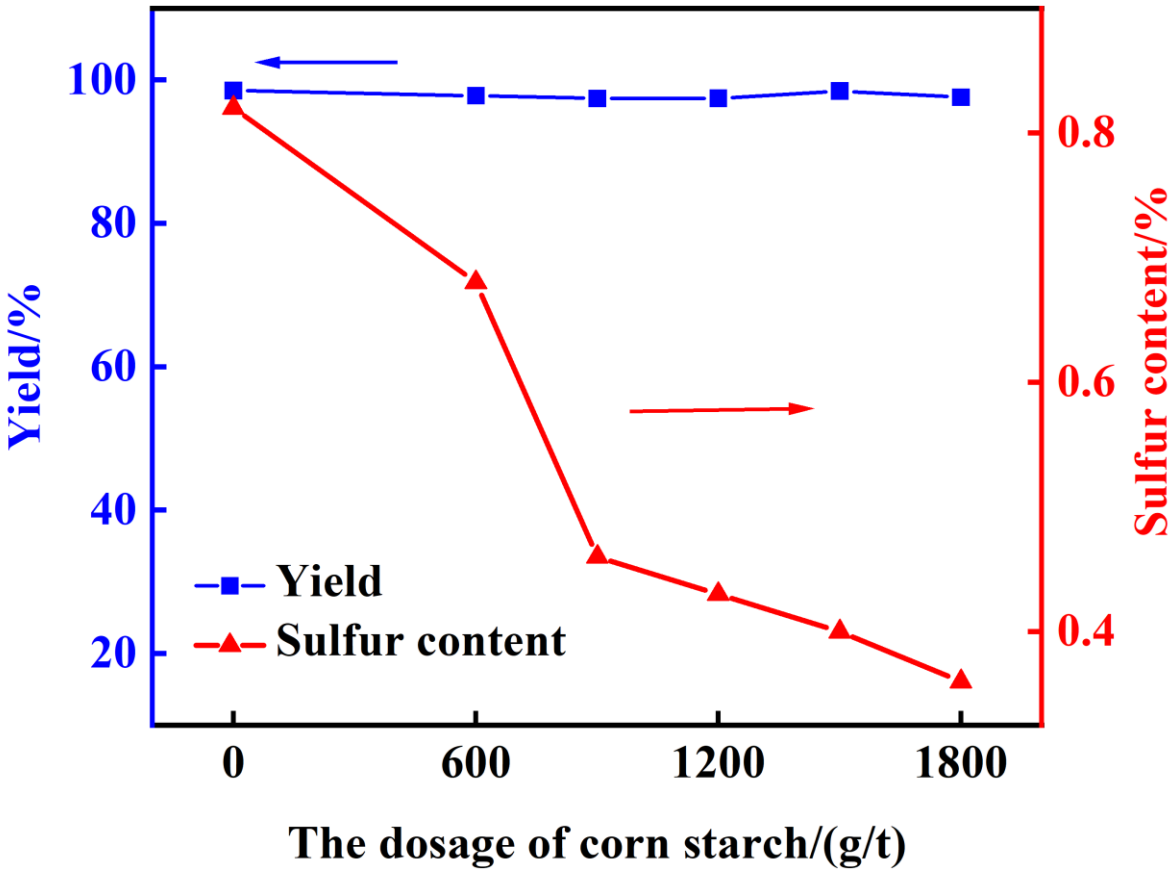


Figure 5.9 The flotation result of low oxidized coal

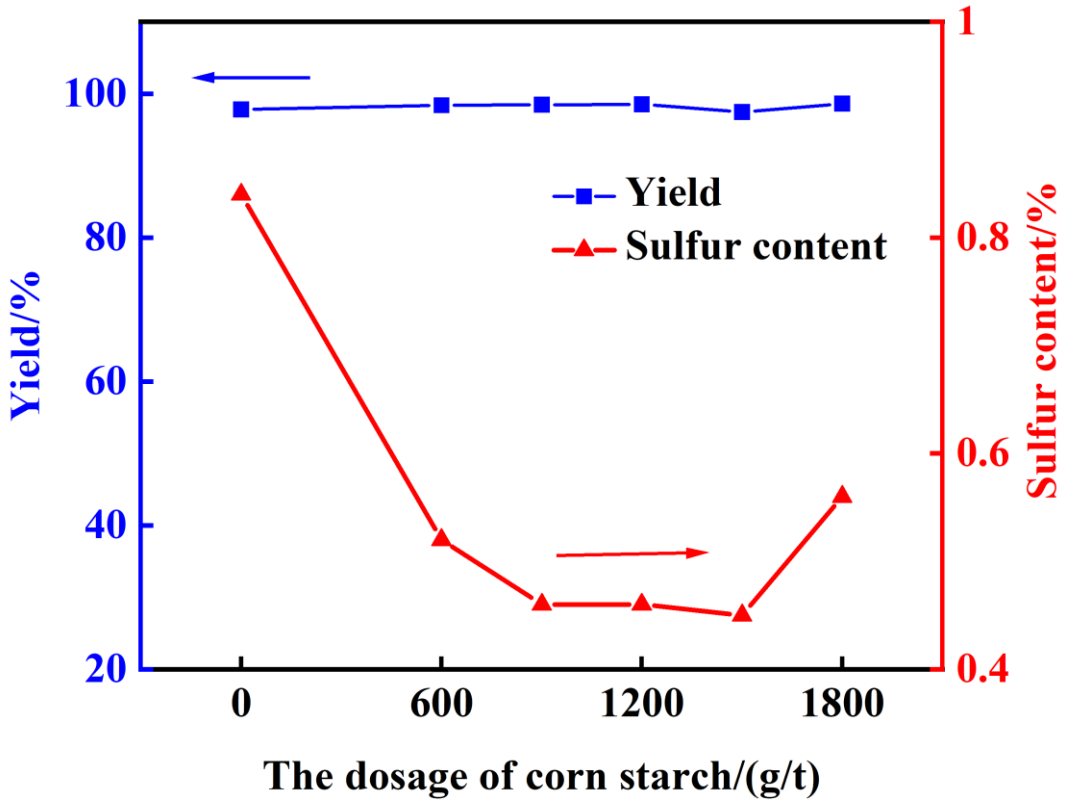


Figure 5.10 The flotation result of medium oxidized coal

The results of the low oxidized coal (L) and medium oxidized coal (M) are shown in Figure 5.9 and Figure 5.10, respectively. The yields of the low oxidized coal and the medium oxidized coal are almost the same, and the medium oxidized coal is still hydrophobic. The sulfur content of the low oxidized coal decreases from 0.82% to 0.4%. The trend of the medium oxidized coal is similar, indicating that the oxidization of the coal is not effective for distinguishing between the hydrocarbons and minerals with corn starch.

5.4 Summary

This chapter presents the results of the corn starch on the froth flotation. The main conclusions are as follows:

(1) Cooked starch is better than raw starch with regard to lowering sulfur content in the real system, demonstrating that the cooked starch could depress pyrite in real systems;

(2) Single factor experiments were conducted to investigate the effects of starch content on the recovery of pyrite. The optimal amount of starch was found to be at 1200 g/t, with the modified pH = 3, and the heated temperature of corn starch at 105℃;

(3) The Box-Behnken design (BBD) was employed to obtain optimized parameters for depressing pyrite with seventeen sets of experiments. The analyses of variance (ANOVA) illustrate that X_1 (the dosage of corn starch), X_2 (the modified pH), X_3 (heated temperature), X_1X_3 (the dosage of corn starch and heated temperature) are significant model terms, whereas X_3^2 (heated temperature) is an extremely significant model term. The F-value of 18.91 and the p-value of lower than 0.0001 imply that the model is significant;

(4) The parameters for the minimum recovery of pyrite are found to be：X_1 = 1490 g/t，X_2 = 4，X_3 = 100℃. Based on the optimized conditions, the predicted yield is 13.92%, which is in agreement with the actual yield of 14.01%;

(5) The effects of corn starch on the depressing flotation of an ideal system (TXM+pyrite) were studied with medium oxidized TXM (more hydrophilic) and low oxidized TXM (less hydrophilic). The yields of both coals were almost the same and the sulfur content of low oxidized coal decreased from 0.82% to 0.4%. The trend for the medium oxidized coal was similar, indicating that the oxidization on coal is not an effective way for distinguishing between the hydrocarbons and minerals with corn starch.

6 Results analyses III - The effect of PAC (polymeric aluminum chloride) on the flotation of pyrite and ideal system TXM + pyrite

Different from corn starch depressing pyrite in alkaline conditioned with Calcium oxide, the acidic conditions adjusted with H_2SO_4 will also be studied with PAC in this chapter. Early studies have shown that when the initial pH is lower than 5.0, the initial hydrolysates of PAC are positive hydrolysates such as $Al(OH)^{2+}$, $Al(OH)_2^{+}$, $Al_2(OH)_2^{4+}$, and $Al_3(OH)_4^{5+}$, which are easy to neutralize the negative charge outside the colloid and further damage the stability of the colloid. The reagent conditions, equipment parameters and pulp concentration of flotation etc. are determined in detail. The Box-Behnken design (BBD) described in chapter 5 is employed to obtain optimized parameters for the dosage of PAC, pH of the flotation slurry, and the concentration of PAC. The effect of PAC on the depressing flotation of ideal system (TXM + pyrite) is studied with both the medium oxidized TXM and low oxidized TXM.

The solution pH is expected to have a significant effect on the species transformation of PAC[172-174]. Zhang et al. [175] found that hydrolytic aluminum species appeared quickly after mixing with water and PAC could rapidly form dissolved aluminum species or precipitates. And the effect of solution pH on the PAC depression will be significantly focused in this study.

6.1 Box-Behnken design of the effect of PAC on the recovery of pyrite

6.1.1 Single-parameter experiments

Single-factor experiments were designed to investigate the effect of the dosage of PAC on the recovery of pyrite. A pH of 3 was set for the flotation slurry adjusted with sulfuric acid (H_2SO_4). The concentration of PAC was set for 100 ml water per 1 g PAC. The dosages of PAC were 0, 100,

200, 300 and 400 mg/L, respectively. The pyrite was first ultrasonically treated for 15 min. For all the flotation tests, the agitation speed of the impeller was kept at 2200 r/min, and the dosages of MEC and DL-2-Octanol were maintained respectively at 2000 g/t and 500 g/t dry feeding pyrite. The pre-conditioning of the pulp was carried out under stirring at 2200 r/min for two minutes. The sample was then conditioned with the PAC for three minutes. Then the MEC and DL-2-Octanol were injected for 3 min, 0.5 min, respectively. The aeration rate was set to 0.1 $m^3/m^2/min$.

Figure 6.1 shows the effect of dosage of PAC on the pyrite recovery. It could be concluded that the optimal amount of PAC is 300 mg /L, and this dosage of PAC was used in the subsequent experiments.

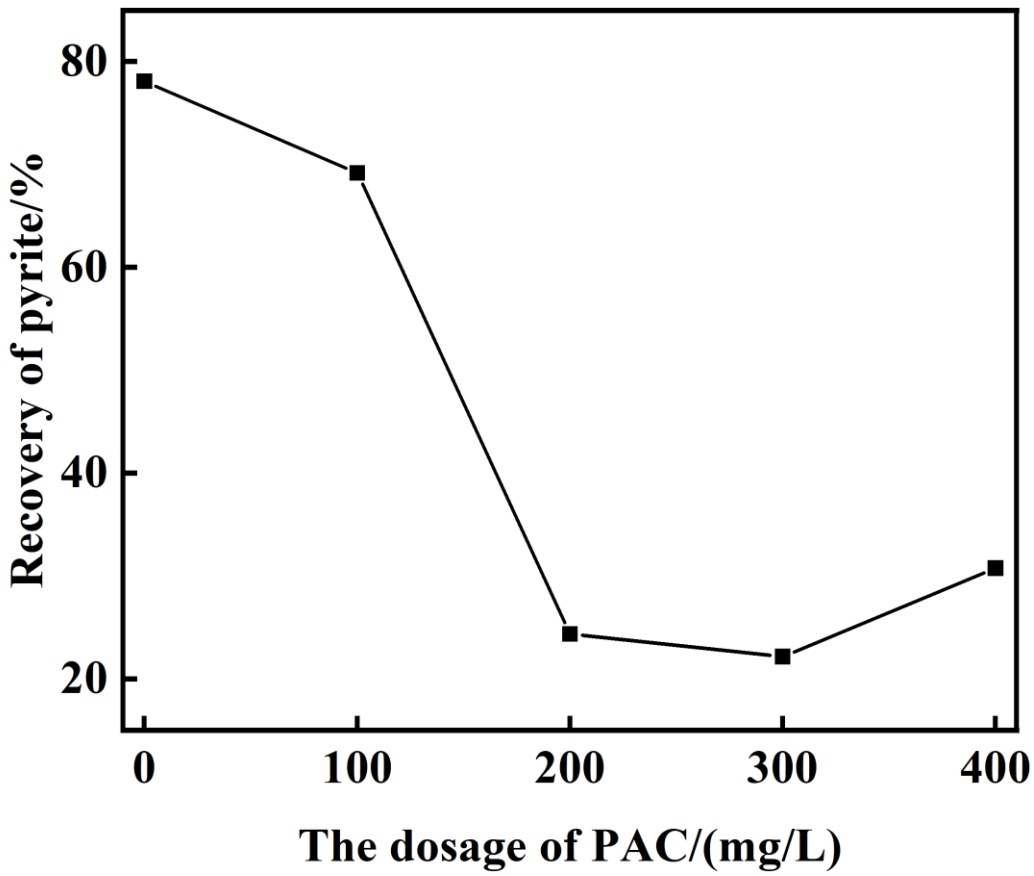


Figure 6.1 Effect of the dosage of PAC on pyrite depression

Single-factor experiments were then designed to investigate the effect of pH of the flotation slurry on the recovery of pyrite. The dosage of PAC was set as 300 mg /L as discussed above. The concentration of PAC was set as 100 ml water per 1 g PAC. The pH values of the flotation slurry were 3, 5, 7, 9 and 11. Other conditions were kept the same as the dosage of PAC experiments above. Figure 6.2 shows the results of the pyrite recovery with the changing of the slurry pH. One can see an optimal pH = 3 from the figure under the conditions of this study. As a result, the dosage of PAC was set as 300 mg /L and the pH = 3 in the subsequent experiments.

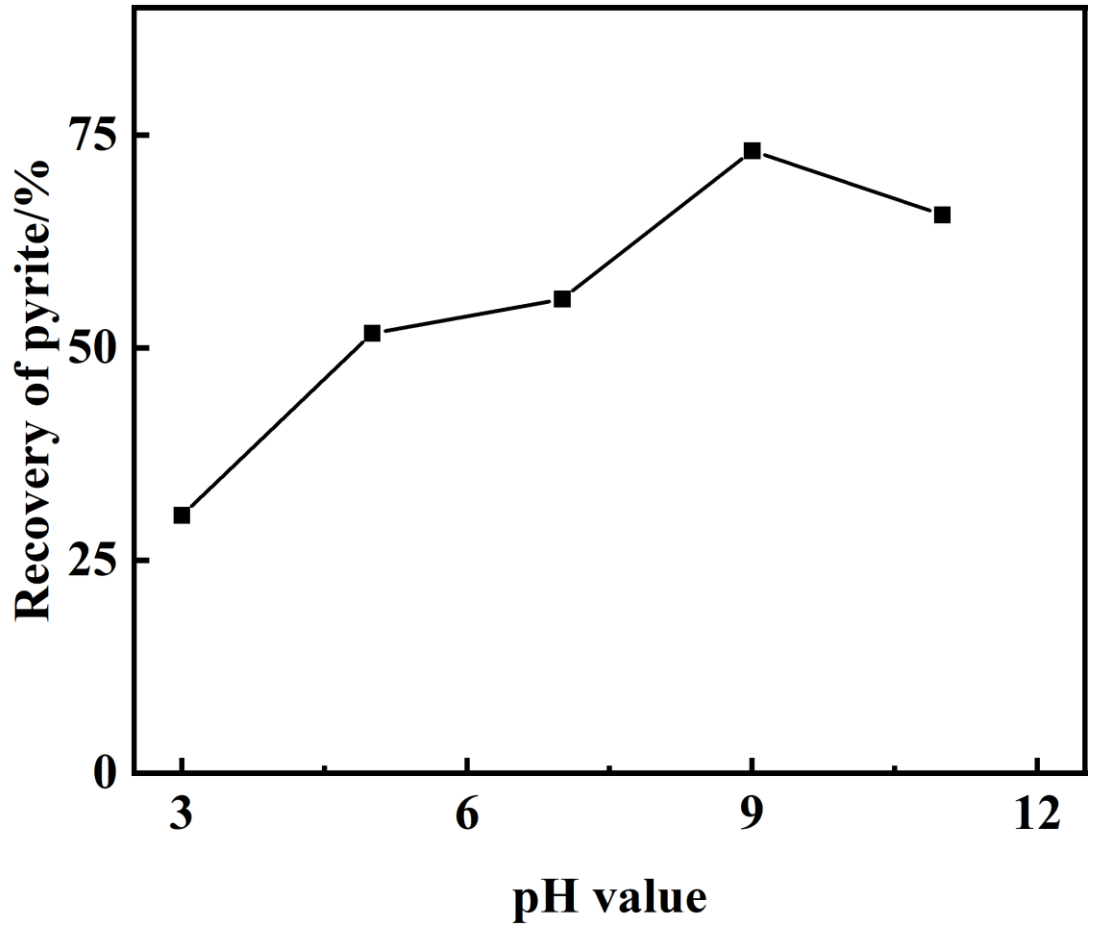


Figure 6.2 Effect of the pH of the flotation slurry on pyrite depression

Single-factor experiments were also designed to investigate the effect of the concentration of PAC on the recovery of pyrite. In this set of experiments, the pH of the flotation slurry was pH = 3, the dosage of PAC was 300 mg /L, and the concentrations of PAC varied to give 25 ml water, 50 ml water, 75 ml water, 100 ml water and 125 ml water per 1 g PAC. Other conditions remained the same as that in previous experiments. Figure 6.3 shows the results. One can see clearly the optimal concentration of PAC at 125 ml water per 1 g PAC.

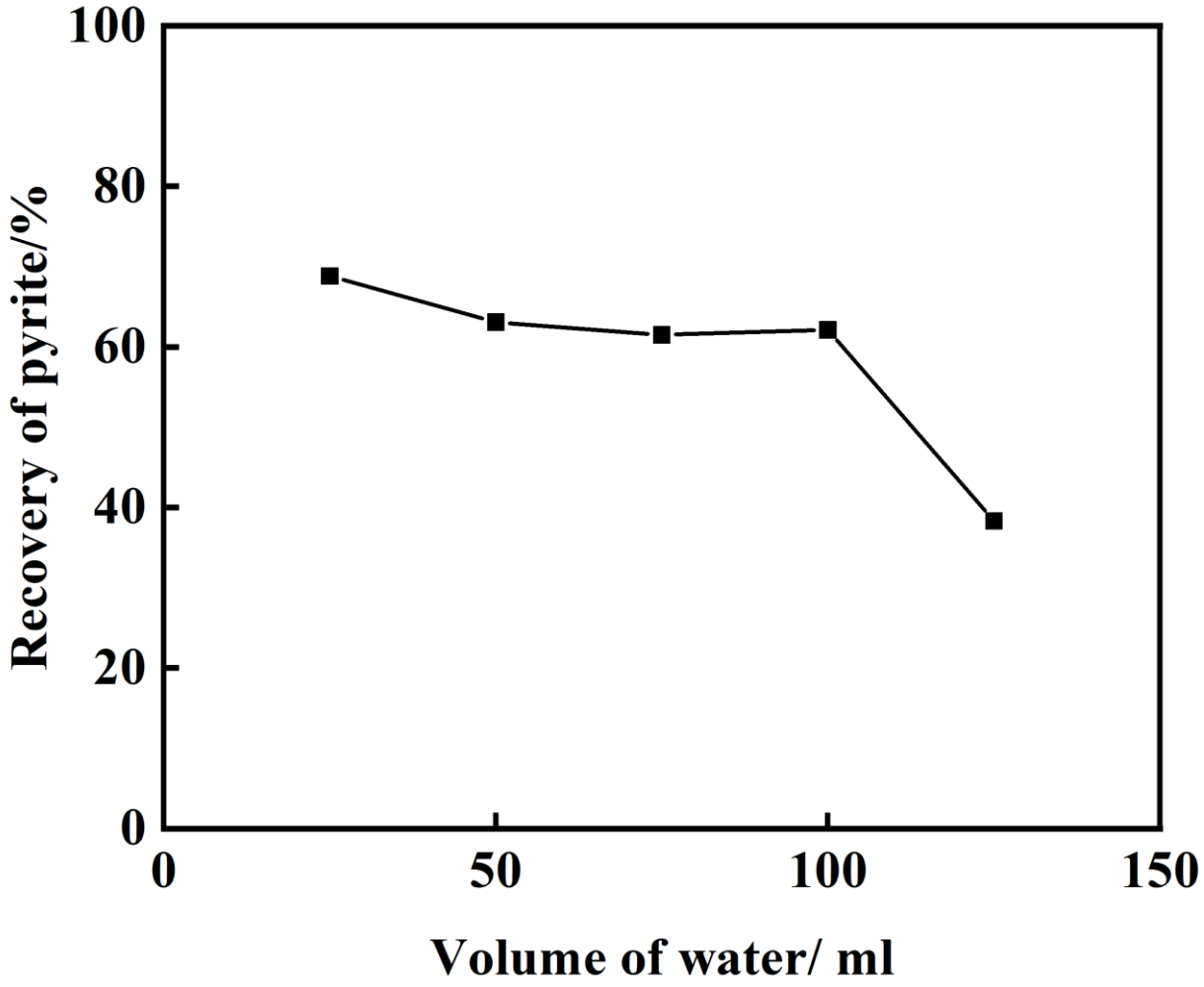


Figure 6.3 Effect of the water dilution of PAC on pyrite depression

6.1.2 Box-Behnken experimental design

The effect of the dosage of PAC, the pH of flotation slurry, and water dilution were investigated using the BBD method. Table 6.1 shows the selected experimental range for each of the parameters, and Table 6.2 gives the BBD plans. One can see seventeen sets of experiments on the single parameters and their interactions on the responses.

Table 6.1 Experimental ranges and factor levels of different variables in the experimental design

Actual parameters	Unit	Code parameters	Level		
			-1	0	1
The dosage of PAC	mg/L	X_1	200	300	400
pH of flotation slurry	-	X_2	5	3	7
Concentration of PAC	mL/g	X_3	75	125	100

Table 6.2 Experimental runs suggested by BBD

Run	Dosage of PAC	pH value	Concentration of PAC
	mg/L(X_1)	(X_2)	mL/g(X_3)
1	-1	0	1
2	1	-1	0
3	-1	1	0
4	0	-1	-1
5	-1	0	-1
6	1	0	-1
7	1	1	0
8	1	0	1
9	-1	-1	0
10	0	1	-1
11	0	-1	1
12	0	1	1
13	0	0	0
14	0	0	0
15	0	0	0
16	0	0	0
17	0	0	0

6.1.3 Statistical analysis

6.1.3.1 Results

The experimental results, together with the predicted responses related to the pyrite recovery are shown in Table 6.3. There are 17 sets of experiments with 12 sets being factorial tests, corresponding to the factorial points. The rest five sets are central tests corresponding to the zero points, which are used to estimate the error.

6.1.3.2 The analysis of variance (ANOVA)

The results of the ANOVA are presented in Table 6.4. As can be seen, X_2^2 (pH of flotation slurry), $X_1^2X_3$ and X_1X_3 (the dosage of PAC and concentration of PAC) are all significant model terms, whereas X_3^2 (concentration of PAC) and $X_1X_2^2$ (the dosage of PAC and pH of flotation slurry) are extremely effective model terms. The linear term of X_2 (pH of flotation slurry) and X_3 (concentration of PAC) are not significant for the pyrite recovery, and the interaction parameters of X_1X_2 (the dosage of PAC and pH of flotation slurry) and the quadratic parameters of X_1^2 are not significant either for the pyrite recovery. The F-value of 5.69 and p-value of 0.0227 imply that the model is significant. Therefore, the correlations can be in good agreement with the experimental results.

The lack of fit p-value of the pyrite recovery is 0.8557, which is not significant, whereas the "Lack of Fit F-value" of 0.16 means the Lack of Fit is not significant relative to the pure error.

Table 6.3 Experimental design and results with response surface method of pyrite sample

Run	Dosage of PAC	pH value	Concentration of PAC	Recovery/ %	
	mg/L(X_1)	X_2	mL/g(X_3)	Actual value	Predicted Value
1	-1	0	1	57.42	57.42
2	1	-1	0	54.25	52.43
3	-1	1	0	29.67	31.49
4	0	-1	-1	55.49	56.31
5	-1	0	-1	63.83	63.83
6	1	0	-1	65.28	65.28
7	1	1	0	56.5	58.32
8	1	0	1	20.83	20.83
9	-1	-1	0	38.23	36.41
10	0	1	-1	57.61	56.79
11	0	-1	1	56.05	58.86
12	0	1	1	62.16	59.34
13	0	0	0	31.72	29.59
14	0	0	0	29.42	29.59
15	0	0	0	30.05	29.59
16	0	0	0	33.94	29.59
17	0	0	0	34.83	29.59

Table 6.4 ANOVA results for developed models for recovery of pyrite

Resource	Degree of freedom df	Regression model			
		Sum of Squares	Mean Square	F Value	P Value
X_1	1	308.7	308.7	4.57	0.0765
X_2	1	0.46	0.46	6.82E-03	0.9369
X_3	1	6.53	6.53	0.097	0.7665
X_1X_2	1	29.21	29.21	0.43	0.5353
X_1X_3	1	361.76	361.76	5.35	0.06
X_1^2	1	86.84	86.84	1.28	0.3003
X_2^2	1	466.78	466.78	6.9	0.0392
X_3^2	1	1320.08	1320.08	19.53	0.0045
$X_1^2X_3$	1	391.58	391.58	5.79	0.0528
$X_1X_2^2$	1	760.31	760.31	11.25	0.0154
Model	10	3845.19	384.52	5.69	0.0227
Residual	6	405.64	55.61	-	-
Lack of fit	2	30.41	15.2	0.16	0.8557
Pure Error	4	375.24	29.52	-	-
Cor Total	16	4250.83	-	-	-

6.1.3.3 Interactions between different operating parameters

The contour map can directly reflect the influences of various factors on the responses, and interactions among optimal process parameters. The center point of the smallest ellipse in the contour map is the extreme point of the response surface. The contour map can also indicate the interactions between factors. The closer to the ellipse, the more significant the interactions. The surface graph is a three-dimensional space composed of response values and factors. When the surface is shaped like a valley, a minimum value exists, whereas a maximum value occurs when the surface is mountain-shaped[176].

The response surface diagrams of the interactions between the dosage of PAC, the pH value of flotation slurry, and the concentration of PAC are shown in Figure 6.4 and Figure 6.5.

The impact of the dosage of PAC and the pH of flotation slurry on the recovery of pyrite are demonstrated in Figure 6.4. As can be observed, the increasing dosage of PAC in a low pH of flotation slurry reduces the recovery of pyrite first but a further increase of the pH value of flotation slurry beyond a certain limit leads to an increase in the recovery of pyrite. This trend can be attributed to the opposite effect of dosage of PAC on the recovery of pyrite.

The impacts of the dosage of PAC and the concentration of PAC on the recovery of pyrite are demonstrated in Figure 6.5. An increasing concentration of PAC at a low dosage of PAC reduces the recovery of pyrite first but a further increase in the concentration of PAC leads to a sharp increase in the recovery of pyrite, which is because of the opposite effect of the concentration of PAC on the recovery of pyrite. The results suggest that the influence of the concentration of PAC on the pyrite recovery is more significant than that of the dosage of PAC or that of the pH of flotation slurry.

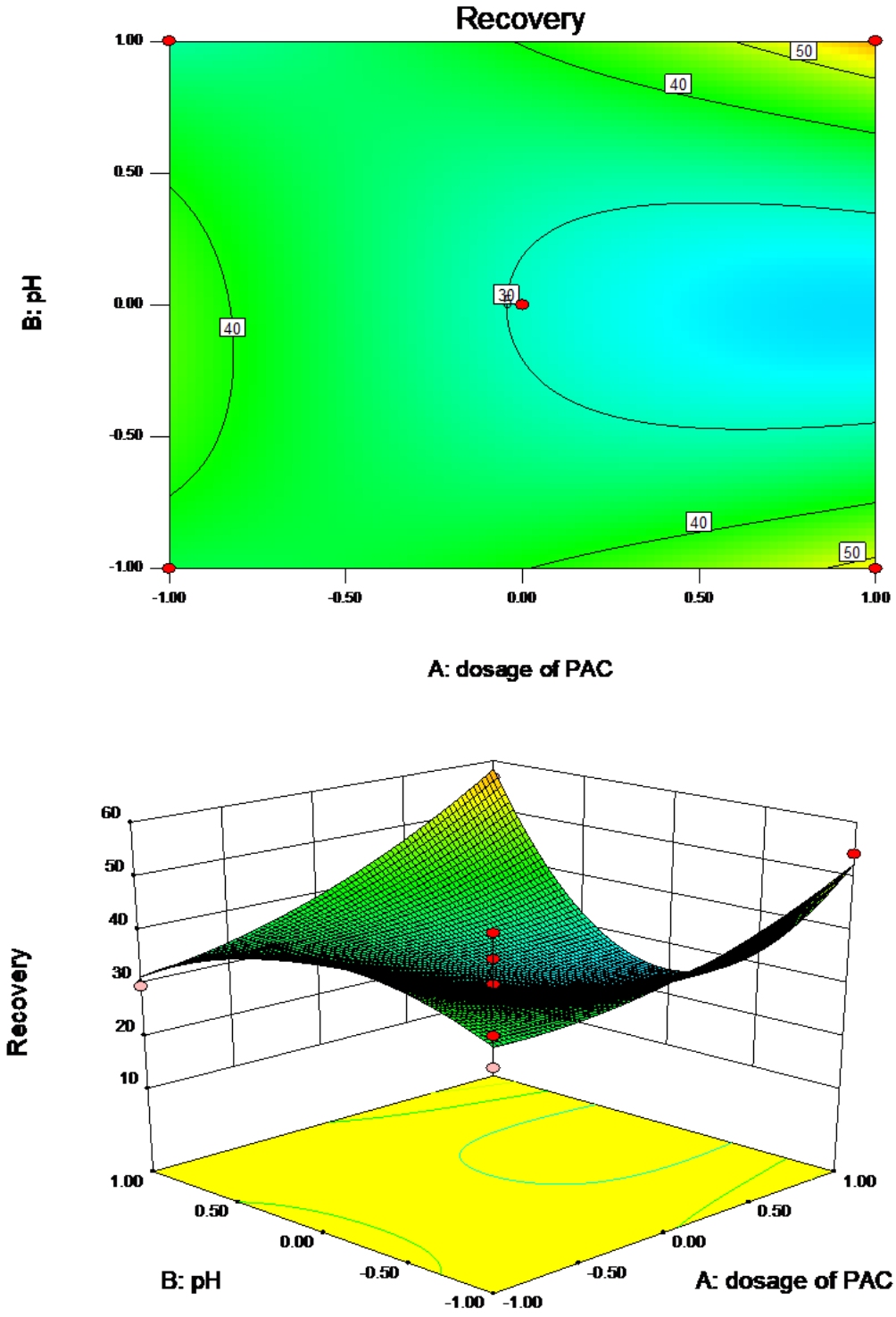


Figure 6.4 The recovery of pyrite as a function of (a) the dosage of PAC and (b) pH of flotation slurry

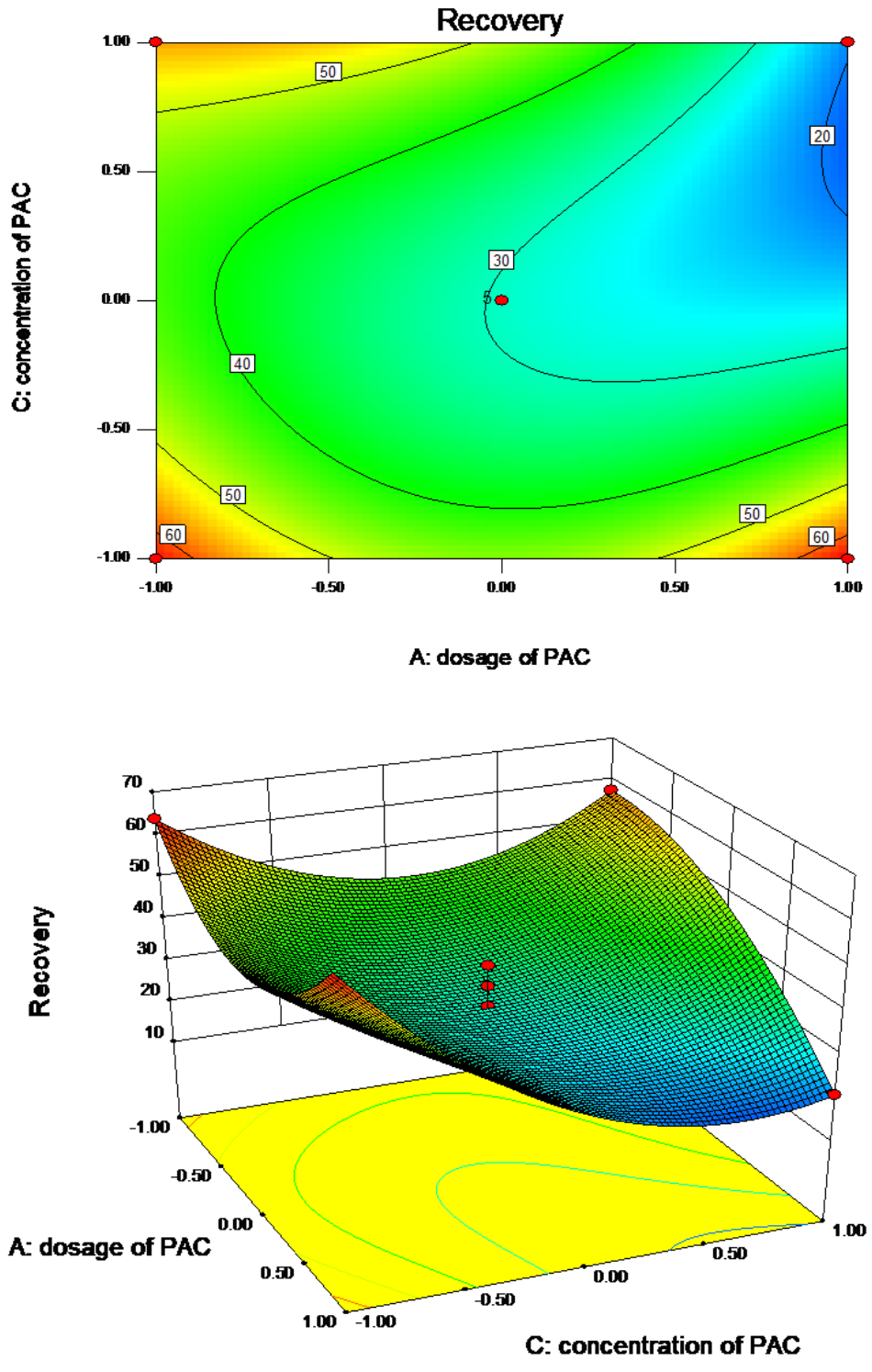


Figure 6.5 The recovery of pyrite as function of (a) the dosage of PAC and (c) the concentration of PAC

6.1.3.4 Multi-objective optimization for the recovery of pyrite considering different parameters

The optimization, as discussed in Chapter 5, is a numerical method based on the 'desirability method'. For optimization, the minimum recovery of pyrite (Y) was selected for each of the responses and as the input parameters. The studied response parameters for the best pyrite recovery were: X_1 = 400 mg/L, X_2 = 3.1, and X_3 = 110 mL/g. Due to the limitation of the equipment in the actual experiments, the above parameters were optimized to give X_1 = 400 mg/L, X_2 = 3, and X_3 = 110 mL/g. According to the optimized conditions, the predicted yield was 18.3%, which compared well with the actual yield of 18.64%.

6.2 The effect of PAC on depressing flotation of an ideal system of TXM+pyrite

In this set of studies, the pH of flotation slurry was pH = 3 adjusted with sulfuric acid (H_2SO_4). The concentration of PAC was 110 mL water per 1 g PAC, and the concentration of the pulp was 100 g/L. The dosages of PAC were set to vary at different concentrations of 100 mg/L, 200 mg/L, 300 mg/L, 400 mg/L and 500 mg/L. For all the flotation tests, the agitation speed of the impeller was kept at 2200 r/min and the dosages of MEC and DL-2-Octanol were maintained at 2000 g/t and 600 g/t dry feeding. The pre-conditioning of the pulp was carried out under stirring at 2200 r/min for two minutes. After this process, the sample was conditioned with corn starch for three minutes. Then MEC and DL-2-Octanol were injected for 3 min, and 0.5 min, respectively. The aeration rate was set to 0.2 $m^3/m^2/min$. The flotation concentrate product was collected until there was no froth product left in the flotation cell.

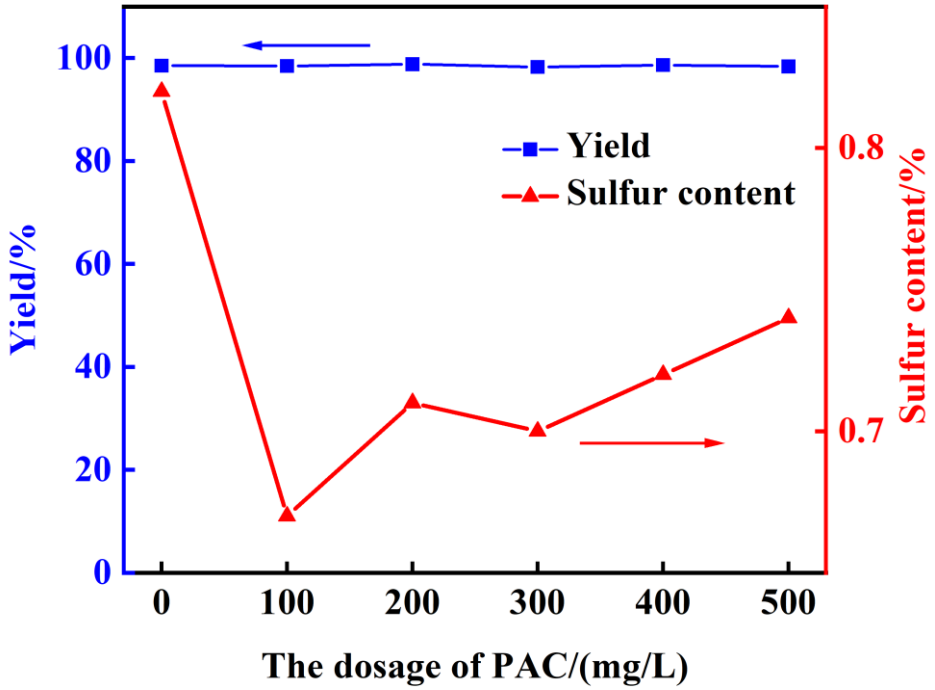


Figure 6.6 The effects of the dosage of PAC on the flotation result of low oxidized coal

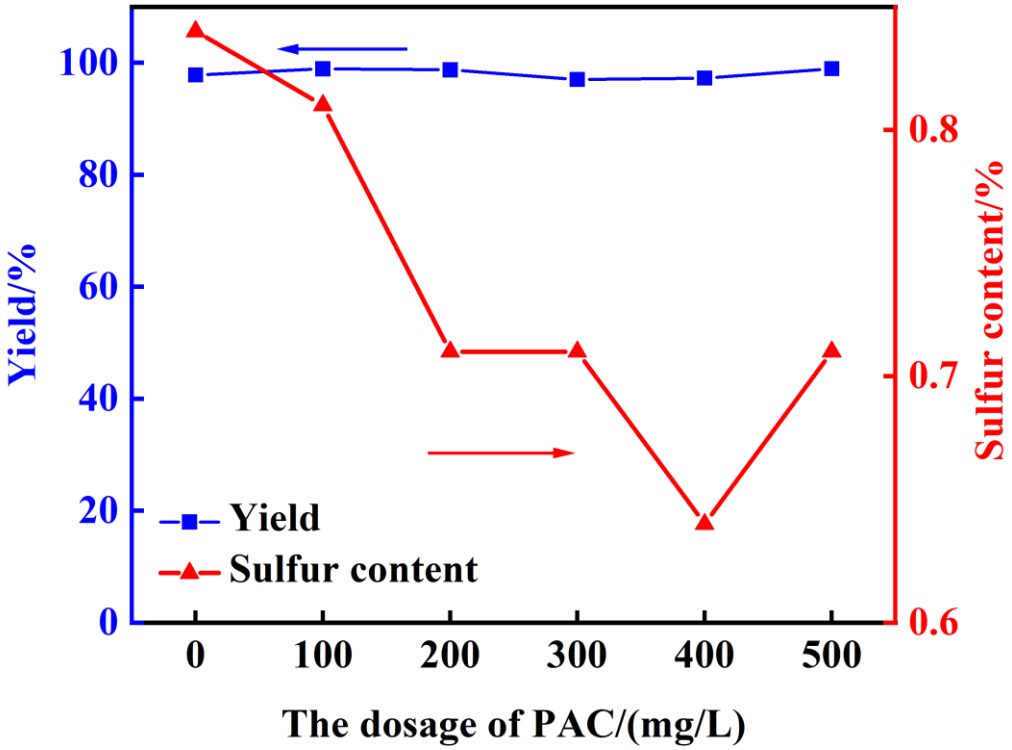


Figure 6.7 The effects of the dosage of PAC on the flotation result of medium oxidized coal

Figure 6.6 and Figure 6.7 show the results with the low oxidized coal (L) and medium oxidized coal (M). The two coals were prepared using the same method as explained in Chapter 5. The yields of the low oxidized coal and the medium oxidized coal are almost the same, and the medium oxidized coal is still hydrophobic. The sulfur content of the low oxidized coal is seen to decrease from 0.82% to 0.67%, and the trend for the medium oxidized coal is similar, indicating that the oxidization on coal is not an effective measure for distinguishing between the hydrocarbons and minerals with PAC.

6.3 Summary of the chapter 6

This chapter presents and discusses the results of the use of PAC for depressing the pyrite recovery. The following are main observations:

(1) Single-factor experiments were conducted to investigate the effects of PAC on the recovery of pyrite. The optimal dosage of PAC was 300 mg /L, the pH of the flotation slurry was pH = 3, and the concentration of PAC was 125 ml water per 1 g PAC;

(2) The Box-Behnken design (BBD) was employed to obtain optimized parameters for depressing pyrite with seventeen sets of experiments. The analyses of variance (ANOVA) illustrated that X_2^2 (pH of flotation slurry), $X_1^2X_3$ and X_1X_3 (the dosage of PAC and concentration of PAC) were all significant model terms, whereas X_3^2 (concentration of PAC) and $X_1X_2^2$ (the dosage of PAC and pH of flotation slurry) were extremely effective model terms. The F-value of 5.69 and p-value of lower than 0.05 implied that the model was significant;

(3) The parameters for the minimum recovery of pyrite were focused to be：X_1 = 400 mg/L，X_2 = 3，X_3 = 110 mL/g. According to the optimized conditions, the predicted yield of 18.3% compared well with the actual yield of 18.64%;

(4) The effects of PAC on depressing flotation of an ideal system (TXM+pyrite) were studied with the medium oxidized TXM (more hydrophilic) and the low oxidized TXM (less hydrophilic). The yields of both coals were almost the same (nearly 99%) and the sulfur content of low oxidized coal was found to decrease from 0.82% to 0.67%, and the trend for the medium oxidized coal was similar, indicating that the oxidization on coal was not effective for distinguishing between the hydrocarbons and minerals with PAC.

7 Results analyses IV-The properties of depressants and interactions with pyrite

In this chapter, Zeta potential method and contact angle from the macro-perspective point of view, XPS (X-ray photoelectron spectroscopy) and FT-IR methods from the microcosmic viewpoint are used to study the interactions of pyrite with depressants for explaining the more hydrophilic properties in flotation. Zeta potential of pyrite samples was treated with different dosages of corn starch and PAC with an electrophoresis method. The hydrophobicity of the samples treated with different amounts of corn starch and PAC was calculated using the contact angle analyses. The X-ray photoelectron spectroscopy (XPS) was used to study the elemental compositions and chemical states without and with corn starch and PAC for physical or chemical adsorption. The surface functional groups were characterized by FT-IR to identify surface chemistry changes without and with corn starch and PAC.

7.1 Zeta potential of pyrite with depressants

The Zeta potential (ζ-potential) of coal particles was measured using the electrophoresis method. In a typical measurement, approximately 30 mg pyrite was transferred to a 30 mL potassium chloride solution (1×10^{-2} M) in a container with a stirrer. The mixture was stirred, at 800 rpm for three minutes, and different dosages of PAC or corn starch were then added with another 5 min agitation, respectively. 1 mL suspension was transported into a tube, and the electrophoretic features were measured with the potential Analyzer (NanoBrook ZetaPALS, Brookhaven, US). This device uses a laser with a wavelength of 633 nm to detect the scattered light at an angle of 90º. All measurements were conducted at the room temperature. For each suspension, ten measurements were conducted, and the mean value was used for the analyses.

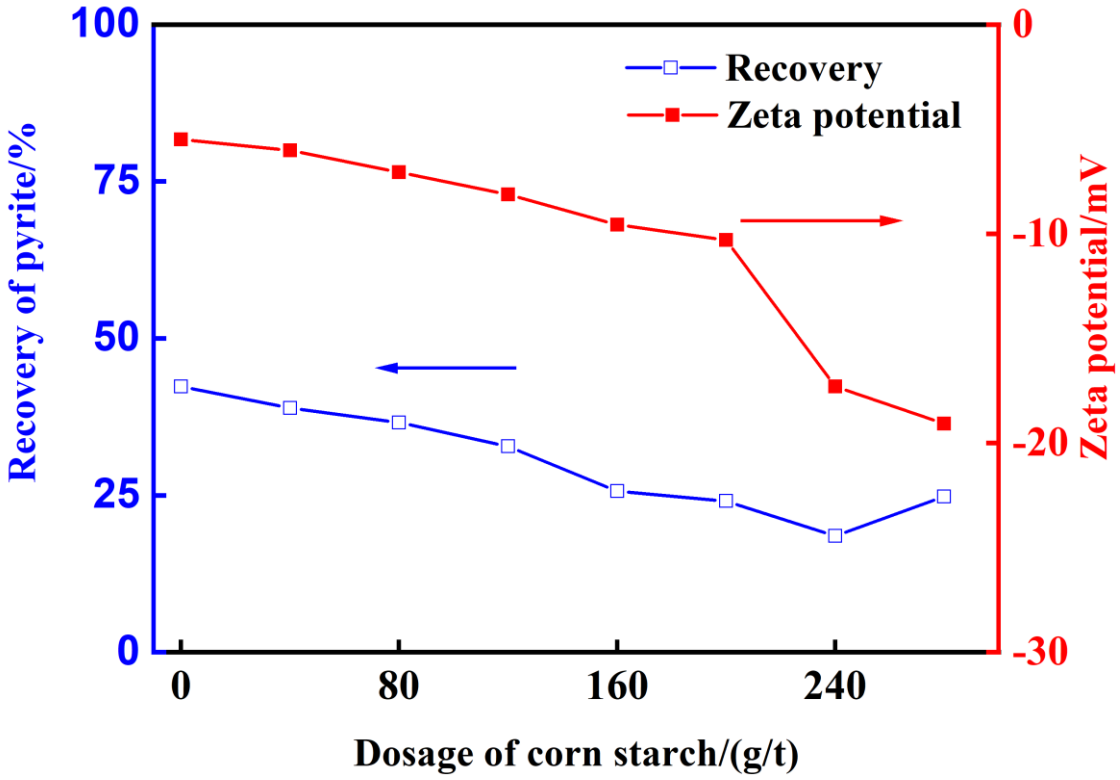


Figure 7.1 Zeta potential and the recovery of pyrite as a function of corn starch concentration at pH = 11

Figure 7.1 and Figure 7.2 show the results of Zeta potential for corn starch and PAC, respectively. The zeta potential as a function of corn starch concentration shows a steady increase in negative values at the starch concentration below ~ 200 g/t, beyond which a sharp increase occurs.

According to the EDLVO theory[177], the electric double layer interaction between particles due to particle surface charges (determined by zeta potential) plays an important role in the dispersion of fine particle. The increasing in negative ζ potential increases the energy barrier[178], which prevents the particles from agglomerating and disperses the fine particles due to the corn starch adsorbing chemically on pyrite surface. It will be further verified by FT-IR and XPS analyses in this chapter.

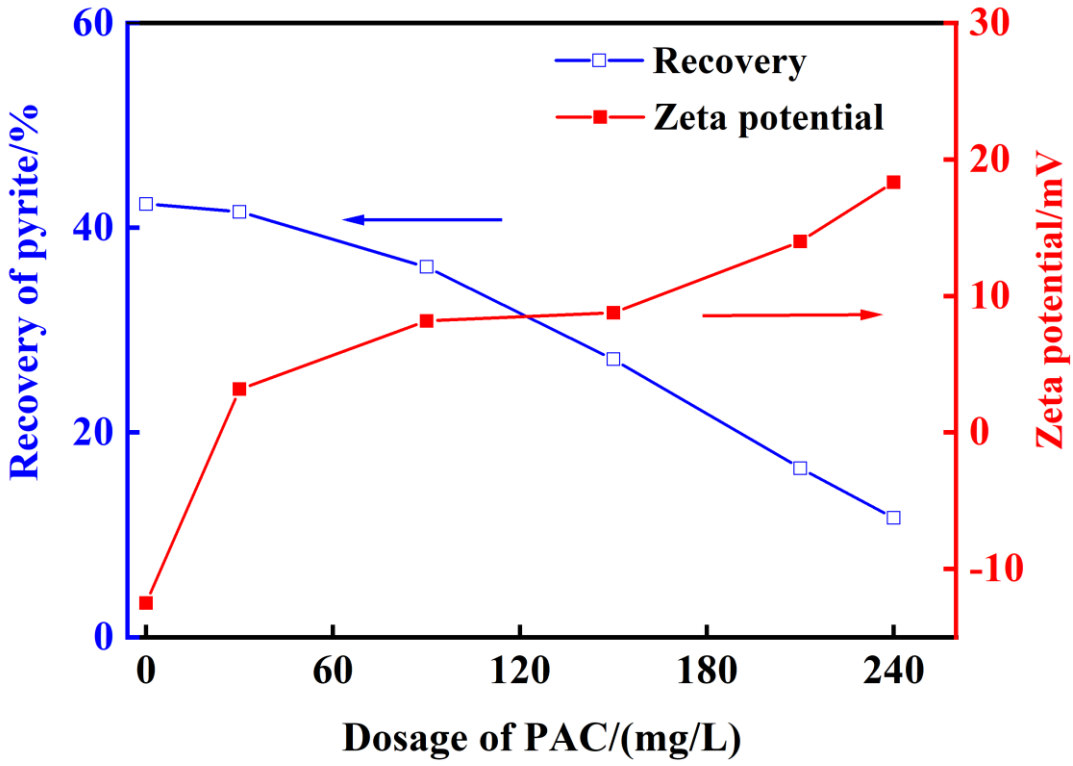


Figure 7.2 Zeta potential and recovery of pyrite with the changing of PAC concentrations at pH=3

The Zeta potential in the presence of PAC (Figure 7.2) shows an increasing trend from negative at zero PAC to positive, and reaches ~ 20 mV at 240 mg/L PAC. As is shown, the main monomer forms of $AlCl_3$ in PAC solution being $Al(OH)_2^+$, $Al(OH)^{2+}$, $Al_3(OH)_4^{5+}$, $Al_2(OH)_2^{4+}$ [99][175] [179][at pH below 5, the increase of potential values indicates the increased adsorption of these positive ions on the surface of pyrite. The adsorption of these ions can lead to an increase in the zeta potential with increasing dosages of PAC. The particles are therefore more hydrophilic and dispersed in the slurry with PAC adsorbed on the pyrite surface.

7.2 Contact angle of pyrite treated with corn starch or PAC

As discussed in Chapter 4, particularly Eq. (4-3), the wettability and floatability of the samples treated with different ratios of corn starch or PAC can be calculated and analyzed. Figure 7.3 and Figure 7.4 show the recovery and contact angle results.

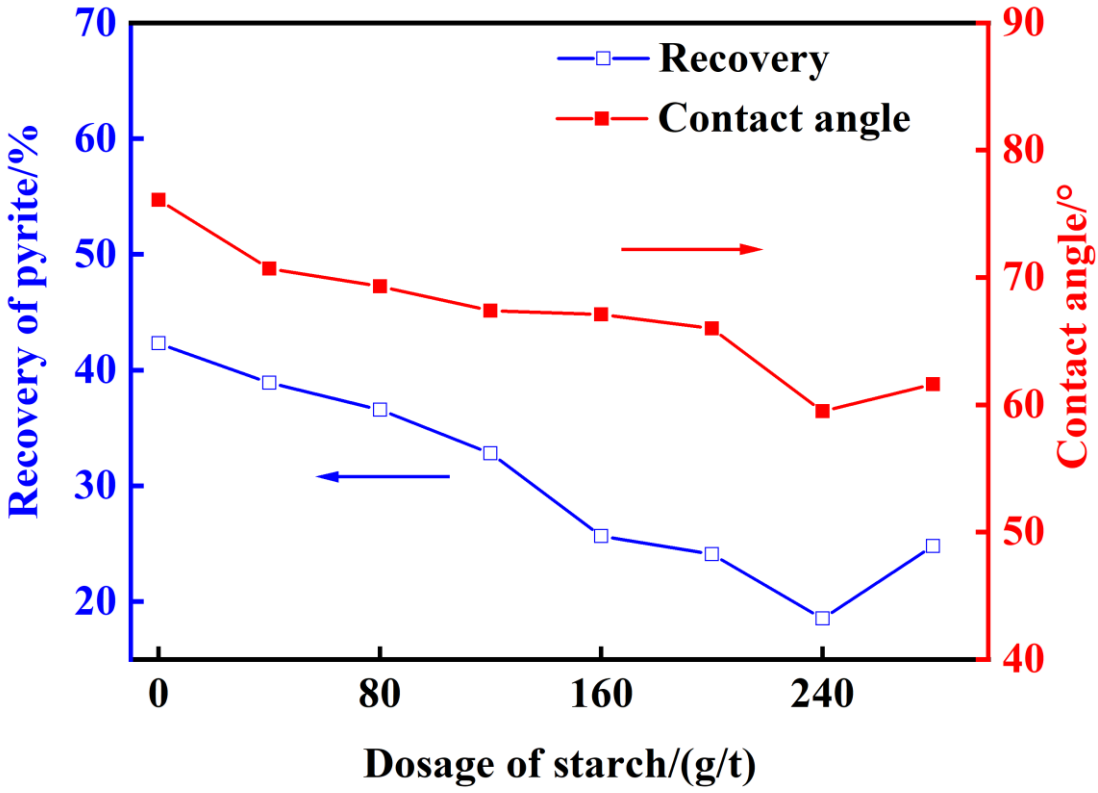


Figure 7.3 Contact angle and recovery of pyrite with the changing of corn starch concentration at pH = 11

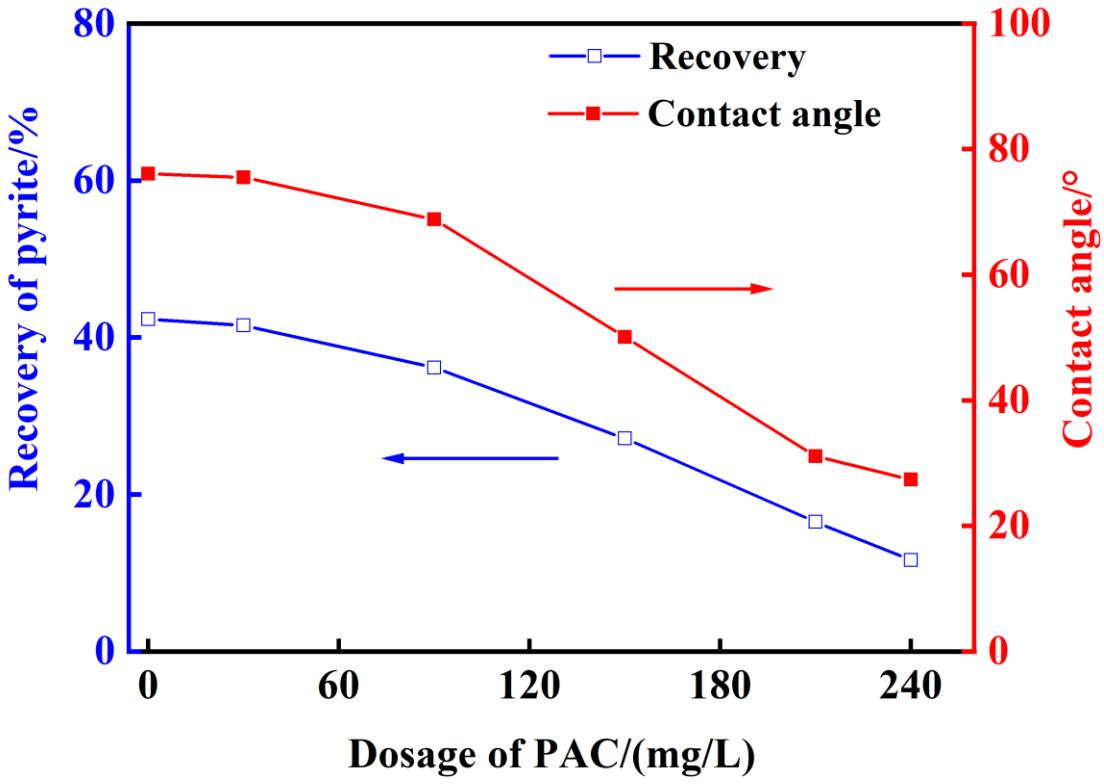


Figure 7.4 Contact angle and recovery of pyrite with the changing of PAC concentration at pH = 3

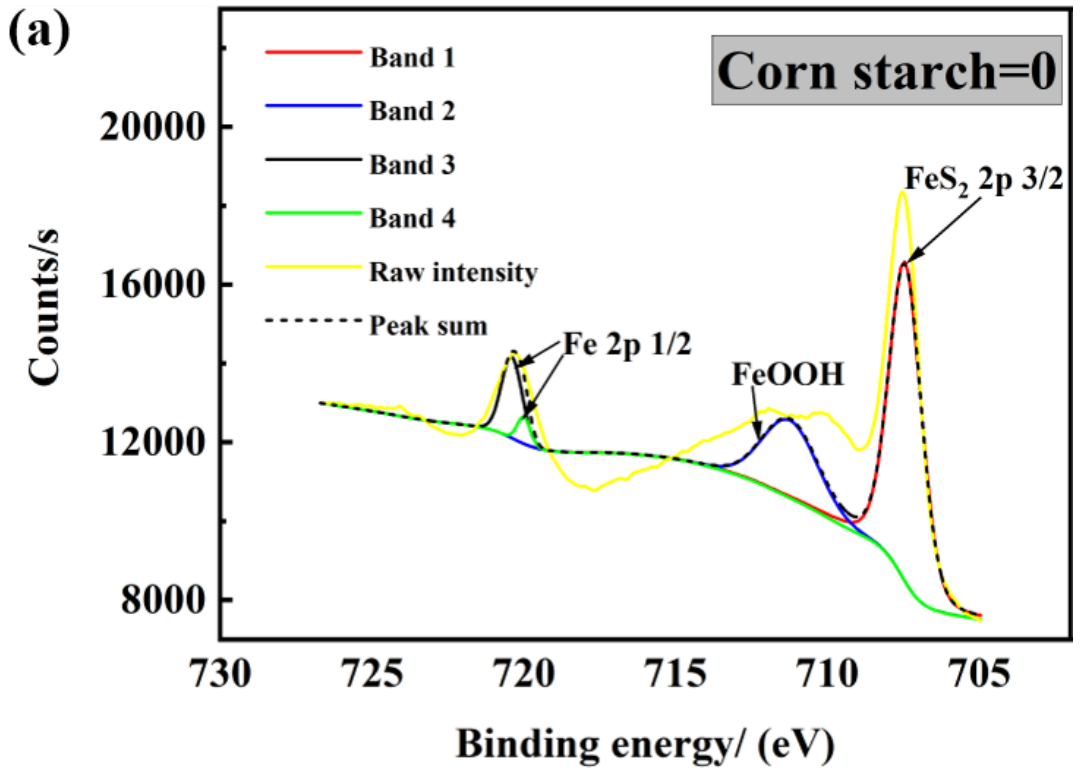
The contact angle of pure pyrite is seen to be the largest, indicating good floatability of the pure mineral. The use of starch or PAC as flotation depressants can effectively change the contact angle thus improve the hydrophilicity of the pyrite. For both starch and PAC, the pyrite with a high contact angle gives a high recovery. Figure 7.3 also shows a minimum contact angle at a dosage of 240 g/t, with the reason of the a great amount of hydrophilic site appearing with the adsorption of $Al(OH)_2^+$, $Al(OH)^{2+}$, $Al_3(OH)_4^{5+}$, and $Al_2(OH)_2^{4+}$.

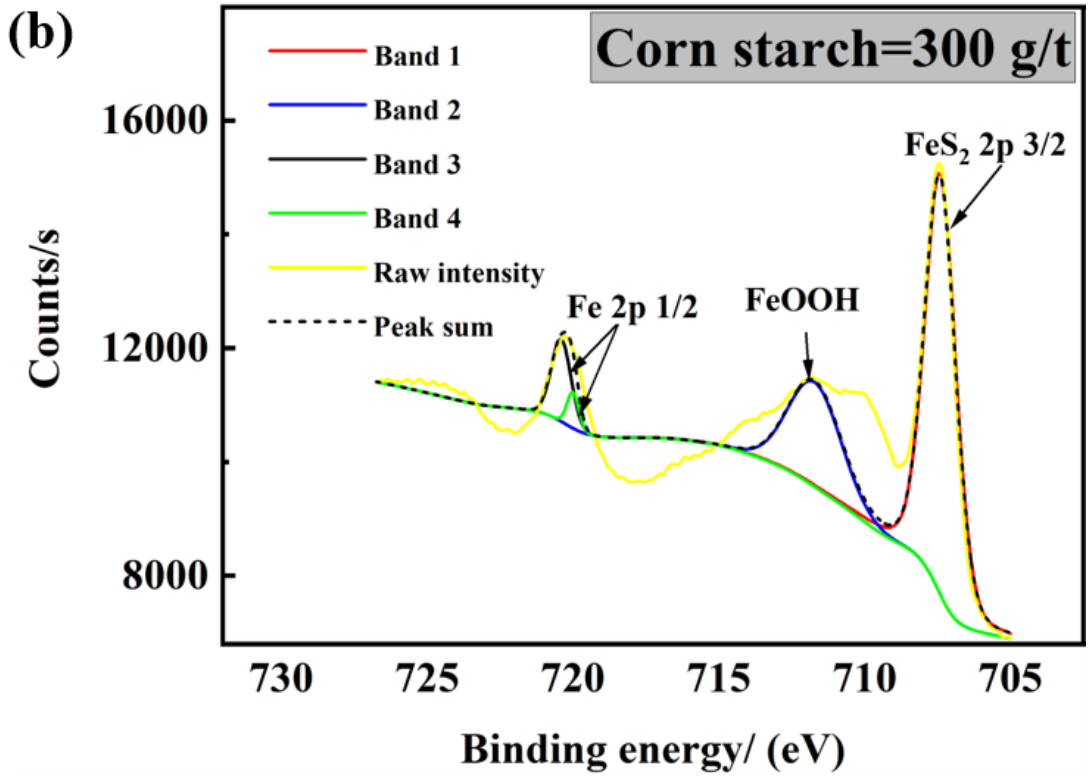
A comparison between Figure 7.3 and Figure 7.4 shows that the contact angle of pyrite with PAC is significantly lower than that with corn starch, indicating that a much more hydrophilic surface is generated with PAC.

7.3 XPS analyses of pyrite with corn starch or PAC

Figure 7.5 shows the fitting procedure of Fe(2*p*) of pyrite without and with corn starch. Samples reacted with corn starch show two distinct peaks at 707.43 eV and 711.23 eV. The former corresponds to Fe(II)-S compounds[181][182] in pyrite and the latter contributes from FeOOH($2p_{3/2}$)[193194195196]. And contribution from Fe(II)-S ($2p_{1/2}$) is around 720 eV binding energy[81]. The strength of both the ($2p_{3/2}$) and ($2p_{1/2}$) peaks of pyrite decreases after the interaction with cooked starch, indicating that pyrite chemically interacted with corn starch.

Figure 7.6 shows the fitting procedure of S(2*p*) of pyrite without and with corn starch. An examination of the mineral shows a S(2*p*) characteristic at 162.8 eV. The spectrum also has two peaks at 169.2 eV and 170.67 eV. The former is due to $S_2O_3^{2-}$ [183], and the latter is attributed to sulfate[184][185]. An identical fit to the S $2p_{3/2}$ spectra composed of disulfide S_2^{2-}($2p_{3/2}$) (S($2p_{3/2}$) = 162.8 eV), S_2^{2-} ($2p_{1/2}$) from bulk pyrite (S($2p_{1/2}$) = 163.9 eV). These results are consistent with previous literature[184-185192].


(a)
Corn starch=0
Band 1
Band 2
Band 3
Band 4
Raw intensity
Peak sum
Fe 2p 1/2
FeOOH
FeS2 2p 3/2
Counts/s
20000
16000
12000
8000
730
725
720
715
710
705
Binding energy/ (eV)


(b)
Corn starch=300 g/t
Band 1
Band 2
Band 3
Band 4
Raw intensity
Peak sum
Fe 2p 1/2
FeOOH
FeS2 2p 3/2
Counts/s
16000
12000
8000
730
725
720
715
710
705
Binding energy/ (eV)

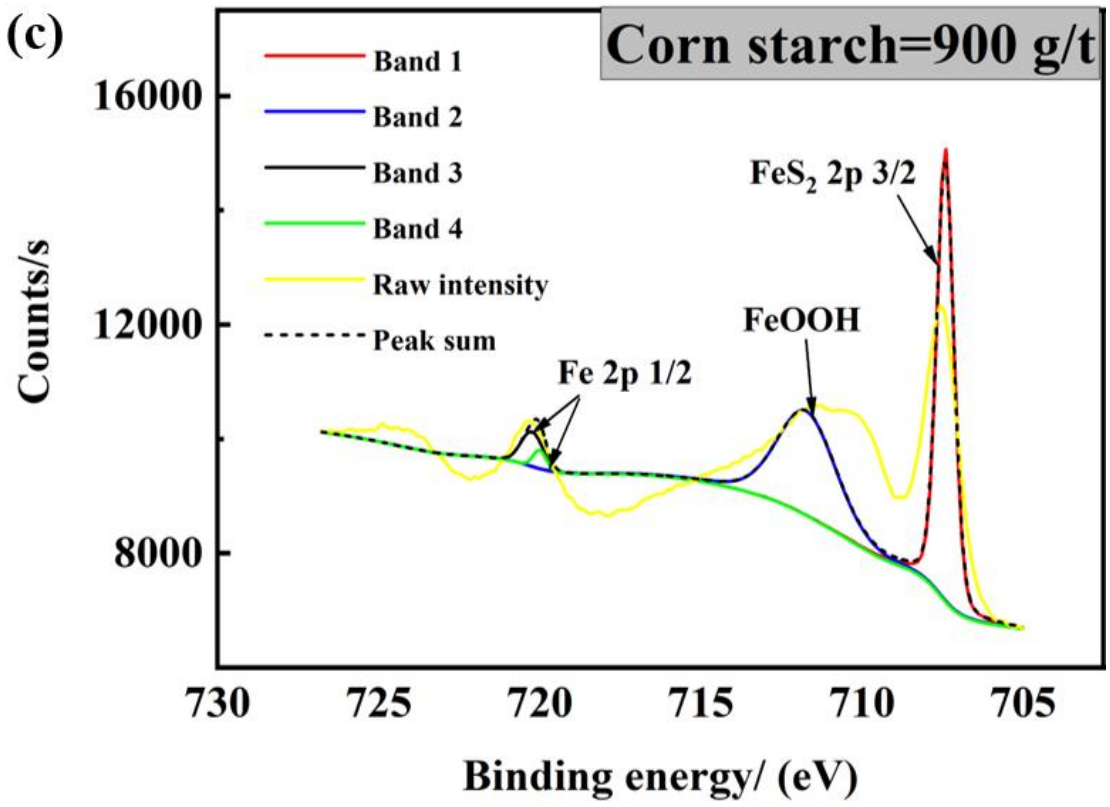
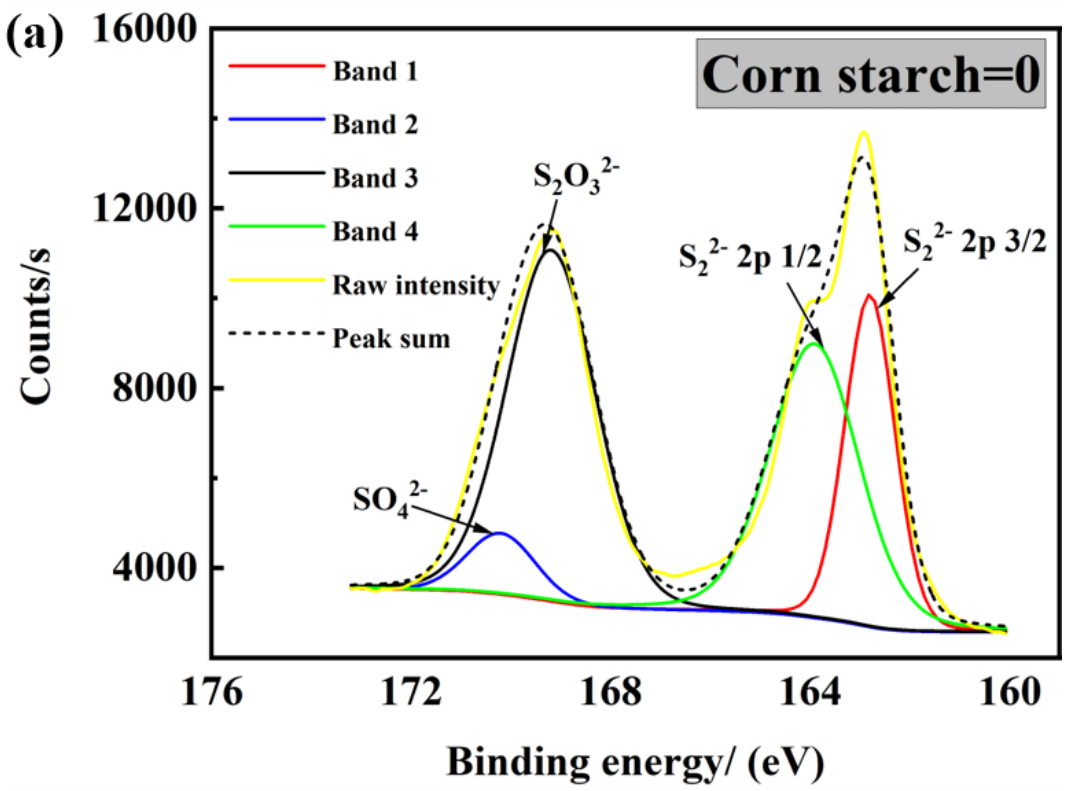
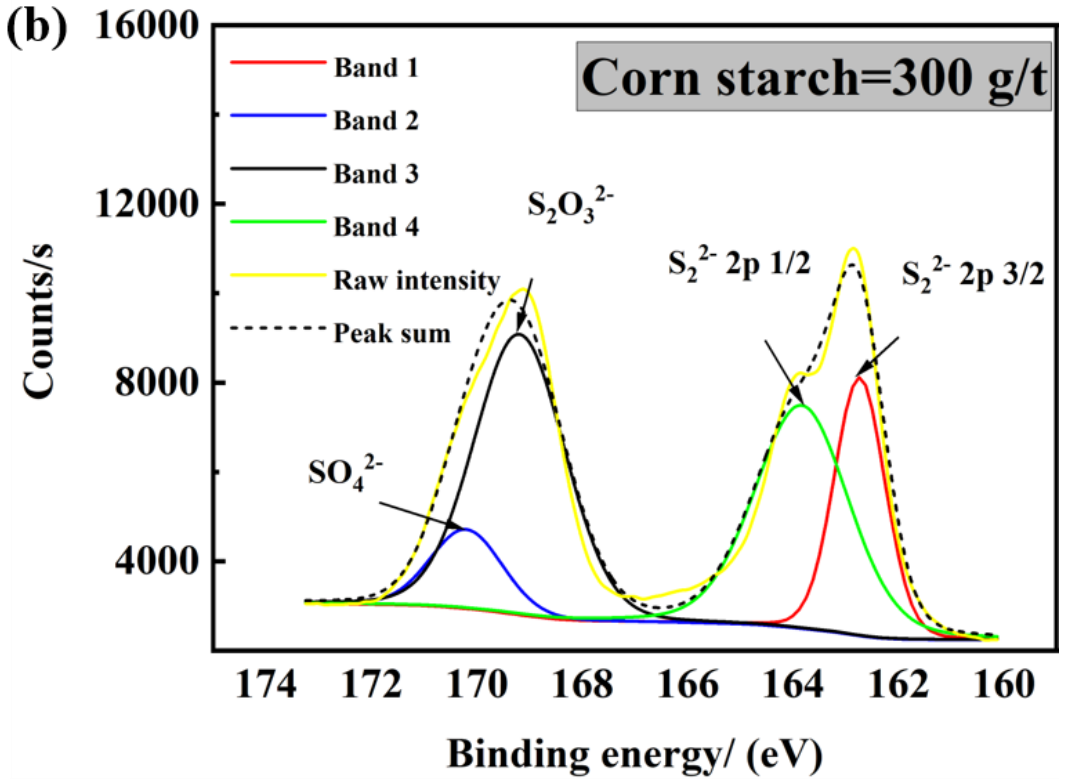


Figure 7.5 XPS results of pyrite without and with corn starch for Fe(2*p*)


(a)
Corn starch=0
Band 1
Band 2
Band 3
Band 4
Raw intensity
Peak sum
$S_2O_3^{2-}$
S_2^{2-} 2p 1/2
S_2^{2-} 2p 3/2
SO_4^{2-}
Counts/s
16000
12000
8000
4000
176
172
168
164
160
Binding energy/ (eV)


(b)
Corn starch=300 g/t
Band 1
Band 2
Band 3
Band 4
Raw intensity
Peak sum
$S_2O_3^{2-}$
S_2^{2-} 2p 1/2
S_2^{2-} 2p 3/2
SO_4^{2-}
Counts/s
16000
12000
8000
4000
174
172
170
168
166
164
162
160
Binding energy/ (eV)

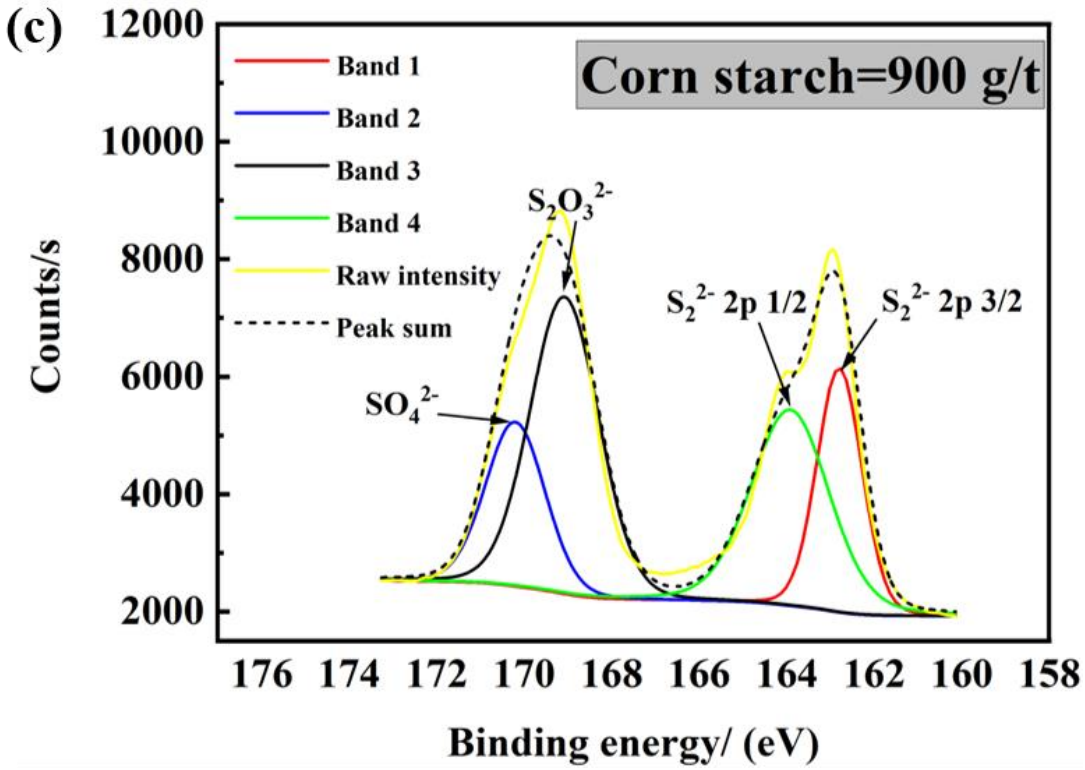


Figure 7.6 XPS results of pyrite without and with corn starch for S(2*p*)

Table 7.1 shows the atomic concentrations of C(1*s*), O(1*s*), S(2*p*), and Fe(2*p*) of raw pyrite and pyrite with starch to characterize changes in mineral composition. The concentrations of Fe decrease from 4.59% to 3.49%, and the concentrations of S decrease from 20.73% to 17.73% with 300 g/t corn starch, which may be beneficial for reducing hydrophobicity of the pyrite surface.

Table 7.2 shows the decoupling of iron and sulfur species based on the data from Figure 7.5 and Figure 7.6. The FeS_2 in pyrite is about 707.43 eV and the FeOOH peak in ferric hydroxide is about 711.23 eV[189][193-196]. The concentration of FeOOH increased significantly from 24.46% (without starch) to 41.46% (900 g/t starch). This may be due to the formation of FeOOH coating after starch adsorption. The concentration of sulfate (SO_4^{2-}) increased from 4.91% to 17.09% after adding 900 g/t corn starch, which improved hydrophilicity of pyrite surface. And the peak of SO_4^{2-} in pyrite

changed from 170.67 eV to 170.20 eV after adsorbing starch, which indicated the chemical adsorption of starch on the pyrite surface.

Table 7.1 Atomic concentrations of main elements on pyrite surface without and with 300 g/t starch and 900 g/t starch

Sample	Atomic concentration/%			
	C(1*s*)	O(1*s*)	S(2*p*)	Fe(2*p*)
Pyrite untreated	28.58	46.09	20.73	4.59
Pyrite treated with 300 g/t corn starch	32.27	46.5	17.73	3.49
Pyrite treated with 900 g/t corn starch	39	44.1	14.36	2.53

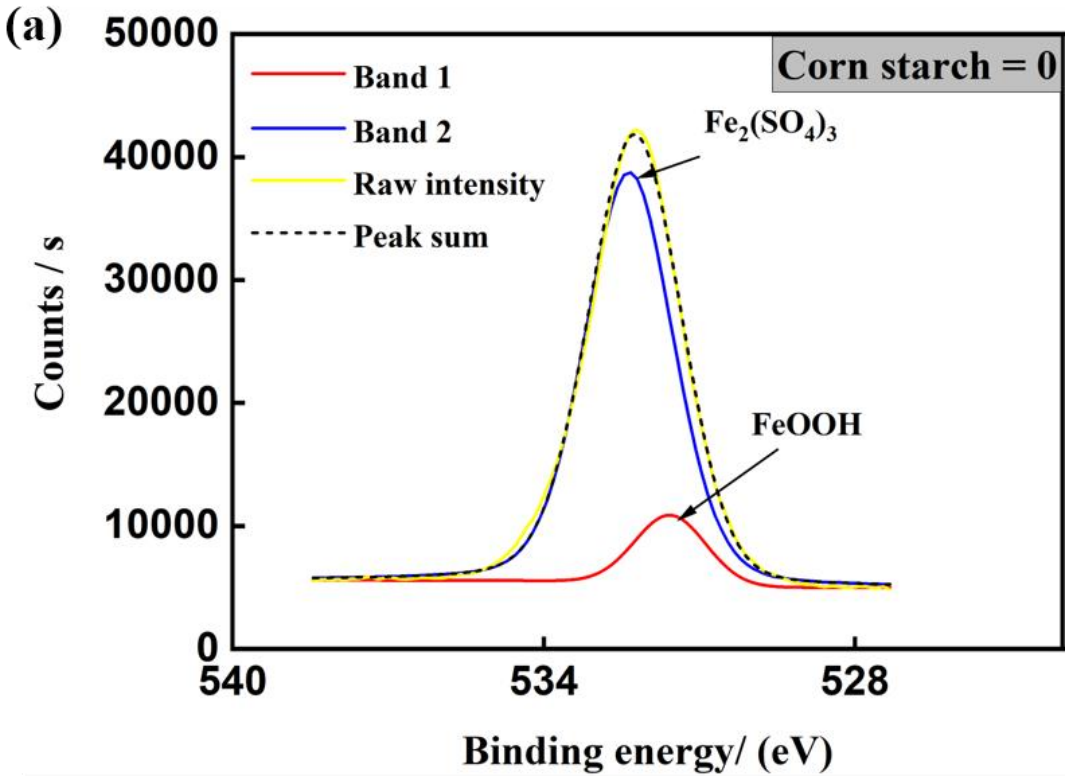
Table 7.2 Binding energies and atomic concentrations of Fe(2*p*) and S(2*p*) for pyrite without and with 300 g/t starch and 900 g/t starch

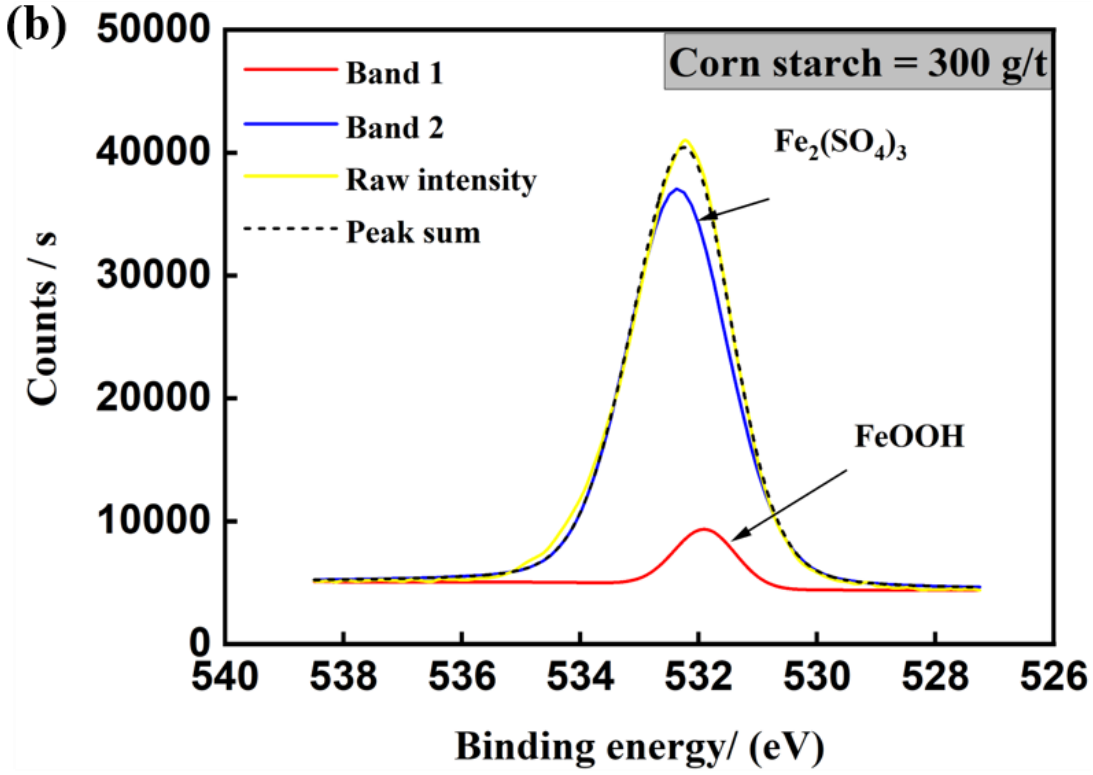
Species	Pyrite untreated		Pyrite treated with 300 g/t cooked starch		Pyrite treated with 900 g/t cooked starch	
	Binding Energy/eV	Atomic concentration/%	Binding Energy/eV	Atomic concentration/%	Binding Energy/eV	Atomic concentration/%
$2p_{3/2}$ FeS_2	707.43	64.08	707.41	65.05	707.41	52.28
$2p_{3/2}$ FeOOH	711.23	24.46	711.71	25.54	711.71	41.46
$2p_{1/2}$ Fe(II)-S	720.00	1.99	720.00	1.96	720.00	1.53
$2p_{1/2}$ Fe(II)-S	720.40	9.47	720.40	7.44	720.24	4.73
$2p_{3/2}$ S_2^{2-}	162.80	21.06	162.73	19.81	162.79	19.21
$2p_{1/2}$ S_2^{2-}	163.90	33.34	163.83	33.09	163.92	27.98
$S_2O_3^{2-}$	169.20	40.69	169.19	38.51	169.07	35.71
SO_4^{2-}	170.67	4.91	170.20	8.59	170.20	17.09

Table 7.3 Binding energies and atomic concentrations of O(1*s*) on pyrite surfaces without and with 300 g/t and 900 g/t starch

Species	Pyrite untreated		Pyrite treated with 300g/t cooked starch		Pyrite treated with 900g/t cooked starch	
	Binding Energy/eV	Atomic concentration/%	Binding Energy/eV	Atomic concentration/%	Binding Energy/eV	Atomic concentration/%
FeOOH	531.56	11.23	531.89	7.53	531.91	0
$Fe_2(SO_4)_3$	532.35	88.77	532.35	92.47	532.35	100

Table 7.3 shows the energies and atomic concentrations of O(1*s*) based on the data as shown in Figure 7.7. The peaks of FeOOH species and $Fe_2(SO_4)_3$ in pyrite occur around 531.56 eV and 532.35 eV, respectively[183]. The concentration of FeOOH is reduced significantly after adding corn starch, whereas $Fe_2(SO_4)_3$ concentration increases significantly from 88.77% to 100%, implying the improved hydrophilicity of the sample surface.


(a)
Corn starch = 0
Band 1
Band 2
Raw intensity
Peak sum
Fe2(SO4)3
FeOOH
Counts / s
Binding energy/ (eV)
50000
40000
30000
20000
10000
0
540
534
528


(b)
Corn starch = 300 g/t
Band 1
Band 2
Raw intensity
Peak sum
Fe2(SO4)3
FeOOH
Counts / s
Binding energy/ (eV)
50000
40000
30000
20000
10000
0
540
538
536
534
532
530
528
526

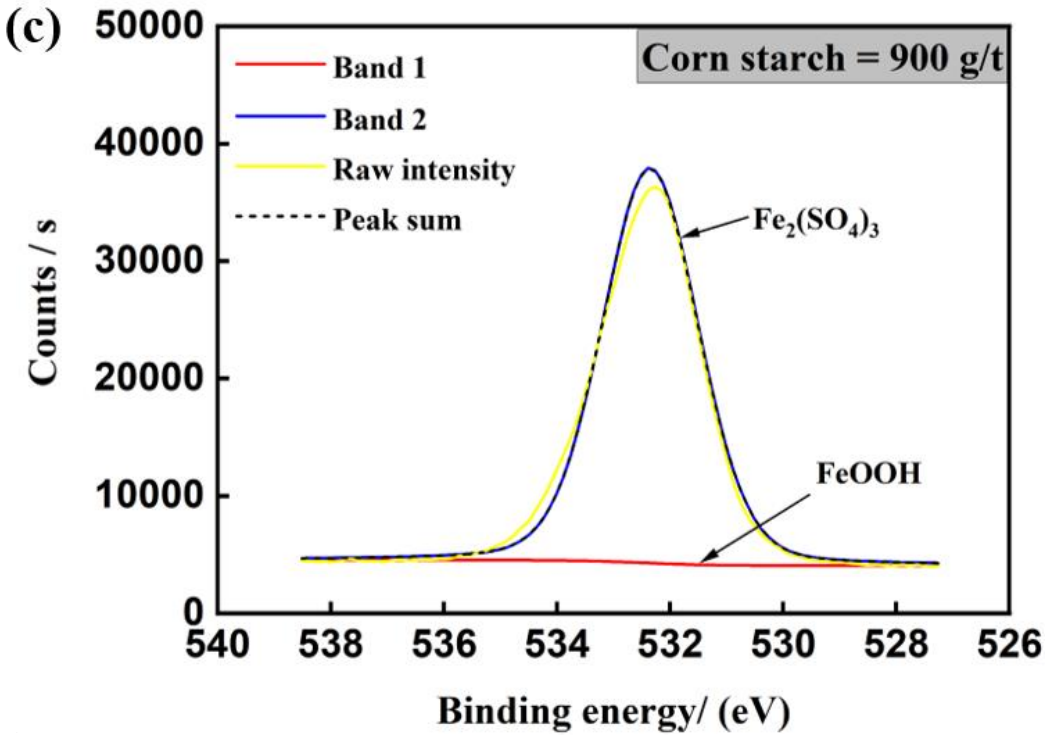
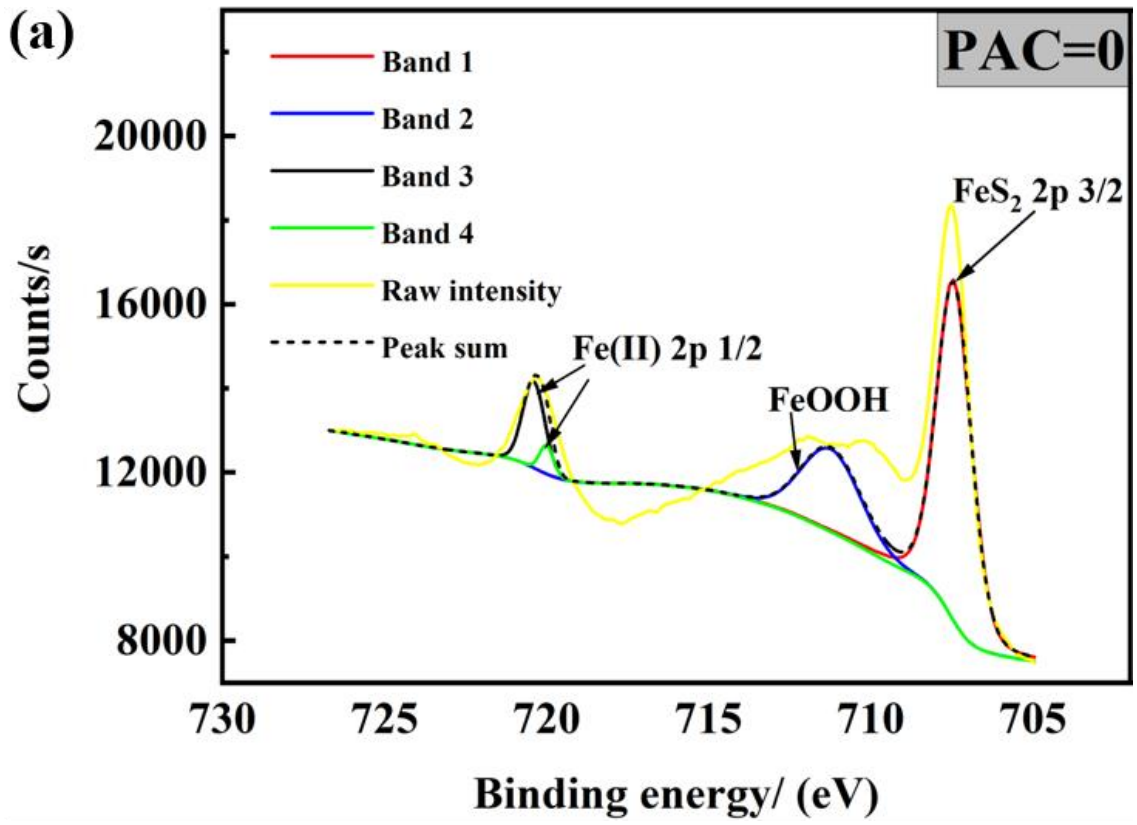


Figure 7.7 XPS results of pyrite without and with corn starch for O(1*s*)

At the same time, the interaction of samples treated with PAC was also studied. Figure 7.8 shows the results of samples reacting with PAC and the fitting procedure of Fe(2*p*) spectra is omitted. Two distinct peaks at 707.43 and 711.23 eV are shown after the reaction with PAC. The former corresponds to Fe(II)-S compounds in pyrite and the latter contributes from FeOOH ($2p_{3/2}$). And contribution from Fe(II)-S($2p_{1/2}$) is around 720 eV binding energy. The concentration of FeOOH increases significantly from 24.46% (without PAC) to 67.41% (400 mg/L PAC). This may be due to the formation of FeOOH coating after PAC adsorption. The strength of both the $2p_{3/2}$ and $2p_{1/2}$ peaks of pyrite decrease after the interaction with PAC, indicating chemical interaction of pyrite with PAC.

Figure 7.9 shows the fitting procedure of S(2*p*) of pyrite without and with PAC. An examination of the mineral shows a S(2*p*) feature at 162.8 eV and 163.9 eV. The spectrum also has two peaks

at 169.2 eV and 170.67 eV. The former is due to $S_2O_3^{2-}$, and the latter is attributed to sulfate. An identical fit to the S($2p_{3/2}$) spectra is composed of disulfide S_2^{2-}($2p_{3/2}$) (S($2p_{3/2}$) = 162.8 eV), S_2^{2-}($2p_{1/2}$) from bulk pyrite (S($2p_{1/2}$) = 163.9 eV). The concentration of sulfate (SO_4^{2-}) increases from 4.91% to 15.68% after adding 400 mg/L PAC owing to the PAC adsorbing on pyrite.



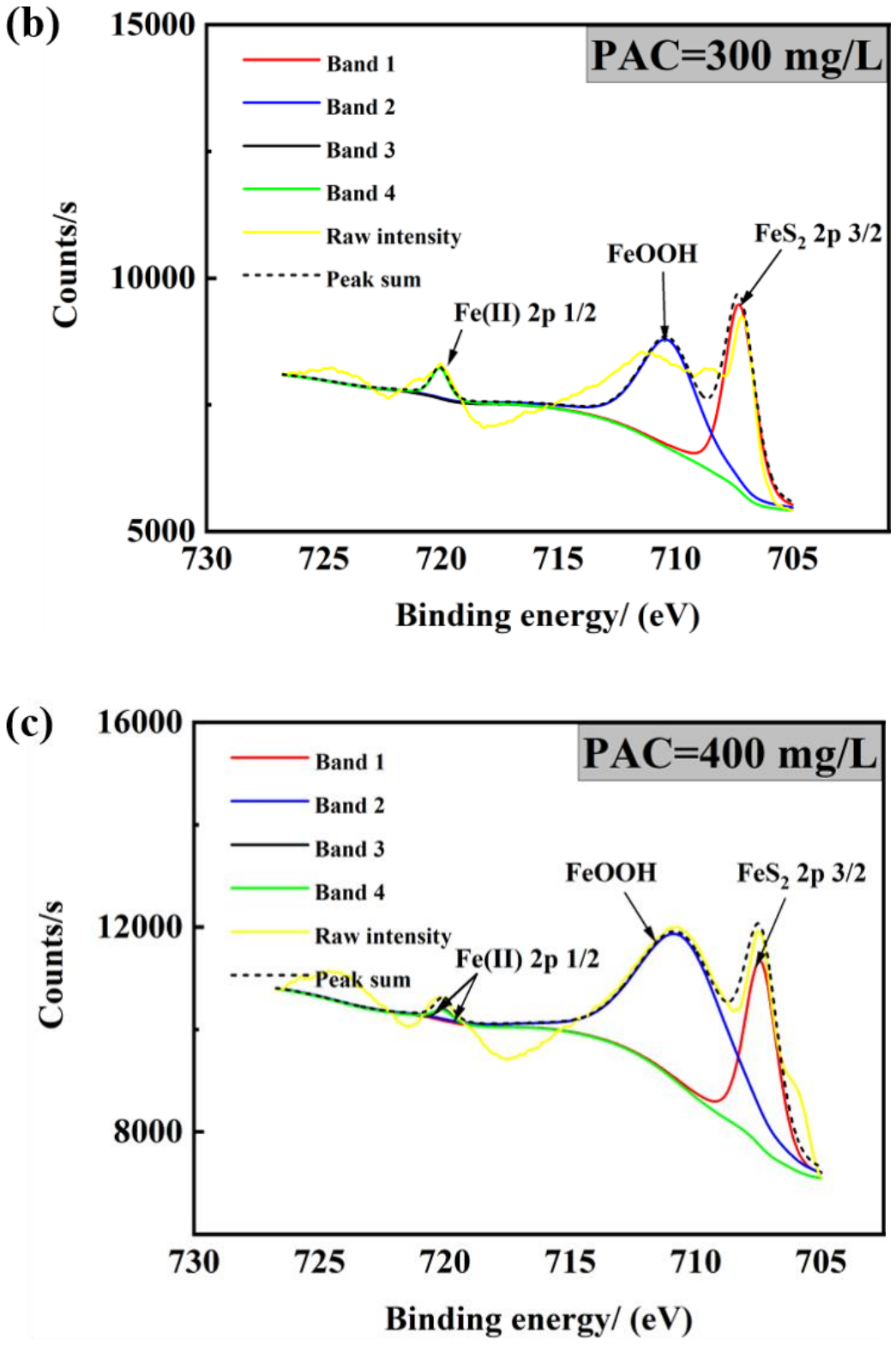
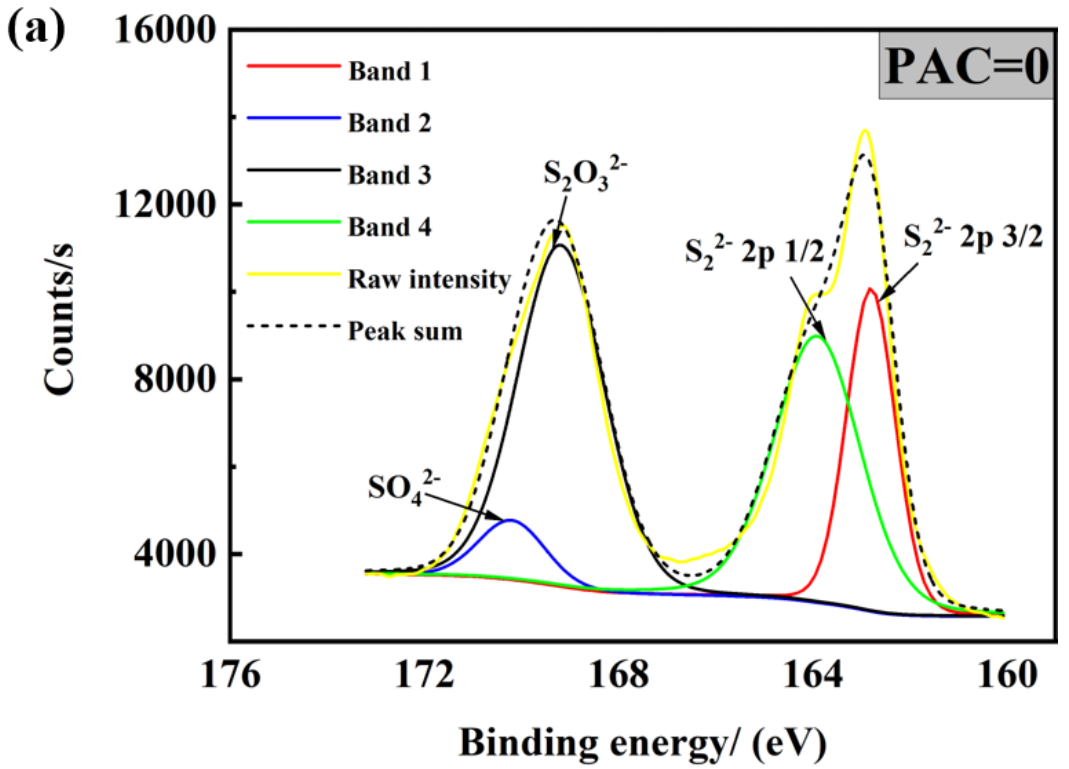
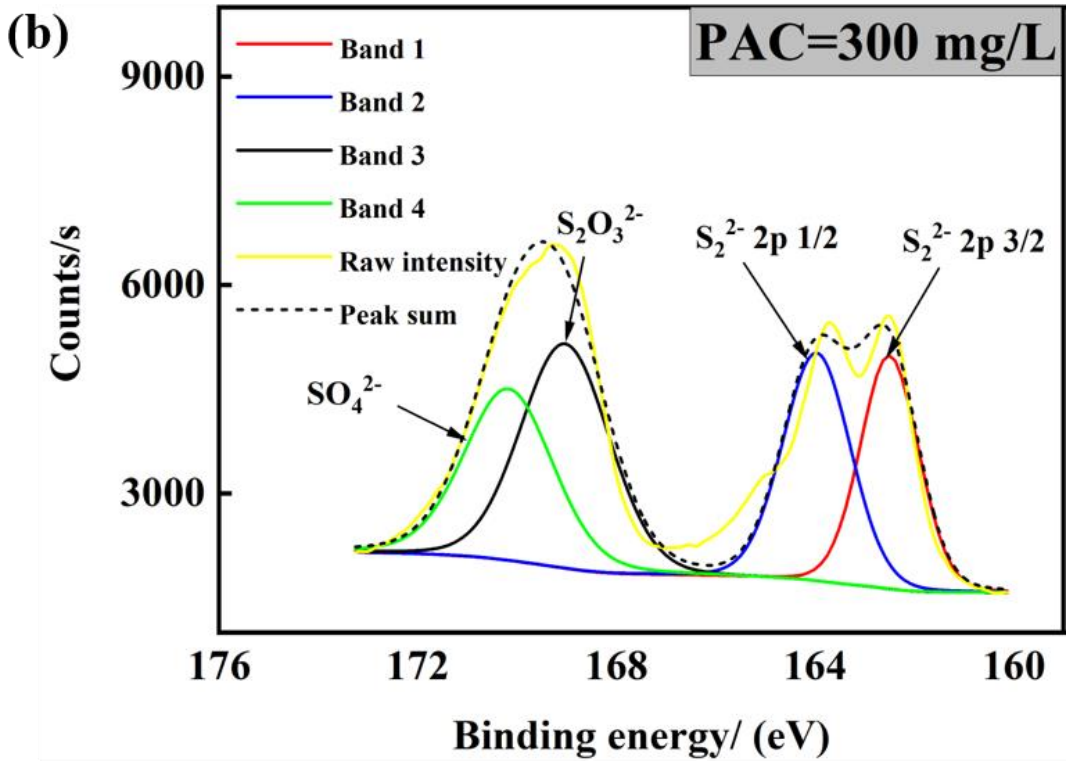


Figure 7.8 XPS results of pyrite without and with PAC for Fe(2*p*)


(a)
PAC=0
Band 1
Band 2
Band 3
Band 4
Raw intensity
Peak sum
$S_2O_3^{2-}$
S_2^{2-} 2p 1/2
S_2^{2-} 2p 3/2
SO_4^{2-}
Counts/s
16000
12000
8000
4000
176
172
168
164
160
Binding energy/ (eV)


(b)
PAC=300 mg/L
Band 1
Band 2
Band 3
Band 4
Raw intensity
Peak sum
$S_2O_3^{2-}$
S_2^{2-} 2p 1/2
S_2^{2-} 2p 3/2
SO_4^{2-}
Counts/s
9000
6000
3000
176
172
168
164
160
Binding energy/ (eV)

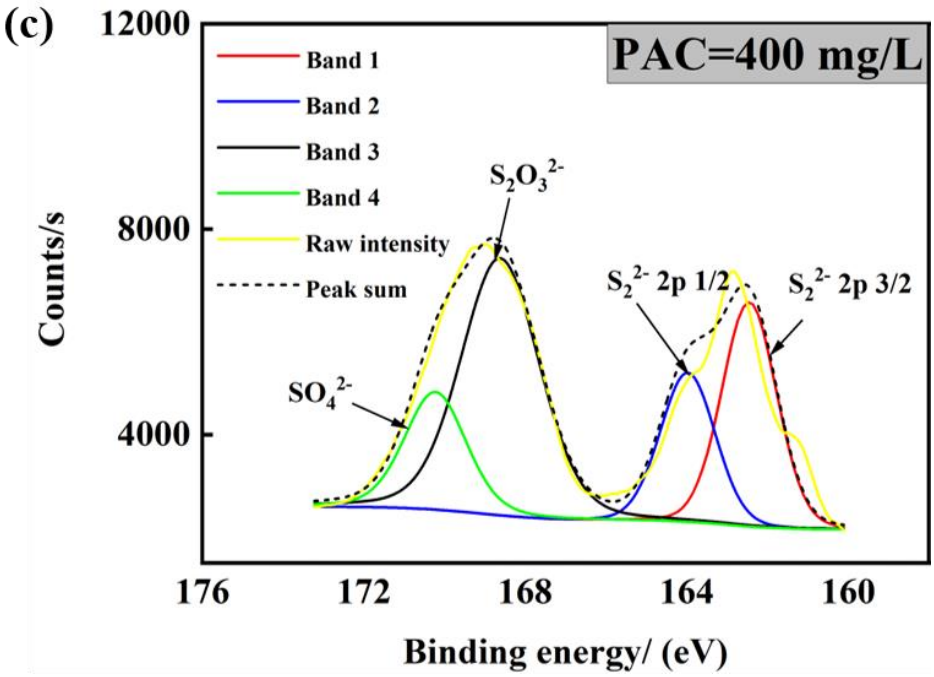
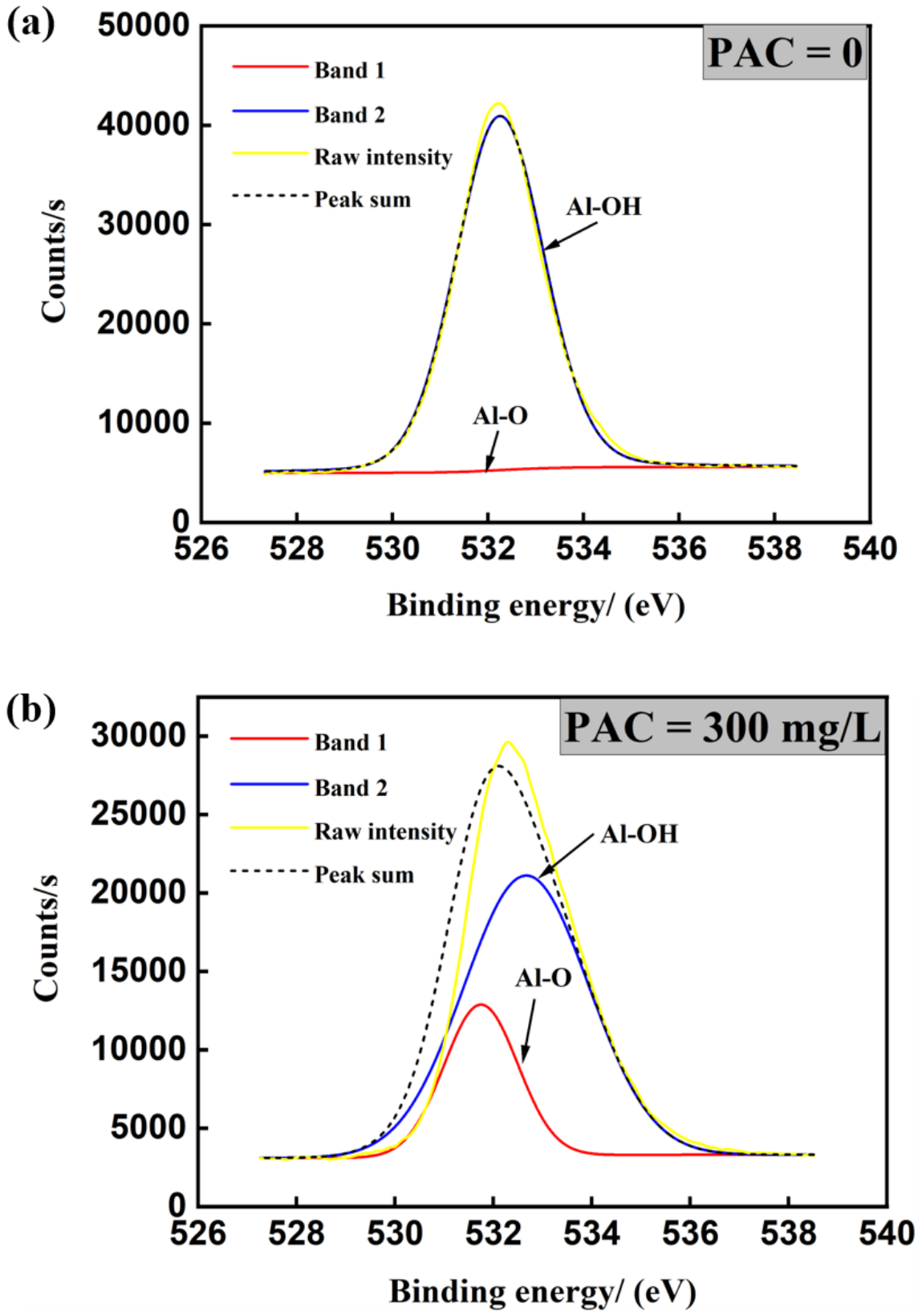


Figure 7.9 XPS results of pyrite without and with PAC for S(2*p*)

Table 7.4 Atomic concentrations of main elements on pyrite surface without and with the addition of 300 mg/L and 400 mg/L PAC

Sample	Atomic concentration/%			
	C(1*s*)	O(1*s*)	S(2*p*)	Fe(2p_3)
pyrite untreated	28.58	46.09	20.73	4.59
pyrite treated with 300 mg/L PAC	24.24	56.51	15.63	3.62
pyrite treated with 400 mg/L PAC	21.65	58.11	16.11	4.12

Table 7.4 shows the atomic concentrations of C(1*s*), O(1*s*), S(2*p*), and Fe(2*p*) on the surface of raw pyrite and PAC-treated pyrite to characterize changes in the mineral composition. The concentrations of O increase from 46.09% to 58.11%, while the concentrations of Fe decrease from 4.59% to 4.12% with 400 mg/L PAC, which is contributive to the hydrophobicity reduction of the pyrite surface.


(a)
PAC = 0
Band 1
Band 2
Raw intensity
Peak sum
Al-OH
Al-O
Counts/s
Binding energy/ (eV)
(b)
PAC = 300 mg/L
Band 1
Band 2
Raw intensity
Peak sum
Al-OH
Al-O
Counts/s
Binding energy/ (eV)

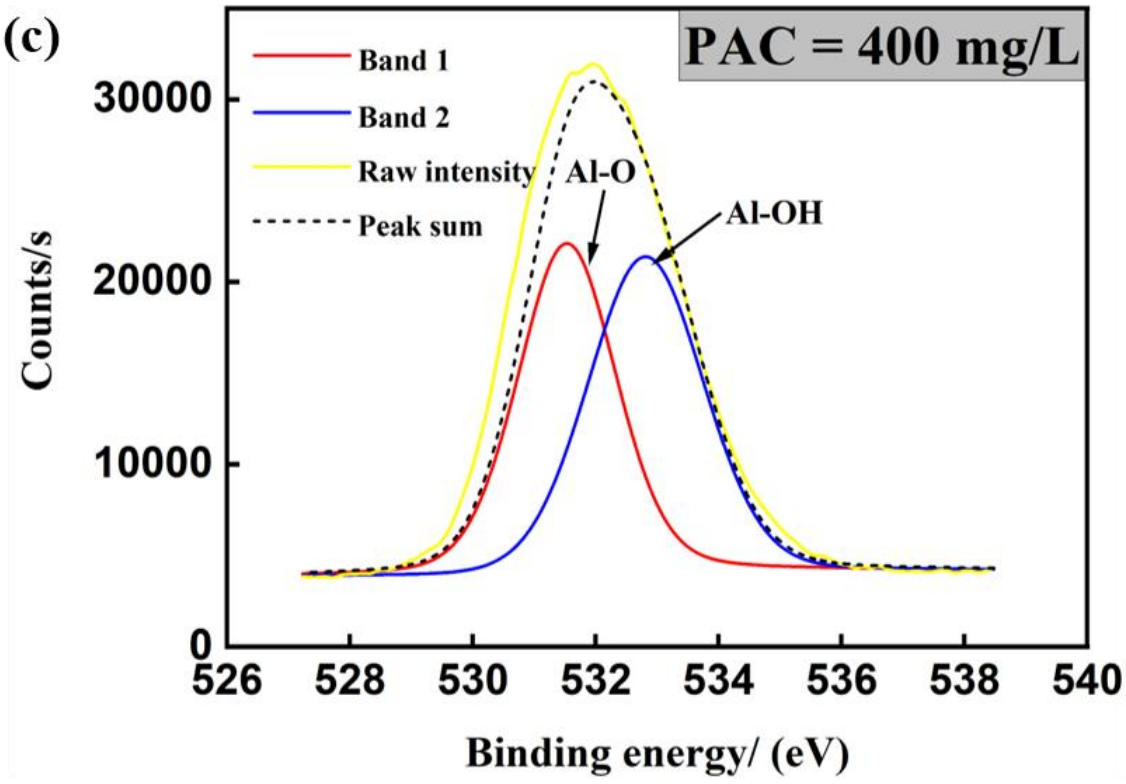


Figure 7.10 XPS results of pyrite without and with PAC for O(1*s*)

Table 7.5 Binding energies and atomic concentrations of O(1*s*) on pyrite surfaces treated with PAC

Species	Pyrite untreated		Pyrite treated with 300 mg/L PAC		Pyrite treated with 400 mg/L PAC	
	Binding Energy/eV	Atomic concentration/%	Binding Energy/eV	Atomic concentration/%	Binding Energy/eV	Atomic concentration/%
Al-OH	531.51	0	531.75	24.28	531.53	48.27
Al-O	532.25	100	532.66	75.72	532.81	51.73

Table 7.5 shows the result of O(1*s*) based on the data from Figure 7.10. The peak of Al-OH[197-200], occurs at around 531.51 eV and the peak at 532.25 eV is attributed to Al-O[201-203]. The concentration of Al-OH increases dramatically from 0% to 48.27% with 400 mg/L PAC, resulting

in the increasing adsorption of $Al(OH)^{2+}$, $Al(OH)_2^{+}$, $Al_2(OH)_2^{4+}$, $Al_3(OH)_4^{5+}$ on pyrite surface, while the area proportions of Al-O peaks reduces dramatically.

7.4 FT-IR of pyrite and samples

The surface functional groups before and after the adsorption of depressants on the pyrite surface were characterized by FT-IR to identify[27] the surface chemistry changes. According to the reference data[204-207], the corresponding relationship between the transmittance band and the functional group can be established in such a way. Figure 7.11 shows the FT-IR spectrums with and without PAC.

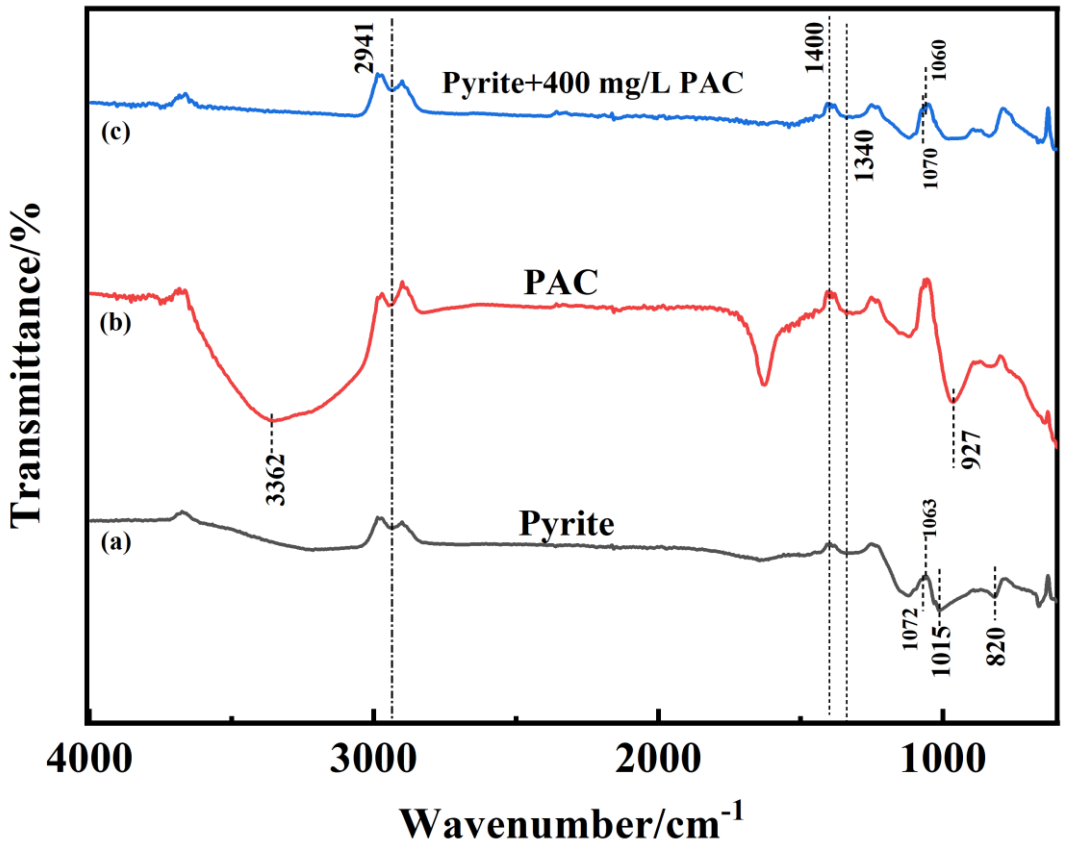


Figure 7.11 FT-IR of pyrite without and with PAC

The FT-IR results of pyrite are shown in Figure 7.11 (a). When PAC is adsorbed on the pyrite sample, the band at 2941 cm^{-1} due to the C-H stretching of the -CH_2 group is very strong at the same position as that of the depressant-free.

The absorption bands ranging at 1200-1000 cm^{-1} are for pyrite, whereas 600-800 cm^{-1} bands are caused by the pyrite oxidized. Meantime, there is a strong band and a bimodal band at 1122 cm^{-1} and 1072 cm^{-1}, respectively[81].

The FT-IR spectra of pyrite after interaction with PAC is described in Figure 7.11(c). The band at 2941 cm^{-1} due to C-H stretching of the -CH_2 groups increases intensity in the case of PAC-adsorbed pyrite samples. The weak shoulder band at 1400 cm^{-1} shows nearly the same wavenumbers after adsorption, which was caused by symmetrical deformations of bending vibrations of -CH_2 and methyl C-OH groups. The wide bands ranging from 1340 cm^{-1} to 1296 cm^{-1} kept the same after adsorption due to bending vibration of methyl (-CH_3) and C-OH groups.

It is interesting to find that the bands at 927 and 3362 cm^{-1} due to hydroxyl with stretching vibration for PAC are missing after adsorption due to chemical interaction of PAC on the surface of pyrite. It is worth noting that there is no band at 1015 cm^{-1} after PAC adsorption owing to chemical interaction.

1072 and 1063 cm^{-1} bands caused by -CH_2OH and CH_2 twisting vibrations[208] shifted slightly changed to 1070 and 1060 cm^{-1} (Figure 7.11 (c)) after PAC treatment because of the pyrite interacting with the -CO groups of the PAC.

The FT - IR result of pyrite without and with corn starch is shown in Figure 7.12 (a). The absorption bands ranging at 1200-1000 cm^{-1} are for pyrite, whereas 600-800 cm^{-1} bands are caused by the

pyrite oxidized. Meantime, there is a strong band and a bimodal band at 1122 cm^{-1} and 1072 cm^{-1}, respectively.

The FT-IR spectra of pyrite after interaction with corn starch is described in Figure 7.12 (c). The bands at 2984 cm^{-1} and 2941 cm^{-1} due to C-H stretching of the -CH_2 groups increase intensity for samples interacted with corn starch. The weak shoulder band at 1462 cm^{-1} shows nearly the same wavenumbers after adsorption, which was caused by the symmetrical deformations of -CH_2 and methyl C-OH.

The bands at 1151 cm^{-1} caused by -CH_2OH and C-OH slightly change to 1153 cm^{-1} after corn starch treatment caused by the -CO groups of the polymers interacting with pyrite.

It is interesting to find that the bands at 1122 and 1032 cm^{-1} for pyrite are missing after corn starch adsorption due to chemical interaction of corn starch on the surface of pyrite. The FT-IR data strengthen the results of the XPS analyses regarding the chemical interaction of the pyrite with polymer.

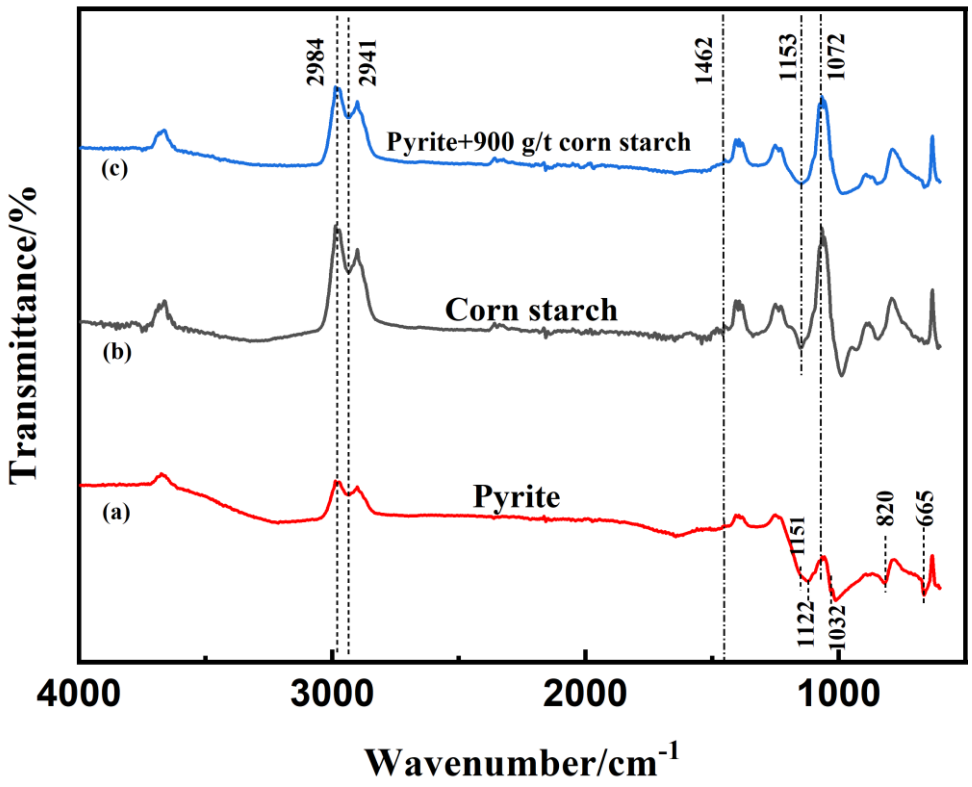


Figure 7.12 FT-IR of pyrite without and with corn starch

7.5 Summary

This chapter presents the zeta potential, the hydrophobicity, X-ray photoelectron spectroscopy (XPS) analyses of pyrite samples in the presence of corn starch and PAC. And the functional groups on the surface of samples are characterized by FT-IR. And the results are as follows:

(1) The Zeta potential as a function of corn starch concentration shows a steady increase of negative values. It will cause an increase in the energy barrier according to EDLVO theory, which prevents the particles from agglomerating. The increased charges disperse the fine particles when corn starch adsorbs on the pyrite surface;

(2) When PAC is used, the Zeta potential changes steadly from -10 mV to + 20 mV at 240 mg/L PAC. The increase of values indicates the growing adsorption of $Al(OH)_2^+$, $Al(OH)^{2+}$,

$Al_3(OH)_4^{5+}$, $Al_2(OH)_2^{4+}$ on the surface of pyrite, resulting in the particles being more hydrophilic and dispersed in the slurry;

(3) The pyrite-free polysaccharide presents a higher value of contact angle. Good agreement is found between the recovery and the contact angle of pyrite, where pyrite with low contact angle values presents low recovery. So the addition of PAC could improve the hydrophilicity of the pyrite and decrease the yield of pyrite in flotation;

(4) The XPS analyses show that the strength of both the $2p_{3/2}$ and $2p_{1/2}$ peaks of pyrite decreases after the interaction with cooked starch, indicating that pyrite chemically interacts with corn starch. The concentration of FeOOH peak in ferric hydroxide treated with 900 g/t starch increased significantly due to the formation of FeOOH coating after corn starch adsorption. And the concentration of sulfate (SO_4^{2-}) increased after adding 900 g/t corn starch, which was due to starch adsorption on the pyrite surface and improved hydrophilicity of pyrite surface. And the peak of SO_4^{2-} in pyrite shifted from 170.67 eV to 170.20 eV after the addition of starch, which indicated the chemical adsorption of starch on the pyrite surface. And the results of samples treated with PAC were similar;

(5) FT-IR of pyrite and samples illustrates that when PAC is adsorbed on the surface of pyrite sample, the band at 2941 cm^{-1} due to the C-H stretching of the $-CH_2$ group is very strong at the same position as that of the PAC-free. The bands at 927 and 3362 cm^{-1} due to hydroxyl with stretching vibration for PAC are missing after adsorption due to chemical interaction of PAC on the surface of pyrite. And it is worth noting that there is no band at 1015 cm^{-1} after PAC adsorption, which is due to chemical interaction;

(6) The FT-IR spectra of pyrite after interaction with corn starch demonstrates that the bands at 2984 cm^{-1} and 2941 cm^{-1} due to C-H stretching of the $-CH_2$ groups increase intensity in the case of corn starch-adsorbed pyrite samples. And the bands at 1122 and 1032 cm^{-1} for pyrite are missing after corn starch adsorption due to chemical interaction of corn starch on the surface of pyrite.

8 Conclusions and future work

The objective of this work is to resolve the problems for Kerosene in flotation: low recovery of clean coal, high sulfur content, poor selectivity and high consumption etc. This work develops a new type of nonionic collector and it is characterized with various methods and used in froth flotation. Then the problem regarding high sulfur content in coal is studied with corn starch and PAC. The recommendations for the future work are also shown in this chapter.

8.1 Conclusions

The new prepared collector MEC is screened through froth flotation. The flotation experiment process, the dosage of reagents, equipment parameters etc. are described in detail. Then the characterizations of MEC are performed and the conclusions are below:

(1) The microemulsions are successfully prepared by mixing Kerosene, blending surfactant (Span 80 and Tween 80 (HLB = 6, 7, 8, 9), MIBC and distilled water. The new collector MEC and Kerosene showed similar trends in the flotation process. When C_R(combustible recovery) = 60% and A (ash) = 16%, the dosage of MEC (HLB = 7) and kerosene are both 1000 g/t. The cost of MEC is estimated at 7400 RMB/ (10^3 t) dry coal slime, which is approximately 50% of that of Kerosene with 14220 RMB/ (10^3 t) dry coal slime. A higher flotation rate is obtained by using MEC compared to Kerosene in the froth flotation;

(2) The average particle size of MEC was 92.5 nm, so it could disperse the oily phase and form small droplets in water to improve the combustible recovery of cleaning coal by improving the collision probability of MEC and coal particle in froth flotation.

(3) The morphology of MEC obtained from Cryo-TEM analysis shows several large spherical droplets with a diameter greater than 100 nm, which is due to the sample damage during the filters adsorbing excess solution for Cryo-TEM analyses;

(4) The conductivity of the microemulsion increases with increasing concentration of mixed surfactant and water concentration. It decreases clearly with the increase of the cosurfactant concentration. And these results confirm the W/O structure of the new collector.

(5) The viscosity of the collector is important for collector molecue spreading on the sample surface in the flotation progress. The viscosity of MEC is 8 mPa·s, which is four times as much as that of water (2 mPa·s), and the microemulsion is Newtonian liquid with constant viscosity. MEC spreads slower than Kerosene on the coal surface because of the higher oil viscosity of MEC, while the viscosity of Kerosene is nearly equal to that of water. The better flotation performance of MEC indicates the dispersing the oily phase and forming small droplets in water offset the side effect of high viscosity spreading on the sample surface;

(6) The addition of MEC or K can reduce the repulsive electrostatic interaction energies (V_E) between particles, and the reduction effect is larger for MEC than for K. The hydrophobic interaction energies (V_H) are much more negative for MEC than for K as well as that for particles without reagent. The total interaction energy (V_T) of MEC is much more negative than that for K and that of particles without reagent, signifying that the particles modified by MEC are prone to combine to give large flocs and enter into the foam area in froth flotation.

And then depressants (PAC and corn starch) are used to depress the pyrite entraining in froth products to improve the quality of cleaning coal. The conclusions are below:

(1) Cooked starch is better than raw starch with regard to sulfur content in the real system, demonstrating that the cooked starch could depress the pyrite in real systems;

(2) Single factor experiments were conducted to investigate the effects of starch content on the recovery of pyrite. The optimal amount of starch was found to be at 1200 g/t, with the modified pH at pH = 3, and the heated temperature of corn starch at 105℃;

(3) The Box-Behnken design (BBD) was employed to obtain optimized parameters for depressing pyrite with seventeen sets of experiments. The analyses of variance (ANOVA) illustrate that X_1 (the dosage of corn starch), X_2 (the modified pH), X_3 (heated temperature), X_1X_3 (the dosage of corn starch and heated temperature) are significant model terms, whereas X_3^2 (heated temperature) is an extremely significant model term. The F-value of 18.91 and the p-value of lower than 0.0001 imply that the model is significant;

(4) The parameters for the minimum recovery of pyrite are found to be：X_1 = 1490 g/t，X_2 = 4，X_3 = 100℃. Based on the optimized conditions, the predicted yield is 13.92%, which is in agreement with the actual yield of 14.01%;

(5) The effects of corn starch on the depressing flotation of an ideal system (TXM+pyrite) were studied with medium oxidized TXM (more hydrophilic) and low oxidized TXM (less hydrophilic). The yields of both coals were almost the same and the sulfur content of low oxidized coal decreased from 0.82% to 0.4%. The trend for the medium oxidized coal was similar, indicating that the oxidization on coal is not an effective way for distinguishing between the hydrocarbons and minerals with corn starch.

(6) Single-factor experiments were conducted to investigate the effects of PAC on the recovery of pyrite. The optimal dosage of PAC was 300 mg /L, the pH of the flotation slurry was pH = 3, and the concentration of PAC was 125 ml water per 1 g PAC;

(7) The Box-Behnken design (BBD) was employed to obtain optimized parameters for depressing pyrite with seventeen sets of experiments. The analyses of variance (ANOVA) illustrated that X_2^2 (pH of flotation slurry), $X_1^2X_3$ and X_1X_3 (the dosage of PAC and concentration of PAC) were all significant model terms, whereas X_3^2 (concentration of PAC) and $X_1X_2^2$ (the dosage of PAC and pH of flotation slurry) were extremely effective model terms. The F-value of 5.69 and p-value of lower than 0.05 implied that the model was significant;

(8) The parameters for the minimum recovery of pyrite were focused to be：X_1 = 400 mg/L，X_2 = 3，X_3 = 110 mL/g. According to the optimized conditions, the predicted yield of 18.3% compared well with the actual yield of 18.64%;

(9) The effects of PAC on depressing flotation of an ideal system (TXM+pyrite) were studied with the medium oxidized TXM (more hydrophilic) and the low oxidized TXM (less hydrophilic). The yields of both coals were almost the same (nearly 99%) and the sulfur content of low oxidized coal was found to decrease from 0.82% to 0.67%, and the trend for the medium oxidized coal was similar, indicating that the oxidization on coal was not effective for distinguishing between the hydrocarbons and minerals with PAC.

(10) The Zeta potential as a function of corn starch concentration showed a steady increase of negative values. It will cause an increase in the energy barrier according to EDLVO theory,

which prevents the particles from agglomerating. The increased charges dispersed the fine particles when corn starch adsorbed on pyrite surface;

(11) When PAC was used, the Zeta potential increased steadily from negative values to be about 20 mV at 240 mg/L PAC. The increase of values indicates the growing adsorption of $Al(OH)_2^+$, $Al(OH)^{2+}$, $Al_3(OH)_4^{5+}$, $Al_2(OH)_2^{4+}$ on the surface of pyrite. So the particles were more hydrophilic and dispersed in the slurry when PAC adsorbed on the pyrite surface;

(12) The pyrite-free polysaccharide presented the higher value of contact angle. Good agreement was found between the recovery and the contact angle of pyrite, where pyrite with high contact angle values presented high recovery. And the addition of PAC could improve the hydrophilicity of the pyrite surface and decrease the yield of pyrite in flotation;

(13) The XPS analysis indicated that the strength of both FeOOH $2p_{3/2}$ and Fe(II)-S $2p_{1/2}$ peaks of pyrite decreased after the interaction with cooked starch, which indicated that pyrite chemically interacted with corn starch. The concentrations of Fe and S decreased to 3.49%, and 17.73% with 300 g/t corn starch, respectively, which would be beneficial for reducing hydrophobicity of the pyrite surface;

(14) The concentration of FeOOH treated with 400 mg/L PAC increased significantly from 24.46% to 67.41%. This may be due to the formation of FeOOH coating after PAC adsorption. And the concentration of O increased from 46.09% to 58.11%, while the concentration of Fe decreased from 4.59% to 4.12%, which would improve the hydrophilicity of the pyrite surface;

(15) FT-IR of pyrite and samples illustrated that when PAC was adsorbed on the pyrite sample, the band at 2941 cm^{-1} due to the C-H stretching of the $-CH_2$ group was very strong

at the same position as that of the PAC-free. The bands at 927 and 3362 cm^{-1} due to hydroxyl with stretching vibration for PAC are missing after adsorption owing to chemical interaction of PAC on the surface of pyrite. And it is worth noting that there is no band at 1015 cm^{-1} after PAC adsorption, which was caused by chemical interaction;

(16) The FT-IR results of pyrite after interaction with corn starch demonstrated that the bands at 2984 cm^{-1} and 2941 cm^{-1} due to C-H stretching of the -CH_2 groups increased intensity for samples adsorbing corn starch. And the bands at 1122 and 1032 cm^{-1} for pyrite are missing after corn starch adsorption due to chemical interaction of corn starch on the surface of pyrite.

8.2 Recommendations for the future work

Based on the results and analyses of this work, the following are the recommendations for the future work:

(1) The new collector MEC could reduce 50% economic cost with similar recovery of cleaning coal compared with the same dosage of Kerosene. However, MEC spread slower than Kerosene on the sample surface because of the high oil viscosity of MEC, so the future work should focus on reducing the viscosity of MEC.

(2) The effective depressants (PAC and Corn Starch) were screened through a large number of flotation tests, the adsorption mechanisms of pyrite and reagents were explored. However, the exact electrochemical adsorption between the active group in depressants and pyrite should be further explored.

(3) Economic and efficient molecule should be selected as the basic skeleton of the self-designed new reagent, then objective polar and non-polar groups are added to it through

chemical reactions according to the basic principles of molecular design. The design of efficient and economic depressants should be the further research.

Bibliography

[1] Xing, Y.; Gui, X.; Liu, J.; Cao, Y.; Zhang, Y.; Li, S., Flotation behavior of hard-to-separate and high-ash fine coal. Physicochemical Problems of Mineral Processing 2016, 52 (2), 703-717.

[2] Reis, A. S.; Barrozo, M. A. S., A study on bubble formation and its relation with the performance of apatite flotation. Separation and Purification Technology 2016, 161, 112-120.

[3] Anh V. Nguyen， Hubbard, A., Colloidal Science of Flotation. Marcel Dekker 2004, 17 (6), 839.

[4] Bharath, K. L.; Nikkam, S.; Udayabhanu, G., Beneficiation of high-ash Indian coal fines by froth flotation using bio-degradable-oil as a collector. International Journal of Coal Preparation and Utilization 2021.

[5] Wang, Y.; Li, Y.; Xia, W.; Peng, Y.; Xie, G., Adsorption of sodium oleate on coal surface with different oxidation degrees and its effect on flotation. Colloids and Surfaces a-Physicochemical and Engineering Aspects 2021, 611.

[6] Yang, Z.; He, Q.; Chang, G.; Xia, Y.; Li, M.; Xing, Y.; Gui, X., Flotation of oxidized coal using coal tar as a new collector. Energy Sources, Part A: Recovery, Utilization, and Environmental Effects 2020, 1-10.

[7] Chandra, A. P.; Gerson, A. R., A review of the fundamental studies of the copper activation mechanisms for selective flotation of the sulfide minerals, sphalerite and pyrite. Advances in Colloid and Interface Science 2009, 145 (1-2), 97-110.

[8] Huang, P.; Cao, M.; Liu, Q., Selective depression of pyrite with chitosan in Pb-Fe sulfide flotation. Minerals Engineering 2013, 46-47, 45-51.

[9] Lowson, R. T., Aqueous Oxidation of Pyrite by Molecular Oxygen. Chemical Reviews 1982, 82 (5), 461-497.

[10] Evangelou, V. P.; Zhang, Y. L., A review: Pyrite oxidation mechanisms and acid mine drainage prevention. Critical Reviews in Environmental Science and Technology 1995, 25 (2), 141-199.

[11] Xu, M.; Xing, Y.; Li, M.; Jin, W.; Cao, Y.; Gui, X., Oxidized coal flotation enhanced by adding n-octylamine. Energy Sources, Part A: Recovery, Utilization, and Environmental Effects 2018, 40 (20), 2394-2399

[12] Zhu, Z.; Yin, W.; Yang, B.; Li, H.; Guo, W.; Yao, J., Investigation on the flotation recovery and kinetics of coking coal using the mixture of oleic acid and kerosene as a novel collector. Journal of Dispersion Science and Technology 2019, 1-7.

[13] Cebeci, Y., The investigation of the floatability improvement of Yozgat Ayrıdam lignite using various collectors. Fuel 2002, 81 (3), 281-289.

[14] Xie, G.; Wu, L.; Li, G.; Yu, H., Coal flotation using wash oil as a new type of collector. Mining Science and Technology (China) 2010, 20 (4), 546-550.

[15] Jizheng, R.; Zheng, F.; Junhua, S.; Jiongtian, L., Preparation and Application of Ultrasonic Emulsified Diesel Collector. Coal Technology 2011, 30 (06), 147-149.

[16] Ming, Z.; Xuqin, D., Application of Non-ionic Emulsified Collector to Slime's Floatation. Journal of Taiyuan University of Technology 1999, (01), 3-5.

[17] Wenze, K.; Hui, W.; Xiaohong, K.; Yuting, L.; Jun, H., Study of flotation performance of Kerosene after ultrasonic emulsification. Journal of China Coal Society 2008, 33 (01), 89-93.

[18] Chang, Z.; Chen, X.; Peng, Y., The interaction between diesel and surfactant Triton X-100 and their adsorption on coal surfaces with different degrees of oxidation. Powder Technology 2019, 342, 840-847.

[19] Laskowski, J. S.; Yu, Z., Oil agglomeration and its effect on beneficiation and filtration of low-rank/oxidized coals. International Journal of Mineral Processing 2000, 58 (1), 237-252.

[20] Boylu, F.; Laskowski, J. S., Rate of water transfer to flotation froth in the flotation of low-rank coal that also requires the use of oily collector. International Journal of Mineral Processing 2007, 83 (3-4), 125-131.

[21] Li, B.; Liu, S.; Fan, M.; Zhang, L., The effect of ethylene oxide groups in dodecyl ethoxyl ethers on low rank coal flotation: An experimental study and simulation. Powder Technology 2019, 344, 684-692.

[22] Xia, Y.; Yang, Z.; Zhang, R.; Xing, Y.; Gui, X., Enhancement of the surface hydrophobicity of low-rank coal by adsorbing DTAB: An experimental and molecular dynamics simulation study. Fuel 2019, 239, 145-152.

[23] Xia, Y.; Zhang, R.; Xing, Y.; Gui, X., Improving the adsorption of oily collector on the surface of low-rank coal during flotation using a cationic surfactant: An experimental and molecular dynamics simulation study. Fuel 2019, 235, 687-695.

[24] Xia, Y.; Rong, G.; Xing, Y.; Gui, X., Synergistic adsorption of polar and nonpolar reagents on oxygen-containing graphite surfaces: Implications for low-rank coal flotation. Journal of Colloid and Interface Science 2019, 557, 276-281.

[25] Liao, Y.; Hao, X.; An, M.; Yang, Z.; Ma, L.; Ren, H., Enhancing low-rank coal flotation using mixed collector of dodecane and oleic acid: Effect of droplet dispersion and its interaction with coal particle. Fuel 2020, 280.

[26] Xie, W.; Cao, G.; Ren, X.; Li, Y., Effect of flotation promoter on the rate of coal slime flotation. Journal of Mining Science 2014, 50 (3), 601-607.

[27] Xing, Y.; Gui, X.; Cao, Y.; Wang, Y.; Xu, M.; Wang, D.; Li, C., Effect of compound collector and blending frother on froth stability and flotation performance of oxidized coal. Powder Technology 2017, 305, 166-173.

[28] Chen, S.; Wang, S.; Li, L.; Qu, J.; Tao, X.; He, H., Exploration on the mechanism of enhancing low-rank coal flotation with cationic surfactant in the presence of oily collector. Fuel 2018, 227, 190-198.

[29] Zhang, W.; Liu, C., The effect of diesel emulsification using sodium petroleum sulfonate on carbon flotation from fly ash. Waste Management 2019, 98, 144-150.

[30] Lu, Y.; Wang, X.; Liu, W.; Li, E.; Cheng, F.; Miller, J. D., Dispersion behavior and attachment of high internal phase water-in-oil emulsion droplets during fine coal flotation. Fuel 2019, 253, 273-282.

[31] Van Netten, K.; Moreno-Atanasio, R.; Galvin, K. P., Fine Particle Beneficiation through Selective Agglomeration with an Emulsion Binder. Industrial & Engineering Chemistry Research 2014, 53 (40), 15747-15754.

[32] Dunstan, T. S.; Fletcher, P. D.; Mashinchi, S., High internal phase emulsions: catastrophic phase inversion, stability, and triggered destabilization. Langmuir 2012, 28 (1), 339-49.

[33] Van Netten, K.; Moreno-Atanasio, R.; Galvin, K. P., Selective agglomeration of fine coal using a water-in-oil emulsion. Chemical Engineering Research & Design 2016, 110, 54-61.

[34] Zhao, X.; Tang, Y.; Zhao, B.; Wu, C.; Li, J.; Chu, C.; Liu, K.; Ding, Y., Collecting behaviors of high internal phase (HIP) emulsion in flotation of ultrafine high-ash content coal slime. International Journal of Coal Preparation and Utilization 2021, 1-21.

[35] Moulik, S. P.; Paul, B. K., Structure, dynamics and transport properties of microemulsions. Advances in Colloid and Interface Science 1998, 78 (2), 99-195.

[36] Reed RL, Healy RN. Some physicochemical aspects of microemulsion flooding: a review. Improved Oil Recovery by Surfactant and Polymer Flooding 1977, 383-437.

[37] Flanagan, J.; Singh, H., Microemulsions: A potential delivery system for bioactives in food. Critical Reviews in Food Science and Nutrition 2006, 46 (3), 221-237.

[38] Chatzidaki, M. D.; Papadimitriou, K.; Alexandraki, V., Microemulsions as Potential Carriers of Nisin: Effect of Composition on Structure and Efficacy. Langmuir 2016, 32 (35), 8988-98.

[39] Lawrence, M. J.; Rees, G. D., Microemulsion-based media as novel drug delivery systems. Advanced Drug Delivery Reviews 2000, 45 (1), 89-121.

[40] Antonietti M, Basten R, Lohmann S. Polymerization in microemulsions-a new approach to ultrafine, highly functionalized polymer dispersions. Macromol Chemistry and Physics 1995, 196 (2), 441-66.

[41] Zhang, P.; Gao, L., Synthesis and Characterization of CdS Nanorods via Hydrothermal Micro-emulsion. Langmuir 2003, 19 (1), 208-210.

[42] Aubert, T.; Grasset, F.; Mornet, S., Functional silica nanoparticles synthesized by water-in-oil microemulsion processes. Journal of Colloid and Interface Science 2010, 341 (2), 201-208.

[43] Richard, B.; Lemyre, J. ; Ritcey, A., Nanoparticle Size Control in Microemulsion Synthesis. Langmuir 2017, 33 (19), 4748-4757.

[44] Vollmer, D.; Vollmer, J., Bending free energy and spontaneous curvature for micelles and microemulsions with weak and strong surfactants. European Physical Journal E 2001, 4 (2), 153-159.

[45] Kahlweit, M.; Strey, R.; Busse, G., Effect of alcohols on the phase behavior of microemulsions. Journal of Physical Chemistry 1991, 95 (13), 5344-5352.

[46] Chiappisi, L.; Noirez, L.; Gradzielski, M., A journey through the phase diagram of a pharmaceutically relevant microemulsion system. Journal of Colloid and Interface Science 2016, 473, 52-59

[47] Penders, M.; Strey, R., Phase Behavior of the Quaternary System H_2O/n-octane/C_8E_5/n-octanol: Role of the Alcohol in Microemulsions. Journal of Physical Chemistry 1995, 99 (25), 10313-10318.

[48] Abbasi, S.; Radi, M., Food grade microemulsion systems: canola oil/lecithin: n-propanol/water. Food Chemistry 2016, 194, 972-9.

[49] Leng, L.; Yuan, X.; Chen, X., Characterization of liquefaction bio-oil from sewage sludge and its solubilization in diesel microemulsion. Energy 2015, 82, 218-228.

[50] Singh, A. V.; Hosseinidoust, Z.; Park, B. W.; Yasa, O.; Sitti, M., Microemulsion-Based Soft Bacteria-Driven Microswimmers for Active Cargo Delivery. ACS Nano 2017, 11 (10), 9759-9769.

[51] Watt, S. L.; Tunaley, D.; Biggs, S., The formation of water-in-oil microemulsions using a concentrated saline aqueous phase. Colloids and Surfaces A-Physicochemical and Engineering Aspects 1998, 137 (1-3), 25-33.

[52] Darrel W. Brownawell, Microemulsions of Water in Hydrocarbon Fuel for Engines. US: 3527581, 1970-09-08.

[53] Edward C; Wenzel; Henry W, Clear and stable liquid fuel compositions for internal Combustion engines. US: 4083698, 1978-04-11.

[54] Counter. J. A; John D. Kildea, Frothers for mineral flotation. US: 0090919, 2015-04-02.

[55] Counter. J. A; John D. Kildea, Collectors for mineral flotation. US: 9266120B2, 2016-02-23.

[56] Ian R.; Isabelle V., Water-in-oil microemulsions useful for oil field or gas field applications and methods for using the same. US: 6581687B2, 2003-01-24.

[57] Li, L.; Lu, X.; Qiu, J.; Liu, D., Effect of microemulsified collector on froth flotation of coal. Journal of the Southern African Institute of Mining and Metallurgy 2013, 113 (11), 877-880.

[58] Zhu, X.; Wei, H.; Hou, M.; Wang, Q.; You, X.; Li, L., Thermodynamic behavior and flotation kinetics of an ionic liquid microemulsion collector for coal flotation. Fuel 2020, 262.

[59] Zhang, R.; Xia, Y.; Guo, F.; Sun, W.; Cheng, H.; Xing, Y.; Gui, X., Effect of microemulsion on low-rank coal flotation by mixing DTAB and diesel oil. Fuel 2020, 260.

[60] Zhao, X.; Liu, S.; Fan, M., Preparation and application of microemulsion based on kerosene and 2-octanol. Coal Science and Technology 2017, 45 (04), 205-210.

[61] Ahmed, H. A. M.; Drzymala, J., Upgrading difficult-to-float coal using microemulsion. Minerals & Metallurgical Processing 2012, 29 (2).

[62] Valdivieso, A. L.; Cervantes, T. C.; Song, S.; Cabrera, A. R.; Laskowski, J. S., Dextrin as a non-toxic depressant for pyrite in flotation with xanthates as collector. Minerals Engineering 2004, 17 (9-10), 1001-1006.

[63] Bicak, O.; Ekmekci, Z.; Bradshaw, D. J.; Harris, P. J., Adsorption of guar gum and CMC on pyrite. Minerals Engineering 2007, 20 (10), 996-1002.

[64] Sun K, Wang X, Li G. Application of chemical reagents in coal preparation industry. Coal Processing and Comprehensive Utilization, 1998, 11(4): 31-32.

[65] Mu, Y.; Peng, Y.; Lauten, R. A., The depression of pyrite in selective flotation by different reagent systems - A Literature review. Minerals Engineering 2016, 96-97, 143-156.

[66] Bulatovic, S. M., Use of organic polymers in the flotation of polymetallic ores: A review. Minerals Engineering 1999, 12 (4), 341-354.

[67] Druschel, G.; Borda, M., Comment on "Pyrite dissolution in acidic media" by M. Descostes, P. Vitorge, and C. Beaucaire. Geochimica Et Cosmochimica Acta 2006, 70 (20), 5246-5250.

[68] Luther, G. W., Pyrite oxidation and reduction: Molecular orbital theory considerations. Geochimica et Cosmochimica Acta 1987, 51 (12), 3193-3199.

[69] Murphy, R.; Strongin, D. R., Surface reactivity of pyrite and related sulfides. Surface Science Reports 2009, 64 (1), 1-45.

[70] Wang, X. H.; Forssberg, K. S. E., Mechanisms of pyrite flotation with xanthates. International Journal of Mineral Processing 1991, 33 (1-4), 275-290.

[71] Shen, W. Z.; Fornasiero, D.; Ralston, J., Effect of collectors, conditioning pH and gases in the separation of sphalerite from pyrite. Minerals Engineering 1998, 11 (2), 145-158.

[72] Boulton, A.; Fornasiero, D.; Ralston, J., Selective depression of pyrite with polyacrylamide polymers. International Journal of Mineral Processing 2001, 61 (1), 13-22.

[73] Mu, Y.; Peng, Y.; Lauten, R. A., Electrochemistry aspects of pyrite in the presence of potassium amyl xanthate and a lignosulfonate-based biopolymer depressant. Electrochimica Acta 2015, 174, 133-142.

[74] Boulton, A.; Fornasiero, D.; Ralston, J., Depression of iron sulphide flotation in zinc roughers. Minerals Engineering 2001, 14 (9), 1067-1079.

[75] Moslemi, H.; Gharabaghi, M., A review on electrochemical behavior of pyrite in the froth flotation process. Journal of Industrial and Engineering Chemistry 2017, 47, 1-18.

[76] Gregory, J.; Barany, S., Adsorption and flocculation by polymers and polymer mixtures. Advances in Colloid and Interface Science 2011, 169 (1), 1-12.

[77] Liu, Q.; Laskowski, J. S., Adsorption of polysaccharides onto sulfides and their use in sulfide flotation. Polymers in Mineral Processing 1999, 71-88.

[78] Laskowski, J. S.; Liu, Q.; O'Connor, C. T., Current understanding of the mechanism of poly saccharide adsorption at the mineral/aqueous solution interface. International Journal of Mineral Processing 2007, 84 (1-4), 59-68.

[79] Ahmadi, M.; Gharabaghi, M.; Abdollahi, H., Effects of type and dosages of organic depressants on pyrite floatability in microflotation system. Advanced Powder Technology 2018, 29 (12), 3155-3162.

[80] Liu, Q.; Laskowski, J. S., On the adsorption mechanism of carboxymethyl cellulose. Polymers in Mineral Processing 1999, 357-372.

[81] Rath, R. K.; Subramanian, S.; Pradeep, T., Surface chemical studies on pyrite in the presence of polysaccharide-based flotation depressants. Journal of Colloid and Interface Science 2000, 229 (1), 82-91.

[82] Feng, B.; Feng, Q.; Lu, Y.; Gu, Y., The effect of PAX/CMC addition order on chlorite/ pyrite separation. Minerals Engineering 2013, 42, 9-12.

[83] Yuliani, S.; Torley, P. J.; D'Arcy, B., Extrusion of mixtures of starch and D-limonene encapsulated with beta-cyclodextrin: Flavor retention and physical properties. Food Research International 2006, 39 (3), 318-331.

[84] Adebowale, K. O.; Afolabi, T. A.; Lawal, O. S., Isolation, chemical modification and physicochemical characterisation of Bambarra groundnut (Voandzeia subterranean) starch and flour. Food Chemistry 2002, 78 (3), 305-311.

[85] Adebowale, K. O.; Lawal, O. S., Functional properties and retrogradation behaviour of native and chemically modified starch of mucuna bean (Mucuna pruriens). Journal of the Science of Food and Agriculture 2003, 83 (15), 1541-1546.

[86] Lawal, O. S., Composition, physicochemical properties and retrogradation characteristics of native, oxidized, acetylated and acid-thinned new cocoyam (Xanthosoma sagittifolium) starch. Food Chemistry 2004, 87 (2), 205-218.

[87] Pugh, R. J., Macromolecular organic depressants in sulphide flotation-a review, 1. Principles, types and applications. International Journal of Mineral Processing 1989, 25 (1-2), 101-130.

[88] Lawal, O. S.; Adebowale, K. O.; Ogunsanwo, B. M., Oxidized and acid thinned starch derivatives of hybrid maize: functional characteristics, wide-angle X-ray diffractometry and thermal properties. International Journal of Biological Macromolecules 2005, 35 (1-2), 71-79.

[89] Wang, Y. J.; Wang, L. F., Physicochemical properties of common and waxy corn starches oxidized by different levels of sodium hypochlorite. Carbohydrate Polymers 2003, 52 (3), 207-217.

[90] Kydros, K. A.; Gallios, G. P.; Matis, K. A., Modification of Pyrite and Sphalerite Flotation by Dextrin. Separation Science and Technology 1994, 29 (17), 2263-2275.

[91] Xu, D. D.; Aplan, F. F., Joint use of metal ion hydroxy complexes and organic polymers to depress pyrite and ash during coal flotation. Mining, Metallurgy & Exploration 1994, 11 (4), 223-230.

[92] Fletcher, B.; Chimonyo, W.; Peng, Y., A comparison of native starch, oxidized starch and CMC as copper-activated pyrite depressants. Minerals Engineering 2020, 156.

[93] Pugh, R. J., Macromolecular organic depressants in sulphide flotation - a review, 2. Theoretical analysis of the forces involved in the depressant action. International Journal of Mineral Processing 1989, 25 (1-2), 131-146.

[94] Bellman, C., Surface modification by adsorption of polymers and surfactants. Polymer surfaces and interfaces 2008, 235-259.

[95] Liu, Q.; Zhang, Y. H.; Laskowski, J. S., The adsorption of polysaccharides onto mineral surfaces: an acid/base interaction. International Journal of Mineral Processing 2000, 60 (3-4), 229-245.

[96] Zhang, H.; Liu, J.; Cao, Y.; Wang, Y., Effects of particle size on lignite reverse flotation kinetics in the presence of sodium chloride. Powder Technology 2013, 246, 658-663.

[97] Bulut, G.; Ceylan, A.; Soylu, B.; Goktepe, F., Role of starch and metabisuphite on pure pyrite and pyritic copper ore flotation. Physicochemical Problems of Mineral Processing 2012, 48 (1), 39-48.

[98] D. Fornasiero, J. Ralston, The interaction of ethyl xanthate with pyrite. Electrochemistry in Mineral and Metal Processing 1992, 191-220.

[99] Duan, J.; Fornasiero, D.; Ralston, J., Calculation of the flotation rate constant of chalcopyrite particles in an ore. International Journal of Mineral Processing 2003, 72 (1-4), 227-237.

[100] Ye, C.; Wang, D.; Shi, B., Alkalinity effect of coagulation with polyaluminum chlorides: Role of electrostatic patch. Colloids and Surfaces a-Physicochemical and Engineering Aspects 2007, 294 (1-3), 163-173.

[101] Yu, W.; J. Gregory; L. C. Campos, Breakage and re-growth of flocs: Effect of additional doses of coagulant species. Water Research 2011, 45, 6718-6724.

[102] Tang, H.; F. Xiao; D. Wang., Speciation, stability, and coagulation mechanisms of hydroxyl aluminum clusters formed by PAC and alum: A critical review. Advances in Colloid and Interface Science 2015, 226, 78-85.

[103] Liang, L.; Peng, Y.; Tan, J.; Xie, G., Intensified Ash Rejection in Coal Flotation by the Aggregation of Gangue Minerals Induced by Polyaluminum Chloride. International Journal of Coal Preparation and Utilization 2018, 38 (4), 180-191.

[104] Liang, L.; Tan, J.; Li, B.; Xie, G., Reducing quartz entrainment in fine coal flotation by polyaluminum chloride. Fuel 2019, 235, 150-157.

[105] Liang, L.; Peng, Y.; Tan, J.; Xia, W.; Xie, G., Effect of polyaluminum chloride on the flotation separation of coal from kaolinite. International Journal of Mineral Processing 2016, 154, 75-80.

[106] Dickinson, E.; Julian McClements, Food Emulsions: Principles, Practices, and Techniques 2nd edition. CRC Press, United States of America 2005.

[107] Hunter, R. J. Foundations of Colloid Science, Volume 1, Oxford University Press, Oxford 1986.

[108] Horne, D. S., Light Scattering Studies of Colloid Stability and Gelation. New Physico-Chemical Techniques for the Characterization of Complex Food Systems: 1995.

[109] Marcus J; Klossek M L; Touraud D, Nano-droplet formation in fragrance tinctures. Flavour & Fragrance Journal, 2013, 28 (5), 294-299.

[110] Marcus J; Müller M; Nistler J, Nano-droplet formation in water/ethanol or isopropanol / mosquito repellent formulations. Colloids & Surfaces A Physicochemical & Engineering Aspects, 2014, 458 (1), 3-9.

[111] Fischer V; Marcus J; Touraud D, Toward surfactant-free and water-free microemulsions. Journal of Colloid & Interface Science, 2015, 453, 186-193.

[112] Klossek M. L.; Touraud D.; Kunz W., Eco-solvents-cluster-formation, surfactantless micro emulsions and facilitated hydrotropy. Physical Chemistry Chemical Physics, 2013, 15 (26), 10971-10977.

[113] Xie, K.; Tang, J.; Fu, D.; Zhang, H.; Gao, A., Preparation of color polymeric nanomaterials containing dispersed dye by sunflower oil synergy and color transfer property by digital inkjet printing. Progress in Organic Coatings 2018, 125, 195-200.

[114] Zech O; Thomaier S; Bauduin P, Microemulsions with an ionic liquid surfactant and room temperature ionic liquids as polar pseudo-phase. Journal of Physical Chemistry B, 2009, 113 (2), 465-473.

[115] Bao, X. N.; Zhang, W. D.; Gang, H. Z., Formation of viscoelastic micellar solutions by a novel cationic surfactant and anionic salt system. Colloids and Surfaces A: Physicochemical and Engineering Aspects 2021, 611, 125795.

[116] Eicke, H. F.; Borkovec, M.; Dasgupta, B., Conductivity of water-in-oil microemulsions: a quantitative charge fluctuation model. Journal of Physical Chemistry 1989, 93 (1), 314-317.

[117] Evans, D. F.; Mitchell, D. J.; Ninham, B. W., Oil, water, and surfactant: Properties and conjectured structure of simple microemulsions. Journal of Physical Chemistry 1986, 90 (13), 2817-2825.

[118] Ninham, B. W.; Chen, S. J.; Evans, D. F., Role of oils and other factors in microemulsion design. Journal of Physical Chemistry 1984, 88 (24), 5855-5857.

[119] Warr, G. G.; Sen, R.; Evans, D. F.; Trend, J. E., Microemulsion formation and phase behavior of dialkydimethylammonium bromide surfactants. Journal of Physical Chemistry 1988, 92 (3), 774-783.

[120] Kallay, N.; Chittofrati, A., Conductivity of microemulsions: Refinement of charge fluctuation model. Journal of Physical Chemistry 1990, 94 (11), 4755-4756.

[121] Testard, F.; Zemb, T., Solute effect on connectivity of water-in-oil microemulsions. Langmuir 2000, 16 (2), 332-339.

[122] Bumajdad, A.; Eastoe, J., Conductivity of water-in-oil microemulsions stabilized by mixed surfactants. Journal of Colloid and Interface Science 2004, 274 (1), 268-76.

[123] Murashova, N. M.; Levchishin, S. Y.; Yurtov, E. V., Effect of Bis-(2-ethylhexyl) Phosphoric Acid on Sodium Bis-(2-ethylhexyl) Phosphate Microemulsion for Selective Extraction of Non-Ferrous Metals. Journal of Surfactants and Detergents 2014, 17 (6), 1249-1258.

[124] Chen, Z.-X.; Deng, S.-P.; Li, X.-K., Micellization and synergistic interaction of binary surfactant mixtures based on sodium nonylphenol polyoxyethylene ether sulfate. Journal of Colloid and Interface Science 2008, 318 (2).

[125] Liu, A.; Fan, M.; Fan, P., Interaction mechanism of miscible DDA-Kerosene and fine quartz and its effect on the reverse flotation of magnetic separation concentrate. Minerals Engineering 2014, 65, 41-50.

[126] Gurses, A.; Doymus, K.; Bayrakceken, S., Evaluation of response of brown coal to selective oil agglomeration by zeta potential measurements of the agglomerates. Fuel 1997, 76 (14-15), 1439-1444.

[127] Han, G.; Wen, S.; Wang, H.; Feng, Q., Effect of starch on surface properties of pyrite and chalcopyrite and its response to flotation separation at low alkalinity. Minerals Engineering 2019, 143.

[128] Smart, R. S.; Skinner, W. M.; Gerson, A. R., XPS of sulphide mineral surfaces: Metal-deficient, polysulphides, defects and elemental sulphur. Surface and Interface Analysis 1999, 28 (1), 101-105.

[129] Harmer, S. L.; Thomas, J. E.; Fornasiero, D.; Gerson, A. R., The evolution of surface layers formed during chalcopyrite leaching. Geochimica et Cosmochimica Acta 2006, 70 (17), 4392-4402.

[130] Mikhlin, Y. L.; Karacharov, A. A.; Likhatski, M. N., Effect of adsorption of butyl xanthate on galena, PbS, and HOPG surfaces as studied by atomic force microscopy and spectroscopy and XPS. International Journal of Mineral Processing 2015, 144, 81-89.

[131] Agar, G. E.; Stratton-Crawley, R.; Bruce, T. J., Optimizing the Design of Flotation Circuit. CIM Bulletin 1980, 73 (824), 173-181.

[132] Duan, J.; Fornasiero, D.; Ralston, J., Calculation of the flotation rate constant of chalcopyrite particles in an ore. International Journal of Mineral Processing 2003, 72 (1-4), 227-237.

[133] Min, M. A.; Nguyen, A. V., An exponential decay relationship between micro-flotation rate and back-calculated induction time for potential flow and mobile bubble surface. Minerals Engineering 2013, 40, 67-80

[134] Yoon, R.-H.; Soni, G.; Huang, K.; Park, S.; Pan, L., Development of a turbulent flotation model from first principles and its validation. International Journal of Mineral Processing 2016, 156, 43-51.

[135] Albijanic, B.; Subasinghe, N.; Park, C. H., Flotation kinetic models for fixed and variable pulp chemical conditions. Minerals Engineering 2015, 78, 66-68.

[136] Feng, D.; Aldrich, C., Effect of preconditioning on the flotation of coal. Chemical Engineering Communications 2005, 192 (7), 972-983.

[137] Ni, C.; Xie, G.; Jin, M.; Peng, Y.; Xia, W., The difference in flotation kinetics of various size fractions of bituminous coal between rougher and cleaner flotation processes. Powder Technology 2016, 292, 210-216.

[138] Xia, Y.; Yang, Z.; Zhang, R.; Xing, Y.; Gui, X., Performance of used lubricating oil as flotation collector for the recovery of clean low-rank coal. Fuel 2019, 239, 717-725.

[139] Honaker, R. Q.; Saracoglu, M.; Huang, Q., Application of hydrophobic and magnetic plastic particles for enhanced flotation recovery. Minerals Engineering 2016, 98, 223-231.

[140] Kowalczuk, P. B.; Zawala, J., A relationship between time of three-phase contact formation and flotation kinetics of naturally hydrophobic solids. Colloids and Surfaces A: Physicochemical and Engineering Aspects 2016, 506, 371-377.

[141] Drzymala, J.; Ahmed, H. A. M., Mathematical equations for approximation of separation results using the Fuerstenau upgrading curves. International Journal of Mineral Processing 2005, 76 (1), 55-65.

[142] Drzymala, J.; Kowalczuk, P. B.; Oteng-Peprah, M., Application of the grade-recovery curve in the batch flotation of Polish copper ore. Minerals Engineering 2013, 49, 17-23.

[143] Bakalarz, A.; Drzymala, J., Interrelation of the fuerstenau upgrading curve parameters with kinetics of separation. Physicochemical Problems of Mineral Processing 2013, 49 (2), 443-451.

[144] Polat, M.; Polat, H.; Chander, S., Physical and chemical interactions in coal flotation. International Journal of Mineral Processing 2003, 72 (1-4), 199-213.

[145] Chen, S.; Wang, S.; Li, L., Exploration on the mechanism of enhancing low-rank coal flotation with cationic surfactant in the presence of oily collector. Fuel 2018, 227, 190-198.

[146] Harimawan, A.; Zhong, S.; Lim, C. T.; Ting, Y. P., Adhesion of B. subtilis spores and vegetative cells onto stainless steel--DLVO theories and AFM spectroscopy. Journal of Colloid and Interface Science 2013, 405, 233-41.

[147] Liu, C.; Zhang, W.; Song, S.; Li, H., Effects of lizardite on pentlandite flotation at different pH: Implications for the role of particle-particle interaction. Minerals Engineering 2019, 132, 8-13.

[148] Piñeres, J.; Barraza, J., Energy barrier of aggregates coal particle–bubble through the extended DLVO theory. International Journal of Mineral Processing 2011, 100 (1-2), 14-20.

[149] Wu, J.; Liu, F.; Yang, H., Effect of specific functional groups on oil adhesion from mica substrate: Implications for low salinity effect. Journal of Industrial and Engineering Chemistry 2017, 56, 342-349.

[150] Xu, Z; R.-H, Yoon, The role of hydrophobia interactions in coagulation. Journal of Colloid and Interface Science 1989, 132 (2), 532-541.

[151] R, Y.; L, M., Application of extended DLVO theory, IV: Derivation of flotation rate equation from first principles. Journal of Colloid and Interface Science 1996, 181, 613-626.

[152] Faghihnejad, A.; Zeng, H., Hydrophobic interactions between polymer surfaces: using polystyrene as a model system. Soft Matter 2012, 8 (9).

[153] Hao, H.; Li, L.; Yuan, Z.; Liu, J., pH-controlled dispersion of micro-fine siderite from hematite and quartz. Powder Technology 2018, 339, 710-716.

[154] R.-H.Yoon, The role of hydrodynamic and surface forces in bubble-particle interaction. International Journal of Mineral Processing 2000, 58 (1-4), 129-143.

[155] Zhao, X.; Meng, Q.; Yuan, Z.; Zhang, Y.; Li, L., Effect of sodium silicate on the magnetic separation of ilmenite from titanaugite by magnetite selective coating. Powder Technology 2019, 344, 233-241.

[156] Zhou, F.; Wang, L.; Xu, Z.; Ruan, Y.; Zhang, Z.; Chi, R., Role of reactive oily bubble in apatite flotation. Colloids and Surfaces A: Physicochemical and Engineering Aspects 2017, 513, 11-19.

[157] Hu, P.; Liang, L.; Li, B.; Xia, W., Heterocoagulation between coal and quartz particles studied by the mineral heterocoagulation quantifying system. Minerals Engineering 2019, 138, 7-13.

[158] Wang, J.; Fu, X.; Hu, E., Experimental study on flocculation flotation of ultra-clean coal from slime. Journal of China Coal Society 2015, 40 (8), 1929-1935.

[159] Wang, Y.; Cao, Y.; Li, G.; Liao, Y.; Xing, Y.; Gui, X., Combined effect of chemical composition and spreading velocity of collector on flotation performance of oxidized coal. Powder Technology 2018, 325, 1-10.

[160] Jia, R. H.; Harris, G. H.; Fuerstenau, D. W., An improved class of universal collectors for the flotation of oxidized and/or low-rank coal. International Journal of Mineral Processing 2000, 58 (1-4), 99-118.

[161] Moxon, N. T.; Bensley, C. N.; Keast-Jones, R.; Nicol, S. K., Insoluble oils in coal flotation: The effects of surface spreading and pore penetration. International Journal of Mineral Processing 1987, 21 (3), 261-274.

[162] Chattopadhyay, A. K.; Shah, D. O.; Ghaicha, L., Double-tailed surfactants and their chain length compatibility in water-in-oil emulsions. Langmuir 1992, 8 (1), 27-30.

[163] Ushikubo, F. Y.; Cunha, R. L., Stability mechanisms of liquid water-in-oil emulsions. Food Hydrocolloids 2014, 34, 145-153.

[164] Wang, X. H.; Forssberg, K. S. E., The solution electrochemistry of sulfide-xanthate-cyanide systems in sulfide mineral flotation. Minerals Engineering 1996, 9 (5), 527-546.

[165] Chen, J.; Li, Y.; Chen, Y., Cu-S flotation separation via the combination of sodium humate and lime in a low pH medium. Minerals Engineering 2011, 24 (1), 58-63.

[166] Szargan, R.; Karthe, S., XPS studies of xanthate adsorption on pyrite. Applied Surface Sciences 1992, 55 (4), 227-232.

[167] Hu, Y.; Zhang, S.; Qiu, G.; Miller, J., Surface chemistry of activation of lime-depressed pyrite in flotation. Transactions of Nonferrous Metals Society of China 2000, 10 (6).

[168] Myers, R. H.; Khuri, A. I.; Carter, W. H., Response Surface Methodology-1966-1988. Technometrics 1989, 31 (2), 137-157.

[169] Khanjani, A.; Sobati, M. A., Performance and emission of a diesel engine using different water/waste fish oil (WFO) biodiesel/diesel emulsion fuels: Optimization of fuel formulation via response surface methodology (RSM). Fuel 2021, 288.

[170] Garg, A.; Jain, S., Process parameter optimization of biodiesel production from algal oil by response surface methodology and artificial neural networks. Fuel 2020, 277.

[171] Elkelawy, M.; Bastawissi, H. A.-E.; Esmaeil, K. K., Maximization of biodiesel production from sunflower and soybean oils and prediction of diesel engine performance and emission characteristics through response surface methodology. Fuel 2020, 266.

[172] Li, T.; Zhu, Z.; Wang, D.; Yao, C.; Tang, H., Characterization of floc size, strength and structure under various coagulation mechanisms. Powder Technology 2006, 168 (2), 104-110.

[173] Wang, D.; Sun, W.; Xu, Y., Speciation stability of inorganic polymer flocculant-PACl. Colloids and Surfaces A: Physicochemical and Engineering Aspects 2004, 243 (1-3), 1-10.

[174] Yang, Z.; Gao, B.; Wang, Y.; Wang, Q.; Yue, Q., Aluminum fractions in surface water from reservoirs by coagulation treatment with polyaluminum chloride (PAC): Influence of initial pH and OH^-/Al^{3+} ratio. Chemical Engineering Journal 2011, 170 (1), 107-113.

[175] Zhang, P.; Wu, Z.; Zhang, G., Coagulation characteristics of polyaluminum chlorides PAC-Al_{30} on humic acid removal from water. Separation and Purification Technology 2008, 63 (3), 642-647.

[176] Gupta S; Manohar C.S. An improved response surface method for the determination of failure probability and importance measures. Structural Safety 2004, 26(2),123-139.

[177] Verwey, E. J. W., Theory of the stability of lyophobic colloids. Journal of Physical and Colloid Chemistry 1947, 51 (3), 631-636.

[178] Song, S. X.; Lopez-Valdivieso, A.; Reyes-Bahena, J. L.; Bermejo-Perez, H. I., Hydrophobic flocculation of sphalerite fines in aqueous suspensions induced by ethyl and amyl xanthates. Colloids and Surfaces a-Physicochemical and Engineering Aspects 2001, 181 (1-3), 159-169.

[179] Dihang, D.; Aimar, P.; Kayem, J.; Koungou, S. N., Coagulation and flocculation of laterite suspensions with low levels of aluminium chloride and polyacrylamids. Chemical Engineering and Processing: Process Intensification 2008, 47 (9-10), 1509-1519.

[180] Liang, L.; Tan, J.; Peng, Y.; Xia, W.; Xie, G., The role of polyaluminum chloride in kaolinite aggregation in the sequent coagulation and flocculation process. Journal of Colloid and Interface Science 2016, 468, 57-61.

[181] Demoisson, F.; Mullet, M.; Humbert, B., Investigation of pyrite oxidation by hexavalent chromium: Solution species and surface chemistry. Journal of Colloid and Interface Science 2007, 316 (2), 531-540.

[182] Ejtemaei, M.; Nguyen, A. V., Characterisation of sphalerite and pyrite surfaces activated by copper sulphate. Minerals Engineering 2017, 100, 223-232.

[183] Cai, Y.; Pan, Y.; Xue, J.; Sun, Q.; Su, G.; Li, X., Comparative XPS study between experimentally and naturally weathered pyrites. Applied Surface Science 2009, 255 (21), 8750-8760.

[184] Jones, C. F.; Lecount, S.; Smart, R. S. C.; White, T. J., Compositional and structural alteration of pyrrhotite surfaces in solution: XPS and XRD studies. Applied Surface Science 1992, 55 (1), 65-85.

[185] Yu, X. R.; Liu, F.; Wang, Z. Y.; Chen, Y., Auger parameters for sulfur-containing compounds using a mixed aluminum-silver excitation source. Journal of Electron Spectroscopy and Related Phenomena 1990, 50 (1-2), 159-166.

[186] Leiro, J. A.; Mattila, S. S.; Laajalehto, K., XPS study of the sulphur 2p spectra of pyrite. Surface Science 2003, 547 (1-2), 157-161.

[187] Mattila, S.; Leiro, J. A.; Laajalehto, K., Surface XPS core-level shifts of FeS2. Applied Surface Science 2003, 212, 97-100.

[188] Mycroft, J. R.; Bancroft, G. M.; McIntyre, N. S.; Lorimer, J. W.; Hill, I. R., Detection of sulfur and polysulfides on electrochemically oxidized pyrite surfaces by x-ray photoelectron spectroscopy and Raman spectroscopy. Journal of Electroanalytical Chemistry 1990, 292 (1-2), 139-152.

[189] Schaufuss, A. G.; Nesbitt, H. W.; Kartio, I.; Laajalehto, K.; Bancroft, G. M.; Szargan, R., Incipient oxidation of fractured pyrite surfaces in air. Journal of Electron Spectroscopy and Related Phenomena 1998, 96 (1-3), 69-82.

[190] Von Oertzen, G. U.; Harmer, S. L.; Skinner, W. M., XPS and ab initio calculation of surface states of sulfide minerals: pyrite, chalcopyrite and molybdenite. Molecular Simulation 2006, 32 (15), 1207-1212.

[191] Von Oertzen, G. U.; Skinner, W. M.; Nesbitt, H. W., Ab initio and x-ray photoemission spectroscopy study of the bulk and surface electronic structure of pyrite (100) with implications for reactivity. Physical Review B 2005, 72 (23).

[192] Wagner, C. D.; Taylor, J. A., Contributions to screening in the solid state by electron systems of remote atoms: Effects to photoelectron and Auger transitions. Journal of Electron Spectroscopy and Related Phenomena 1982, 28 (3), 211-217.

[193] Schaufuss, A. G.; Nesbitt, H. W.; Kartio, I., Reactivity of surface chemical states on fractured pyrite. Surface Science 1998, 411 (3), 321-328.

[194] Murphy, R.; Strongin, D. R., Surface reactivity of pyrite and related sulfides. Surface Science Reports 2009, 64 (1), 1-45.

[195] Nesbitt, H. W.; Muir, I. J., X-ray photoelectron spectroscopic study of a pristine pyrite surface reacted with water vapour and air. Geochimica et Cosmochimica Acta 1994, 58 (21), 4667-4679.

[196] Uhlig, I.; Szargan, R.; Nesbitt, H. W.; Laajalehto, K., Surface states and reactivity of pyrite and marcasite. Applied Surface Science 2001, 179 (1-4), 222-229.

[197] Liang, L.; Tan, J.; Peng, Y.; Xia, W.; Xie, G., The role of polyaluminum chloride in kaolinite aggregation in the sequent coagulation and flocculation process. Journal of Colloid and Interface Science 2016, 468, 57-61.

[198] McCafferty, E.; Wightman, J. P., Determination of the concentration of surface hydroxyl groups on metal oxide films by a quantitative XPS method. Surface and Interface Analysis 1998, 26 (8), 549-564.

[199] Rotole, J. A.; Sherwood, P. M. A., Nordstrandite ($Al(OH)_3$) by XPS. Surface Science Spectra 1998, 5 (1), 32-38.

[200] Wang, J.; Xie, L.; Liu, Q.; Zeng, H., Effects of salinity on xanthate adsorption on sphalerite and bubble–sphalerite interactions. Minerals Engineering 2015, 77, 34-41.

[201] Chen, M.; Wang, X.; Yu, Y. H.; Pei, Z. L.; Bai, X. D.; Sun, C.; Huang, R. F.; Wen, L. S., X-ray photoelectron spectroscopy and auger electron spectroscopy studies of Al-doped ZnO films. Applied Surface Science 2000, 158 (1), 134-140.

[202] Hinnen, C.; Imbert, D.; Siffre, J. M.; Marcus, P., An in situ XPS study of sputter-deposited aluminium thin films on graphite. Applied Surface Science 1994, 78 (3), 219-231.

[203] Jin, S.; Atrens, A., ESCA-studies of the structure and composition of the passive film formed on stainless steels by various immersion times in 0.1 M NaCl solution. Applied Physics A 1987, 42 (2), 149-165.

[204] Zhang, W.; Honaker, R. Q.; Groppo, J. G., Flotation of monazite in the presence of calcite part I: Calcium ion effects on the adsorption of hydroxamic acid. Minerals Engineering 2017, 100, 40-48.

[205] Li, Q.; Lin, B.; Wang, K.; Zhao, M.; Ruan, M., Surface properties of pulverized coal and its effects on coal mine methane adsorption behaviors under ambient conditions. Powder Technology 2015, 270, 278-286.

[206] He, Q.; Wan, K.; Hoadley, A.; Yeasmin, H.; Miao, Z., TG-GC-MS study of volatile products from Shengli lignite pyrolysis. Fuel 2015, 156, 121-128.

[207] Meng, F.; Yu, J.; Tahmasebi, A.; Han, Y.; Zhao, H.; Lucas, J.; Wall, T., Characteristics of Chars from Low-Temperature Pyrolysis of Lignite. Energy & Fuels 2014, 28 (1), 275-284.

[208] Sokolovic, J. M.; Stanojlovic, R. D.; Markovic, Z. S., Activation of oxidized surface of anthracite waste coal by attrition. Physicochemical Problems of Mineral Processing 2012, 48 (1), 5-18.